UNCLASSIFIED

AD NUMBER

AD847204

NEW LIMITATION CHANGE

TO

Approved for public release, distribution unlimited

FROM

Distribution authorized to U.S. Gov't. agencies and their contractors; Critical Technology; OCT 1968. Other requests shall be referred to Air Force Office of Scientific Research, Attn: SEEP, 1400 Wilson Boulevard, Arlington, VA 22209.

AUTHORITY

AFOSR ltr, 12 Nov 1971

AD847304

Project THEMIS

D D C
FEB 5 1969
C

College of Engineering
UNIVERSITY OF UTAH
Salt Lake City, Utah

2. This document is subject to special export controls and each transmittal to foreign governments or foreign nationals may be made only with prior approval of AROD (Durham).

Annual Report
1 September 1967--31 August 1968

THE CHEMISTRY AND MECHANICS OF COMBUSTION

WITH

APPLICATIONS TO ROCKET ENGINE SYSTEMS

October 1968   UTEC DO 68-065

A Project THEMIS Program
through the
U. S. Air Force Office of Scientific Research

M. L. Williams
Program Manager

College of Engineering
UNIVERSITY OF UTAH
Salt Lake City, Utah

FOREWORD

As part of Project THEMIS, the Department of Defense, acting through
the U. S. Air Force Office of Scientific Research with Dr. B. A. Wolfson
as Cognizant Scientist, awarded an integrated applied research program
concerned with the "Chemistry and Mechanics of Combustion with Applica-
tion to Rocket Engine Systems" to the University of Utah. This investi-
gation in the College of Engineering is under the general direction of
Professor M. L. Williams as Program Manager and was initiated in September
1967.

The purpose of this program, which is integrated with our academic
objectives, is to study the interdependence of combustion processes and
the physics-mechanical behavior of solid fuel materials within the context
of a rocket engine system. It is intended to capitalize upon a quanti-
tative understanding of molecular structure, which affects both the
combustion and mechanics behavior, and treat the propellant fuel and
associated inert components as a materials system--from processing, to a
determination of the constitutive equation as needed to assess structural
integrity, and failure under various environmental and loading conditions.
Concurrently, the tasks are concerned with propellant as an energy source--
from ignition, through burning, gas dynamics, interaction with nozzle
and insulation components, and consideration of electron noise and radar
attenuation in the plume.

Six task areas are presently envisioned, each of which is under the
direction of a Principal Investigator. Coordination of the various tasks
is accomplished by regular meetings of the senior investigators and
appropriate external consultants from industrial and government organiza-
tions. The six areas, not necessarily of equal emphasis, include:

1. Combustion and Transport Mechanisms
2. Flow and Heat Transfer
3. Ablation Mechanisms
4. Radiation Attenuation and Plasma Physics
5. Mechanics of Solids
6. Transition to Detonation Mechanisms

External comments are solicited and direct contact with the individual
investigators is encouraged.

PREFACE

The establishment of a Proj   THEMIS program at the University of
Utah has, in conjunction with other associated research, permitted the
College of Engineering to embark upon a consolidated and integrated series
of investigations in the general area of combustion and combustion related
research. As a particular and immediate result of Project THEMIS, several
specific studies, which have the molecular morphology as the common thread
affecting both the combustion and mechanical behavior, have been initiated.
While as individual components they supplement a broader program, they
also comprise individual tasks and as such are being reported separately.
Their internal coordination and integration with the broader academic and
research program of the College is being accomplished through frequent
meetings of the senior investigators.

A study of the combustion process is intimately associated with an
accurate knowledge of chemical kinetics, as analytically established and
experimentally verified. Many of the present observations of polymer
decomposition have been made at unrealistically low burning rates. In the
studies planned for Task 1, measurements will be made at rates two orders
of magnitude faster than conventional ones. Preliminary experiments with
a PBAA solid fuel shows that a pressure dependent endotherm exists in the
solid before the gaseous products are evolved, thus illustrating a reason
for our concern with the molecular chemical structure and the associated
kinetics. These internal processes are important also in Task 6, wherein
we inquire as to the possibility of internal heating from the passage of a
viscoelastic shock wave through the solid causing sufficient temperature
rise to trigger ignition or detonation. This latter situation is an
interesting illustration of thermo-mechanical coupling which can exist in
a rate dependent material. While such responses have been calculated for
linear viscoelastic media subjected to (weak) stress waves, the equation
of state and the coupled heat and equilibrium equations are considerably
more complicated for higher rate and more intense loadings.

As a conjunction of portions of Tasks 1 and 6 wherein the chemical
structure may affect both the combustion and the mechanical behavior,

Task 5 seeks to pursue in greater detail the appropriate form of the equations governing deformation of a rate sensitive solid. As a point of departure, the joint thermo-mechanical state will be reviewed, both analytically and experimentally, with especial emphasis upon the non-linear effects introduced by geometry, such as "dewetting" of propellant binder and oxidizer, and by the material itself, such as the large deformations which are characteristic of rubberlike media. Ultimately it is hoped to incorporate into these equations any chemical effects sensitive to high rate loading input. Such inclusion would possess the incidental advantage of providing a reference point in the event the ablation studies of Task 3 indicate strong coupling between materials and structural integrity. The principal objective of Task 3 is to attain methods for controlling the chemical kinetics of the sub-surface internal endothermic-exotheric reactions, with particular reference to the possibility of weight reduction in rocket components such as nozzles.

Inasmuch as Task 3 will examine the interdependency of pyrolysis of materials and surface chemical attack during combustion along the interface between the ablating material and the flowing gas, some aspects of this task are closely related to the aims of Task 2 which is concerned with temperature and velocity measurements in a turbulent boundary layer subject to mass injection and combustion. Both subsonic and supersonic gas flow will eventually be considered in measuring heat transfer characteristics which as already mentioned are essential to the proper design of ablating components such as nozzles. The present experiments, which include injection of air into air and nitrogen and hydrogen into air through a porous wall, have required the development of a temperature sensor which has worked well uncooled in non-combustive gas flow. Preliminary experiments using a cooled sensor in the combustion zone have yielded encouraging results.

The last of the current tasks, Task 4, has yet to be integrated fully into the overall program; its impact will depend upon the success of its exploratory study into the use of microwave techniques as a diagnostic tool for deducing the electron temperature in the combustion chamber. The attenuation of microwave radiation has been used for many years to measure ionization density and collision frequency in the combustion products behind the exit plane of the exhaust. The present study is directed toward achieving similar results inside the combustion chamber. The initial results have been encouraging and lead us to hope that concurrent improvements in data

reduction can include analytical provision for pressure waves, non-uniform combustion, and source-sink reactions which are occurring in the chamber. Such deductions and proper interpretation of the electron temperature should be of considerable value in achieving the objectives of Task 1 wherein the chemical kinetics of combustion are being investigated. Finally, one other application of microwave diagnostic techniques has been tried with reasonable initial success. As an extension of the ultrasonic, non-destructive test (NDT) technique commonly used to detect internal flaws in metals, microwave radiation techniques have been used to find internal voids in filled, solid fuel materials. Ultrasonic waves are too easily attenuated and subsequent evaluation is frequently non-discriminating. At the present time, a satisfactory microwave antenna design has been designed and used in the pilot experiments. If the outcome from all the present test components is successful, flaws as small as one-thousandth of an inch in size could be detected in typical solid rocket fuels.

While the tasks discussed here have not been completely defined, it is believed that a balance between definition and flexibility has been maintained which is appropriate to the time the work has been in development. Comments are solicited from the technical community and direct communication with the individual senior investigators is encouraged.

THE CHEMISTRY AND MECHANICS OF COMBUSTION

WITH

APPLICATION TO ROCKET ENGINE SYSTEMS

TABLE OF CONTENTS

THE CHEMISTRY AND MECHANICS OF COMBUSTION

WITH

APPLICATION TO ROCKET ENGINE SYSTEMS

TASK 1   Combustion and Transport Mechanisms

A. D. Baer
N. W. Ryan

October 1968

College of Engineering
UNIVERSITY OF UTAH
Salt Lake City, Utah

PREFACE

Task 1, as outlined in the original proposal, was to be a study of gas-gas mixing at the boundary between two fast-moving gas streams. Work on this task was postponed for the first year of the project in order to permit intensified effort on other tasks.

A review of the project as a whole, in the light of an opportunity afforded by changes in the sponsorship of related combustion projects, now leads us to propose replacing the task on mixing with one on polymer decomposition mechanisms. We look upon this change as a means to strengthen the project by initiating the investigation of molecular mechanisms of combustion, later expanding to the study of molecular mechanisms of thermo-mechanical and chemico-mechanical behavior of propellant materials.

The investigators have already reported some work on polymer decomposition (AFOSR Final Report 67-1901), and this work is still in progress under other sponsorship. It has been concerned almost exclusively with measurements of the thermal effects attending the rapid heating of polymers and propellant-like materials, very limited work having been done on the chemical aspects. The thermal approach under other sponsorship should be completed in September 1968 and a combined thermal and chemical approach will be initiated as Task 1 under THEMIS at that time.

.0 INTRODUCTION

The several conventional methods developed for the study of the
ermal decomposition of polymeric and composite materials (DTA, TGA,
`C) suffer from the defect that. at the small heating rates employed,
ie high-temperature decomposition mechanisms probably active in combustion
rocesses are not observed; the virgin material is consumed or altered by
w-temperature mechan ms before the decomposition temperatures associated
th combustion processes are reache. The work already performed at this
icility has employed heatin, rates 50 to 100 times as great as those
ed in conventional studies.

Briefly, the studies with PBAA polymer have revealed that, if heating
kes place in an inert environment, a pressure-dependent endotherm is
served well before a significant amount of gaseous product is evolved.
heating takes place in the presence of hot oxygen, or even in nitrogen
en the polymer contains twenty percent or more of ammonium perchlorate,
e first significant event is an exotherm; and it is observed well before
visible flame signals ignition. The dependence of the temperatures at
ich these events occur on heating rate, pressure, and oxygen temperature
rmits some inferences concerning mechanism but serves mainly to identify
i partially to characterize events whose chemistry must be studied before
iful result can be published.

Studies now in progress define the problems which will be investigated
Task 1. The current study has yielded data concerning the polymer-
gen reaction which can be used to discriminate between proposed mechanisms
· the reaction. However, since these data were obtained under transient
ditions, their mechanistic interpretation must account for time-dependent
perature and concentration variations in the solid and gas phases; and
engthy and very complex data-analysis scheme must be developed. It is
posed to determine the polymer-oxidative-species reaction mechanism by
eloping and applying such a scheme to the existing data and to the
ults of additional tests which may be required. Considerable effort
i be directed to develop sampling and analytical techniques that can be
d with methods of rapid heating of small test specimens. Professors

Boyd and Futrell will provide supporting talent in methods of spectroscopy, mass spectroscopy, and polymer characterization.

In the following years of the task, it is expected that the methods developed will be exploited in additional reaction-mechanism studies; and experiments in thermo-mechanical and chemico-mechanical phenomena--supporting Task 3, 5, and 6--will be initiated.

THE CHEMISTRY AND MECHANICS OF COMBUSTION
WITH
APPLICATIONS TO ROCKET ENGINE SYSTEMS

TASK 2 Flow and Heat Transfer

L. K. Isaacson

October 1968

College of Engineering
UNIVERSITY OF UTAH
Salt Lake City, Utah

PREFACE

A basic objective of the Project THEMIS program, "The Chemistry and Mechanics of Combustion with Applications to Rocket Engine Systems," at the University of Utah, has been the consideration of solid propellants as an energy source and the study of the means required to convert this energy into reliable propulsion work. Six research tasks were undertaken in the areas of combustion and transport mechanisms, flow and heat transfer, ablation mechanisms, radar attenuation and plasma physics, mechanics of high solids loaded systems, and transition to detonation mechanisms. Task 2 of this program, "Flow and Heat Transfer," has been concerned with the study of the turbulent boundary layer with mass injection and combustion. Characteristics of hot-film sensors, both uncooled and cooled, have been examined, with the result that these sensors may be used as reliable diagnostic tools in reasonably high temperature environments.

In the area of solid-propellant rocket design, the results of this program should aid in the understanding of the behavior of ablator response to the combustion gas environment for solid propellant rocket nozzles ana insulators, and should provide information concerning gas-gas phase m. n and combustion processes which would aid in the understanding of propellant ignition and combustion phenomenon.

Several aspects of this research are directly comparable to situations occurring in solid propellant rocket systems presently being developed. For example, the injectants used in Task 2, up to this point, have been air into air, and various mixtures of hydrogen and nitrogen into an air turbulent boundary layer. Mixtures of comparable compositions, i.e., light gas with heavy gas (H_2 with CO) occur in the combustion products of the Poseidon Stage One and Poseidon Stage Two rocket motors. Hence, the results of Task 2 concerning the turbulent mixing and transport characteristics for boundary layer injection should be applicable in the evaluation of the heat transfer occurring in present day solid propellant rocket motors.

During this past year, the supersonic combustion simulation facility has been completed. This facility provides the capability for simulating combustor inlet conditions for air-breathing systems operating in the Mach number range of from five to twelve, with an upper altitude limitation of 130,000 ft. It is anticipated that the information and capability obtained from the use of the subsonic combustion wind tunnel will be directly applicable in the supersonic combustion facility.

The use of the water-cooled hot-film sensor will be extended to the supersonic wind tunnel. Because of the increased ruggedness of the hot-film sensor, it is anticipated that the hot-film probe will yield turbulent mixing and combustion data in the supersonic range, which are normally very difficult to obtain.

The specific results obtained under Task 2 of Project THEMIS for the period 1 September 1967 to 31 August 1968 will be presented under three separate sections. These sections, with a brief summary for each, are as follows:

Subsonic Turbulent Boundary Layer with Heat and Mass Transfer

Studies of the subsonic turbulent boundary layer with both mass and heat transfer from a porous surface have been completed. Results indicate that a temperature inner law and a temperature defect law may be written which describes the resultant temperature distribution across the thermal boundary layer. The temperature inner law and the temperature defect law are expressions from which the local temperature in the boundary layer at a given distance from the surface may be determined, given the surface skin-friction coefficient, the surface heat transfer, and the mass-injection velocity at the wall.[9, 10] Presence of the heated porous surface causes a significant increase in longitudinal turbulent velocity fluctuation intensity. These results were obtained using hot-film sensors.

Studies of the effect of variable composition on the response of hot-film sensors in an isothermal turbulent boundary layer have also been completed. Mixtures of hydrogen and nitrogen were injected across the porous plate into the subsonic turbulent boundary layer. The mixture compositions were varied from pure hydrogen to pure nitrogen. Concentration, dynamic pressure, and hot film power dissipation profiles were

obtained across the boundary layer. The power dissipation profiles were obtained with constant temperature hot-film sensors and the results indicate that a significant increase in heat flux is produced when the environment consists of a mixture of hydrogen and air or hydrogen and nitrogen. Variable composition was found to significantly increase the longitudinal turbulent velocity fluctuation intensity.

A technique was developed where the three profiles discussed above were utilized in determining the velocity profile across the boundary layer. The turbulent shear stress and eddy viscosity distribution were then obtained from the results.

Subsonic Turbulent Boundary Layer with Injection and Combustion

Preliminary profiles of temperature, dynamic pressure, and heat flux to a cooled probe have been obtained through the flame zone of a turbulent boundary layer with hydrogen transpiration and combustion. These results indicate that the cooled probe may be used in the flame zone for the acquisition of turbulent mixing and combustion data. An intensive effort is underway to obtain detailed profiles of temperature, dynamic pressure, static pressure, concentration, and sensor heat flux across the turbulent boundary layer and through the flame zone.

Supersonic Combustion Boundary-Layer Facility

A supersonic boundary layer channel with an open jet section has been installed and is undergoing calibration. The tunnel plenum and mixing chamber has been designed for a total pressure of 200 psi and a steady flow temperature of 2500^{0}F. The Mach 2.5 and 3.0 water-cooled nozzle blocks are rated at a steady-state operating temperature of 1500^{0}F with the capability of withstanding much higher temperatures for short periods of time. It is anticipated that the porous-wall test section and injection manifold will be fabricated and installed during this coming year.

TABLE OF CONTENTS

TASK 2 Flow and Heat Transfer

1.0 INTRODUCTION

During the past decade, solid propellant rocket motor technology has reached a high level of capability for designing and developing operational solid propellant rocket systems. This capability has been achieved primarily through an extensive motor components testing program, wherein many major tests have been conducted to prove each design concept. As a result of this testing, empirical correlations of motor performance and nozzle thermal protection performance have been achieved. However, these correlations have been largely restricted to the type of propellant and type of nozzle insulating material for which they were developed and have not been readily extended to new propellant formulations and new nozzle insulating materials.

Solid-propellant rocket motor performance and nozzle structural integrity can be adequately predicted only if the surface erosion rate and the thermal penetration rates can be accurately evaluated. A fundamental requirement for the evaluation of these rates is an understanding of the heat flux from the hot, usually turbulent, boundary layer to the ablating surface. Task 2 of Project THEMIS is an experimental and theoretical program of research directed toward clarifying some of the basic mechanisms occurring in the turbulent boundary layer with heat transfer and mass injection. One of the basic problems remaining to be solved in rocket nozzle heat transfer analysis is the description of the turbulent transport properties in the turbulent boundary layer occurring on the nozzle surface.

Another area of major interest in propulsion development, and of interest to Task 2 of Project THEMIS, is the rapidly expanding field of hypersonic flight in the earth's atmosphere. In fact, in recent years the literature on hypersonic flight in the Mach 6 to 12 range has considered a large variety of missions and vehicle configurations which have included some scheme for employing air-breathing propulsion with air-augmentation of rocket motors or utilization of supersonic combustion in a basic ramjet cycle, commonly classified as a scramjet. However, Henry[1]

has recently pointed out that some of the assumptions on which these studies are based have not been substantiated through experimental results. One of the basic problems which remains to be explored is the matter of how to inject the fuel to obtain uniform distribution without significant thrust penalties and undue flow disturbances. Another major problem is that of ignition when the range of operation of the supersonic combustor extends toward the low flight Mach number regime.

To gain further insight into solutions for these problems in both solid-propellant rocket technology and supersonic combustion, a means must be developed by which local flow characteristics such as velocity, temperature, concentration, and turbulent transport properties may be obtained. Recently developed constant temperature anemometry equipment with cooled film sensors may be suitable for obtaining such information. It has been the objective of Task 2 to pursue the study of (1) uncooled hot film sensors in turbulent boundary layers with mass transfer, and (2) cooled film sensors in combustion zones of turbulent boundary layers with hydrogen injection. It is anticipated that the use of the cooled probe will be extended to supersonic combustion phenomena.

The results of this program will be two-fold: first, the character- istics of a subsonic turbulent boundary layer with mass transfer, heat transfer, and combustion will be better understood. Second, the capabil- ities of the hot film sensor, both uncooled and cooled will be better understood. In fact, the uncooled hot film sensor has been shown to be a reliable means for obtaining information concerning turbulent flow quantities in low temperature environments. In addition, methods have been developed for utilizing the uncooled hot film sensor in a region of varying concentration of a turbulent boundary layer to obtain many of the characteristics of the boundary layer.

These results will be reviewed with a discussion of the preliminary results obtained with the cooled probe in the combustion zone.

Finally the present status of the supersonic facility will be reviewed.

2.0 SUBSONIC TURBULENT BOUNDARY LAYER WITH HEAT AND MASS TRANSFER

2.1 *Transpired Turbulent Boundary Layer with Heat Transfer*

While the first phase of this project was underway prior to the initiation of Project THEMIS, its foundation is pertinent to our present program. This research was conducted by S. J. AlSaji and has been reported in detail in his dissertation.[2] Several aspects of his results will be discussed.

The purpose of his project was to study the effects of transpiration and heat transfer on a turbulent boundary layer upon a flat plate. Particular attention was devoted to (1) development of a universal temperature inner law and a temperature defect law and (2) development of a mathematical model and approximate analytical solution for the Spalding function relating the surface heat transfer to the skin friction with mass transfer.

The temperature inner law and the temperature defect law are expressions from which the local static temperature in the turbulent boundary layer may be determined for a particular distance from the surface. For mass injection into the boundary layer, the blowing velocity must be known in addition to the surface skin-friction. The development of these laws, and corroborating data, will be presented in this section.

The flow model was the turbulent boundary layer on a semi-infinite, smooth, porous flat plate immersed in a uniform stream of fluid. This flow was simulated on the top wall of the subsonic combustion wind tunnel in the Thermal Science Laboratory of the Department of Mechanical Engineering. Air was used both as the fluid in the mainstream and as the fluid injected through the porous wall. The mainstream velocity was kept constant at 25 feet per second, and the rate of transpiration was also kept constant along the axial distance.

Measurements were made within the boundary layer at several stations along its axial length. The mean velocity profiles were measured by use of pitot tubes and with hot-film sensors. The longitudinal turbulent intensity was also measured by means of the hot-film technique. Mean-temperature profiles were obtained by use of a small-bead thermistor.

The data on the untranspired turbulent boundary layer were used to determine the nature of the flow in the tunnel and to provide a basis of comparison for the transpired data. A universal law of the wall and a universal velocity-defect law were obtained for the nontranspired case. It was concluded that the boundary layer was two-dimensional.

The mean-velocity profiles for the isothermal transpired boundary layer and the transpired boundary layer with heat transfer were correlated in the form of Stevenson's law of the wall,[3, 4] and the modified velocity-defect law.[5, 6]

The mean-temperature profiles for the transpired turbulent boundary layer were correlated in the form of a temperature inner law,[7] and a temperature defect law.[8] These results have been submitted for publication.[9, 10]

2.2 *Temperature Inner Law for Turbulent Boundary Layers with Transpiration*

The mean-temperature profile of the untranspired turbulent air boundary layer on a flat plate is expressed by a temperature inner law, which, for a moderate temperature difference, is:

$$\frac{\tau}{q} = \frac{\tau_w}{q_w} = \text{constant} \tag{1}$$

where τ is the local shear stress, q is the local heat flux in the normal direction, and the subscript w denotes these quantities evaluated at the wall.

In the inner-law region for untranspired turbulent boundary layers, mixing length theories,[7, 8] indicate that the mean temperature profile is correlated as

$$t^+ = F \log_{10} y^+ + E, \tag{2}$$

where

$$t^+ = (T_w - T) \circ c_p \frac{u_\tau}{q_w} \tag{3}$$

$$y^+ = y \, u_\tau / \nu \tag{4}$$

$$u_\tau = \frac{\tau_w}{\rho} \tag{5}$$

$$\nu = \mu/\rho, \tag{6}$$

and y is the distance normal to the surface. We shall show that a temperature inner law for turbulent boundary layers with mass transfer and surface heat transfer may be developed which reduces to Equation (2) as a special case and which is predicted from experimental results.

The energy equation for the turbulent incompressible boundary layer on a flat plate may be written as

$$\rho c_p \left(u \frac{\partial T}{\partial x} + v \frac{\partial T}{\partial y} \right) = -\frac{\partial}{\partial y} (q), \tag{7}$$

where

$$q = -(k + k_t) \frac{\partial T}{\partial y} . \tag{8}$$

However, in the inner region of the boundary layer, where the turbulent thermal conductivity k_t is much larger than the molecular thermal conductivity k, Equation (8) may be written

$$q = -k_t \frac{\partial T}{\partial y} . \tag{9}$$

Therefore, Equation (7) for the inner region yields

$$\frac{q_w}{\tau_w} = \frac{q}{\tau} = -\frac{k_t}{\mu_t} \frac{dT}{du} , \tag{10}$$

where

$$\frac{k_t}{\mu_t} = \frac{1}{Pr_t} c_p, \tag{11}$$

and Pr_t is the turbulent Prandtl number.
Equation (10) may thus be written as

$$\frac{dT}{dy} = -\frac{Pr_t}{c_p} \frac{q_w}{\tau_w} \frac{du}{dy} \tag{12}$$

b-5

Prandtl mixing-length concepts, the turbulent shear stress may
be ten as

$$\tau = \rho \; L^2 \; \left| \frac{\partial u}{\partial y} \right| \; \left(\frac{\partial u}{\partial y} \right),$$ (13)

whi In the inner region of the turbulent boundary layer, the shear
str is given by

$$\tau = \mu_t \; \frac{\partial u}{\partial y} .$$ (14)

Com tion of these results yields an expression for the turbulent
the conductivity in the form

$$k_t = \rho \frac{c_p}{Pr_t} \; L^2 \; \left| \frac{\partial u}{\partial y} \right| .$$ (15)

Uti ng Equation (12), the heat flux may be written

$$q = - \frac{c_p^2}{Pr_t^2} \; \left(\frac{\tau_w}{q_w} \right) L^2 \; \left| \frac{\partial T}{\partial y} \right| \left(\frac{\partial T}{\partial y} \right) .$$ (16)

troducing Prandtl's proposed relationship for the mixing length,
L,

$$L = Ky,$$ (17)

whe is the mixing-length constant, yields

$$q = - \frac{c_p^2}{Pr_t^2} \; \left(\frac{\tau_w}{q_w} \right) K^2 y^2 \; \left| \frac{\partial T}{\partial y} \right| \left(\frac{\partial T}{\partial y} \right) .$$ (18)

r Couette-flow boundary-layer approximations, which are applicable
in case, the energy equation may be written as

$$\rho \; c_p \; v \frac{dT}{dy} = - \frac{d}{dy} (q) .$$ (19)

Sun ution of q from Equation (18) yields

$$\rho \; c_p \; v_w \frac{d(T_w - T)}{dy} = \rho \frac{c_p^2}{Pr_t^2} \left(\frac{\tau_w}{q_w} \right) K^2 y^2 \left(\frac{d(T_w - T)}{dy} \right)$$ (20)

b-6

After integration and rearrangement, Equation (20) becomes

$$-\frac{1}{K}\frac{dy^+}{y^+} = \frac{d(T_w - T)}{\left[\dfrac{Pr_t^{\,2} q_w}{c_p} \dfrac{1}{\tau_w} v_w (T_w - T) - C_1\right]^{\frac{1}{2}}}$$ (21)

where C_1 is a constant of integration.

Integrating again and rearranging yields the results

$$\frac{1}{K}\ell n\, y^+ = 2\frac{u_\tau}{v_w}\left[\left(\frac{c_p}{Pr_t^{\,2}}\frac{\tau_w}{q_w}\right)\frac{v_w}{u_\tau^{\,2}}(T_w - T) - C_1\right]^{\frac{1}{2}} + C_2$$ (22)

where C_2 is a constant of integration.

Since the shear stress at any point in the boundary layer is given by

$$\tau - \tau_w = \rho_w v_w u \, ,$$ (23)

we may write, from Equations (23) and (1)

$$q - q_w = \rho_w\, v_w\, c_p\, [T_w - T] \, .$$ (24)

If Equations (24) and (16) are valid at the same time, then $C_1 = -\dfrac{1}{Pr_t^{\,2}}$, and Equation (22) can be written as

$$\frac{1}{K}\ell n\, y^+ = 2\frac{u_\tau}{v_w}\left[\left(\frac{c_p}{Pr_t^{\,2}}\frac{\tau_w}{q_w}\right)\frac{v_w}{u_\tau^{\,2}}(T_w - T) + \frac{1}{Pr_t^{\,2}}\right]^{\frac{1}{2}} + C_2 \, .$$ (25)

With u_τ defined as $(\tau_w/\rho)^{\frac{1}{2}}$, Equation (25) becomes

$$\frac{1}{K}\ell n\, y^+ = 2\frac{u_\tau}{v_w}\left(\frac{1}{Pr_t}\right)\left[\frac{v_w}{u_\tau}\frac{\rho c_p (T_w - T) u_\tau}{q_w} + 1\right]^{\frac{1}{2}} + C_2 \, .$$ (26)

Defining the non-dimensionalized temperature as

$$t^+ = (T_w - T)\,\rho c_p\,\frac{u_\tau}{q_w} \, ,$$ (27)

b-7

Equation (26) may be written as

$$\frac{1}{K} \ln y^+ = 2 \frac{u_\tau}{v_w Pr_t} \left[\left(\frac{v_w}{u_\tau} t^+ + 1\right)^{\frac{1}{2}} - 1 \right] + \left(C_2 + 2\frac{u_\tau}{v_w Pr_t}\right). \quad (28)$$

If the turbulent Prandtl number, Pr_t, is assumed to be unity, then Equation (28) becomes

$$2\frac{u_\tau}{v_w} \left[\left(\frac{v_w}{u_\tau} t^+ + 1\right)^{\frac{1}{2}} - 1 \right] = \frac{1}{K} \ln y^+ + D \quad (29)$$

which is the temperature-inner-law equation for the transpired turbulent boundary layer. This reduces to the non-transpiring temperature inner law for the case when $v_w = 0$. It should be noted that this expression applies with Couette-flow approximations, where the pressure gradient is zero in the axial direction, the untranspired turbulent boundary layer is in equilibrium, and the convective energy term, $\rho c_p u \, \partial T/\partial x$ is neglected.

The local skin friction coefficient was obtained from the experimental results correlated in the form of the velocity law of the wall for transpiration, while the local wall heat flux was obtained from an energy balance across the injection hoods. With these parameters experimentally determined, the temperature data were plotted as a function of the reduced temperature t^+ and injection velocity v_w, for the corresponding non-dimensionalized distance, $y^+ = y\, u_\tau/\nu$, for three values of the injection parameter, $F = \rho_w v_w/\rho_e u_e$. These are shown in Figures 1, 2, and 3. Note that the turbulent Prandtl number has been set to unity. These results indicate that the temperature inner-law correlation may be obtained in the form

$$\frac{2u_\tau}{v_w} \left[\left(1 + \frac{v_w}{u_\tau} t^+\right)^{\frac{1}{2}} - 1 \right] \text{ versus } y^+.$$

The figures also imply the universality of the temperature inner law for different x positions and for various transpiration rates. The logarithmic portions of Figures 1, 2, and 3 yield the value of 0.464 for the constant K and a value of -6.20 for the value of D.

b-8

Figure 1. Experimental non-dimensional temperature plotted versus non-dimensionalized distance indicating temperature law of the wall. $F = \rho_w v_w / \rho_1 u_1 = 2.96 \times 10^{-3}$. $T_1 = 535$ R.

y-axis: $\dfrac{2u_1}{v_w} \, t^+ \left[(1 + \dfrac{v_w}{u_1} t^+)^{\frac{1}{2}} - 1 \right]$

x-axis: $\dfrac{y u_\tau}{D}$

Legend:
$F = 2.96 \times 10^{-3}$
$\triangle$ $Re_x = 8.50 \times 10^5$
$\times$ $Re_x = 3.20 \times 10^5$
$\bigcirc$ $Re_x = 7.17 \times 10^5$
$\square$ $Re_x = 6.85 \times 10^5$

b-9

Figure 2. Experimental non-dimensionalized temperature plotted versus non-dimensionalized distance indicating temperature law of the wall. $F = \rho_w v_w / \rho_1 u_1 = 10^{-3}$. $T_1 = 535$ °R.

Legend:

$F = 4.78 \times 10^{-3}$

$\triangle$ $Re_x = 8.50 \times 10^5$
$\times$ $Re_x = 8.20 \times 10^5$
$\bigcirc$ $Re_x = 7.17 \times 10^5$
$\square$ $Re_x = 6.85 \times 10^5$

x-axis: $\dfrac{y u_\tau}{\nu}$

y-axis: $\dfrac{2 u_1}{u_\tau}\left[\left(1 + \dfrac{t^+}{u_1/v_w}\right)^{\frac{1}{2}} - 1\right]$
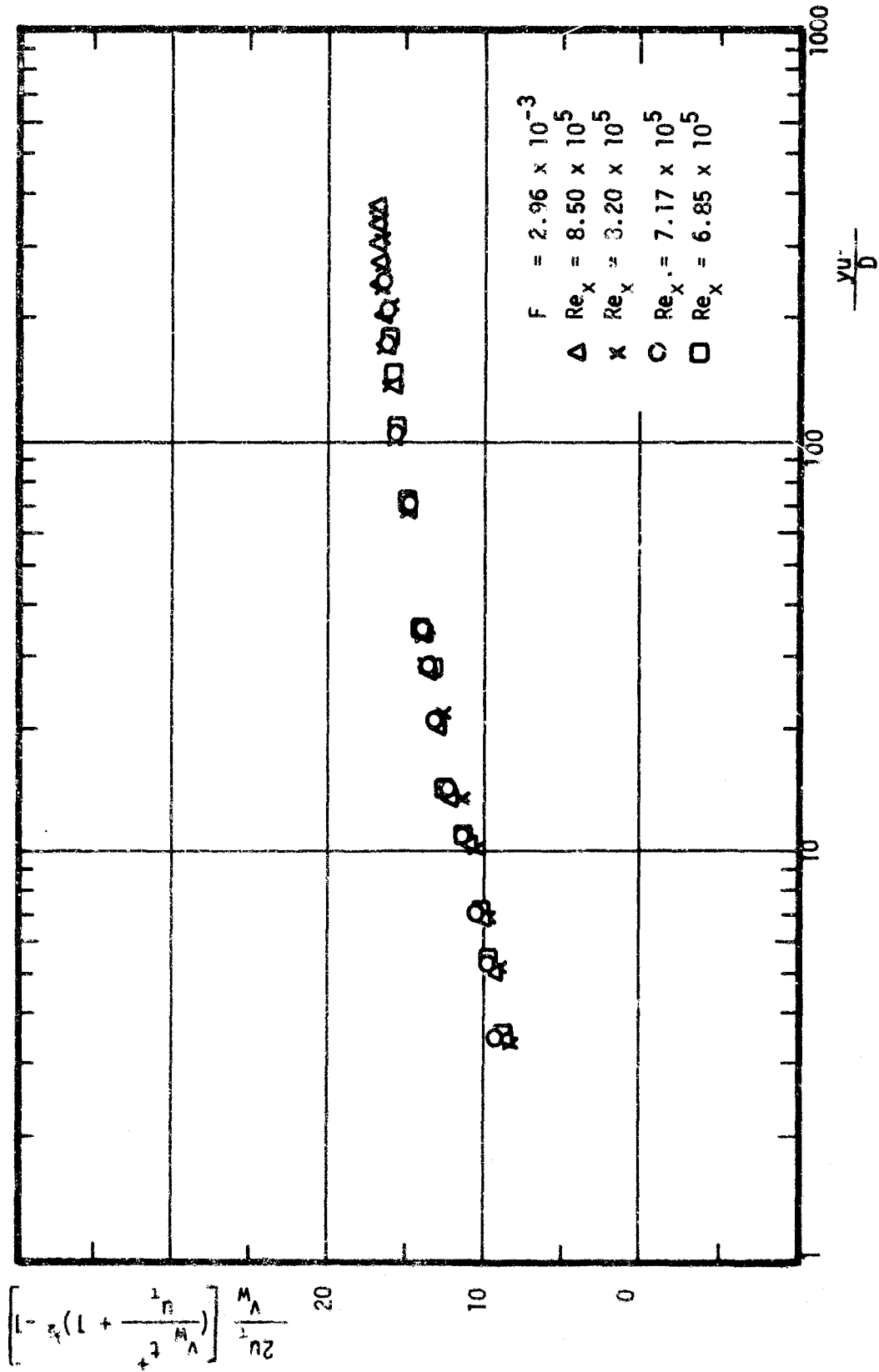
b-10

Figure 3. Experimental non-dimensionalized temperature plotted versus non-dimensionalized distance indicating temperature law of the wall. $F = \rho_w v_w / \rho_1 u_1 = 6.26 \times 10^{-3}$. $T_1 = 536$ R.
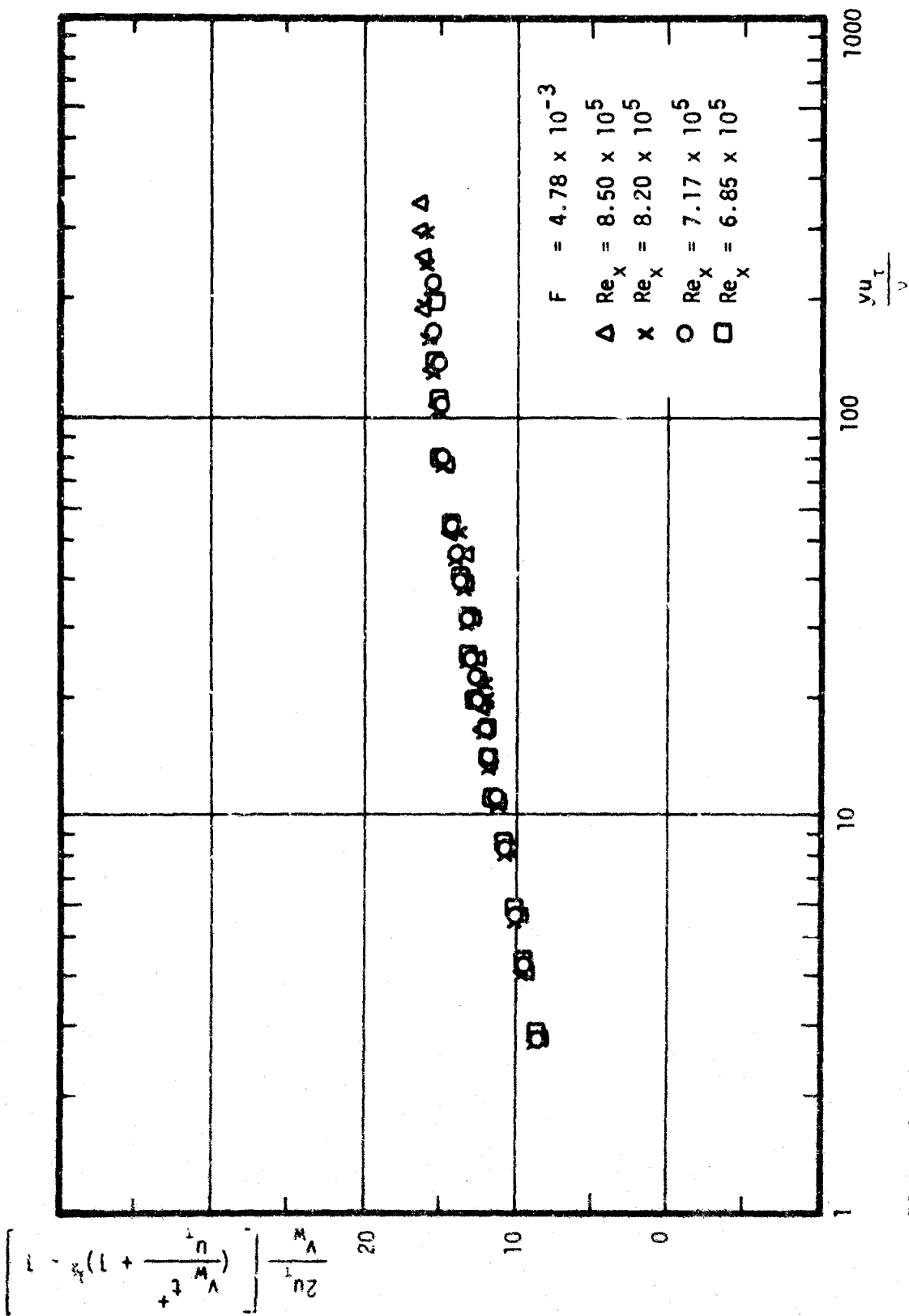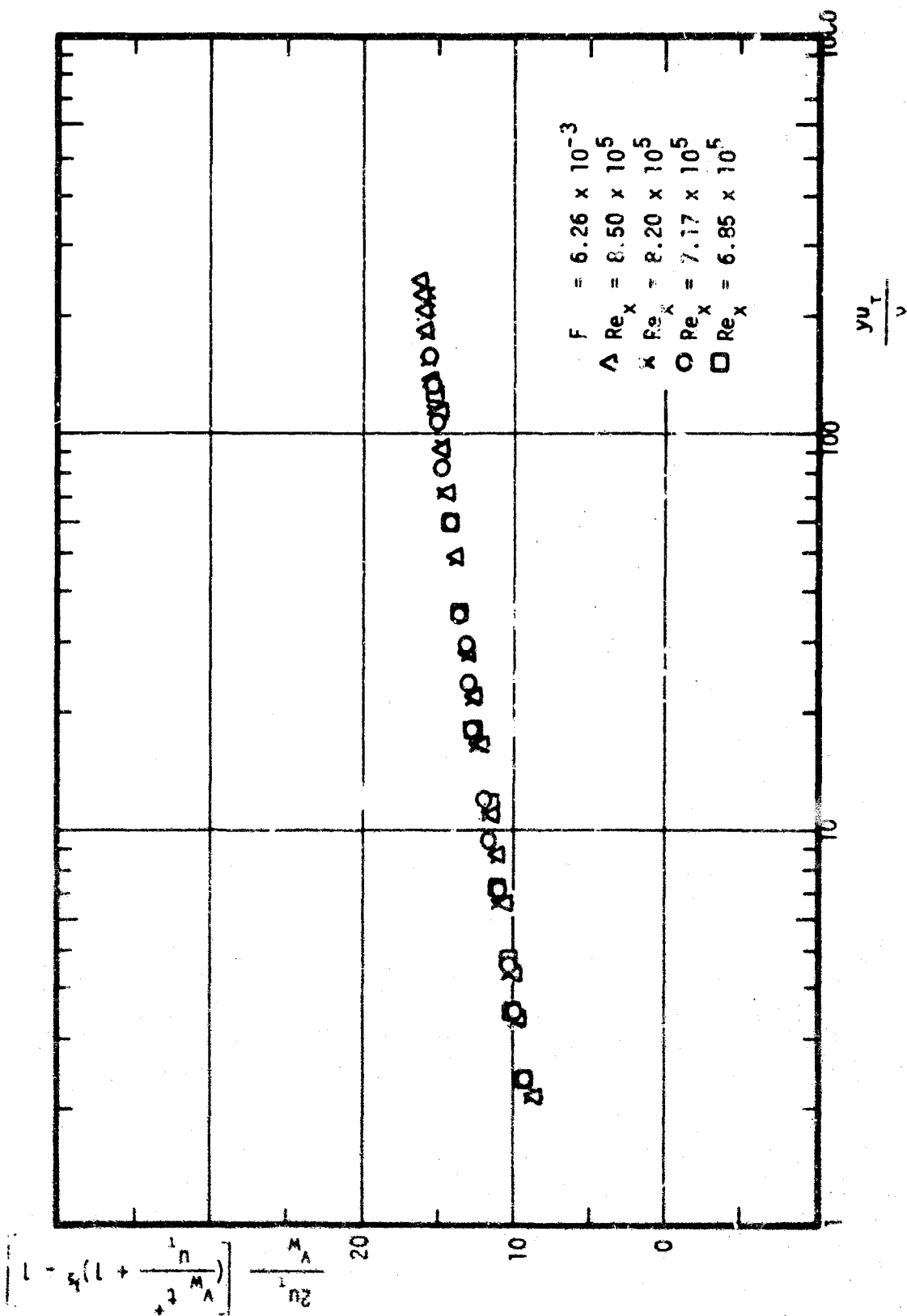
2.3 Temperature Defect Law for the Turbulent Boundary Layer with Transpiration

An expression is presented for the mean temperature distribution in the outer region of turbulent boundary layers with injection of heated gas through a porous wall. The equation presented shows agreement with experimental results obtained with heated air injected across a porous plate into a subsonic air turbulent boundary layer.

The equation for the temperature distribution through the inner region of a turbulent boundary layer with transpiration and heat transfer derived from mixing-length theory, may be written as[2, 9]

$$\frac{2u_\tau}{Pr_t v_w} \left[(1 + \frac{v_w}{u_\tau} t^+)^{1/2} - 1 \right] = \frac{1}{K} \ln \frac{yu_\tau}{\nu} + D \tag{1}$$

where K is the von Karman constant in the mixing-length theory and D is, in general, a function of v_w, u_τ, and Pr_t. v_w is the blowing velocity normal to the porous surface, $u_\tau = (\tau_w/\rho_w)^{1/2}$ is the friction velocity at the wall, and $t^+ = \rho_w c_p u_\tau/q_w(T_w - T)$ is a non-dimensionalized temperature. Pr_t is the turbulent Prandtl number.

For a turbulent boundary layer over an impermeable surface with zero pressure gradient and with heat transfer, Johnk and Hanratty[7] and Brundrett and Burroughs[8] postulate for the inner region a relationship of the form

$$t^+ = A \ln \frac{yu_\tau}{\nu} + B, \tag{2}$$

In addition, Johnk and Hanratty[7] indicate that a relationship of the form

$$t_1^+ - t^+ = f(y/\delta_t) , \tag{3}$$

where t_1^+ is t^+ evaluated at the free-stream temperature, may be applicable over the outer region of the boundary layer. Hence, if any overlap exists between the inner and outer regions of the boundary layer, the arguments of Millikan[11] would indicate that the equation for the mean temperature distribution in the inner and outer regions of the turbulent boundary layer with heat transfer (but without transpiration) should be of the form

$$t_1^+ = A \ln (\frac{yu_\tau}{\nu}) + \phi(y/\delta_t) \tag{4}$$

b-12

where $\phi(y/\delta_t)$ is a universal function, having the constant value $\phi(0)$ throughout the inner region.

It follows that

$$t_1^+ - t^+ = -A \ln\left(\frac{yu_\tau}{\nu}\right) + \phi(1) - \phi\left(\frac{y}{\delta_t}\right) = f(y/\delta_t) \qquad (5)$$

is the temperature defect law in the outer region of the boundary layer, whereas

$$t^+ = A \ln\left(\frac{yu_\tau}{\nu}\right) + \phi(0) \qquad (6)$$

is the law of the wall for the temperature distribution through the inner region.

In the case with injection into the boundary layer with a heated wall, these relationships must be modified to take into account the heat transfer due to the finite transpiration velocity at the wall. When the external pressure gradient is zero, the temperature inner-law with injection is

$$\frac{2u_\tau}{Pr_t v_w}\left[\left(1 + \frac{v_w t^+}{u_\tau}\right)^{\frac{1}{2}} - 1\right] = A \ln\frac{yu_\tau}{\nu} + B \qquad (7)$$

The equation for both the inner and outer regions may now be written as

$$\frac{2u_\tau}{Pr_t v_w}\left[\left(1 + \frac{v_w t^+}{u_\tau}\right)^{\frac{1}{2}} - 1\right] = A \ln\frac{yu_\tau}{\nu} + \phi\left(\frac{y}{\delta_t}\right) \qquad (8)$$

where B of Equation (7) is equal to $\phi(0)$.

It follows that

$$\frac{2u_\tau}{Pr_t v_w}\left[\left(1 + \frac{v_w t_1^+}{u_\tau}\right)^{\frac{1}{2}} - \left(1 + \frac{v_w t^+}{u_\tau}\right)^{\frac{1}{2}}\right] = -A \ln\left(\frac{y}{\delta_t}\right) + \phi(1) - \phi\left(\frac{y}{\delta_t}\right)$$

$$\qquad (9)$$

$$= F(y/\delta_t)$$

This expression may be described as a "modified temperature defect-law with injection and zero pressure gradient."

b-13

Stevenson[5, 6] plots the function

$$\frac{2u_\tau}{v_w} \left[(1 + \frac{v_w}{u_\tau} u_1)^{\frac{1}{2}} - (1 + \frac{v_w}{u_\tau} u)^{\frac{1}{2}} \right] = F(y/\delta_t) \qquad (10)$$

against (y/δ_{t_0}) for various values of x for the case of injection on an axisymmetric surface and for a flat plate and shows that for the velocity field, $F(y/\delta_{t_0})$ is a universal function. Stevenson defined the term δ_0 as the value of y at which the left-hand side of Equation (10) is equal to unity.

Following this procedure we shall define δ_{t_0} for $Pr_t = 1$ as the value of y at which

$$\frac{2u_\tau}{v_w} \left[(1 + \frac{v_w t_1^+}{u_\tau})^{\frac{1}{2}} - (1 + \frac{v_w t^+}{u_\tau}) \right] = 1 . \qquad (11)$$

A comparison with experimental results will now be presented. It can seen from Equation (9) that the results should fall onto one curve when the term

$$\frac{2u_\tau}{v_w} \left[(1 + \frac{v_w t_1^+}{u_\tau})^{\frac{1}{2}} - (1 + \frac{v_w t^+}{u_\tau})^{\frac{1}{2}} \right] \qquad (12)$$

is plotted against y/δ_{t_0}. Figures 4 and 5 present results obtained from the experiments reported by AlSaji.[2] These results collectively imply that $F(y/\delta_t)$ is a universal function at least for constant Pr_t.
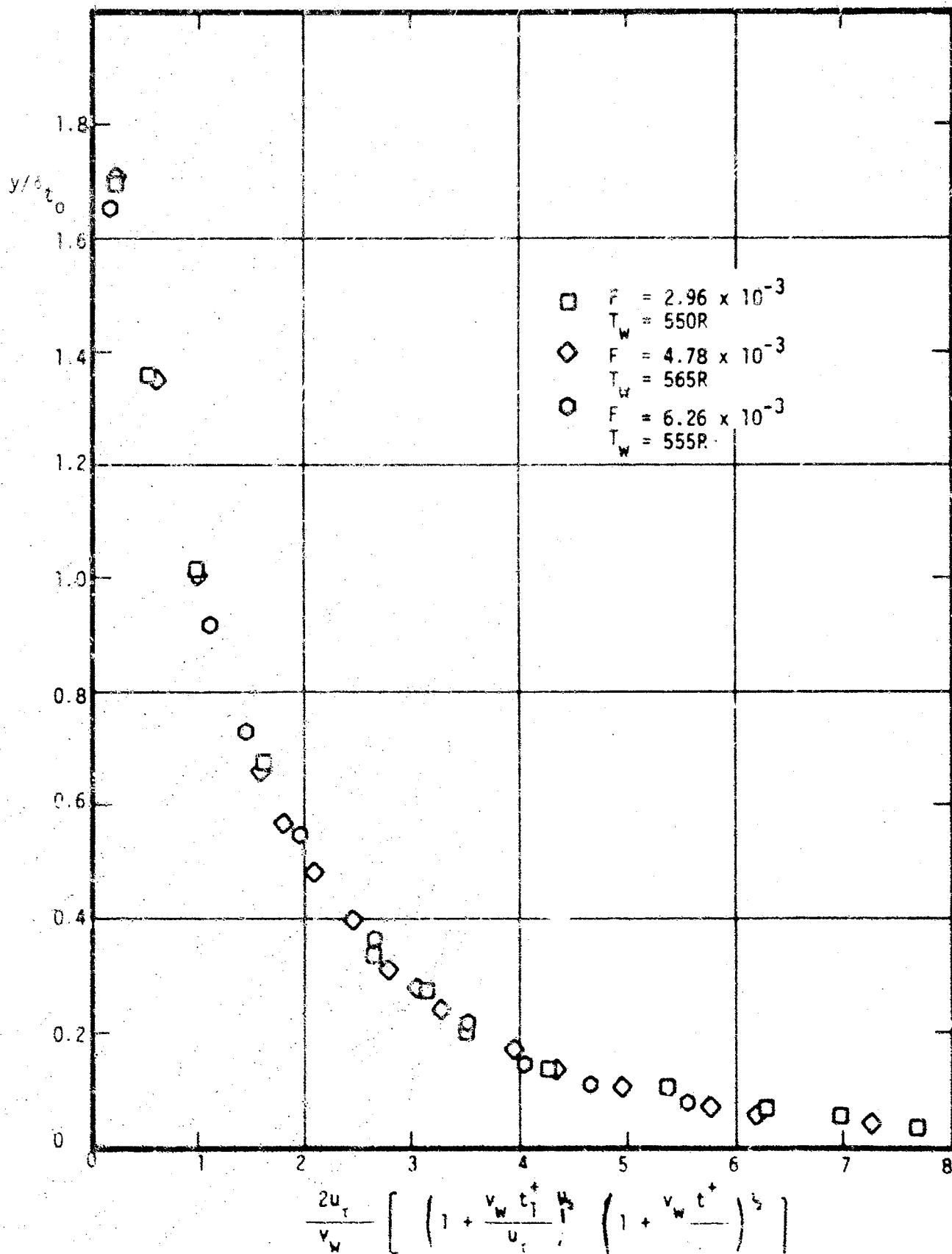
Figure 4. Experimental temperature defect for the turbulent boundary layer with transpiration and heat transfer. $T_1 = 536$ R. $F = \rho_w v_w / \rho_1 u_1$. Δt_o is the value of y at which $F(y/\delta_t) = 1$.
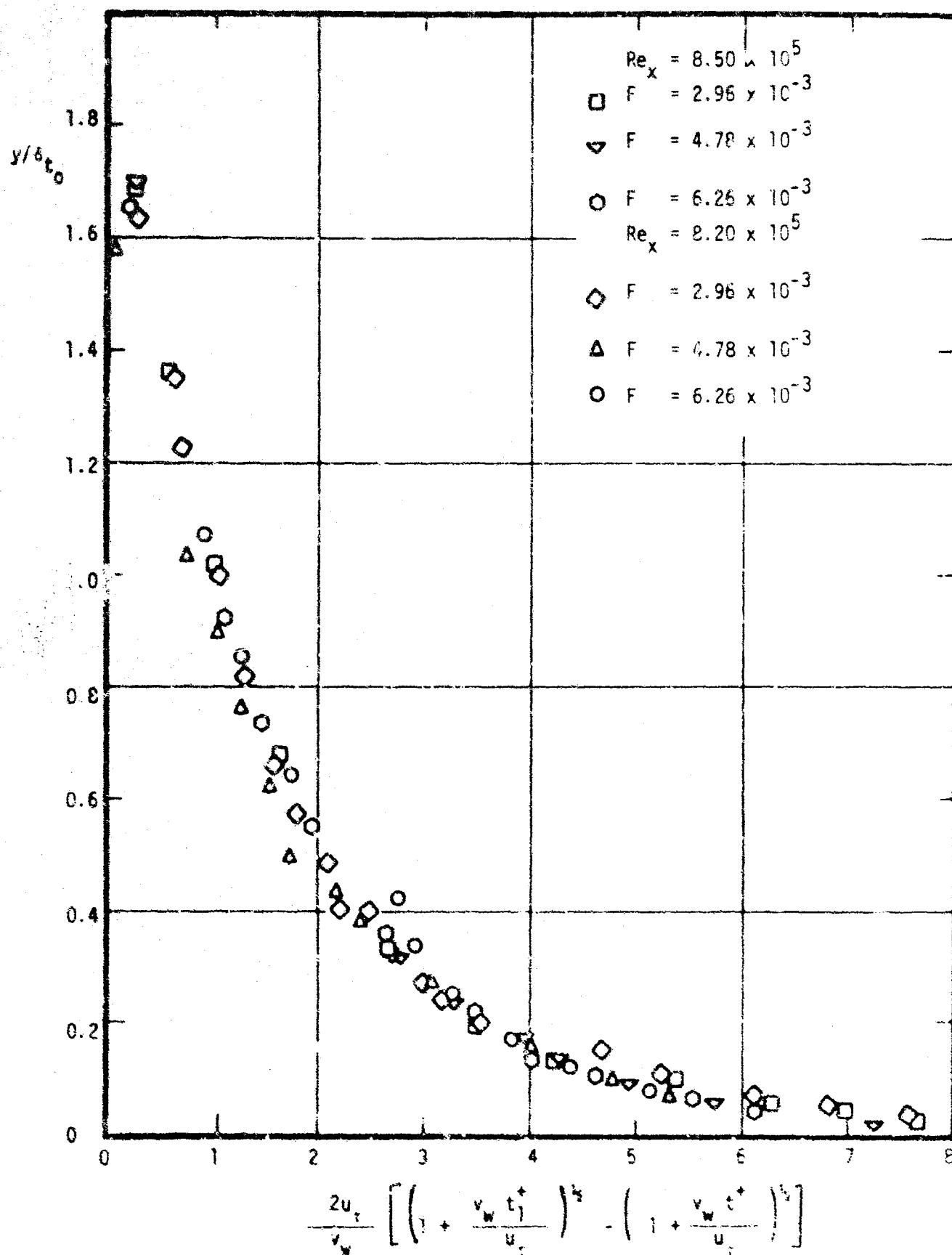
b-15

Figure 5.   Experimental temperature defect at two stations for the turbulent boundary layer with transpiration and heat transfer.

b-16

2.4   *Effects of Wall Temperature on Longitudinal Turbulent Intensity*

The longitudinal turbulent intensity for the transpired turbulent boundary layer with heat addition was calculated from the single hot-film constant-temperature anemometer data. These results are presented in detail in reference (2). Comparison of the parameter $\sqrt{u'^2}$ / u versus y / δ when the wall was heated with the results for the unheated wall, for the same transpiration rate, shows that heat addition certainly increases the longitudinal intensity. For a transpiration rate of F =$(\rho_w v_w / \rho_1 u_1)$ = 6.26 x 10^{-3}, an increase of 12.5% at the wall is indicated while the effect diminishes as y/δ approaches 0.50. The thermal boundary layer extends out to approximately y/δ of 0.50.

The data for the transpired turbulent boundary layer with heat addition clearly indicate that the increase in the longitudinal turbulent intensity is dependent on both the blowing rate, $(\rho_w v_w / \rho_1 u_1)$, and the temperature difference, T_w - T. It should be mentioned that heat addition will decrease the density at the wall, ρ_w, which, in turn, causes an increase in the transpiration velocity at the wall, v_w. This result would seem to cast doubt on the results of recent studies[18] which attribute increased turbulent levels near the wall in burning boundary layers to the combustion process itself.

2.5   *Behavior of Hot-Film Sensors in the Turbulent Boundary Layer with Isothermal Foreign-Gas Injection*

The hot-wire anemometer and the more recently developed hot-film sensor have become important tools in measuring both mean values and fluctuations of various phenomena in fluids. Many of the limitations of anemometry methods are well-known, but many are also overlooked, whether known or unknown. One of the latter is the difficulty of obtaining data by which the experimenter may distinguish among the various factors affecting the probe: velocity, temperature, and composition. Measurements in an isothermal boundary layer composed only of air are straightforward. However, if concentration variations are significant across the boundary layer, the sensor behavior is more complex.

The purpose of this phase of the program which was conducted by T. H. Smith[30] and supported in part by Project THEMIS, was to determine the sensor response to simultaneous variations of velocity and concentration. The turbulent boundary layer with foreign-gas injection provided an excellent

b-17

en   ent for the studies, since a great number of differing concentrations
ac   he boundary layer were readily available. Hydrogen-nitrogen mix-
tu.   re chosen as the injectants, with concentrations ranging from pure
hy   to ure nitrogen. This choice was made because of an unusual
pro   of hydrogen-nitrogen or hydrogen-air mixtures. For these mix-
tun   here is a very sharp minimum in the mixture molecular Prandtl
nun   t intermediate concentrations.

      hot-film sensor was treated as a miniature heated cylinder. The
hea   nsfer from the cylinder in the environment described above was
inv   ated.

2. revious Work

re appears to have been no directly applicable work done previously
on   specific subject. However, the foreign-gas injected turbulent
bou   layer has been investigated by many workers[12-19] Hot-wire
beh   was treated extensively in a theoretical paper by Corrsin.[20]
Valu contributions toward combating problems of anemometry are also
ava   e[21, 22, 23, 24]   Each of these investigations was of
ass   cz in the present unifying study.

2.5 heory of Hot-Film Sensor Behavior

      behavior of the hot-film sensor, a small ceramic cylinder coated
wit   d and platinum and a protective quartz film, was investigated
ine   cally. The results are directly applicable to constant-temperature
ann   er systems with associated linearizers. The linearizer squares
the   age signal from the anemometer twice, giving a velocity-related
si

      implified analysis for an isothermal air environment was presented,
us   ng's equation for the heat transfer law:

$$P = A + B \sqrt{\bar{U}} \ (T_s - T_e) \tag{1}$$

wh

        P = power dissipated from sensor

        $\bar{U}$ = velocity

        T_s = sensor operating temperature

        T_e = environment temperature

        A, B = constants related to fluid properties and
               sensor geometry

and the bars denote time-averaged quantities.

It was verified that for this case

$$\frac{m'}{\bar{M}} = \frac{u'}{\bar{U}} \qquad (2)$$

where

m' = root-mean-square of linearizer fluctuations

$\bar{M}$ = time-averaged linearizer output

u' = root-mean-square velocity fluctuation

The mean response of the sensor in an environment with velocity and concentration fluctuations was derived using

$$Nu = 0.42 \, Pr^{0.20} + 0.57 \, Pr^{0.33} \, Re^{0.50} \qquad (3)$$

for the basic heat transfer relationship, where

Pr = Prandtl number = $\mu \, C_p / K$

Nu = Nusselt number = hd/K

Re = Reynolds number = $\rho U d / \mu$

d = sensor diameter

The following expression was shown to express the sensor power dissipation:

$$\bar{P} = \frac{\bar{E}_b^2 R_s}{(R_s + R_3 + R_{xc})^2} = \frac{0.42\pi\ell[K_a + f(\bar{\Gamma})\Delta K]}{\alpha R_0}\left[\frac{(\mu_a + g\,(\bar{\Gamma})\Delta\,\mu)\,(C_{pa} + \bar{\Gamma}\,\Delta C_p)}{(K_a + f\,(\bar{\Gamma})\Delta\,K)}\right]^{0.20}$$

$$+ \frac{0.57\pi\ell\,[K_a + f\,(\bar{\Gamma})\Delta\,K]}{\alpha R_0}\left[\frac{(\mu_a + g\,(\bar{\Gamma})\Delta\,\mu)\,(C_{pa} + \bar{\Gamma}\Delta\,C_p)}{K_a + f\,(\bar{\Gamma})\Delta\,K}\right]^{0.33}$$

$$\frac{(\rho_a + \bar{\Gamma}\,\Delta\,\rho)d}{\mu_a + g\,(\bar{\Gamma})\Delta\,\mu}^{0.50} \, (\bar{U})^{0.50} \qquad (4)$$

where

$\bar{E}_b$ = time-averaged bridge voltage

R_s = sensor operating resistance

R_3 = internal anemometer resistance in bridge leg

R_{xc} = resistance of external circuitry except sensor

and the rest of the notation is as in Corrsin.[20]

The fluctuating response of the sensor was shown to be

$$\frac{m'}{M} = \frac{2}{B_1\sqrt{\overline{U}}}\left\{\left[\left(\overline{A}_1 + \frac{\overline{B}_1\sqrt{\overline{U}}}{2}\right)\overline{T}\,\frac{df\,(\overline{T})}{d\overline{T}}\,\frac{\Delta K}{K} + \frac{\overline{T}\,\overline{B}_1\sqrt{\overline{U}}}{2}\left(\frac{\Delta\rho}{\rho} + \frac{\Delta C_p}{\overline{C}_p}\right)\right]\frac{\gamma}{\overline{T}} + \left[\frac{\overline{B}_1\sqrt{\overline{U}}}{2}\right]\frac{u}{\overline{U}}\right\}_{rms} \tag{5}$$

where A_1 and B_1 are constants related to fluid properties and the rms signifies the root-mean-square of the expression in the braces. It is seen that two new terms arise due to the concentration fluctuations, γ' and the cross term $\overline{\gamma u}$.

It has been shown that Equation (5) reduces to the simple Equation (2) for an air-only boundary-layer environment.

2.5.3 Apparatus and Procedure

The subsonic wind tunnel of the Thermal Science Laboratory, with the 7" x 7" x 8' test section was used for these studies. Two 12" x 6" porous plates formed part of the test section top wall. Various gases were injected through the plates into the boundary layer. Hoods erected over the plates insured even distribution of the injectant. The free stream velocity was 25 ft/sec, and the temperature was approximately ambient.

Six different injectant cases were studied. The injectants, symbolic designations, and injection rates $F = (\rho V)_w/(\rho U)_s$, were as follows:

INJECTANT	DESIGNATION	RATE F
none	Z-	0
air	A-	6.4×10^{-3}
hydrogen	H-	3.5×10^{-4}
nitrogen	N-	6.2×10^{-3}
hydrogen (2.2% by mass) in nitrogen	NH-	5.8×10^{-3}
hydrogen (7.0% by mass) in nitrogen	NH-	4.3×10^{-3}

For each case, several basic quantities were measured at 22 points through the boundary layer at a given point 68" downstream from the initiation of the turbulent boundary layer. Dynamic pressure was measured with a Pitot probe and micromanometer, and the temperature with a thermocouple bead

b-20

and potentiometer (to verify thermal equilibrium and uniform temperature across the boundary layer). Concentration samples were extracted and analyzed using a gas chromatograph. The power dissipation from the hot-film probe was measured and the linearizer indications of velocity and turbulence level (neither of which accounts for concentration effects) were obtained. A true rms voltmeter was used to obtain the turbulence level from the linearizer output.

2.5.4 Results

The data were reduced using the University of Utah Univac 1108 digital computer facilities. Profiles of velocity, concentration, power dissipation, and linearizer output mean-value and fluctuation intensity were determined. Thermal conductivity and viscosity of the gas mixture at each location in the boundary layer were calculated, together with the constant pressure specific heat. The behavior of the molecular Prandtl number across the boundary layer is presented in Figure 6. Power dissipation and sensor loss correction profiles gave Nusselt number, Nu, profiles. The experimental values of the Nusselt number were compared with those pre-dicted by Equation (3), with very good agreement being found. A Gaussian least-squares curve-fitting of the Nusselt number expression

$$Nu = f(Re, Pr) \tag{6}$$

in the form

$$Nu = c_1 \ Re^{c_2} \ Pr^{c_3} , \tag{7}$$

yielded the expression

$$Nu = 1.000 \ Re^{0.355} \ Pr^{0.327} , \tag{8}$$

compared with the literature value[25] of

$$Nu = 0.9031 \ Re^{0.385} \ Pr^{0.31} . \tag{9}$$

The experimental power dissipation profiles were compared with those predicted by an equation based on Equation (4), again with good agreement. Finally, the experimental velocity profiles were found to compare favorably with those predicted using power dissipation profiles and Equations (3) or (4).

The profiles of dimensionless linearizer output, $\bar{M}/\bar{M}_\infty$, (analogous to velocity when no concentration effects are present) and power dissipation, P/P_∞, showed a dramatic effect of concentration at distances less than 0.4 inches from the wall. (see Figures 7 and 8) An investigator ignoring the
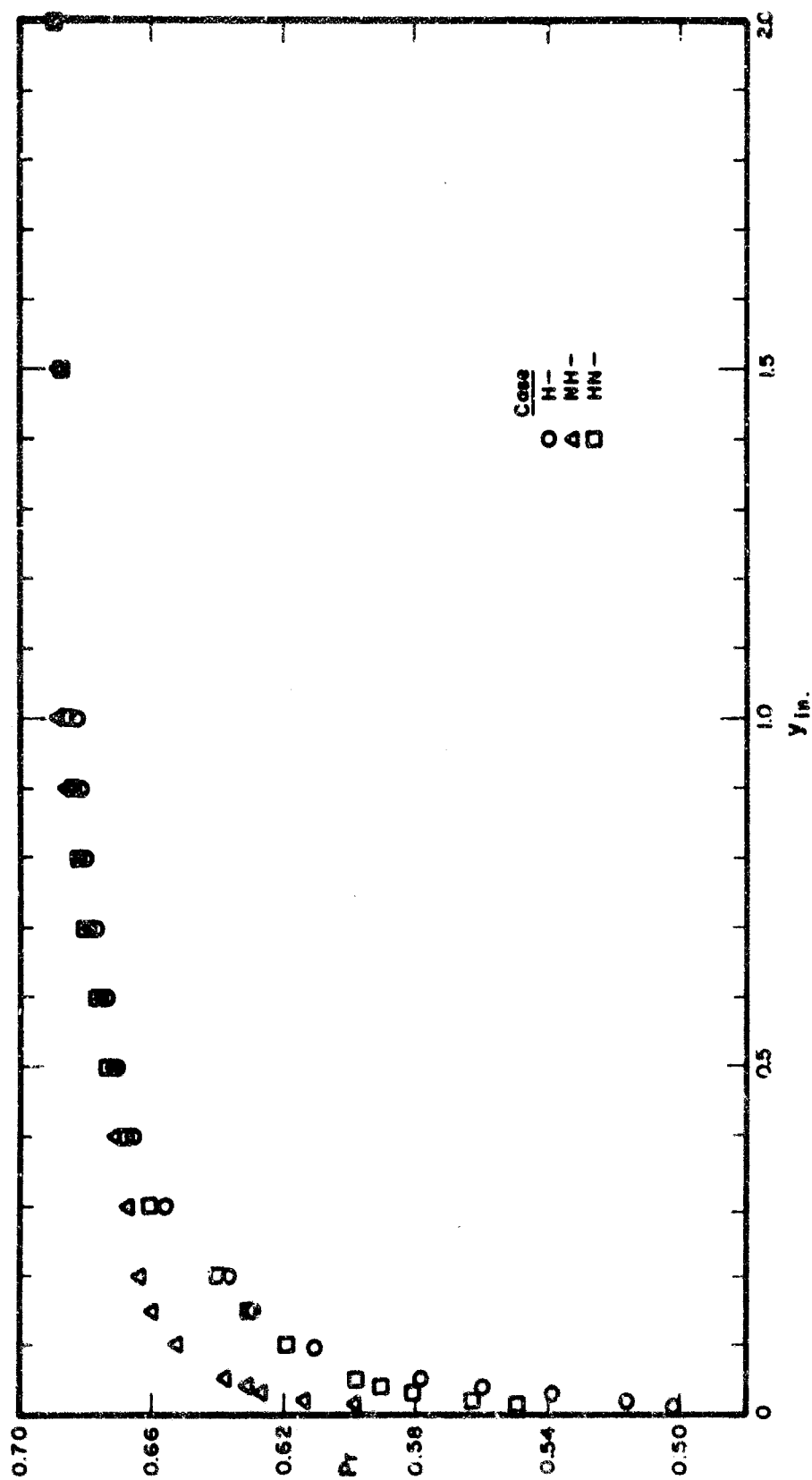
Figure 6. Variation of the molecular Prandtl number across the turbulent boundary layer with foreign-gas injection.

b-22
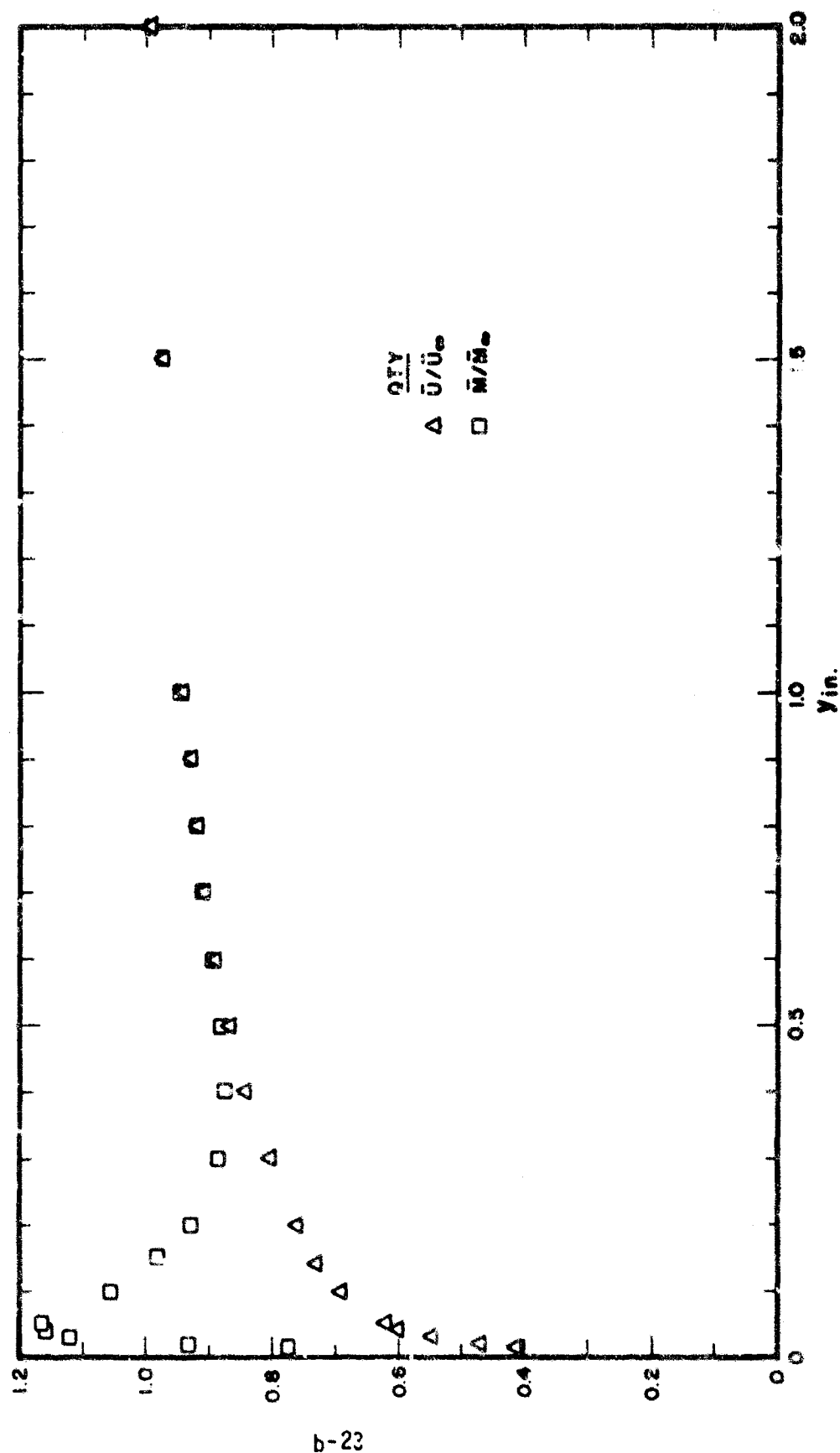
Figure 7. Dimensionless linearizer output $\overline{M}/\overline{M}_\infty$ compared with velocity ratio $\overline{U}/\overline{U}_\infty$ for a turbulent boundary layer with foreign-gas injection.
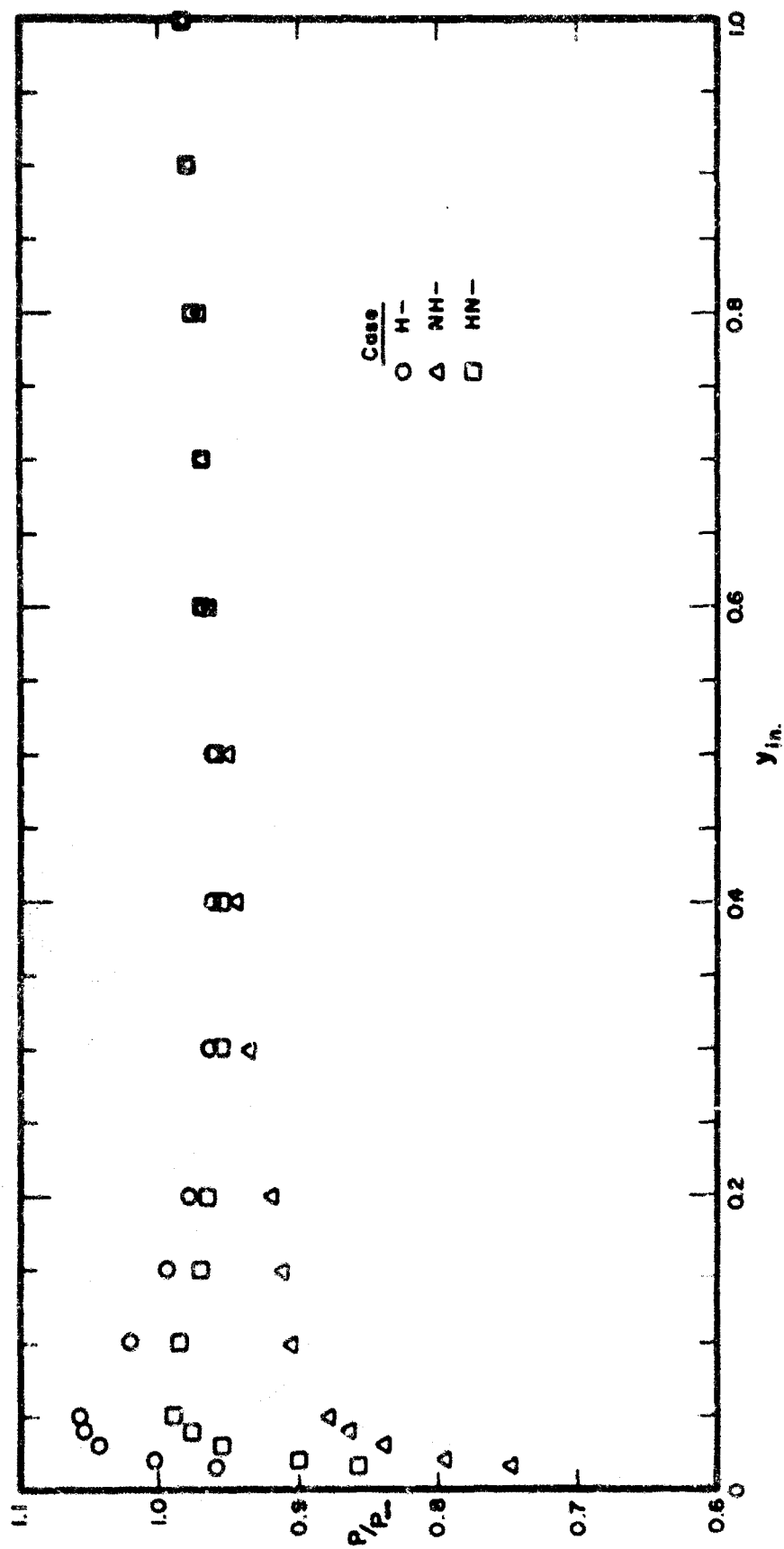
b-23

Figure 8. Dimensionless power dissipation from a constant temperature hot-film sensor across a turbulent boundary layer with foreign gas injection.

b-24

effects of concentration on the sensor behavior and, therefore, upon linearizer output would be led to gross errors in his velocity profiles, whereas Equations (3) and (4) and the velocity profile prediction mentioned earlier lead to very good agreement with the true velocities.

Figures 9 and 10 show the concentration effects upon the turbulence levels $m'/\bar{M}\infty$ and $m'/\bar{M}$, respectively, indicated by the linearizer and an rms voltmeter. It is seen that although case H- has by far the lowest injection rate (from which one might suppose it to show the lowest turbulence readings), it generally has the highest indicated turbulence intensities for y <0.3 inch. This is in qualitative agreement with Equation (5) which indicates the effect of concentration fluctuations upon the turbulence intensity $m'/\bar{M}\infty$.

The conclusion may thus be drawn from the experimental evidence of this section and the accompanying theory that an investigator ignoring concentration effects upon the sensor would make errors in the velocity and turbulence intensity profiles of such magnitudes as to seriously affect the validity of his results. The errors are significant even for as little as 2.2% by weight of hydrogen in the injectant. This conclusion suggests that further consideration be given the data of Wooldridge and Muzzy[19] in which concentration effects were ignored for 4% by weight hydrogen mixtures with nitrogen.

It has also been shown that the hot-film sensor may be used to obtain power dissipation measurements which, when used with Equations (3) or (4) and concentration profiles, obviate the need for time-consuming dynamic-pressure measurements except as an additional check on the data.

2.6   *A New Turbulent Prandtl Number Determination Method for Injected, Variable-Property Flow*

The need for additional data clarifying the behavior of the turbulent Prandtl number across the boundary layer has been mentioned by Kestin and Richardson[26] and by Spalding.[31] The turbulent Prandtl number may be defined as

$$Pr_T(y) \equiv \bar{C}_p(y)\ \epsilon_M(y)/\epsilon_H(y)\ ;$$ (10)
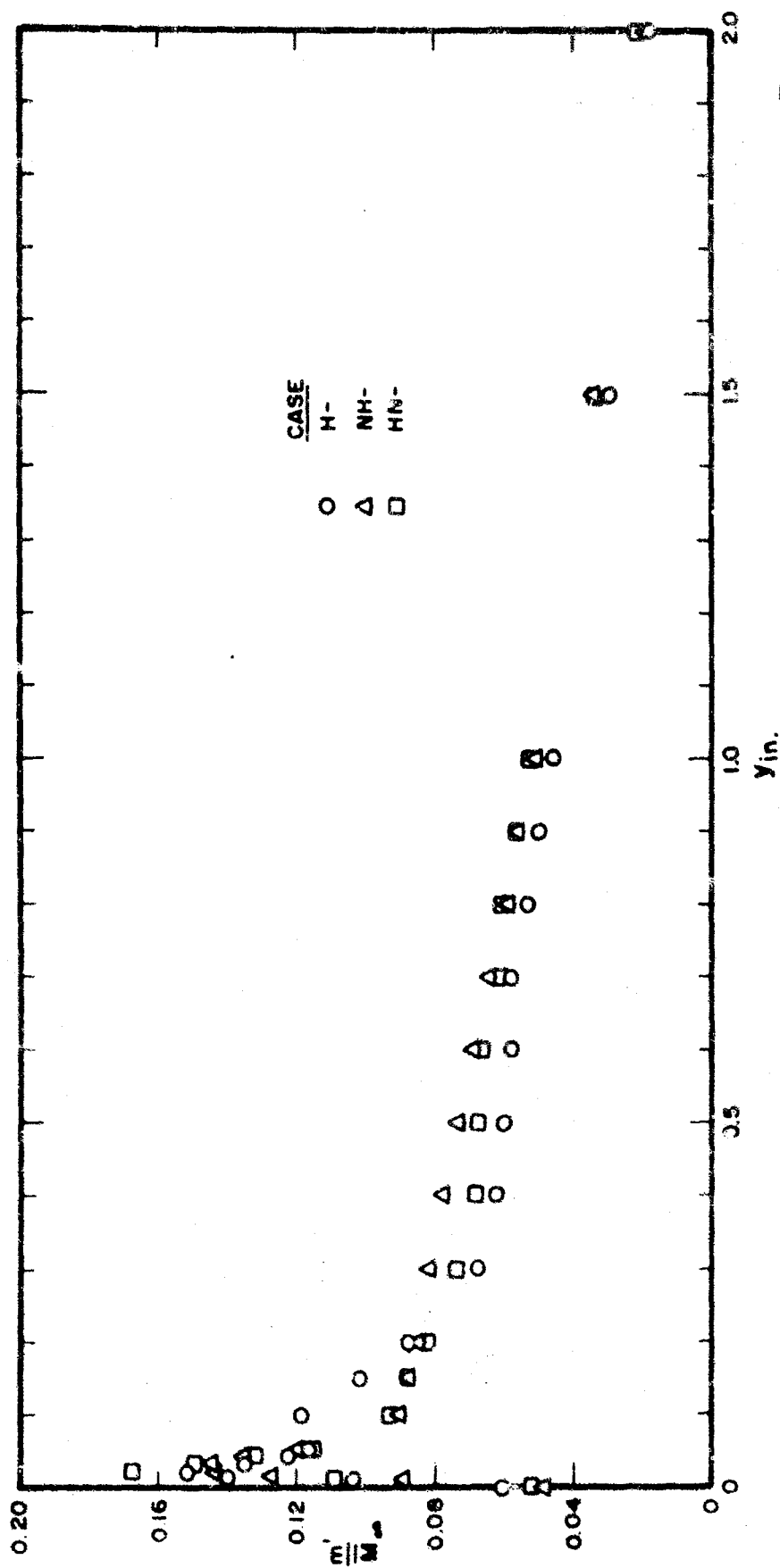
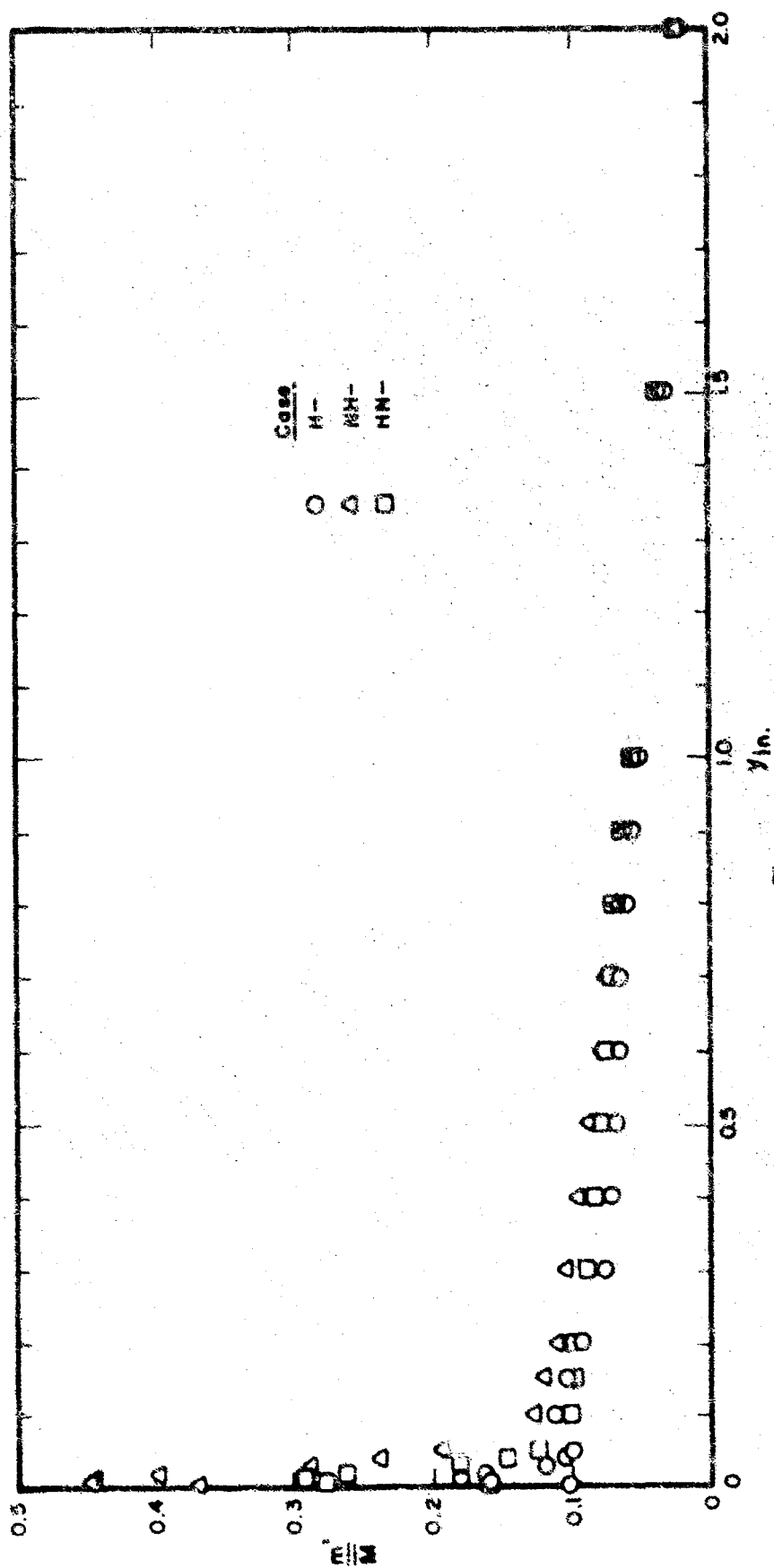Figure 9. Effect of concentration gradient through the boundary layer on the turbulence level, $m'/\overline{M}_\infty$.

b-26

Figure 10. Hot film turbulence output, $m'/\overline{m}$, as a function of location in a turbulent boundary layer with foreign-gas injection.

b-27

where

$$\epsilon_M(y) = \text{eddy viscosity}$$

and

$$\epsilon_H(y) = \text{eddy conductivity}$$

In Equation (10) ϵ_M and ϵ_H are turbulent counterparts of the molecular viscosity and thermal conductivity, respectively. They are functions not only of the fluid properties but also of the flow characteristics. X-wire probes are usually employed to measure these quantities, but this method is complex and may be inaccurate, especially near the wall.[24]

An alternate method has been devised through integration of the complete turbulent equations of continuity, momentum, and energy. The method requires only mean velocity and temperature profiles, is applicable to variable property fluids, and includes the injection of air or of foreign gases. Mean concentration profiles are required with foreign-gas injection. A computer program has been written which evaluates the velocity component perpendicular to the wall, the turbulent shear stress, the turbulent heat transfer, the eddy viscosity and conductivity, and the turbulent Prandtl number, all as a function of the distance from the wall. Data of AlSaji[2] for air injection with a heated wall were used as input to the computer program, and good results were obtained, (see Figures 11 and 12).

2.7 *A New Method for Determining Skin Friction in the Turbulent Boundary Layer with Foreign-Gas Injection*

Determination of the skin-friction coefficient in the foreign-gas-injected boundary layer is quite difficult. Extrapolation of velocity profiles to the wall gives poor accuracy, as does the use of the momentum-integral method.

A new method has been devised, based on the corresponding approach of Stevenson[3] for air injection. Stevenson's method was based on the "law of the wall" equation for the inner region in which the skin friction appears implicitly. The present method is based on a corresponding inner law for the foreign-gas-injected boundary layer derived from the theories of Spalding, Auslander, and Sundaram[17] and of Rubesin and Pappas.[16] The solution has been written in a computer program which may be used for any case in which the injectant is lighter than air. (The method of solution has also been pointed out for the heavier-than-air case.)

b-28
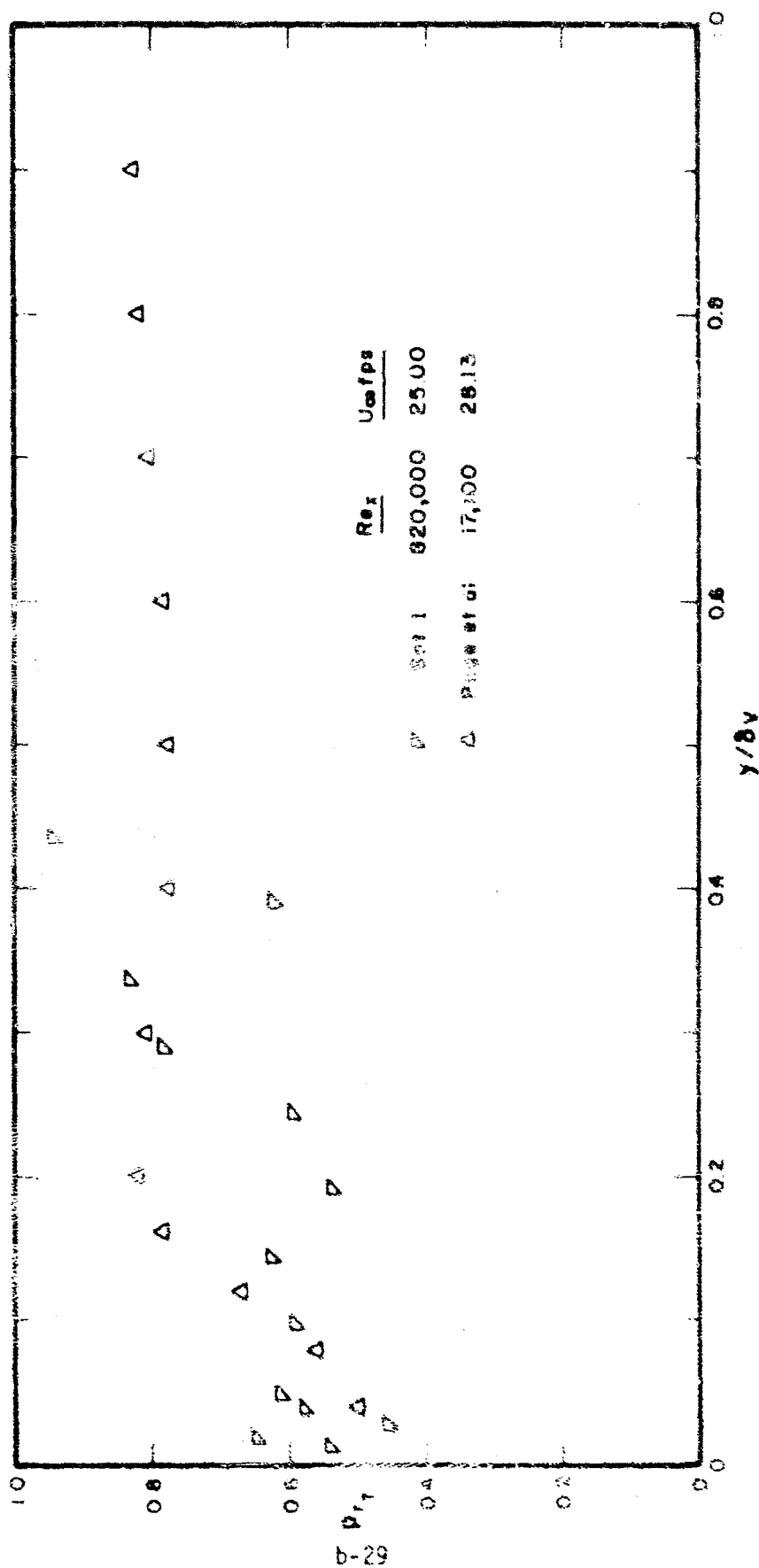
Figure 11. Turbulent Prandtl number profiles through the boundary layer.

b-29
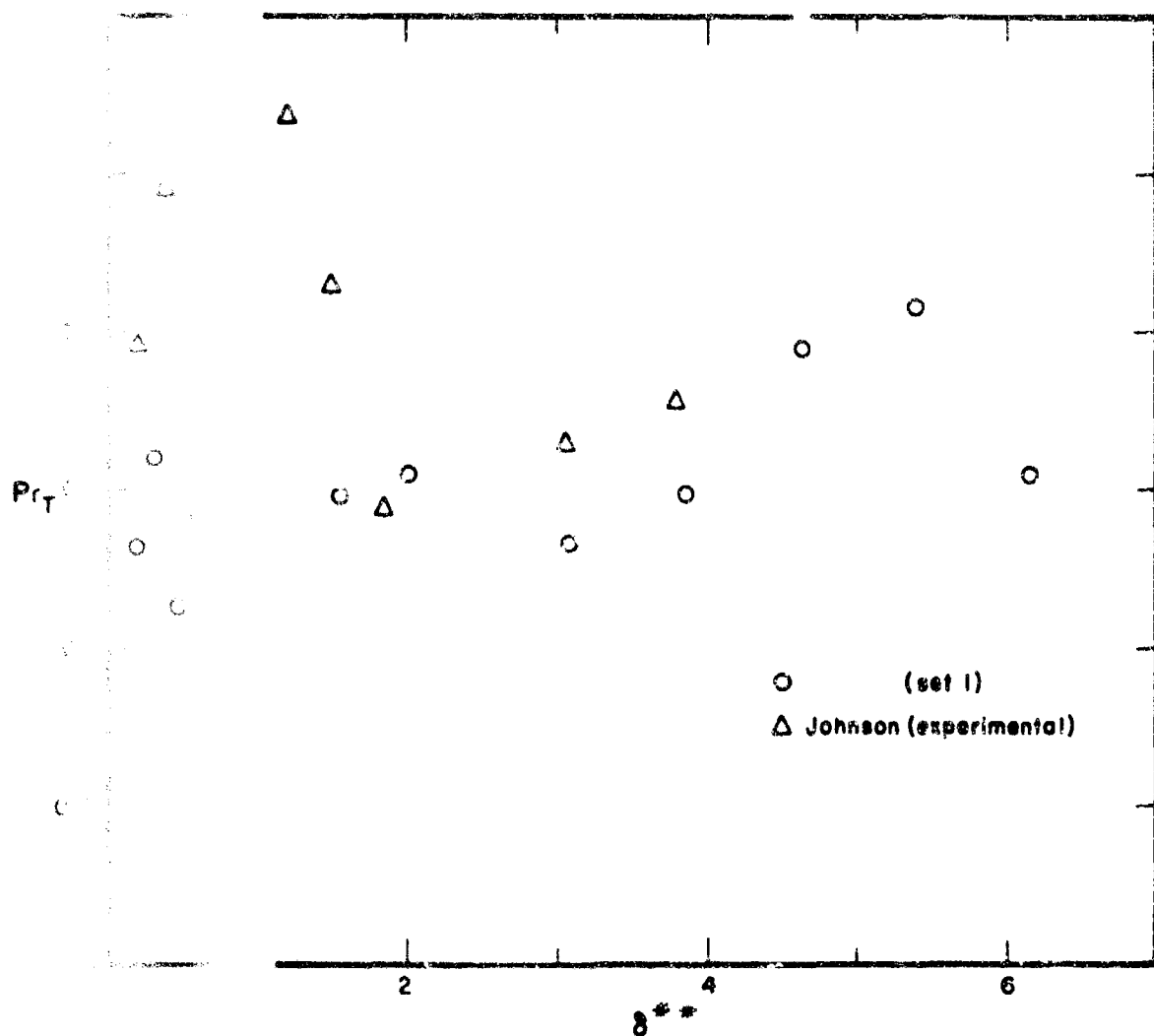
Figure   Turbulent Prandtl number profiles through the boundary layer.

Curves of the quantity U/U_∞ as a function of $\log_{10} yU_\infty/\nu_w$ for different values of c_f at 9 specified injection rates have been plotted (Figure 13) for hydrogen injection. The subscript w denotes the value at the wall. To use the graphs, one plots a few experimental values of U/U_∞ versus $\log_{10} yU_\infty/\nu_w$ on the chart corresponding to the experimental flow rates; interpolation between two graphs may be necessary. The points fall between two of the c_f curves, whereupon interpolation gives the estimated skin-friction coefficient. Values of the skin-friction coefficient, c_f, for the case of nitrogen injection have been computed and compared with the values determined by other methods. Good agreement was achieved. The method described may also be used to find approximate skin-friction coefficient values for cases in which the injectant is a gas mixture.

Figure 13. Adaptation of Stevenson's method for determining skin friction coefficient to the case for a variable composition turbulent boundary layer. F = 0.005

b -32

3.0 SUBSONIC TURBULENT BOUNDARY LAYER WITH INJECTION AND COMBUSTION

Turbulent boundary layer-combustion studies have been initiated in
the Thermal Science Laboratory subsonic combustion wind tunnel. The goals
of these studies are first; to determine the response characteristics of
an internally cooled hot-film sensor in the combusting turbulent boundary
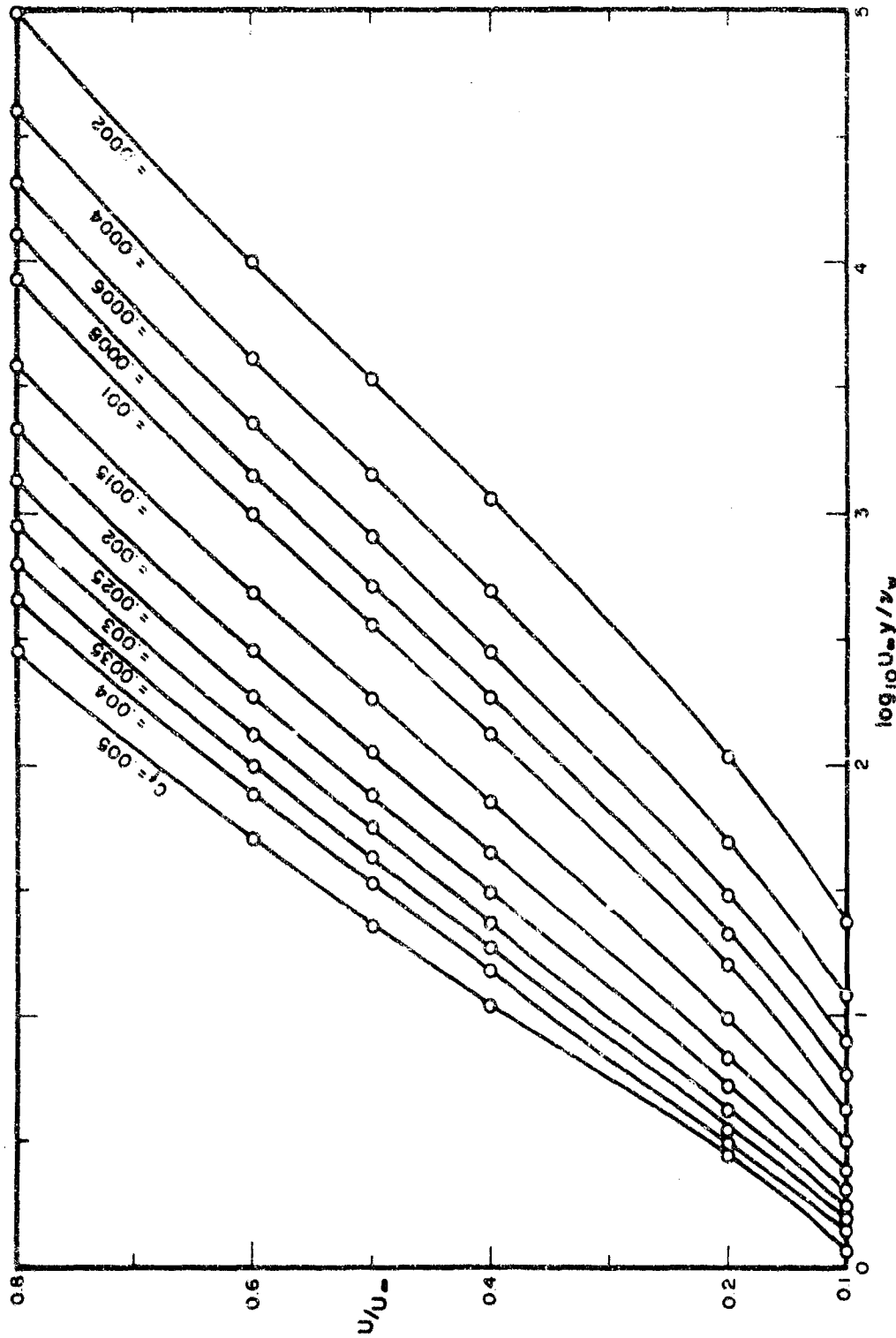layer and second; to study the characteristics of the boundary layer
itself. In studying the probe, consideration will be given to its appli-
cation in determining both mean flow quantities (velocity, temperature
and composition) and the character of turbulent fluctuations about the
mean values in terms of magnitude and spectral distribution. This program
is being carried out by J. W. Jones, as his doctoral research project.

3.1 *Equipment*

The cooled probe presently in use is a Thermo-Systems model HF-52
modified to a boundary-layer configuration. Additionally, a multiple
probe for measuring temperature, dynamic and static pressure and for
drawing samples to determine composition has been designed and will soon
be constructed. This probe will allow simultaneous measurements to be
made in the same horizontal and vertical plane. To date, individual
probes have been used to measure temperature and dynamic pressure.

The subsonic combustion wind tunnel and associated mass injection
equipment used is that which has been described in the previous sections
of this report.

For data acquisition and analysis a Thermo-Systems series 1050 constant
temperature anemometer with power supply, signal conditioner, linearizer,
temperature switching circuit and correlator are being used. The outputs
of the cooled probe-anemometer system are simultaneously recorded on a
Honeywell 7600 magnetic tape recorder and displayed on a Hewlett-Packard
Model 3400 A true rms volt meter. The anemometer system performance is
monitored on a Tektronix Model 551 dual-beam oscilloscope. Mean quantity
values are read out on a Honeywell Model 333 digital volt meter. The
spectral distribution of turbulent fluctuations is analyzed by means of a
General Radio type 1800A ware analyzer. All pressure measurements are

b-33

made with a Miriam Instrument micromanometer.

3.2   *Test Procedure*

To take best advantage of previous work accomplished at our facility
(AlSaji[2] and Smith,[30] a tunnel free-stream speed of 25 fps is used. The
injected nitrogen-hydrogen mixtures give F values on the order of those
used in the non-combustion foreign gas injection studies reported in the
previous sections.

Testing procedures are as follows. The instrumentation reference
values and calibrations are checked. The tunnel is started and the
flow velocity established. The injection is started and the
nitrogen and hydrogen flow rates established. The injected mixture is
then ignited in the tunnel. Once initiated, the combustion in the boundary
layer over the porous plates is self-sustaining. The tunnel is
allowed to run until the plates reach thermal equilibrium. This is
determined by monitoring the output of thermocouples imbedded in the porous
plates. It should be noted here that there is a considerable temperature
gradient axially along the first plate. However, temperatures along
the second plate are relatively constant ($\pm$ 30^{0}F). All boundary-layer
profile measurements are obtained at a point midway in the second plate.
(see Figure 14). The y-distances are measured from the plate surface, the
x-distance from the point of initiation of the turbulent boundary-layer
and all the present profiles are on the lateral centerline of the test
section.

3.3   *Test Results*

To date all tests have been run at $U\infty$ = 25 fps. Preliminary tests
have been conducted to determine the injectant rates and composition which
will provide a combustible mixture. It was found that if combustion was
initiated with the free-stream velocity decreased to about $U\infty$ = 14 fps
and gradually increased to the test $U\infty$ = 25 fps a mixture with ~2% by mass
hydrogen with F = 8.24 · 10^{-3} would give self-sustaining combustion. Most
tests to date have been run with ~ 3% by mass hydrogen mixture with
F = 11.9 x 10^{-3}. Future tests will extend the range of mixtures used in
both composition and injection rate.

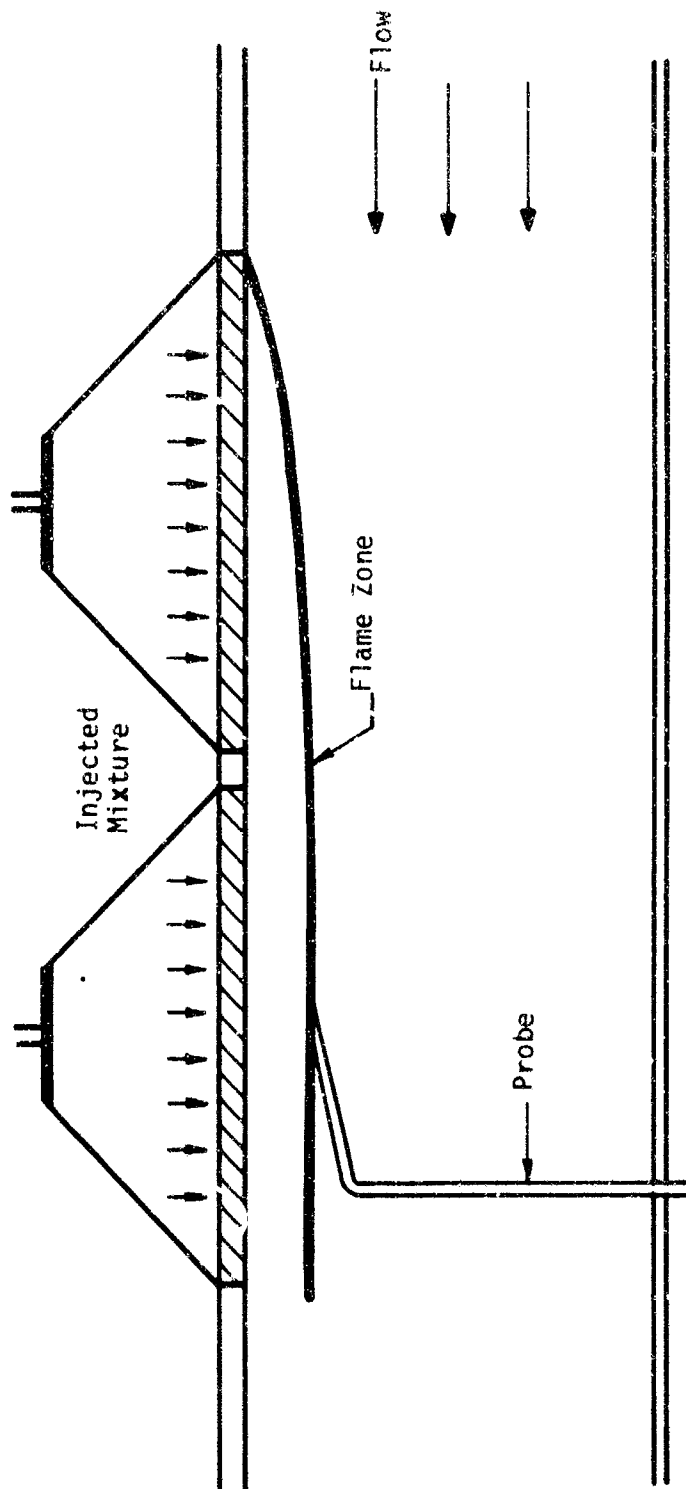The cooled probe has been used with both water and nitrogen employed

Figure 14. Schematic diagram of the subsonic combustion wind tunnel with combustion occurring in the boundary layer.

as a coolant. The nitrogen coolant gives greater sensitivity but cannot be used in high temperature regimes in the present probe. On the other hand, the cooling capacity of the water is such that the probe may be used through the combustion zone. However, with water cooling, the present probe is not sensitive to a change of velocity at the low ($U\infty$ = 25 fps) velocities presently being used. This does have an advantage for the present in that it eliminates one variable in interpreting the probe output. Temperature fluctuations are sufficiently strong that the water-cooled probe has very adequate sensitivity in a combustion environment. Other possible cooling fluids are being considered. Examples of probe output are shown in Figure 15. As the rate of energy received by the sensor (or given up by it, depending on the relationship of the probe surface temperature to the environment temperature) is dependent on local concentration as well as temperature, the fluctuations shown are not solely due to temperature. Observation of these traces show a basic change in the character of the phenomena with distance normal to the surface. In cooler regions of the flow, the traces show a predominately high power dissipation with spikes which indicate "bursts" of higher temperature gas brought to the probe by turbulent motion. In hotter regions of the flow the trace shows a predominantly lower power dissipation level with spikes in the opposite direction indicating "bursts" of cooler gas passing over the sensor.

Dynamic pressure, temperature, and energy flux profiles have been obtained for the case

$$(\rho v)_w = 18.70 \times 10^{-3} \text{lbm/hr}^2\text{sec},$$

$$F = 11.9 \times 10^{-3},$$

with an injectant composition as follows:

	Mass	Volume
Hydrogen	2.83%	28.8%
Nitrogen	97.17%	71.2%

An example of a mean temperature profile obtained with a 0.012 inch diameter cromel-alumel thermocouple probe is shown in Figure 16. The variation of boundary-layer composition and velocity also affects the
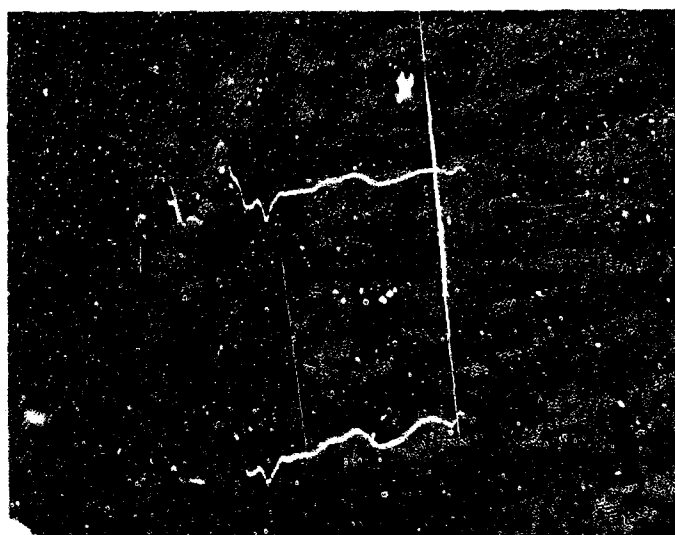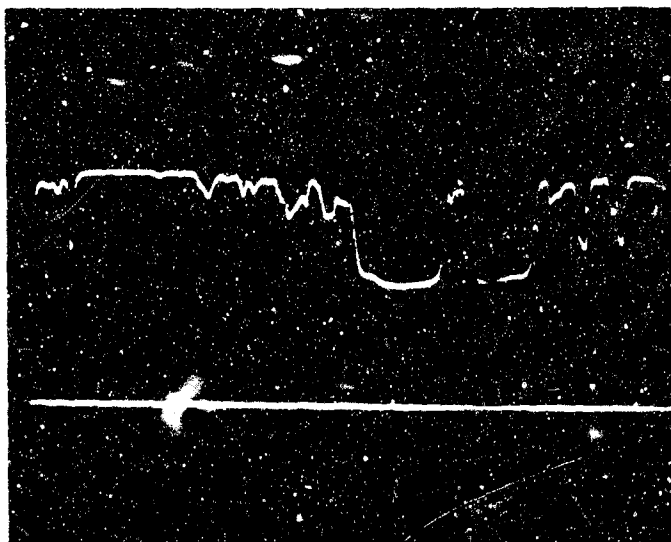
Figure 15. Typical oscilloscope traces of the output of the water-cooled film sensor in and near the combustion zone. The upper trace indicates the response when the probe is outside the zone, while the lower trace indicates the response of the probe in the zone.

b-37

the thermocouple readings and thus Figure 16 does not give the true values of the local mean temperature. It does, however, give an important first look at the environment and better than an order of magnitude look at the temperatures. The dynamic pressure measurements will not yield the velocity profile until the concentration profile is determined.

A significant benefit of the present tests has been to obtain a familiarity with the equipment and instrumentation being used. Another important contribution is that sufficient data on operations and environment has been obtained to map out continuing careful studies of both the cooled-probe and the combusting turbulent boundary-layer.

3.4 Continuing Work

With the use of the multiple head probe mentioned in the equipment section and the cooled-probe anemometer system, the characteristics of the cooled-probe will be determined. By varying the probe surface temperature, coolant and the composition and temperature of the boundary-layer, the effects of composition, temperature, and velocity on the total energy flux to the probe will be studied.[27] In this process a great deal of information on the boundary layer behavior will also be obtained. The distribution of turbulent fluctuations, both spectrally and with position, will be studied.

The variation of total energy flux to the probe is equal to the decrease in the amount of power required to maintain the constant probe surface temperature. In turn, this energy flux may be related to the probe environment by expression such as those given in References 28 and 29. From Reference 28 for heat transfer to a small cylinder, the heat transfer correlation may be written as

$$\frac{Nu}{Re^{\frac{1}{2}} \, Pr^{0.4}} = \text{constant} = \frac{C_D \, Q/\pi \, k \, (h_e - h_s)}{(\frac{\rho VD}{\mu})^{\frac{1}{2}} \, (\frac{\mu C_p}{k})^{0.4}} \quad (1)$$

where

Q = total energy flux

D = probe diameter

ρ = local environment density

μ = local environment viscosity
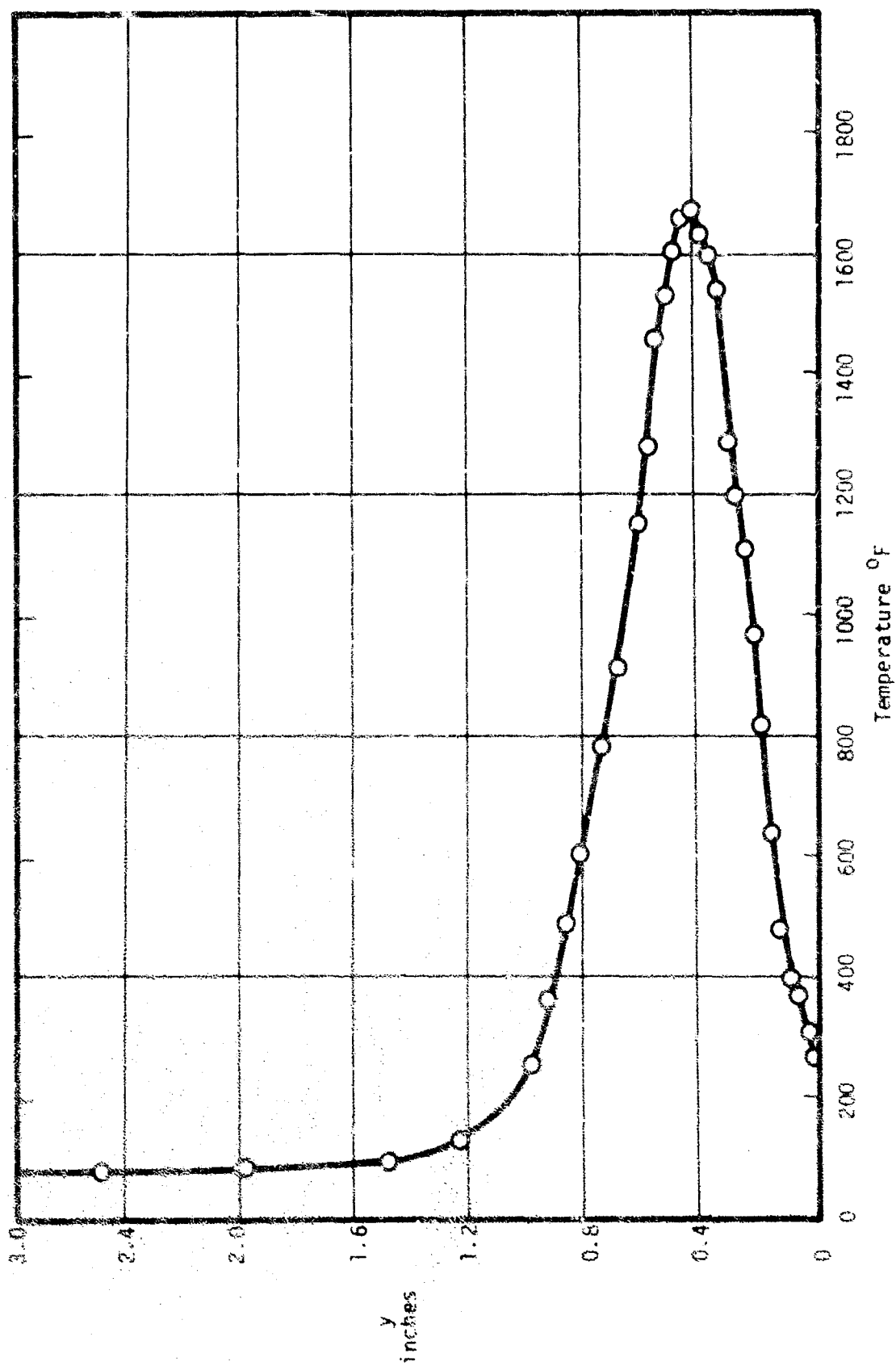
Figure 16. Temperature profile through the combustion zone.

b-39

C_p = local environment specific heat

k = local environment thermal conductivity

$(h_e - h_w)$ = enthalpy potential between environment and probe surface

From this it is clearly seen that variations in temperature, velocity and pressure all interact to a large extent and affect the heat transfer rate. By the means previously outlined, it is these interactions that are to be studied.

Additionally, since heat transfer is the quantity of major interest in problems involving combusting turbulent boundary layers, the ability to directly measure heat flux from the environment provides a powerful tool.

The major goals of this work are first; to gain sufficient information on the cooled probe characteristics to determine its most effective use in this and other combusting turbulent boundary-layer environments, and second; to provide a better understanding of the phenomena occurring in a combusting turbulent boundary layer.

4.0 SUPERSONIC COMBUSTION BOUNDARY LAYER

4.1 *Facility*

The growing interest in very high speed, high altitude flight has opened a new realm of propulsion analysis. The achievement of high speeds at high altitudes requires a powerful propulsive unit or engine. To date the rocket has served well in this area, but as the demand increases for more efficient means of propulsion, the oxygen of the atmosphere will have to be utilized. This has led to the consideration of air breathing engines for high supersonic and hypersonic atmospheric flight propulsion. Studies have shown that the potential performance of the supersonic combustion ramjet (scramjet) far exceeds the performance of even the most efficient chemical rockets.

In order to investigate the conditions encountered and the problems to be overcome in this new regime, it becomes necessary to simulate these conditions in a ground facility. Since no one facility can reproduce all the conditions likely to be encountered, it is necessary to devise different but complimentary facilities.

Figure 17 illustrates the general air intake procedure for a typical scramjet engine. The geometry illustrates how the simulation is possible. The air in the combustion chamber has passed through one or more oblique shock waves to decrease the speed from that of the free stream and to increase the static pressure and temperature. The free stream Mach number is still greater than 1, hence the combustion process will occur in a supersonic air stream.

A recent paper by Henry[1] indicates that the most pressing problems to be solved are concerned with the processes of mixing, ignition, and combustion of the fuel and oxidizer. It has been found that more efficient mixing occurs when the fuel is injected radially into the air stream, but significant stagnation pressure and axial thrust losses are incurred. A minimum stagnation pressure loss is realized, along with a significant increase in axial thrust, when the fuel is injected along the axis of the combustor, with mixing allowed to occur through a turbulent diffusion pro-
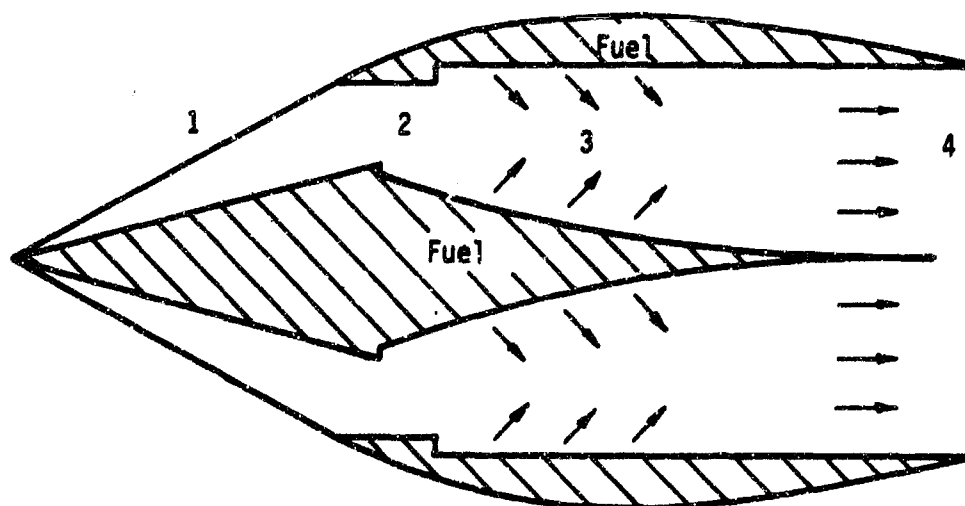
FLIGHT MODEL
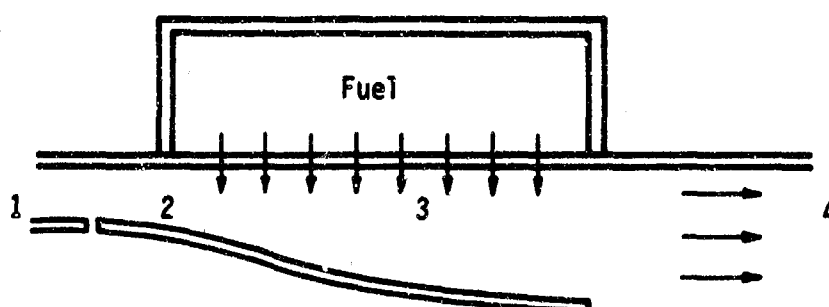
LABORATORY MODEL

Station	Legend
1	Ambient region (flight) or air heater (laboratory)
2	Inlet region (flight) or settling chamber (laboratory)
3	Combustor inlet
4	Combustor discharge

Figure 17. Typical flight and laboratory geometries employed for hypersonic flight simulation.

cess. However, the process of mixing for this case is so slow that exorbitant combustor lengths are required. Hence, an optimum fuel injection method must be found. Because of an insufficient amount of design knowledge concerning turbulent mixing and combustion phenomenon, such information will, of necessity, be found experimentally. The facility installed at the University of Utah has been designed to obtain such information. The design, installation, and calibration of this facility has been carried out by R. W. Harmer and D. L. Boyd.

In the simulation of conditions occurring in the combustor of a scramjet, it is not necessary to duplicate Mach number or velocity. It is more important to duplicate static pressure, static temperature, and residence time of the fuel and air in the combustion chamber. With these requirements in mind, the capabilities of the system may be examined. The nozzle blocks available to the supersonic combustion channel have been designed to provide test section Mach numbers of 2.5 and 3.0. In addition, the tunnel plenum chamber, diffuser, and exhaust system have been designed for a steady-state operation at a temperature of 3000R and a stagnation pressure of 200psia. With these basic parameters as a starting point, Table 1 presents the simulation conditions that would be selected for auto-ignition studies of hydrogen using the Mach 2.5 nozzle.

When completed, the facility will have the capability for simulating the combustor environment for a flight Mach number of 12 at an altitude of 130,000 ft. The present capability of the facility is also presented in Table 1 and indicates a capability for simulating flight Mach numbers of 9 and 10 at flight altitudes of 80,000 and 120,000 ft., respectively. This restriction is introduced by the utilization of a natural gas-fired burner in the pebble-bed heater, which produces a maximum bed temperature of 2600°R. This can be overcome by utilization of a propane-fired burner with oxygen enrichment.

The tunnel calibration, using an open-jet test section, is underway at the present time and should be completed in the next quarter.

A listing of the facility components is presented in the next two sections.

TABLE 1

SUMMARY OF THE SIMULATION CONDITIONS

	FLIGHT	LABORATORY	FLIGHT	LABORATORY
FREE FLIGHT MACH NUMBER	12		12	
FREE FLIGHT TOTAL TEMPERATURE	9375°R		9500°R	
FREE FLIGHT TOTAL PRESSURE	20,000 psia		30,000 psia	
ALTITUDE	130,000 ft		120,000 ft	
STATIC PRESSURE	1 psia	1 psia	2 psia	2 psia
STATIC TEMPERATURE	1400°R	1400°R	1400°R	1400°R
STAGNATION PRESSURE	2590 psia	17.1 psia	4720 psia	34.2 psia
STAGNATION TEMPERATURE	9375°R	3150°R	12,880°R	3150°R
VELOCITY	11,900 ft/sec	4580 ft/sec	11,700 ft/sec	4580 ft/sec
MACH NUMBER	6.5	2.5	6.4	2.5
REYNOLD'S NUMBER	1.3×10^7 /ft	5×10^6 /ft	1.28×10^7 /ft	5×10^6 /ft

TABLE 1 CONTINUED

SUMMARY OF THE SIMULATION CONDITIONS

	FLIGHT	LABORATORY	FLIGHT	LABORATORY
FREE FLIGHT MACH NUMBER	11		11	
FREE FLIGHT TOTAL TEMPERATURE	8000°R		7865°R	
FREE FLIGHT TOTAL PRESSURE	18,000 psia		23,000 psia	
ALTITUDE	120,000 ft		110,000 ft	
STATIC PRESSURE	1 psia	1 psia	2 psia	2psia
STATIC TEMPERATURE	1175°R	1175°R	1100°R	1100°R
STAGNATION PRESSURE	4150 psia	36.8 psia	10,500 psia	73.5 psia
STAGNATION TEMPERATURE	12,700°R	3200°R	12,800°R	3100°R
VELOCITY	11,800 ft/sec	5050 ft/sec	11,800 ft/sec	4870 ft/sec
MACH NUMBER	7.0	3.0	7.25	3.0
REYNOLD'S NUMBER	1.89×10^7 /ft	8.0×10^6 /ft	1.9×10^7 /ft	7.85×10^6 /ft

TABLE 1 CONTINUED

SUMMARY OF THE SIMULATION CONDITIONS

	FLIGHT	LABORATORY	FLIGHT	LABORATORY
FREE FLIGHT MACH NUMBER	10.0		9.0	
FREE FLIGHT TOTAL TEMPERATURE	6900°R		5550°R	
FREE FLIGHT TOTAL PRESSURE	7000 psia		17,00 psia	
ALTITUDE	120,000 ft		80,000 ft	
STATIC PRESSURE	2 psia	2 psia	2 psia	2 psia
STATIC TEMPERATURE	1150°R	1150°R	925°R	925°R
STAGNATION PRESSURE	1060 psia	34.0 psia	1060 psia	73.5 psia
STAGNATION TEMPERATURE	6900°R	2600°R	5550°R	2600°R
VELOCITY	8320 ft/sec	4160 ft/sec	7450 ft/sec	4460 ft/sec
MACH NUMBER	5.0	215	5.0	3.0
REYNOLDS'S NUMBER	1.32×10^7 /ft	6.66×10^6 /ft	1.64×10^7 /ft	9.0×10^6 /ft

b-46

4.1.1. Tunnel Inlet Pressure and Heater System

The following listing describes the equipment which is presently utilized to provide the pressure and heating cpapbility for the supersonic flow facility.

1. Compressor: Gardner-Denver two-stage piston compressor, designed for 350 psi maximum pressure, delivers 350 standard cubic feet of air per minute, shuts off approximately when receiver tank pressure reaches 350 psi and restarts at 320 psi.

2. After-cooler: Heat exchanger designed to remove heat put into air from compression.

3. Oil desiccator: Designed to handle 350 standard cubic feet of air per minute compressed to 350 psi with dry-o-lite activated alumina desiccant.

4. Receiver tank: Designed for a pressure of 400 psi and a temperature of 650°F.

5. Air dryer: Desiccant dryer designed to handle 350 standard cubic feet of air per minute at 400 psi.

6. Storage tanks: Eight cylindrical tanks of approximately 52.9 cubic feet each with a total capacity of 423 ft.^{3}, rated at 2800 psi, presently used to 350 psi.

7. Storage tank shut-off valves: Hand-operated 3000 psi, 1½" gate valve. Two Glove Pressure Controllers for inlet pressure regulation, from 3000 psi inlet to 150 psi outlet.

8. Pneumatic inlet valves: Four pneumatic inlet valves and one pebble-bed bypass valve (two 3", one 1", one 3/4", and one 1½" bypass) are hand loaded with air to open. Valves are installed with upstream pressure on top of the valve seats. One 3" valve is auxiliary and is not presently connected.

9. Orifice Plate: A 3/4" aluminum plate with a 0.953" diameter orifice is located upstream of the pebble-bed and downstream of the control valves to limit flow for safety purposes.

10. Pebble-bed heater: A natural gas fired pebble-bed heater

with 1" diameter alumina pebbles, designed to deliver 2600°R air at 300 psi.

11. Pebble-bed exhaust valve: Hand-operated 250 lb, 4" glove valve.

12. Pebble-bed gate valve: Crane hand-operated, 250 lb., 8" gate valve.

4.1.2   Downstream Flow and Test System

The basic hot flow system, downstream of the pebble-bed heater, consists of the following items:

1. Hot gas valve with cooled body and flanges.

2. Plenum chamber with settling screens and bypass air injector, made of 304 SS and completely water cooled for steady-state operation at 200 psi and 3000°R.

3. Transition section for adaptation to rectangular nozzle block made of 304 SS and completely water cooled.

4. Nozzle blocks for 3.0 and 2.5 Mach numbers made of 304 SS completely water cooled and prestressed for hot operation.

5. Free jet test section with access ports for various calibration probes and test probes. Equipment is fabricated to be readily adaptable for full length test section to study reacting boundary layer with mass injection.

6. Diffuser section made of 304 SS and completely water cooled

7. Expansion joint made of 304 SS and completely water cooled.

8. Cooler which is counterflow 128 tube heat exchanger rated for 850 BTU/sec. at 60 gpm water flow rate.

9. Ejector system to permit control of the compression ratio of the wind tunnel and to assist in reducing the exhaust stack temperature.

10. Probe positioner with clutch operated servo-motor, potentiometer, and 0.001"control vernier with zero backlash.

4.2 Channel

Figure 18 presents a schematic diagram of the supersonic combustion boundary layer channel to be fabricated and installed during the next year. This channel has been designed to allow probing of the turbulent boundary layer with injection and combustion which develops along the top wall of the channel. The test section dimensions would be as follows: Height = 1.50", Width = 2.75", Length = 21.0". The top wall would include a porous plate with dimensions of 2.25" in width and 15.0" in length. The porous plate would also act as the bottom surface of an enclosed fuel injector hood. This hood would be treated as an energy and mass control volume for the evaluation of surface heat and mass transfer.

It is anticipated that the use of this supersonic combustion channel would allow the acquisition of accurate turbulent mixing and combustion data, along with pilot ignition characteristics for application in the design of supersonic combustors for flight in the Mach number range from 5 to 12. It is also anticipated that the cooled sensor employed in the subsonic combustion wind tunnel will be incorporated into the testing program for this facility.

With the development of this proposed test section and its incorporation into the existing wind tunnel facility, a capability will be acquired by which information may be obtained concerning basic problems of mixing, ignition, and combustion in supersonic flow streams. The acquisition of such information should provide a more complete formulation upon which future designs of supersonic combustion propulsion systems may be based.

Pilot Ignition Gas

Water-Cooled Mach 2.5 or 3.0 Nozzle Block

Hydrogen-Nitrogen Injection Lines

Porous Inconel Top Wall of Supersonic Combustion Channel

Water-Cooled Diffuser

Adjustable Bottom Plate (Inconel)

Water-Cooled Plenum and Adaptor Section

Probe Access Ports

Film-Cooled Vycor Windows (Both Sides of Test Section)

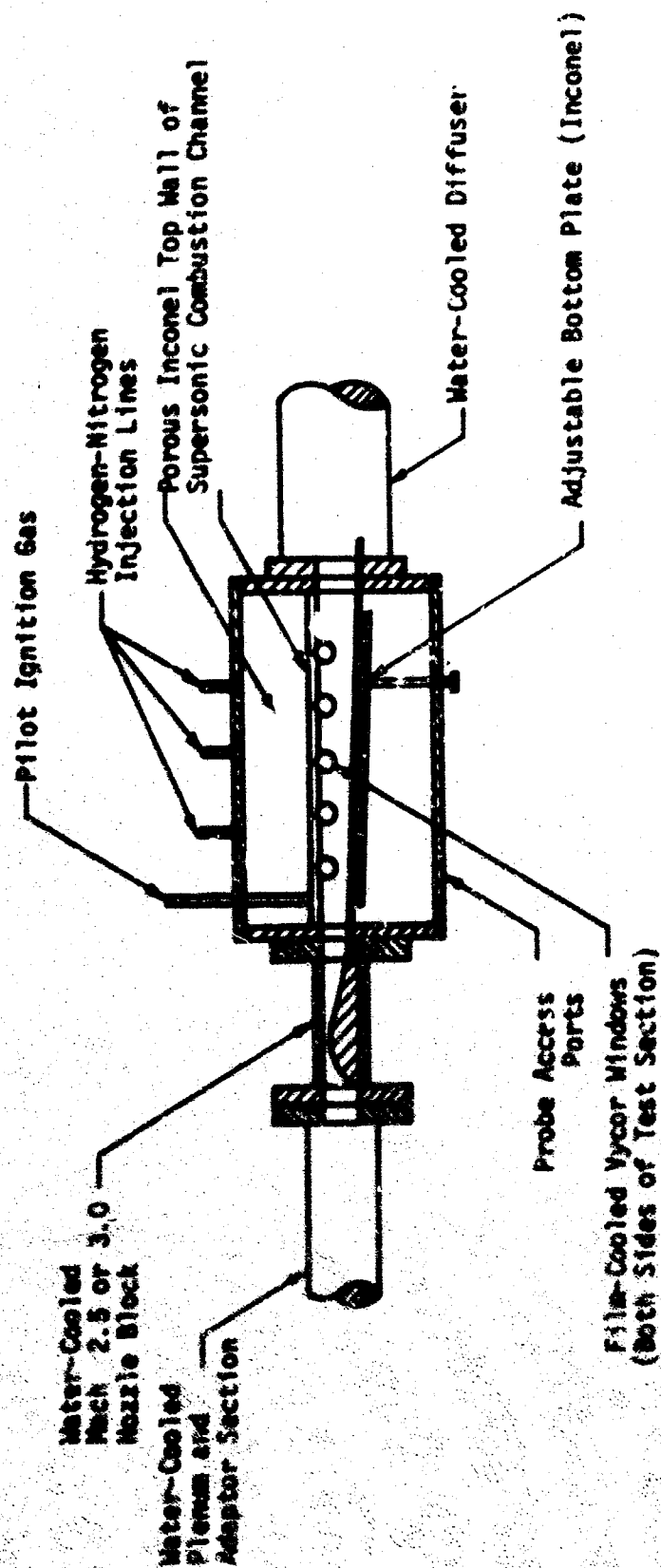Figure 18. Schematic diagram of the proposed water-cooled supersonic combustion boundary layer channel. The test section dimensions would be as follows: Height = 1.50". Width = 2.75", Length = 21.0". The porous plate would be manufactured from five micron Inconel powder to eliminate catalytic internal reactions. Pilot ignition would be provided in the boundary layer for tests with low stagnation temperature.

REFERENCES

1. Henry, J. R., "Recent Research on Fuel Injection and Mixing and Pitoted-Ignition for Scramjet Combustors," Paper presented at the Twelfth Symposium (International) on Combustion.

2. AlSaji, S. J., "The Transpired Turbulent Boundary Layer with Heat Transfer," Ph.D. thesis, Department of Mechanical Engineering, University of Utah, May 1968.

3. Stevenson, T. N., "A Law of the Wall for Turbulent Boundary Layers with Suction or Injection," College of Aeronautics, Report 166, 1963.

4. Stevenson, T. N., "Inner Region of Transpired Turbulent Boundary Layers," AIAA Journal, Vol. 6, No. 3, March 1968, pp. 553-554.

5. Stevenson, T. N., "A Modified Velocity Defect Law for Turbulent Boundary Layers with Injection," College of Aeronautics, Report 170, 1963.

6. Stevenson, T. N., "Turbulent Boundary Layers with Transpiration," AIAA Journal, Vol. 2, No. 8, August 1964, pp. 1500-1502.

7. Johnk, R. E., and Hanratty, T. J., "Temperature Profiles for Turbulent Flow of Air in a Pipe. I: The Fully Developed Heat Transfer Region," Chemical Engineering Science, Vol. 17, 1962, pp. 867-878.

8. Brundrett, E., and Burroughs, P. R., "The Temperature Inner-Law and Heat Transfer for Turbulent Air Flow in a Vertical Square Duct," International Journal of Heat and Mass Transfer, Vol. 10, 1967, pp. 1133-1143.

9. Isaacson, L. K., and AlSaji, S. J., "Temperature Inner-Law for Turbulent Boundary Layers with Transpiration," submitted for publication to the AIAA Journal.

10. Isaacson, L. K., and AlSaji, S. J., "Temperature Defect Law for Turbulent Boundary Layers with Transpiration," submitted for publication to the AIAA Journal.

11. Millikan, C. B., "A Critical Discussion of Turbulent Flows in Channels and Circular Tubes," Proceedings of the Fifth International Congress of Applied Mechanics, Cambridge, Massachusetts 1938, pp. 386-392.

12. Kulgein, N. G., "Transport Processes in a Combustible Turbulent Boundary Layer," Journal of Fluid Mechanics, Vol. 12, 1962, pp. 417-437.

13. Leadon, B. M., and Scott, C. J., "Transpiration Cooling Experiments in a Turbulent Boundary Layer at $M = 3$," Journal of Aeronautical Sciences, Vol. 23, 1956, pp. 798-799.

14. Muzzy, R. J., "Surface Mass Addition into a Turbulent Boundary Layer," AIAA Journal, Vol. 5, 1967, pp. 1029-1032.

15. Pappas, C. C., and Okuno, A. F., "Measurements of Skin Friction of the Compressible Turbulent Boundary Layer on a Cone with Foreign Gas Injection," Journal of Aeronautical Sciences, Vol. 27, 1960, pp. 321-333.

16. Rubesin, M. W., and Pappas, C. C., "An Analysis of the Turbulent Boundary-Layer Characteristics on a Flat Plate with Distributed Light-Gas Injection," NACA Technical Note 4149, National Aeronautics and Space Administration, Washington, D. C., 1958.

17. Spalding, D. B., Auslander, D. M., and Sundaram, T. R., "The Calculation of Heat and Mass Transfer through the Turbulent Boundary Layer on a Flat Plate at High Mach Numbers, with and without Chemical Reaction," Supersonic Flow, Chemical Processes and Radiative Transfer, edited by Olfe, D. B. and Zakkay, V., MacMillan Co., New York, 1964, pp. 211-276.

18. Wooldridge, C. E., and Muzzy, R. J., "Boundary-Layer Turbulence Measurements with Mass Addition and Combustion," AIAA Journal, Vol. 4, 1966, pp. 2009-2016.

19. Wooldridge, C. E., and Muzzy, R. J., "Measurements in a Turbulent Boundary Layer with Porous Wall Injection and Combustion," Tenth Symposium (International) on Combustion, Academic Press, New York, 1965, pp. 1351-1362.

20. Corrsin, S., "Extended Applications of the Hot-Wire Anemometer," NACA Technical Note 1864, National Aeronautics and Space Administration, Washington, D. C., 1949.

21. Champagne, F. H., Sleicher, C. A., and Wehrman, O. H., "Turbulence Measurements with Inclined Hot-Wires. Part 1: Heat Transfer Experiments with Inclined Hot-Wire," Journal of Fluid Mechanics, Vol. 28, 1967, pp. 153-175.

22. Hinze, J. O., Turbulence: An Introduction to its Mechanism and Theory, McGraw-Hill Book Co., Inc., New York, 1959.

23. Tritton, D. J., "Note on the Effect of a Nearby Obstacle on Turbulence Intensity in a Boundary Layer," Journal of Fluid Mechanics, Vol. 28, 1967, pp. 433-437.

24. Wills, J. A. B., "The Correction of Hot-Wire Readings for Proximity to a Solid Boundary," Journal of Fluid Mechanics, Vol. 12, 1962, pp. 388-396.

25. Kreith, F., Principles of Heat Transfer, 2nd edition, International Textbook Co., Scranton, Pennsylvania, 1965.

26. Kestin, J., and Richardson, P. D., "Heat Transfer Across Turbulent Incompressible Boundary Layers," International Journal of Heat and Mass Transfer, Vol. 6, 1963, pp. 147-189.

27. Blakshear, P. L., Jr., and Fingerson, L., "Rapid Response Heat Flux Probe for High Temperature Gases," ARS Journal, November 1962, pp. 1709-1715.

28. Cutting, J. C., Fay, J. A., Hogan, W. T., and Moffatt, W. C., "A Non-Catalytic Surface for Dissociated Combustion Gases," Planetary and Space Science, Vol. 3, 1961, pp. 53-60.

29. Zakkay, V., and Krause   "Mixing Problems with Chemical Reaction," Supersonic Flow Chemical Processes and Radiative Transfer, edited by Clft, D. B. and Zakkay, V., MacMillan Co., New York, 1964.

30. Smith, T. H., "Hot-Film Characteristic in a Transpired Turbulent Boundary-Layer with Variable Composition," Ph.D. Dissertation, Department of Mechanical Engineering, University of Utah, September 1968.

31. Spalding, D. B. "Contribution to the Theory of Heat Transfer Across a Turbulent Boundary Layer," International Journal of Heat and Mass Transfer, 7:743-761, 1964.

THE CHEMISTRY AND MECHANICS OF COMBUSTION
WITH
APPLICATIONS TO ROCKET ENGINE SYSTEMS

TASK 3   Ablation Mechanisms

J. D. SEADER

October 1968

College of Engineering
UNIVERSITY OF UTAH
Salt Lake City, Utah

PREFACE

This task involves an investigation of the thermal response of ablative materials to the mechanics and chemistry of combustible gas flow in certain components of a rocket motor system, as, for example, nozzles. Particular attention is being focused upon matters which have been largely ignored in the past:

Phase I: The interdependent effects of pyrolysis, surface chemical attack, and boundary layer combustion

Phase II: The kinetics of subsurface reactions

Phase III: The effects of surface-active agents to minimize and make more uniform the surface attack.

The general approach being taken involves an understanding of the important kinetic, transport, and surface effects at a molecular structure and interaction level. Unlike most previous ablation studies, chemical catalysis is being utilized to provide additional degrees of freedom towards the development of more efficient ablative structures.

During the 1967-68 academic year, effort was initiated on Phases I and II. Some background discussion and details of the accomplishments to date are presented in subsequent sections. A laboratory for the fabrication and bench scale evaluation of ablative composites has been completed. In addition, the use of a specially designed tunnel (with an adjacent control room) for hazardous experiments was secured for the installation of a hybrid rocket testing motor and a hot gas flow facility. These facilities are described below under Phase II. Effort on Phase III was begun only recently. Hence only some background material and the results of a brief literature search are presented at this time.

Before discussing the component phases in detail, it should be noted that all of them comprising TASK 3 of Project THEMIS are closely related to TASK 2 which deals with gas flow and heat transfer. In particular, the knowledge gained concerning chemically-reacting boundary layers will provide an essential interface, and the high temperature supersonic

flow facility currently being installed under Task 2 will provide a well-controlled environment for ablative material response studies. In addition, the consultative assistance of Professors R. H. Boyd, H. Eyring, and J. H. Futrell in the areas of polymer chemistry and physics, chemical reaction mechanisms, and mass spectroscopy, respectively should be acknowledged, especially in guiding the experimental work. Professors A. D. Baer and N. W. Ryan's broad background in solid propellant combustion has also provided an important contribution to our progress.

TABLE OF CONTENTS
TASK 3 Ablation Mechanisms

1.0 PHASE I   INTERDEPENDENT EFFECTS OF PYROLYSIS, SURFACE CHEMICAL
ATTACK AND BOUNDARY LAYER COMBUSTION--N. Burningham*

1.1 *Introduction*

The ablation of a reinforced plastic is a highly complex phenomenon
involving coupled mass, momentum and energy transfer mechanisms. Since
materials may ablate by melting, sublimation, vaporization, internal and
surface chemical reactions, or by any combination of these physical and
chemical processes, a description of the ablation process requires an
analysis of the energy and mass transport within the ablating material
coupled with the adjacent boundary layer.

The objectives of this phase of the Task 3 program are the investi-
gation of the thermal response of ablative materials to coupled environ-
ments, including inert and combustive atmospheres. Thus, the interdependent
effects of transpiring pyrolysis products, surface chemical attack and
boundary layer combustion are being studied. It is anticipated that
sufficient data will be collected on ablative materials properties and
thermal response that an existing digital-computer program, discussed in
in Appendix B,   can be utilized to predict and optimize thermal response
of ablative materials in a variety of environments.

The experimental work of this phase of the Task 3 program is proceeding
in three areas: a) determination of the kinetics of pyrolysis and
identification of pyrolysis-gas species, b) ablation experiments without
environmental coupling and, c) ablation experiments with environmental

---

* Mr. Norman W. Burningham received a B.S. degree in Chemical Engineer-
ing in 1960 from Princeton University with Honors in Engineering, and an
M. S. degree in the same field from the University of Denver in 1965
where his thesis was entitled "Analysis of an Internally Ablating Heat
Shield." He has also attended the University of Colorado and the
California Institute of Technology. From 1961 to 1965, he was employed
by the Martin Company, where he made significant technical contributions
in the research and development of advanced high temperature composite
materials. Since 1966, he has been on leave from the Martin Company to
pursue a Ph.D. degree at the University of Utah. He began work on Project
THEMIS in September 1967.

coupling. The kinetics of decomposition is being investigated by thermogravimetric (TGA) and differential thermal analysis (DTA or DSC) techniques. Pyrolysis gases from test samples will be collected and identified in a mass spectrometer. A study of ablation without coupling will be conducted in an arc-image furnace (described under Phase 2) with an inert environment. Results of these experiments should permit the establishment of a base line for the thermal response of ablative systems. A hot-gas-flow facility (described under Phase 2) will be utilized to study the effects of environmental coupling on ablative performance. It is believed that a sufficiently simple experimental procedure will be found such that the coupled effects can be treated singly or in a sequence and thus permit individual evaluation.

1.2 *Resin Pyrolysis*

To date in this program, the principal emphasis has been placed on the development of TGA techniques and their utilization to understand the kinetics of decomposition of resin materials. A vital part of the kinetic analysis is the identification of the decomposition gas species. The effluent gases provide the best key to precisely specify individual decomposition reactions. It is also essential that pyrolysis gases be completely identified in order that the chemical reactions between decomposition gases, char and boundary flow species might be studied.

One critical question which must be considered concerns the applicability of TGA data to rocket nozzle liner applications. Thermogravimetric analysis does provide a means of carrying out the pyrolysis reactions in an inert environment which simulates that of the pyrolysis zone. Also, the TGA method provides a programmed heating rate environment which forms the char, and permits the gases to escape at pyrolysis temperatures with essentially no secondary cracking and, hence provides a direct measure of primary char formation.

The essential difference between TGA tests and an actual ablation case is the heating rate. In usual TGA experiments, temperature rise rates of samples are on the order of 1^0 to 30^0C per minute while in an actual ablation application test, temperature rise rates of 5000^0 to 8000^0C per minute can be encountered.

Some authors, therefore, have concluded that TGA data may have no direct connection to material responses in normal ablative conditions. For example, Melnick and Nolan[1] have developed an apparatus capable of conducting TGA-type tests on large samples at very h h heating rates and have compared kinetic parameters (assuming a single chemical reaction) for customary TGA heating rates with those obtained in their high heating rate system. Tremendous disagreements in the values obtained led them to the conclusion that no correlation between the two types of test existed and that the normal, low heating rate technique is invalid. However, in reaching this conclusion the authors have committed several vital errors which are believed to negate their conclusions.

First, they fail to recognize that several distinct chemical reactions were occurring whose cumulative effect is represented in their thermogram. Of particular significance for their composite system of nylon-phenolic is the fact that the two constituents decompose essentially independently over different temperature ranges. Furthermore, the phenolic constitutent, as discussed below, decomposes by at least two different types of reactions. They next compare data from a short duration heating rate test, for which it is very unlikely that sample temperature was either uniform or equal to the programmed temperature, to results of a low heating rate test of extended duration. The high heating rate test, therefore, strongly emphasizes the early portion of the thermogram giving overwhelming predominance to early reactions which may have radically different kinetic parameters than the effective overall kinetic parameters for all decomposition reactions representing the entire thermogram.

On the other hand, other authors conclude the equivalence of high and low heating rate tests. Parker and Winkler[2] tested a variety of phenolic resins and determined char yields for heating rates up to 25 cal/cm^2-sec^2. They observed that char yields were essentially the same as those for TGA tests. They tentatively concluded that primary char forming processes for phenolics are independent of polymer heating rate over temperature rise rates varying from 2^0 to 5000^0C per minute. The fallacy in this conclusion is that the final amount of char formed is not a sufficient measurement or indication of the detailed kinetic processes which have occurred. It is conceptually possible for the kinetic mechanisms

to vary and still yield approximately the same amount of char.

We are finally left with the conclusion that the question of the validity of ordinary TGA tests is yet unsolved, and therefore we believe that further investigation is required.

1.3 Resin Systems

The resins which are being evaluated in this program have been selected to provide a broad variety of chemical types including those in present general use as well as some of the most promising new resin. Because of their almost universal application (novolac) phenolics and epoxies are being studied. Also some of the new and promising resins, such as p-polyphenylene, polyphenylene oxide, polyimides(PI), polybenzimidazoles (PBI) and other heterocyclics such as polyazomethines and polyimidazopyrrolones are considered. Some of these polymeric structures are shown in Table 1.

Certainly the most widely used resin system in ablative applications has been the phenolics. Their broad utilization has encouraged the development of an extensive literature on phenolic ablation. However, even for these best characterized ablative resin, many questions remain unanswered.

Phenolic resins as a group of compounds include a considerable number of materials which are modifications of the original phenol-formaldehyde condensation polymer. As a class these polymers are readily available from numerous suppliers. Phenolics have excellent molding and laminating properties and exhibit desirable strength characteristics. The ease with which phenolics can be successfully combined with many types of reinforcement to form effective thermal protective systems no doubt accounts, in part at least, for their extensive usage. However, phenolic materials as a class have relatively low char yields ranging from about 25-50%. Also, while approximately 50% of the pyrolysis gas is composed of hydrogen, the remainder is made up of considerably higher molecular weight gas species. Therefore, phenolics do not exhibit the most desirable characteristics.

It is only recently that the kinetics of phenolic thermal decomposition has begun to be understood. Early investigators studying the pyrolysis of phenolic, alone or in conjunction with a reinforcement, arbitrarily characterized the kinetics of decomposition by a single-step process.

c-4

TABLE I.   CHARACTERISTIC STRUCTURES
OF PROSPECTIVE ABLATIVE POLYMERS.
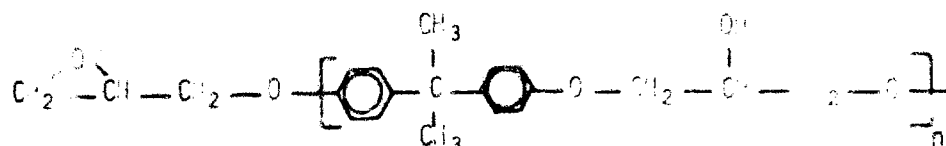
1.   Epoxy
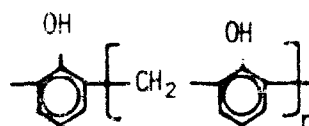
2.   Phenolic

3.   p-polyphenylene

4.   Polyphenylene oxide

5.   Polyimide

c-5
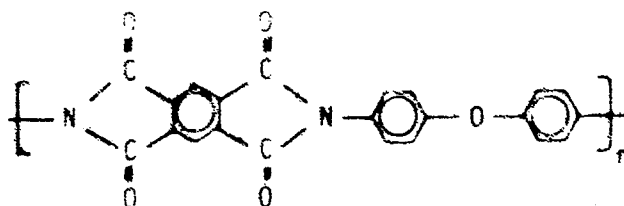
TABLE I (CONTINUED)
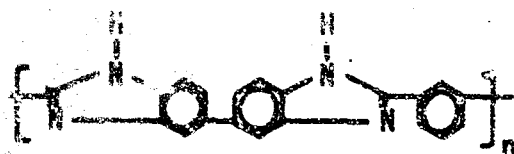
5. Polybenzimidazole
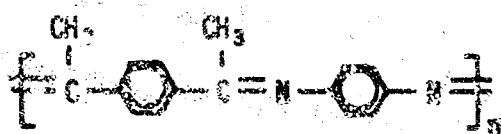
7. Polyazomethine
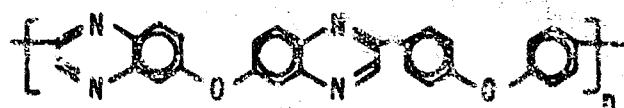
8. Polyquinoxaline
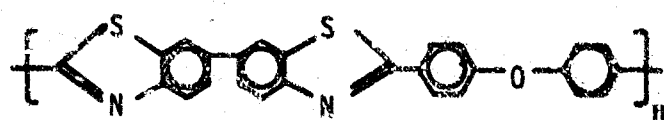
9. Polybenzothiazole

Generally, it was assumed that the decomposition reactions were irreversible and that homogeneous kinetics apply. Also, an empirical, pseudo-order rate expression of the classical form is assumed to be appropriate. Thus the reaction is described by the generalized expression

$$ -\frac{1}{M_0} \frac{dM}{dt} = k \, f \left(\frac{M}{M_0}\right) \tag{1} $$

where the specific rate k is given by the Arrhenius relation;
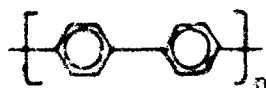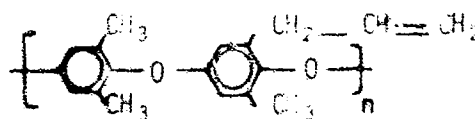
$$ k = A \, e^{-E/RT} \tag{2} $$

the function $f(M/M_0)$ usually has the form

$$ f\left(\frac{M}{M_0}\right) = (M - M_r/M_0)^n \tag{3} $$

The combined expression is then,

$$ -\frac{1}{M_0} \frac{dM}{dt} = (M - M_r/M_0)^n A e^{-E/RT} \tag{4} $$

The kinetic parameters, activation energy E, pre-exponential factor A, and order of reaction n are then determined from the rate equation using TGA data. The data processing techniques are discussed in a later section.

The particular assumed form of the rate equation given by Equation (4) is generally attributed to H. L. Friedman[3] who seems to be one of the first to have used and popularized it. Even though the form has been widely used it is open to serious criticism. First, since there are undoubtedly several chemical reactions proceeding simultaneously, no single rate expression could possibly account for them, except for considering only a gross average of properties. It has often been observed that attempts to fit phenolic decomposition in this way have been less than successful. For example, the evidence of TGA weight loss curves for phenolic clearly indicates that at least two major reactions are occurring. Curves shown in Figure 1 for USP 502 phenolic obtained with the TGA apparatus described below are of the same form as those obtained by Goldstein.[4] The complex curvature of these thermograms indicate at least two principal weight loss regions. The kinetic parameters obtained assuming a single rate law have no obvious connection with the physical meanings normally associated with

c-7

FIGURE 1. TGA CURVES FOR USP-502 PHENOLIC RESIN

Temperature °C

Residual Weight Fraction

c-8
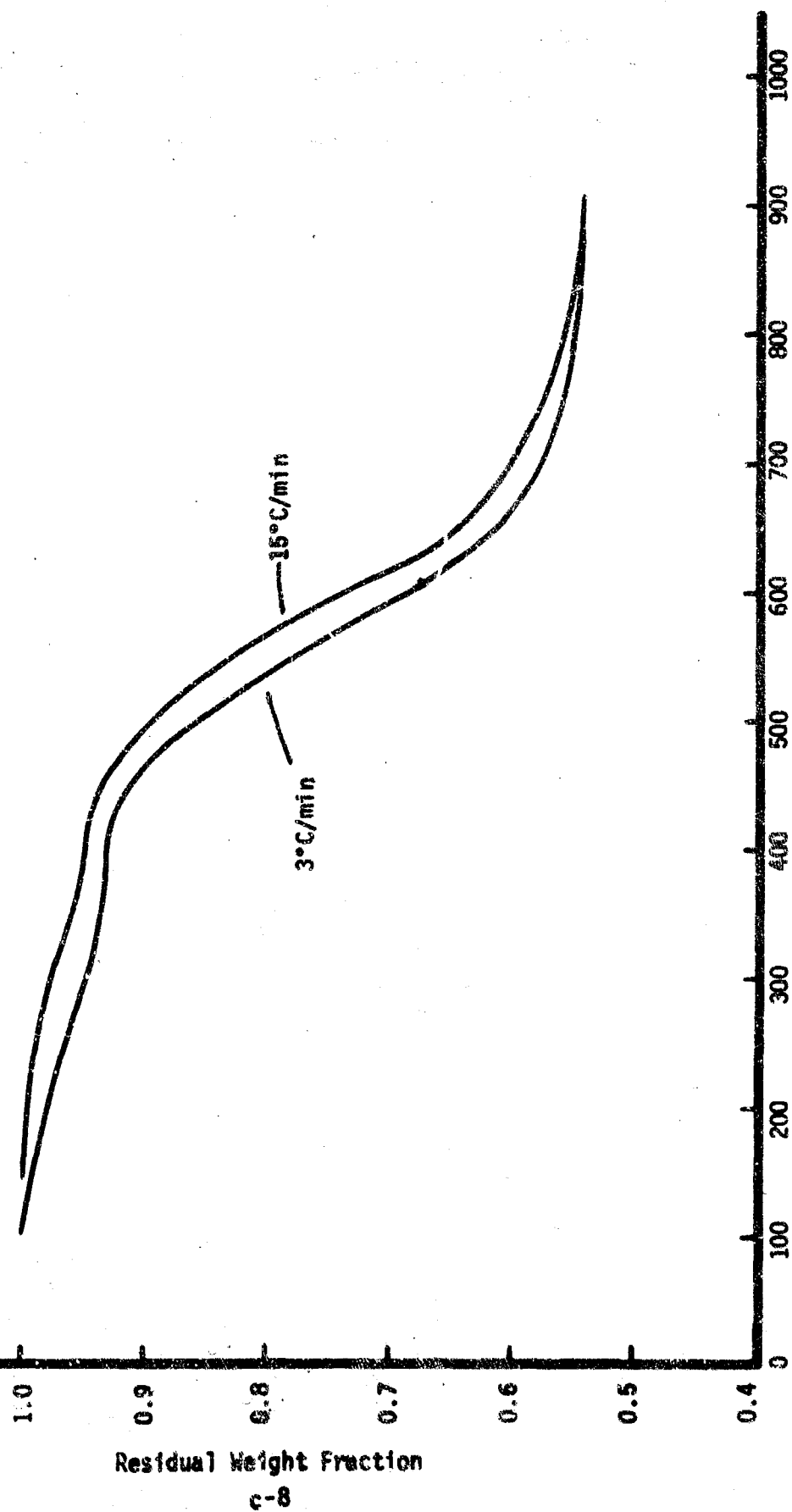
them.

Recently some investigators have used the form in equation
(4) but have applied it separately to the major reactions observed.[4]
Goldstein has successfully applied a rate equation of the type of
equation (4) to the decomposition of CTL-91LD phenolic by using it
twice, once to each of the predominant reaction regions he iden-
tified. After determining kinetic parameters, Goldstein was then
able to predict weight loss curves with greatly increased accuracy.
Kratch and co-workers[5] have extended this idea of multiple re-
action mechanisms to include a combination of three basic reactions.

Another way to analyze the decomposition reaction is to find a
model which describes the process on a macroscopic scale. One such
model has been successfully used by metallurgists to predict thermal
decomposition of explosives.[20]

Consider the decomposition reaction as occurring by way of an
activated state at the interface between a newly formed product
nucleus and the initial reactants. The nucleus grows as a sphere
of radius, r, as the reaction proceeds. The rate of reaction is
proportional to the number of reactant molecules. Therefore, it
can be written

$$\frac{dn}{dt} = -\frac{4\pi r^2}{\lambda^2} k \tag{5}$$

where the quantity n is the number of reactant molecules, λ^2
is the molecular area of the activated state, and k is the reaction
rate constant.

Maximum interfacial area is reached when $r = r_0$, the radius
at which the growing spherical nuclei touch and begin to overlap.
The fraction reacted, R, is the ratio of the sphere of products of radius
r inside a sphere of reactants of radius r_0. For N_0 nuclei

$$R = \frac{N_0 \, 4/3 \pi r^3}{N_0 \, 4/3 \pi r_0^3} = \frac{r^3}{r_0^3} . \tag{6}$$

The number of reactant molecules is obtained by subtracting the sphere of products from the sphere of reactants and dividing by the molecular volume,

$$n = \frac{\frac{4}{3\pi r_0^3} - \frac{4}{3\pi r^3}}{\lambda^3} \tag{7}$$

Differentiating equation (7) and equating the result with (1), the expression for the rate of growth of the nuclei is obtained

$$\frac{dr}{dt} = \lambda k' \tag{8}$$

According to this equation, the radius varies linearly with time.

If equation (6) is differentiated with respect to time and combined with (4), the result is

$$\frac{dR}{dt} = \frac{3\lambda k'}{r_0} R^{2/3} \tag{9}$$

When Equation (9) is integrated

$$R^{1/3} = \frac{\lambda k'}{r_0} (t - t_0) \tag{10}$$

Thus the fraction reacted to the one third power varies linearly with time.

The fraction reacted is related to the measured weight by the ratio of the weight loss, Δw, to the weight loss at the inflection point, Δw_i. Thus

$$R = \frac{1 - w_m/w_0}{1 - w_i/w_0} \tag{11}$$

and

c-10

$$(1 - w_m/w_0)^{1/3} = k'' (t-t_0) \tag{12}$$

Values of k'' are evaluated from a plot of equation (12) which only applies to the inflection point of the weight loss versus time curves.

For reactions beyond the inflection point, a similar but more cumbersome derivation gives an equation which applies to the rest of the reaction

$$1 - \left(\frac{w_m/w_0 - w_f/w_0}{w_m/w_0 - w_f/w_0} \right)^{1/3} = k_2 (t-t_0) \tag{13}$$

where w_f is the weight at complete reaction.

This type of an approach would be useful in analysis of rate of char formation in ablation if a single reaction were occurring.

Occasionally phenolic weight loss curves do not exhibit the complex curvature illustrated in Fig. 1. Such data may be in error or they may be correct representations for a different form of phenolic. In either case, these considerations indicate a need for a mechanism of decomposition. Knowledge of a mechanism would permit direct formulation of a rate expression.

Such a detailed mechanism has been proposed by Parker and Winkler[2] to explain the thermal decomposition of phenolic polymers in inert environments. These investigators suggest that the thermograms obtained from TGA analysis of phenolics can be explained by assuming that the stable chars observed result from the coalescence of certain benzenoid structures in the principal chains of the polymer. They suggest that the initiation step for the pyrolysis, given as (I) in Fig. 2, is the homolytic scission of the carbon-carbon bond connecting the aromatic pendant group to the main chain. Thermodynamically, this bond is the weakest C-C bond in the chain. Pendant group elimination can occur on either side of the single bonded phenol ring to give both a phenol radical and a cresol radical (III and III-a). Next a rapid abstraction of hydrogen atoms follows

c-11

FIGURE 2. PRINCIPAL STEPS IN NONOXIDATIVE THERMAL DEGRADATION
OF PHENOLIC NOVOLAC RESINS
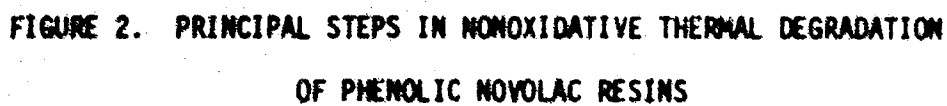
to give phenol and cresol as primary products. The free radical main chain intermediates (II) and (IV) formed are expected to rearrange to give intermediates (VI) and (VII). It is postulated that char formation proceeds through a stable intermediate, shown as (VIII), formed by termination of the main chain radical pairs (VI) and (VII). The formation of this stable bond prevents elimination of those aromatic rings initially bonded by two or more methylene groups in the principal chain. Thus, only those phenolic ring structures which are multiple bonded in the virgin polymer are retained in the thermally crosslinked intermediate, which loses methane and carbon monoxide above 500°C to give unstable char. Thermally stable char is depicted as forming by continued crosslinking of the aromatic rings in char (IX) with elimination of hydrogen and water. The final char retains only those aromatic carbons multiply bonded in the original polymer. Parker and Winkler apply their proposed mechanism to other published data with considerable success. Certainly the proposed mechanism is an important step in understanding phenolic thermal decomposition.

The mechanism of Parker and Winkler is somewhat different than another proposed by Madorsky[6]. Madorsky suggested that the primary mechanism of thermal degradation was the scission of bonds as indicated by the dotted line,
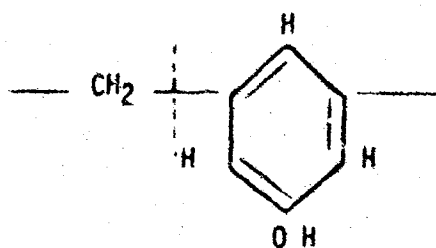
At temperatures of pyrolysis of about 360°C he determined the main volatile constituents to be acetone, propylene, propanol and butanol. The compounds CH_4, CO, CO_2 were thought to result from the complete breakdown of the benzene ring at between 800 and 1200°C. The free radicals resulting from this thermal cracking could either recombine or strip the crosslinked residue of hydrogen and oxygen.

The two mechanisms differ on the location of initial chain scisson and on the source of such gases as CO_2, CO, and CH_4. Also Parker and Winkler detected phenol and cresols which were not observed by Madorsky. The rearrangement proposed by Parker and Winkler yielding char is also another significant difference. Even though the mechanism of Parker and Winkler seems to fit more data better than Madorsky's, neither approach can be completely rejected. Differences in basic polymeric structure and methods of gas analysis could easily have contributed some of the differences between the two methods.

In general, the reinforcements used in conjunction with a resin in composite fabrication have little effect on the thermal response of the resin. In the case of nylon-phenolic composites, the total weight loss curve can be considered as the sum of the independently determined thermograms for the nylon and the phenolic. However, for silica reinforcements a series of highly endothermic reactions with carbon are possible at post-pyrolytic conditions, which can significantly alter the ablation response characteristics. A more complete discussion of these reactions is given in Phase II of this report.

The epoxies represent another class of materials which has been extensively used in thermal protective systems. Like the phenolics, they are readily available in many modified forms, are generally easily molded and laminated, and are chemically and mechanically compatible with essentially any reinforcement.

Less is known of the exact nature of the pyrolysis of epoxies than is the case for phenolics. No detailed mechanism of decomposition has been proposed. However, several studies have successfully correlated epoxy structural types and curing agents as a function of the char yield.[7] Fleming has studied ten different epoxy types in conjunction with nine curing agents and has been able to predict char yields. Char yields for epoxies are generally much lower than for phenolics ranging from 10% to 20%.

The ablation of an epoxy illustrates one of several types of coupling of desirable properties which occur in ablation systems. Ideally an ablator would decompose producing a large quantity of low molecular

weight gas so that heat blockage by mass injection into the boundary layer will be maximized. At the same time the ideal ablator would form a tough, stable char layer in order to maximize heat blockage by minimizing heat conduction to undecomposed ablator and substructure.

In actual cases it seems that the ablator characteristics obtainable represent a trade off between the desirable extremes. Thus, systems which produce the best chars usually produce less voluminous gas decomposition products. In the past several years, the greatest advances in ablative systems have been made by the development of new resins which are stable at much higher temperatures than previously possible. Also generally characteristic of these new high temperature resins is their highly aromatic or heterocyclic nature which produces a high amount of char residue. Included in this group are the polyphenylenes, polyimides, polybenzimidazoles, polyimidazopyrrolones and polyazomethenes. There are obviously a large number of specific polymer formulations possible within these class types. Work has been done on a number of specific examples which seem to have outstanding properties.

Polyphenylene structures have been investigated by Vincent[8] and have been observed to form a hard dense char layer as they degrade essentially by the elimination of hydrogen. Parks[9] has conducted an extensive comparison of eleven resins likely to exhibit desirable ablative properties and has ranked them according to mass loss rate, erosion rate, char formation, mechanical strength and TGA performance. The outstanding resin studied was polybenzimidazole (PBI) which was superior in almost every test. However, Dickey and co-workers[10] also investigating PBI resins, showed that conventional PBI resins degrade rapidly in air environments by the oxidative scission of the imidazole ring at the = NH group. This decomposition produced no char. When the PBI was thermally crosslinked by the elimination of the = NH group, it showed a resistance to oxidation similar to that of graphite. Also, recent advances in resin technology have reduced the difficulties in fabricating with PBI which once limited this resin's use.

Many heterocyclics are presently being investigated and reported

in the literature.[11, 12] The most promising of these new polymers
will be included in evaluations conducted in this program. One of the
primary selection criteria must necessarily be the processability
and general handling characteristics of the candidate resin. Several
resins which seem to have excellent ablation properties are so diffi-
cult to handle that it is essentially impossible to use them in com-
posites. Recognizing this difficulty, chemists are now modifying
good ablation structures to enhance processability.[12]

A concept to which the plastics industry has devoted little
attention thus far is the possibility of catalyzing desired pyrolysis
reactions. The catalysis of the endothermic silica-carbon reactions
is such an example. The appropriate selection of beneficial char
reactions rather than unprofitable decomposition would certainly en-
hance the performance of some ablative resins.

1.4 *Reinforcements*

The fabrication of efficiently ablating composites of the best
resin systems obviously requires a high performance reinforcement.
Two reinforcements have to date far surpassed all others in this
regard: graphite (carbon) and high silica. Both of these materials
combine characteristics of high strength, high temperature stability
and ease of fabricability. The work done in this program will
utilize principally these two reinforcements.

Other refractory reinforcements such as zirconia and magnesia
have been used in high temperature applications in combination with
phenolic and epoxy resins. However, fabricated composites incor-
porating these reinforcements exhibit poor structural strength and
are in general inferior in performance to graphite and silica
reinforced composites. Further advances in the properties of these
materials is necessary before they will occupy a competitive position.

Another recent advance which may alter the present concepts of
thermal protection is the development of a 3-D composite. Lurie and
co-workers[13] have fabricated structural composites which have re-
inforcement in three mutually perpendicular directions. These 3-D
composites have outstanding structural properties and their ablative

c-16

performance was about the same as normally fabricated samples using the same components.

1.5 *TGA Apparatus*

The thermogravimetric analysis (TGA) system being used in this program is built around a Cahn Model RG Automatic Recording Electrobalance. This balance as shown schematically in Fig. 3 is a high sensitivity null point instrument in which a light source photocell is the detector. An electromagnetic D'Arsonval movement supplies the restoring force. The loop gain of the servo system is in excess of 1000, so that the actual beam deflection under load is very small, and the balancing torque is equal to the sample torque. The torque motor used in the balance is as linear as precise weights and precision potentiometers can determine. Thus, the balancing current is a direct measure of the sample weight to an accuracy of better than $\pm$ 0.05% and a precision of better than $\pm$ 0.01% of full scale sample weight.

The balance beam has three loops: loop A has a maximum load of 1 gm; loop B load maximum is 2.5 gm; and loop C is used to support tare weights for the other loops. The permissible weight change is 0 to 200 mg for loop A and 0 to 1000 mg for loop B. The smallest weight change that can be reliably detected depends on total load, but for small samples it is 2×10^{-7} gm.

The balance mechanism is mounted in a glass vacuum bottle accessory which permits operation in reduced pressure or flow-through environments. Samples are suspended in hangdown tubes whose size has been selected to provide optimum sensitivity and minimum noise for flow through experiments.[14]

The Cahn balance system has been used extensively in high precision TGA work and has been shown to be stable in a wide variety of operating conditions.[15, 16]

The furnace used in conjunction with the balance is a Marshall Model No. 1123 base-metal furnace with a maximum operating temperature of 2200°F. The furnace has a heating zone one foot long which is provided with shunt taps to effectively control the temperature profile along the length of the furnace. Thus far the central 7-inch section

FIGURE 3.   SCHEMATIC DIAGRAM OF THE CAHN ELECTROBALANCE
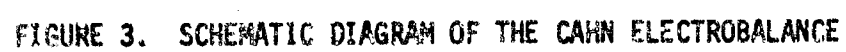
of the furnace has been controlled steadily with a maximum temperature deviation of ± 4.0°F. However, it is possible to reduce the deviation to approximately ± 1°F, thus providing a large region of constant thermal conditions.

The temperature of the Marshall furnace is controlled by an F & M model 240M-25 Temperature Programmer. This control device has a true proportional power output which permits smooth temperature programming and control from ambient to 1000°C. The solid state circuitry has a maximum power output of 2500 watts. A temperature sensitivity of less than 0.1°C is possible. The controller can function to provide constant temperature operation before, after, or between programmed periods. Programming rates of 0.5, 1, 2, 3, 4, 5, 7.5, 10, 15, 20, 25, 30°C/min. are available.

The output of the Cahn electrobalance takes the form of a DC electrical signal which is the input to a Mosely Model 7001A X-Y Plotter. This instrument, handling 11 x 17 in. paper, has input sensitivity ranges from 0.1 mv/inch to 20 v/inch with continuous variable control between calibrated positions. Accuracy of at least 0.2% full scale, linearity of 0.1% on all ranges and an integrated time base applicable to either axis at speeds from 0.01 to 20 in/sec. are all within recorder capability. Figure 4 illustrates the apparatus.

A great deal of effort has been directed toward developing an efficient laboratory technique for TGA work using the described system. Initially it was observed that building vibrations picked up by the sensitive balance mechanism and transmitted to the recorder as noise completely precluded the use of small samples and the high sensitivity ranges on recorder balance. A filter tuned to eliminate noise in the region of 60 cps helped to reduce vibrational noise levels and also minimized noise pick up due to electrical ground loops. Isolation of the table supporting the TGA apparatus by shock absorbing castors further reduced noise in the recorder. However, normal building vibration can, at times, still limit the use of the most sensitive ranges.

It is desirable that TGA samples be as small as practicable
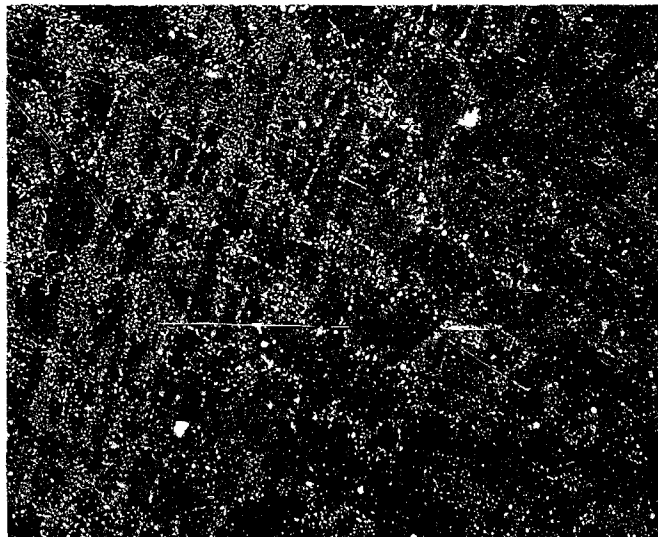
FIGURE 4.   TGA EQUIPMENT ASSEMBLY

c-20

in order that temperature uniformity might be closely approached and temperatures of transitions more accurately identified. Sample sizes on the order of 10 mg may be close to optimum for the system being used. For resin specimens, test samples have been prepared by grinding cured polymer and using the powder fraction which passes through an 80 mesh screen. Two typical thermogram curves for USP-502 phenolic resin obtained from 50 mg powdered samples are shown in Figure 1. The curves represent only preliminary information as temperature measurements have since been improved.

Once TGA weight loss curves have been experimentally obtained, the determination of the kinetic parameters, activation energy E, pre-exponential factor A and reaction order n, can be accomplished by several means. The technique of Friedman[3] will be considered in detail. This author assumed that the following general equation held.

$$ -\left(\frac{1}{w_0}\right)\left(\frac{dw}{dt}\right) = Ae^{-\Delta E/RT}\, f\,(w/w_0) \qquad (14) $$

where w = weight or organic material, and w_0 = original weight of plastic. Taking logarithms of equation (14) gives

$$ \ell n\left[-\left(\frac{1}{w_0}\right)\left(\frac{dw}{dt}\right)\right] = \ell n\,A + \ell n\,f\,(w/w_0) - \frac{\Delta E}{RT} \qquad (15) $$

Values of $(1/w_0)(dw/dt)$ are determined and plotted against $1/T$ as a function of (w/w_0). The slope of each line is equal to $-\Delta E/R$ while the intercept is $\ell n[A\,f\,(w/w_0)]$. The function $f\,(w/w_0)$ is then assumed to have the form

$$ f\left(\frac{w}{w_0}\right) = [(w - w_f)/w_0]^n $$

where w_f is the final weight of char and n = kinetic order of reaction. Multiplying the previous equation by A and taking logarithms yields

$$ \ell n\,[A\,f\,(w/w_0)] = \ell n\,A + n\,\ell n\,[(w - w_t)/w_0] \qquad (16) $$

c-21

A plot of $\ln [A\ f\ (w/w_0)]$ versus $\ln [(w - w_t)/w_0]$ should then give a straight line where the slope is n and the intercept is $\ln A$.

It should be noted that in the technique of Friedman all the kinetic parameters are determined by graphical means. Another widely referenced procedure is that of Freeman and Carroll[17] which is basically similar in approach to the one just outlined.

Another example of a technique for kinetic parameter determination is the computer approach of Anderson[18]. The expression used in this reference for the degradation of a reinforced resin system is

$$\frac{d\rho}{dt} = - \rho vp \left(\frac{\rho_2}{\rho vp}\right)^N (1 - F_{RC})\ B\ e^{-(E/RT)} \qquad (17)$$

where

ρ = density of a system at any time

ρ_2 = density of remaining resin

ρvp = initial density of system

N = order of reaction

F_{RC} = mass fraction of resin that chars

B = pre-exponential constant

E = activation energy

T = local temperature

t = time

From TGA analysis, information in the form of $\rho/\rho vp = f(T)$ is obtained for a fixed (dT/dt). The fraction of resin that chars can be expressed as $F_{RC} = \rho c - (1-F)\rho vp/F\rho vp$ where ρc = char density and F = resin fraction in initial system. The density of remaining resin can be expressed as

$$\rho_2 = F\rho vp \left(\frac{\rho - \rho c}{\rho vp - \rho c}\right) = F\ \rho vp \left(\frac{\frac{\rho}{\rho vp} - \frac{\rho c}{\rho vp}}{1 - \rho c/\rho vp}\right) \qquad (18)$$

and finally in combined form

$$Be^{-\left(\frac{E}{RT}\right)} = \frac{\frac{d}{dt}\left(\frac{\rho}{\rho vp}\right)\left(\frac{dT}{dt}\right)}{F^N\left(\dfrac{\dfrac{\rho}{\rho vp} - \dfrac{\rho c}{\rho vp}}{1 - \dfrac{\rho c}{\rho vp}}\right)^N \dfrac{\left(1 - \dfrac{\rho c}{\rho vp}\right)}{F}} \qquad (19)$$

This final expression is solved over small temperature increments by finite difference techniques. The Anderson program computes $Be^{-(E/RT)}$ as a function of temperature. However, the reaction order must be assumed and the other kinetic parameters are again graphically evaluated. This computer technique has been prepared and run on Univac 1108 for several groups of published data yielding kinetic constants in reasonable agreement with the published results.

The techniques of Friedman, Freeman and Carroll, and Anderson may be taken as representative of those types of TGA data analysis which use the differential form of the rate law. They all involve the inherently inaccurate problem of graphical differentiation, require constant rates of temperature rise and utilize cumbersome slope taking operations for determination of kinetic parameters.

Because of these difficulties, the use of integrated forms of the rate law are being considered. Such techniques avoid graphical or numerical differentiation. The most promising general approach appears to be the quasilinearization approach of Bellman.[21] This technique requires a reasonable initial guess of kinetic parameters, but then systematically and rapidly converges to optimized values.

The limitations and restrictions noted for the differential methods are not found in the quasilinearization approach. No form of differentiation is required, graphical methods are not needed and greater versatility in experimental approach is possible. For example, the requirement of constant rate of temperature rise previously required is no longer a restriction. Temperature rise may be programmed at varying rates in order to emphasize and permit

c-23

accurate calculations of critical regions of the thermogram. It
may even be possible to combine isothermal with non-isothermal con-
ditions during a single run. Once the data are obtained, the quasi-
linearization technique is handled completely on the digital computer
thus avoiding any intermediate hand manipulation.

1.6 *Gas Analysis*

In conjunction with thermogravimetric analysis, two other types
of experimental analysis are required in this program. First, it is
necessary that the gas species evolved during the thermal decomposition
be identified as a function of the temperature. Techniques of gas
chromatography and mass spectroscopy are both acceptable procedures
for this determination. Because of greater availability, a high
resolution mass spectrometer will be used.

Pyrolysis gases will be collected at reduced pressures in a
flow-through TGA apparatus. An inert gas, such as nitrogen, is
continuously fed into the flow-through system to prevent pyrolysis
gases from reaching the delicate balance mechanism and to act as a
collector for the gas species to be analyzed. With this approach,
it is desirable that the mass spectrometer be attached directly
to the TGA system or that chemical reactions between gas species
are frozen.

1.7 *DSC Analysis*

A second experimental approach which will be used along with
TGA is differential scanning calorimetry (DSC). Available for use
in the Chemical Engineering Laboratory is a Perkin-Elmer differential
scanning calorimeter. This sophisticated equipment permits the
measurement of the heat required by the various thermal reactions.
It should, therefore, be of great value in identifying the different
regions of a TGA thermogram. The work of Sykes and Nelson[19] is
an example of this use of DSC data.

1.8 *Direction of Continuing Research*

It is anticipated that during the following year work on this

project will include the identification of the effects associated with the flow of a combusting gas past an ablating surface. The results obtained from the Task II studies will be utilized wherever possible. Specifically, the following items will be completed.

1. Thermolgravimetric analysis of ablation polymers will will effected resulting in an identification of the kinetics of pyrolysis. As a part of this analysis, pyrolysis gas species will be collected and identified employing mass spectrometry.

2. Composite ablative samples will be studied in an arc image furnace to evaluate ablative performance in a non-environmental coupled situation.

3. The hot gas facility described in Phase I will be used to evaluate the thermal decomposition of polymers subjected to a combusting gas environment.

2.0 PHASE II KINETICS OF SUBSURFACE REACTIONS - J. Chidley[*]

2.1 *Introduction*

For rather short periods of time, of the order of one minute, structures may be protected by ablative materials from continuous exposure to high heat fluxes and high temperatures. Much longer times can be tolerated if the exposure is periodic or intermittent. The most commonly used ablative materials for thrust-chamber insulation and lining applications have been composites of an elastomer and/or plastic reinforced with a more refractory material to support the resin and charred resin during the ablation process and hold the composite together.

One such composite, phenolic-silica, consists of a high-purity silica cloth impregnated with a phenol-formaldehyde resin which is cured to a tough laminated structure. Much research emphasis has been and is being applied to the development of ablative materials tailored to specific applications.[22]

In use, ablative composites absorb incident radiative and/or convective thermal energy to some extent by surface and internal endothermic chemical reactions. For composites containing plastic resin and inorganic reinforcements, the following classes of internal chemical reactions are thermodynamically feasible.

1. decomposition (pyrolysis) of resin to form char and gases; e.g.,[23]
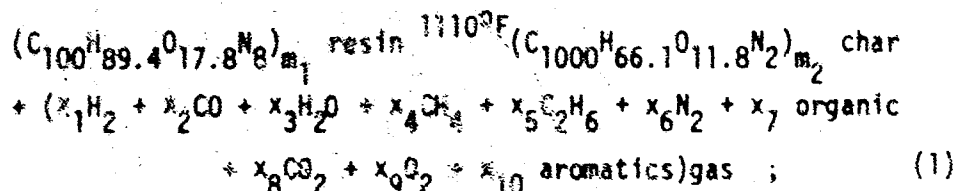
$$(C_{100}H_{89.4}O_{17.8}N_8)_{m_1} \text{ resin } \xrightarrow{1110°F} (C_{1000}H_{66.1}O_{11.8}N_2)_{m_2} \text{ char}$$
$$+ (x_1H_2 + x_2CO + x_3H_2O + x_4CH_4 + x_5C_2H_6 + x_6N_2 + x_7 \text{ organic}$$
$$+ x_8CO_2 + x_9O_2 + x_{10} \text{ aromatics)gas} \quad ; \qquad (1)$$

2. thermal cracking of, or reactions among pyrolysis gases as they percolate through the insulative porous char to the exposed surface or the ablative composite; e.g.,

---

[*] Mr. John D. Chidley received a B.S. degree in Chemical Engineering from the California Institute of Technology in 1965. Since then he has attended the University of Utah where he is a candidate for a Ph.D. in Chemical Engineering. He began work on this phase of the program in September 1967.
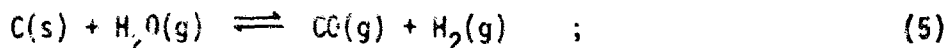
$$CH_4(g) \rightleftharpoons C(s) + 2H_2(g) \quad , \tag{2}$$

$$\text{Benzene } (g) + 9H_2(g) \rightleftharpoons 6CH_4(g) \quad ; \tag{3}$$

3. char oxidation of the pyrolysis gases; e.g.,

$$C(s) + CO_2(g) \rightleftharpoons 2CO(g) \quad , \tag{4}$$

$$C(s) + H_2O(g) \rightleftharpoons CO(g) + H_2(g) \quad ; \tag{5}$$

4. reactions between the char and reinforcement; e.g.,

$$SiO_2(s) + C(s) \rightleftharpoons SiO(g) + CO(g) \quad , \tag{6}$$

$$SiO_2(s) + 2C(s) \rightleftharpoons Si(\ell) + 2CO(g) \tag{7}$$

$$SiO_2(s) + 3C(s) \rightleftharpoons SiC(s) + 2CO(g) \tag{8}$$

and subsequent reactions:

$$SiC_{(s)} + 2SiO_{2(s)} \rightleftharpoons 3SiO(g) + CO(g) \quad , \tag{9}$$

$$SiO_2(s) + Si(\ell) \rightleftharpoons 2SiO(g) \tag{10}$$
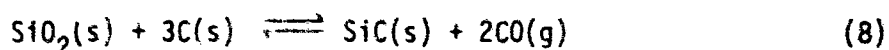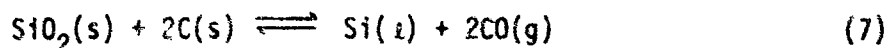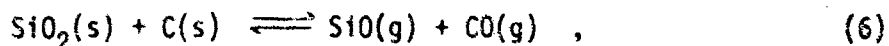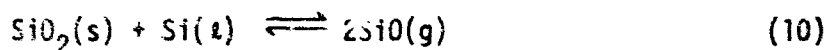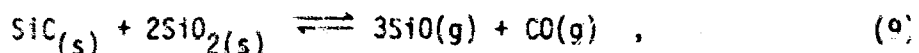
In the development of an understanding of the internal ablation processes, the decomposition or pyrolysis reactions of class 1 have received the most attention. These pyrolysis reactions are very important because they produce a porous char which can quite effectively insulate the virgin composite thermally from the high-energy external environment and thereby curtail the overall internal ablation rate.

Of the three classes of postpyrolytic chemical reactions, those of class 4 are considerably more endothermic than the reactions of the other two classes. For this reason, class 4 reactions have received some attention.

Despite the high endothermicity of the $C-SiO_2$ reactions, their desirability in ablative composites is not necessarily justified. If, as pointed out by Gutman,[24] the $C-SiO_2$ reactions lead to a breakdown of the reinforced-char structure, with subsequent surface erosion, then the overall ablation rate may increase rapidly and become intolerable. But, as discussed by Ladacki,[25] when dimensional integrity is not essential, the additional endothermic heat sink provided by the $C-SiO_2$ reactions may more than compensate for any resulting surface erosion.

To date, a thorough study of the desirability or undesirability of the $C-SiO_2$ reactions for the entire range of reentry and thrust-chamber appli-

cations has not been reported. A potential area of desirability might be
in those regions of thrust chambers where surface erosion is not generally
experienced and where the internal insulation weight should be optimized.
Such situations are common in small liquid-propellant space engines and in
the thrust chamber and blast tube of certain solid rocket motors, where the
heat fluxes are not too severe. The importance of weight reduction in solid-
rocket-motor insulation was discussed by Hribar.[26]

By catalyzing the silicon-carbide-formation reaction, as given by
Equation (8), so that it is rapid at the lower temperatures experienced, it
may be possible to obtain the endothermic benefit and corresponding reduction
in char depth, resulting possibly in reduction of the necessary wall thick-
ness. By carefully manipulating the silica-resin ratio in the composite, a
char stoichiometry might be achieved which would result in the elimination
of subsequent SiC reactions, which could result in rapid surface erosion.
Going one step further, the subsequent reactions might be tolerated to a
predetermined extent because of their own high endothermicity, if severe
char degradation could be avoided. Most of the work reported so far has been
concerned with systems in which a low pressure of CO and high silica excess
were present, thus encouraging reactions such as (9).

2.2 Theoretical Considerations - Thermodynamics

Standard heats of reaction for internal ablation reactions are summarized
in Table 1. Note that if one assumes that one gram of resin pyrolyzes to a
char containing 0.45 grams carbon, and the carbon reacts with silica accord-
ing to reaction (8), the heat absorbed by the $C-SiO_2$ reaction is approxi-
mately 5.8 times the heat absorbed by pyrolysis.

Unfortunately, some discrepancies exist among the thermodynamic data
reported by various investigators. Some of these discrepancies are due to
the advent of better data for heats of formation in recent years. Thus one
must be very careful when comparing the findings of different investigators
to take note of the data used by them in their analyses.

Also, some investigators have found that their data are well fit by a
variety of expressions. For example, Baird and Taylor,[27] in measuring the
free energy of SiC by observing equilibrium pressure of CO over SiO_2 and
SiC and C mixtures, determined a free energy of formation for the reaction

Table 1

Reaction	$\Delta H_{25^\circ C}$ cal/gm-mole
1	+265 (cal/gm resin for pyrolysis @ 1000°F (2)
2	+17,889
3	-127,154
4	+41,220
5	+31,382
6	+166,880
7	+164,660
8	+144,020
9	+356,620
10	+169,100

ΔH_{25} values for equations 2 to 10 were calculated from data in the Janaf Thermochemical Tables and U.S.B.S. Circular 600.

$Si(\ell) + C(graphite) \longrightarrow SiC$ of

$$\Delta G^0 = -14,700 + 5.74T \text{ cal} .$$

They considered the data of Humphrey,[28] et al for the entropy term more accurate, and thus adjusted their equation to $\Delta G^0 = -19,250 + 8.3T$ cal to incorporate Humphrey's ΔS of 8.3 cal/mole °R. The fit thus obtained was still "probably within experimental error".

With the exception of CO, all of the species in reaction (8) are assumed to be solids of unit activity. Thus, the partial pressure of CO and the temperature are the variables of interest in the equilibrium of reaction (8). Reactions (6) and (7) are also governed by p_{CO} and temperature. Thus Beecher and Rosensweig[29] stressed the importance of the equilibrium CO pressure. They concluded that if the reaction kinetics were sufficiently rapid, the formation of silicon carbide would be dominant over a temperature range of approximately 1800°C to 2000°C. Rosensweig and Beecher[30] give the equilibrium CO pressure as

$$p_{CO} = 10^{(8.71-\frac{15,100}{T})}$$

where p_{CO} = atm, T = °K.

Baird and Taylor,[27] however, give an expression, based on their experimental results, as

c-29

$$P_{CO} = 10^{(8.95-16,150/T)}$$

where again P_{CO} = atm, $T = {}^{\circ}K$.

Klinger,[36] et al give a standard free energy of reaction for the equation

$$SiO_2(\alpha \text{ quartz}) + 3C(s) = SiC(s) + 2CO(g)$$
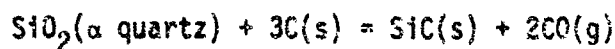
of

$$\Delta G_T^0 = 143,480-79.56T \quad (cal/gm-mole)$$

The following equation for the equilibrium pressure of CO has been derived from the free-energy expression.

$$P_{CO} = 10^{(8.69-\frac{15,680}{T})}$$

CO pressures calculated from these equations are as follows:

Table 2

T, $^{\circ}K$	P, atm		
	Rosensweig & Beecher	Baird & Taylor	Klinger, et al
1500	.0436	.0155	.0174
1750	1.20	.525	0.544
2000	14.45	7.58	7.15
2250	100.0	58.9	53.1

Ladacki,[31] and Carey and Coulbert,[32] among others, have treated the problem of thermodynamic equilibrium by the technique of calculating equilibrium composition resulting from a specified initial composition of C and SiO_2, and allowing for production of all possible chemical species. Wide temperature and pressure ranges have been covered. Again, however, discrepancies are noted. The results of Ladacki and of Carey and Coulbert differ in that those of Carey and Coulbert predict a liquid silicon phase at temperatures just higher than those where SiC is stable, where the work of Ladacki[33] does not. Otherwise the results are at least qualitatively similar. The results of Ladacki and of Carey and Coulbert are shown in Figures 1 and 2 for an initial composition of 82% SiO_2, 15% C, at 5 psia.

In summary, it appears on the basis of available reports that at a given pressure, a temperature favoring the formation of SiC by Equation (8) can be found. However, a precise prediction of this temperature is currently
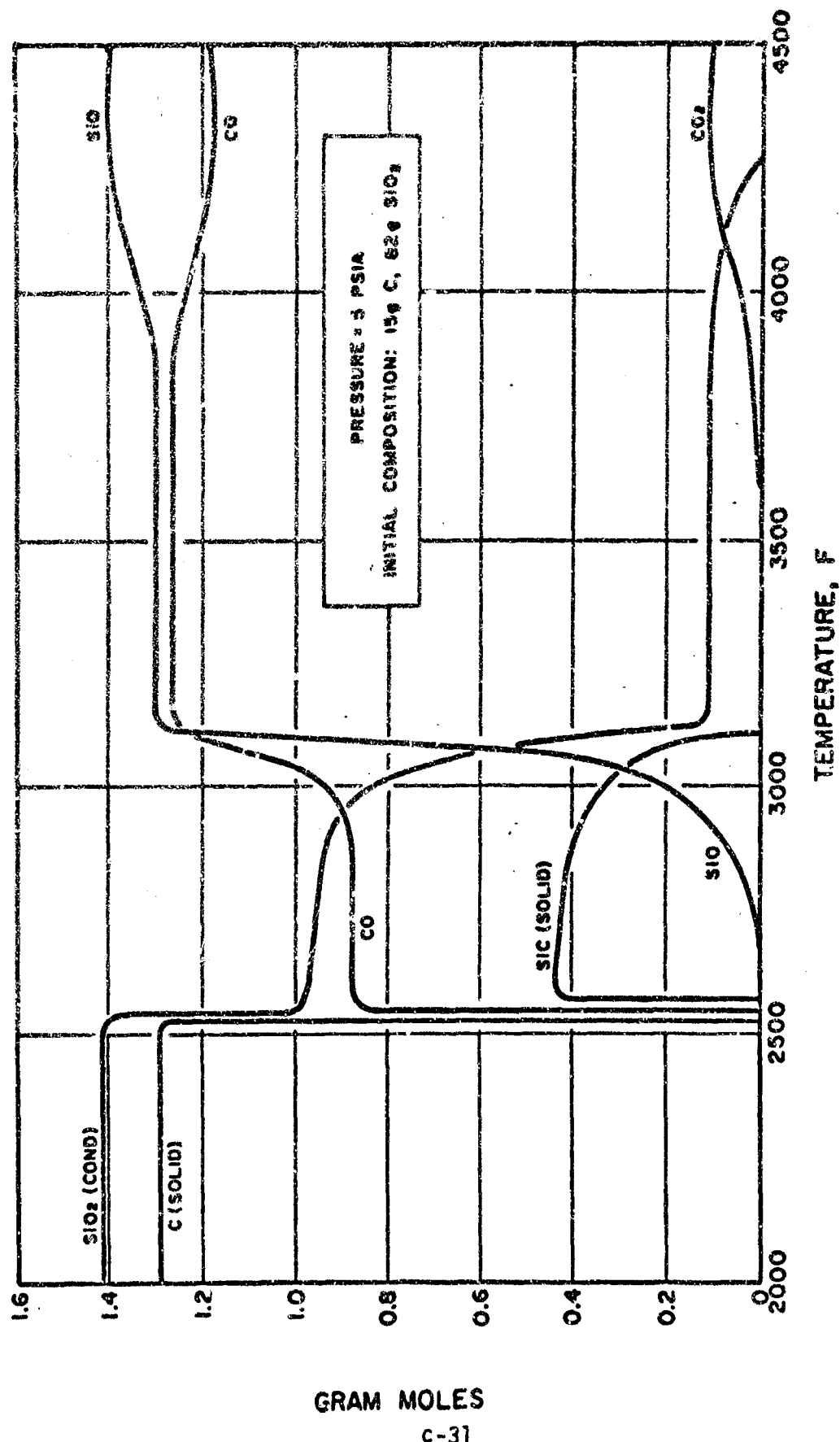
FIGURE 1. EQUILIBRIUM COMPOSITION FOR THE C-SiO$_2$ SYSTEM (from Ladacki).

C-31
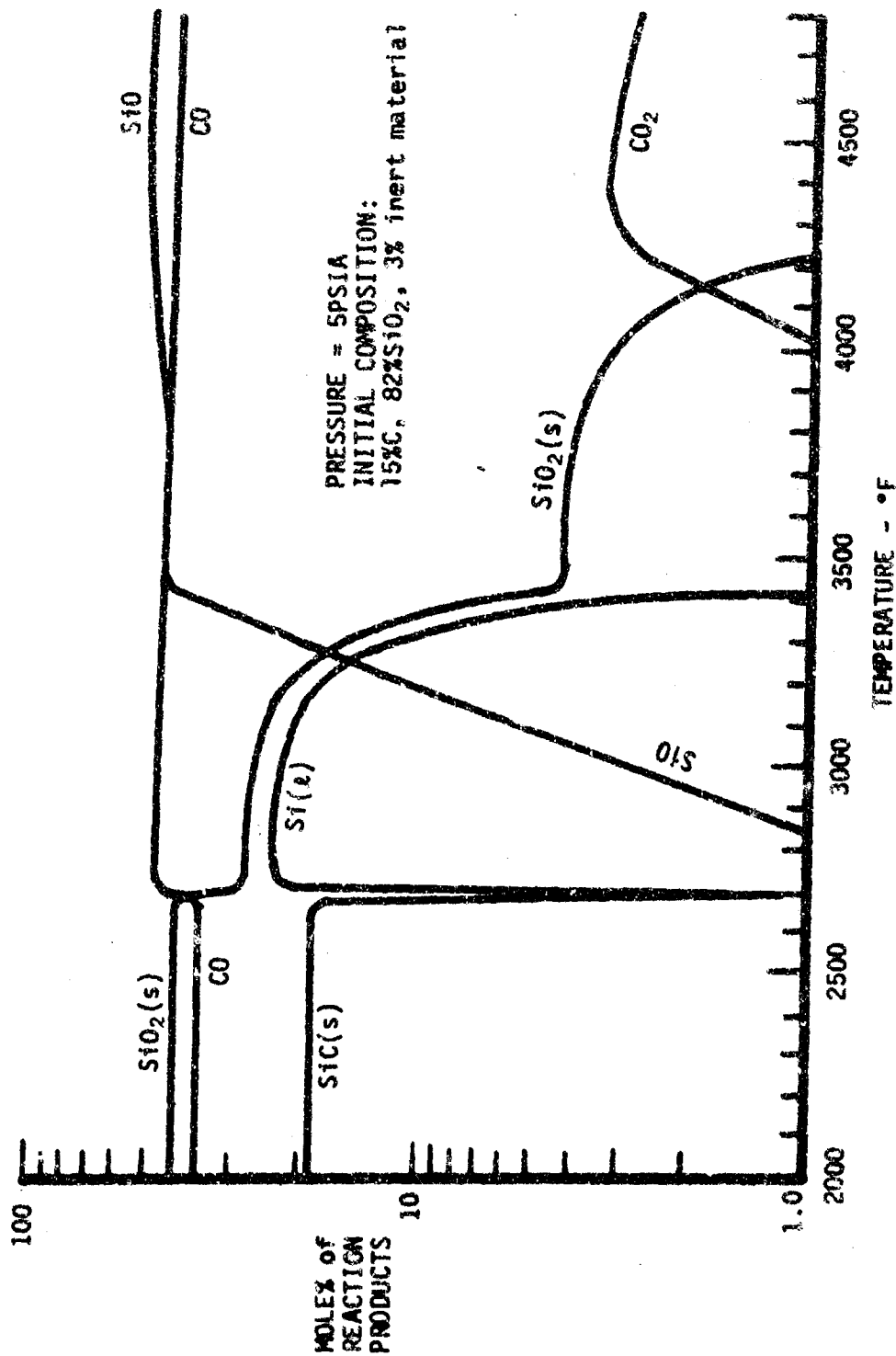
FIGURE 2. EQUILIBRIUM COMPOSITION FOR THE C-SiO₂ SYSTEM (from Carey and Coulbert).

c-32

doubtful because of the high degree of accuracy required of free energy values.

2.2.1 State of the Silica

For most silica-containing composites the silica will initially be present as the fibers comprising the woven cloth reinforcement. These fibers consist almost entirely of vitreous silica, according to their manufacturers.

As discussed by Sosman,[34] at atmospheric pressure, vitreous silica is thermodynamically unstable at all temperatures below 1723°C, the melting point of cristobalite. However, at ambient temperatures, no movement toward crystalline arrangement has been detected. Silica gains sufficient mobility to begin crystallizing only upon heating to a red temperature or higher.

This crystallization is commonly called devitrification since it usually results in conversion of the transparent homogeneous glass into a white, chalky mass of minute crystals.

At pressures and temperatures of interest, several stable and meta-stable phases of silica are possible. Very large pressure differences are needed to significantly alter the temperature ranges of stability of these phases. Each phase also exhibits high-low inversions. (The nomenclature of Sosman will be followed in this report. He recommends the use of high and low rather than α and β due to inconsistency in the literature in the application of the greek-letter notations. Thus high and low are used to indicate high-temperature and low-temperature modifications, respectively.)

High-low inversions of the phases of silica al exhibit the character-istics described for the inversion point between low-quartz and high-quartz under atmospheric pressure at 573° ± 1°C. The principal features of the high-low quartz inversion, quoting Sosman,[34] are

    1. On rising temperature, a gradual increase in the rate of change of all properties, noticeable at 50°C or more before the inversion point is reached.

    2. An entire absence of such a preliminary effect, with falling temperature, on the high-temperature side of the inversion point.

    3. A change of symmetry at the inversion point.

    4. An abrupt change in nearly all of the physical properties at the inversion point.

5. The very small rate of change in properties above 573°C as compared with the rate of change between 0° and 573°C.

Other important features are noted by Sosman. The inversions occur promptly when the inversion pressure or temperature is reached, completing themselves in some instances in a few seconds. The inversions are reversible, and the difference in energy content between high and low modifications is relatively small.

Twenty-two known phases of silica are presented in the following table, Table 3, which is based on one presented by Sosman.[34] Since tridymite exhibits several inversions in both its stable and metastable forms, the notation S-I, S-II, etc. for the stable form inversions and M-I, M-II, etc. for the metastable form inversions was adopted.

It is questionable whether in a practical ablative material the phenomenon of devitrification is of importance. The expected devitrification at temperatures and pressures of interest would be conversion of the vitreous silica to cristobalite, even at temperatures well below 1470°C, where trydymite S is the stable phase since the glass still crystallizes first to cristobalite in absence of flux or solvent. It is known[34] that the crystallization of vitreous silica to cristobalite begins only at the surface and proceeds inward, which accounts for faster devitrification rates seen in powdered glasses. It is also fairly certain that water vapor accelerates devitrification.

One should, however, realize that the rates of devitrification of vitreous silica into any of the crystalline phases are extremely slow. Sosman[34] gives 1/2 hour as the time needed to convert 60% of a sample of powdered vitreous silica to cristobalite at 1600°C. Since the exposure times of ablative materials are generally much less than the times associated with devitrification, it is not expected that devitrification would affect the behavior of the ablative material to any great degree. However, it is possible that an unforeseen catalysis of devitrification could occur due to the presence of pyrolysis gases, char, and potential catalysts of the char-silica reactions. The surface state of the silica fibers would also be expected to exert a large influence on the rate of devitrification, since it starts on the surface and never in the body of the silica.

Although devitrification is not expected to influence the char-reinforce-

Table 3
THE TWENTY-TWO PHASES OF SILICA

Mode	Temperature range (°C)	Relative stability (S = stable) (M = metastable)	Pressure (K bar)
CRYSTALLINE SILICA			
Quartz			
low	-273 to 573	S	0
high	573 to 867	S	0
Tridymite			
S-I	-273 to 64	M	0
S-II	64 to 117	M	0
S-II	117 to 163	M	0
S-IV	163 to 210	M	0
S-V	210 to 475	M	0
S-VI	475 to 867	M	
	867 to 1470	S	0
M-I	-273 to 117	M	0
M-II	117 to 163	M	0
M-III	above 163	M	0
Cristobalite			
low	-273 to 272	M	0
high	272 to 1470	M	
	1470 to 1723	S	0
Coesite	ca. 300 to 1700		15-40
Keatite	monotropic? (unstable everywhere)		ca. 0.8-1.31
Stishovite	unknown		ca. 160
Silica W	monotropic (unstable everywhere)		formed by oxidation of gaseous SiO
AMORPHOUS SILICA			
liquid	above 1723	S	0
vitreous	-273 to 1723	M	0
supra-piezo-vitreous		M	ca. 35
compacted vitreous		M	ca. 100 and lower
Silica M	indefinite	(produced from all other phases by high-speed neutrons)	

ment reactions, due to the relative sluggishness of devitrification, the possibility deserves careful consideration. Klinger,[35] et al, used a single crystal of low quartz in their studies. They found that at temperatures of $1550^{\circ}C$ and $1600^{\circ}C$ and times of 190 and 150 minutes, respectively, the quartz used in their silica-graphite reactions was better than half converted to low cristobalite. Klinger and his co-workers postulated that an increased reaction rate of the silica-graphite reactions which correlated with an unexpected disappearance of low cristobalite was due to interatomic changes occurring during the transformation from quartz to cristobalite which increased the reactivity of the silica. Other investigators have not specifically considered the effect of the state of the solid silica on reaction rates. Probably as important as the state of the SiO_2 is the degree of contact between the carbonaceous and siliceous phases of the char, in a practical ablative material.

2.2.2 Kinetic Considerations

No studies of the kinetics of $C-SiO_2$ reactions at other than vacuum conditions has come to our attention. The investigations of Beecher and Rosensweig and of Blumenthal,[36] et al, have been confined to vacuum conditions for a temperature range of $1300^{\circ}C$ to $1700^{\circ}C$. Those of Klinger,[35] et al were performed in the range $1378^{\circ}C$ to $1765^{\circ}C$ and also at vacuum conditions.

Unfortunately, all of the char-reinforcement reactions (6), (7), (8) are thermodynamically possible at the low pressures employed and the temperature ranges used. Thus the rate of reaction measured by the investigators is not necessarily that of the SiC formation reaction (8). In fact all of the investigators follow the reaction by measuring the CO pressure produced.

Although the initial studies of Beecher and Rosensweig[29] indicated rapid formation of SiC in the temperature range where it is thermodynamically dominant, the work of Blumenthal,[36] et al led to a reexamination and correction of those studies. As a result, the kinetics of the $C-SiO_2$ reaction were found to be relatively slow except at very high temperatures, where SiO_2 is molten but very viscous.

Several rate expressions have been put forth for the depletion of carbon or more precisely, the production of CO by C-SiO reactions. They are not, however easily comparable since fairly variant systems were used to generate them.

Beecher and Rosensweig,[29] suggested the following zero order rate
expression for the reactions occurring in samples of char from pyrolyzed
fiberglass-reinforced phenolic plastic.

$$\frac{dn_c}{dt} = kv \exp(- E/RT)$$

where n_c = grams carbon

v = volume of reacting mass

k = 10^{10} gm/cm^3 min

ΔE = 92,000 cal/mole

They assumed that the reaction is heterogeneous, occurring at carbon-silica
interfaces randomly distributed throughout the volume. Beecher and Rosensweig
give no data concerning the magnitude of the interfacial areas. It is
assumed that silica was in excess in their samples.

Blumenthal,[36] et al, studied the reactions between carbon and silica
in pelleted mixtures of 17mµ graphite powder with 2.8µ low-cristobalite
powder prepared from decomposition of silicic acid and with 15mµ colloidal
silica powder. They also studied samples of a charred silica-reinforced
phenolic resin. The molar ratio of SiO_2 to C was 0.86 in the char samples
and 1.0 or 3.0 in the pelleted samples. SiO_2 was thus in stoichiometric excess
for the SiC- formation reaction. A temperature range of 1300°C - 1600°C was
covered. It was found that the kinetics of the carbon-silica reactions in
the char were very similar to the reaction kinetics in the pelleted samples.
Romie,[37] suggested a first order rate expression based on the results of
Blumenthal, et al

$$\frac{-dC}{dt} = 15.5 \exp(20-62,500/T)C$$

where C = gm carbon/cm^3

t = time in hours

T = temperature, °R

Blumenthal and co-workers noted an increase in rate for those samples with
greater interfacial area between silica and carbon and presumed that initally
the silica surface area controlled the interfacial area due to the smaller
surface area of the silica.

Klinger,[35] et al performed experiments similar to those of Blumenthal,

c-37

using a high purity single crystal of low-quartz as a silica source. It was powdered and particles between 105 and 149μ in diameter were used in the experiments. Graphite powder used was less than 44μ in diameter. The temperature range covered was 1378° to $1765^\circ C$. The molar ratio of SiO_2 to C was 0.111 for all runs. Thus graphite was in stiochiometric excess for the SiC formation reaction in the experiments of Klinger, et al.

Klinger, et al found their data were correllated by a linear rate law based on the silica surface area. Modified to give carbon depletion, this equation can be written as

$$\frac{dC}{dt} = \frac{7.45 \times 10^5 \times 12}{5.1} \exp(-117,000/RT) \; gm/cm^2 sec$$

$$= 1.75 \times 10^6 \exp(-117,000/RT) \; gm/cm^2 sec$$

where C is in grams carbon/cm^2 silica surface area. The assumption was made that the silica powder was spherical in order to obtain the area of the powder to be used in deriving the equation from experimental data.

For experiments proceeding beyond a certain time (120 min @$1545^\circ C$, 20 min @$1586^\circ C$, and 7 min @$1610^\circ C$) the rate increased sharply and continued to accelerate. The data in this region were correlated by

$$\frac{dn_{co}}{dt} = k_a \, n_{co}^{1/3}$$

where n_{co} = moles CO. Klinger et al give an activation energy for this reaction of 122 ± 20 kcal, but do not report the pre-exponential factor of the rate constant. They interpret the accelerated reaction as being due to increased activity of the silica during a phase change from quartz to cristobalite. The change in structure is due to breaking of interatomic bonds rather than displacement of atoms. Klinger, et al. also found that the onset of the accelerated graphite-silica reaction coincided with the increase in velocity of transformation of the quartz.

The results of calculations based on the equations of Beecher and Rosensweig, of Romie, and of Klinger are presented in Table 4 and Fig. 3. Table 4 includes reaction times for 50% and 90% depletion of carbon, and equilibrium CO pressure based on the predictions of Beecher and Rosensweig. Fig. 3 presents plots of carbon depletion versus time for the three rate expressions at temperatures of $2500^\circ F$, $2800^\circ F$, and $3100^\circ F$.

c-38
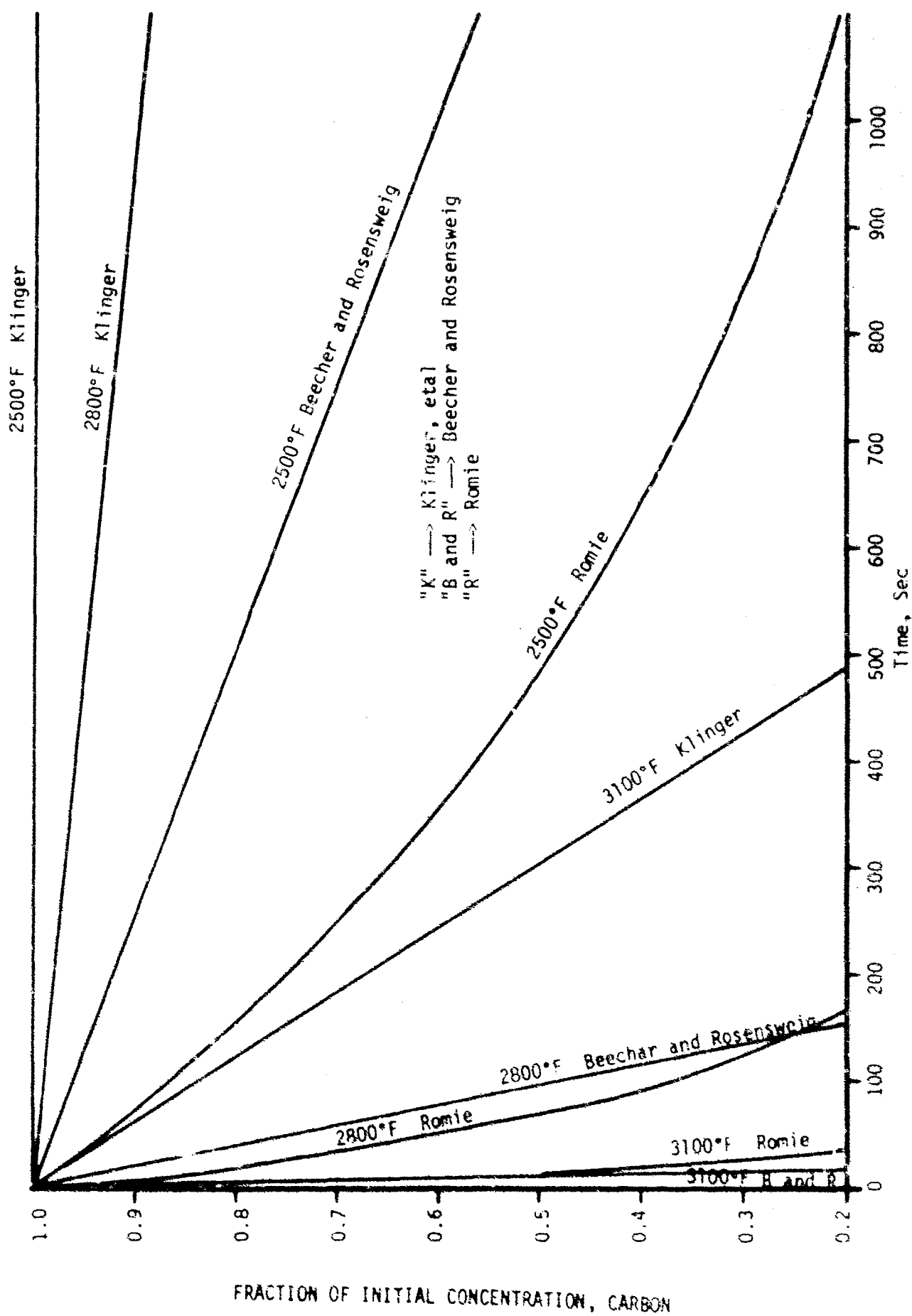
FIGURE 3. KINETICS OF C-SiO$_2$ REACTIONS

The figure axes and labels:

- Vertical axis (left): FRACTION OF INITIAL CONCENTRATION, CARBON — values from 1.0 down to 0.2
- Horizontal axis: Time, Sec — values 0, 100, 200, 300, 400, 500, 600, 700, 800, 900, 1000

Curve labels:
- 2500°F Klinger
- 2800°F Klinger
- 2500°F Beecher and Rosensweig
- 2500°F Beecher and Rosensweig
- 2500°F Romie
- 3100°F Klinger
- 2800°F Beechar and Rosensweig
- 2800°F Romie
- 3100°F Romie
- 3100°F B and R

Legend:
"K" $\longrightarrow$ Klinger, etal
"B and R" $\longrightarrow$ Beecher and Rosensweig
"R" $\longrightarrow$ Romie

c-39

Table 4

	T		50%			90%		P_{CO} psia
°F	°C	B & R	Romie	Klinger	B & R	Romie	Klinger	
2500	1371	1,250	486	122,310	2,250	1,613	220,158	5.0
2600	1427	505	247	39,160	909	820	70,483	9.9
2700	1482	215	131	13,225	387	434	27,00	18.0
2800	1538	95	72	4,710	171	238	8,478	34.7
2900	1593	44	41	1,785	79	136	3,213	11.8
3000	1649	22	24	730	40	80	1,314	105
3100	1705	11	15	305	20	49	543	175

These results are based on the application of the three rate laws presented above to a system consisting of a hypothetical reinforced char layer with a carbon spatial density of 0.25 gm/cm^3 and a silica spatial density of 1.1 gm/cm^3. The silica is presumed present as fibers with a diameter of 0.001 cm and a specific gravity of 2.2 gm/cm^3. The surface area of the silica, necessary for the application of the linear rate expression of Klinger, thus reduces to the expression:

$$\frac{SiO_2 \text{ area}}{cm^3 \text{ char}} = \frac{2}{D} \frac{cm^2}{cm^3} \text{ char}$$

$$= 2000 \text{ cm}^2/cm^3 \text{ char}$$

The equations of Beecher and Rosensweig and of Romie predict similar reaction times for a given degree of carbon depletion, especially at the upper range of temperature. Klinger's rate expression, however, predicts reaction times from one to two orders of magnitude longer. Klinger's data were found using low quartz with an excess of graphite, whereas those of Romie were based on two silica-carbon ratios, i.e., equimolal and three to one silica to carbon. The experiments of Blumenthal, et al, upon which Romie based his equation, were carried out with colloidal silica and carbon black. Rosensweig and Beecher refer to their samples as "char from pyrolyzed fiber-glas -reinforced phenolic plastic". Since Klinger, et al, based their measurements on silica surface area, the effects of variant particle size should

not be a factor in their equation. It is possible that the much slower reaction times predicted by Klinger's equation are due to the silica being present as quartz, since when the quartz began to invert to cristobalite, large increases in reaction rate were noted.

2.2.3 Effect of Catalysis

The effect of a catalyst is to change the rate of a reaction without changing itself over the course of the reaction. If a catalyst were found that could catalyze the silicon-carbide formation reaction and thereby significantly increase the rate at lower temperatures, one might obtain the endothermic benefits and corresponding reduction in char depth.

Experiments conducted by Cutler[38] in 1956 with silica and carbon showed that transition metals were effective in catalyzing the synthesis of silicon carbide. It was believed, therefore, that transition metals would be effective also with silica and char in pyrolyzed ablative composites. The preliminary experiments performed here previously (see the paper "Catalysis of Internal Endothermic Ablation Reactions Between Char and Reinforcements" included in the Appendix) support the premise that a significant char layer reduction can be realized.

Catalysis of similar reacitons has been reported by Rakszawski,[39] et. al. who found that the addition of 510 ppm of Fe resulted in a 170-fold increase at $1000^\circ C$ in the reactivity of graphite over that of pure graphite in the carbon-carbon dioxide reaction. They also noted a trend toward increased catalytic effect with a decrease in Fe particle size. Rakszawski, et. al briefly review several theories as to the mechanism of catalysis of the $C-CO_2$ reaction by Fe. It has been postulated that the gasification of carbon (by desorption of CO from the surface of graphite) would be enhanced if electrons were transferred from the graphite to a catalyst. It is suggested that transition elements accept electrons because of the non-stoichiometric character of their oxides. Also, transition metals are believed to be able to accept electrons as a result of their d-orbitals being unfilled. Thus they would be able to catalyze the oxidation of graphite by accepting its electrons and enhancing the desorption of CO.

Another possible mechanism is dissociation of CO_2 on Fe to give CO and adsorbed oxygen atoms. The oxygen atoms are supposed to be highly mobile on

the Fe surface and thus could diffuse to a free carbon interface, there to react forming gaseous CO.

The large increase noted by Rakszawski in the rate of the C-CO_2 reaction is of interest because this reaction might be expected to display a similarity to C-SiO_2 reactions, in that silica and carbon are members of the same column of the periodic table. Also, the reactions both produce CO, toward which the behavior of the catalyst would be expected to vary little, regardless of which reaction produced it. The actual mechanism of catalysis, then, remains to be seen, and should be emphasized in subsequent work.

2.2.4 Possible Catalysts

To be an acceptable potential catalyst material, the compound considered must be capable of being incorporated into a composite material without detrimentally altering the properties of the material. Metals can be and have been introduced as fine powders and as powdered oxides. These solid forms have the advantage that they do not disturb the resin phase of the material, but the disadvantage that a uniform dispersal is difficult to achieve.

Therefore, it was felt that a compound soluble in the resin phase might be the best way of introducing a potential transition metal catalyst. A uniform dispersion in the resin, and very small particle size were expected.

Investigation of available transition metal compounds indicated that metal-organic compounds of the ferrocene system might well serve the purpose. These compounds are soluble in phenolic resin systems of interest, sometimes with the aid of a co-solvent, such as benzene, which can be easily removed from the uncured resin by evaporation after impregnation and prior to curing of the laminate.

As compared to many metal-organic compounds, ferrocene and the other metallocenes are remarkable stable. The components of a ferrocene molecule are, essentially, two cyclopentadienate anions and one ferrous cation, Fe^{++}. The actual structure is best shown as in Fig. 4, where the dotted lines indicate that the ferrous ion is equally shared by each carbon atom.

Many substituted metallocenes are known, some of which are liquids at room temperature (e.g. n-butyl ferrocene). The more reactive metallocenes can be kept in solution, although some, such as cobaltocene, are poisonous or flammable. Ferrocene itself is recoverable from solution in concentrated
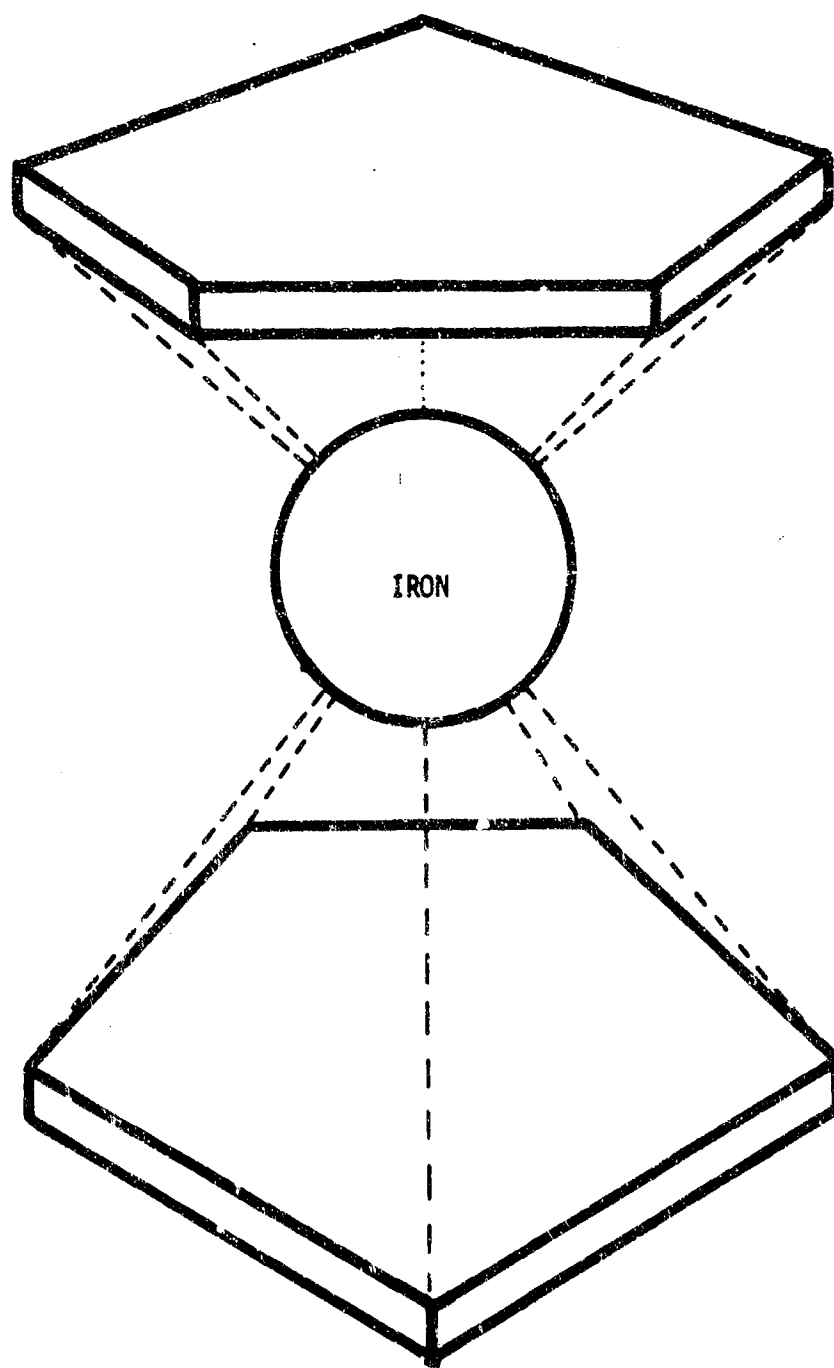
FIGURE 4.   FERROCENE (DICYCLOPENTADIENYL IRON).

c-43

sulfuric or hydrofluoric acid. Ferrocenes also possess the advantage that the organic portion is entirely composed of carbon and hydrogen, especially of carbon. The entire non-metallic portion of the molecule would be expected to contribute to char formation and to cooling by liberating hydrogen gas. In addition, the metal weight percent of ferrocenes is much higher than in many metal-organic compounds.

Other compounds of the transition metals may also prove useful for certain metal additions. Rakszawski,[39] et al, obtained good catalytic activity in their investigation of graphite-CO_2 reactions by introducing iron in the form of ferric oxalate.

Carbonyls of several metals, including nickel, iron, cobalt, and chromium are known and might be used for the introduction of the metals into the resin phase. Carbonyls are, however, generally quite toxic and flammable, as well as being quite volatile at room temperatures. These properties would tend to discourage their use. The structure of Iron Carbonyl is shown in Fig.5.

Metal chelates and organic salts of the metals are possible means of introducing desired transition metals into the resin phase; however, generally the weight % of metal in these compounds is not as good as that of the ferrocenes, necessitating greater possible disturbance in the resin. These compounds, however, might be used to pretreat the reinforcement, or silica, phase of a composite, thus resulting in a material wherein most of the catalyst would be concentrated at the phase boundaries. Several possible compounds of this class are shown in Fig. 5.
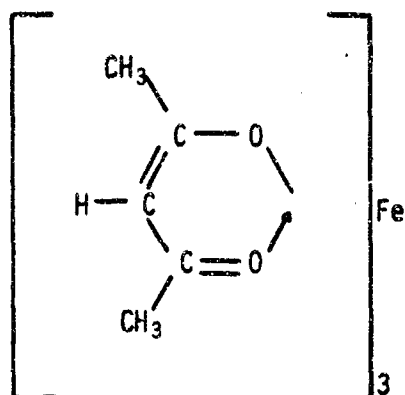
Ferric Acetylacetonate

Iron Pentacarbonyl
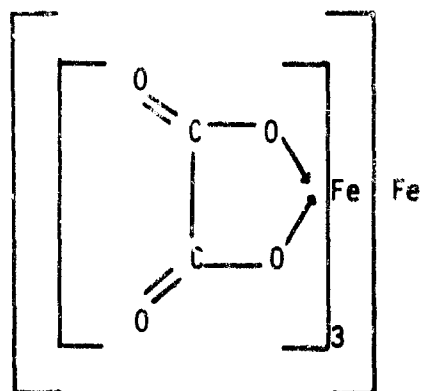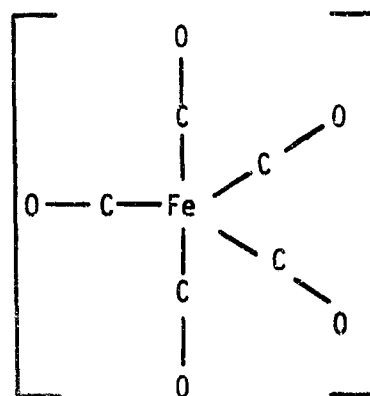
Ferric Oxalate

FIGURE 5.   TRANSITION METAL CATALYST STRUCTURES.

c-45

2.3 *Experimental Work*

Actual experimental work has included the development of techniques
for uniformly manufacturing satisfactory laminates for testing in the
laboratory. Preliminary charring tests have been performed on laminates
made from commercially prepared pre-impregnated silica-phenolic material
and on hand laid materials made up with and without powdered and soluble
catalyst materials. These tests were performed in arc-imaging furnaces as
described below. Also, a small hybrid plexiglass-oxygen rocket motor has
been built and fired. After some redesign, this motor will be used to
determine the effect of combustion on the thermal response of ablative
materials. Pre-installation preparation for a hot-gas flow facility is
underway. The facility will be used for studying the effect on composite
materials of high-temperature environments generated by controlled combustion
of liquid fuels (e.q. methanol) with air-oxygen mixtures.

These phases of the work are discussed in more detail below.

2.3.1 Fabrication Technique

Even before Project THEMIS, a Wabash hydraulic press, shown in Fig. 6
was available for our research work. This press had been used to fabricate
small samples of laminated composites. The press is capable of exerting a
pressure of twelve tons on a 3.14 square inch ram. The platens of the press
can be electrically heated up to $600^{0}F$, and the temperature is thermo-
statically controlled. The platens are 10" x 7" in dimension.

It has been found that the tendency of a composite to delaminate upon
release from the press or upon heating in the arc-imaging furnace is related
to the methods used in impregnating the cloth used in the composite with the
A-state, or liquid resin, and to the treatment given the samples during the
time they are in the press. At first, samples had been made by brushing
powdered catalysts onto commercially prepared prepreg sheets approximately
1/32-inch thick or onto the silica cloth reinforcement of the hand-laid
samples. Resin was applied to the reinforcement of hand-laid samples with
a paint brush.

It was found that removal of air bubbles in hand-impregnated cloth
could be accomplished by a brief exposure of the wet, just-soaked cloth to
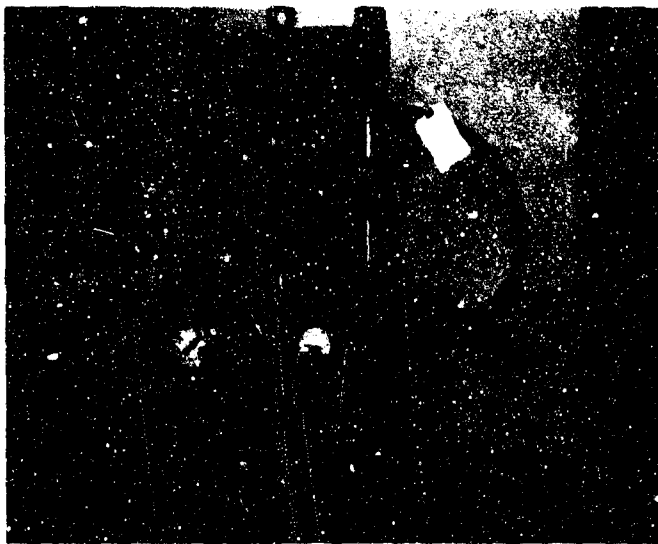a vacuum. Impregnation of hand-laid samples is now accomplished by sand-

FIGURE 6.   WABASH HYDRAULIC LAMINATING PRESS

wiching the resin and silica cloth between two cellophane sheets and working the resin through the cloth manually by rolling a length of soft rubber hose over the outside of the sandwich. When a uniform-appearing impregnation is obtained, the sandwich is put in a vacuum chamber and left until offgassing of bubbles ceases. It is felt that the release of the vacuum also helps to force the resin into the interstices of the cloth.

The impregnated cloth is allowed to become dry to the touch before curing in the press. This stage is often called the 'B-stage'. The material can be easily handled, but is not cured completely.

Curing is done in the press, generally at temperatures around 300°F and at various pressures. Release of the pressure just before set-up of the resin has been found beneficial in preventing delaminations. A large volume of gas usually accompanies this pressure release, which is probably a partial reason for the reduced amount of delamination.

2.3.2 Image Furnace Tests

Preliminary experiments with metal and metal oxide catalysts are described in detail in the AIAA paper included in the Appendix. These tests were conducted in an arc-imaging furnace employing a Hg-Xe lamp as the energy source. The tests were made with a heat flux of 45 cal/cm^2 sec and heating times ranged from 5 to 45 seconds. The results of the tests were that the measured char depths of samples containing transition metal powders were, without exception, less than those for control samples prepared simultaneously but containing no potential catalyst. The percentage of char depth reduction ranged from 5% to 25%.

More recent tests have been attempted utilizing catalysts such as n-butyl ferrocene, in an arc-imaging furnace utilizing the same lamp as in the preliminary tests, but in an entirely different configuration. The present furnace was built up to study propellant burning problems and unfortunately is in many respects less suitable than the original furnace was. The present furnace delivers a larger 'hotspot' approximately 3/4" in diameter and probably a much lower radiant flux. Calibration of the furnace has not as yet been possible, but will shortly be accomplished. This furnace is shown in Fig. 7. The recent tests have been plagued by delamination
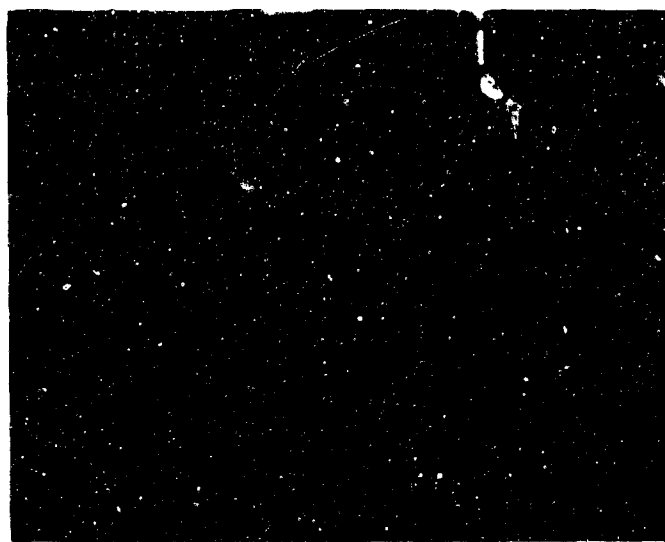
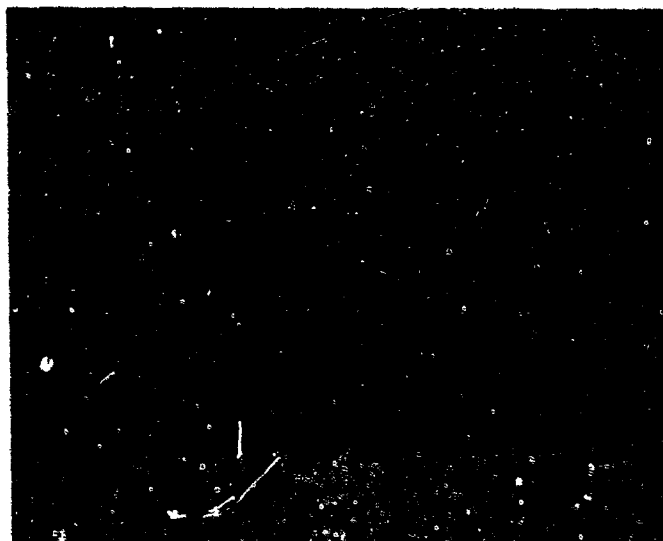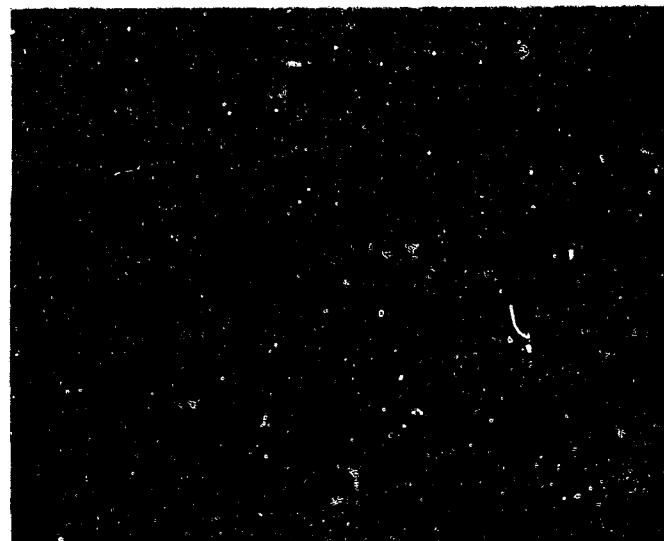FIGURE 7. MERCURY-XENON IMAGING FURNACE

problems which were not noted in the preliminary tests. These recent tests
were on hand-laid samples whereas most of the preliminary tests were made
with prepreg laminates. Also, the recent tests, because of the large hot
spot of the present furnace, used 2" square pieces of laminate, as con-
trasted with the 1 cm discs used in the preliminary tests. It is possible
that the delaminations may be due to the large area under low flux, applied
perpendicularly to the plies. The chars developed under these conditions
may not be porous enough to pass the gases produced. More probably, the
delamination is due to inexperience in the art of laying up the materials.

In the most recent tests, the cellophane sandwich-vacuum bubble
removal technique was used for impregnation of some samples. These samples
showed little or no delamination. A comparison of samples made by this
new technique and those made by the older paintbrush method after exposure
to the arc-imaging beam is shown in Fig. 8. It may be more realistic to
fabricate samples so that the flux can be applied end-grain, since in use
the materials generally would be laid up so that the heat flux would not
be perpendicular to the laminations, as illustrated in Fig. 9.

2.3.3 Hybrid Rocket Motor

A small hybrid rocket motor operating on plexiglas fuel and gaseous
oxygen was built as a senior thesis project and fired many times. The
rocket consists of two machined metal plates bracketing a replaceable
cylinder of plexiglas, and held together by carriage bolts. A graphite
nozzle can be inserted and held in place by one plate. The other plate is
attached to a chamber in which propane is spark-ignited to initiate com-
bustion of the plexiglas. Oxygen, propane, and nitrogen lines, incorporating
solenoid shut-off valves, feed into the ignition chamber and thence into the
plexiglas cylinder. This system is illustrated schematically in Fig. 10.

The present system has a pronounced tendency to leak. It is being re-
designed both to eliminate the leaks and to provide more flexibility of con-
figuration. The redesigned rocket will incorporate new end plates for more
structural rigidity and easier disassembly. Blocks of ablative
material can be located both within and downstream from the plexiglas fuel
so that the effects of combustion on the thermal response of the test materials

Exposed Surfaces

FIGURE 8.   ABLATIVE COMPOSITES AFTER FURNACE EXPOSURE.

heat flux

gas flow

Undesirable Orientation of Plies

heat flux

gas flow

Preferred Orientation of Plies
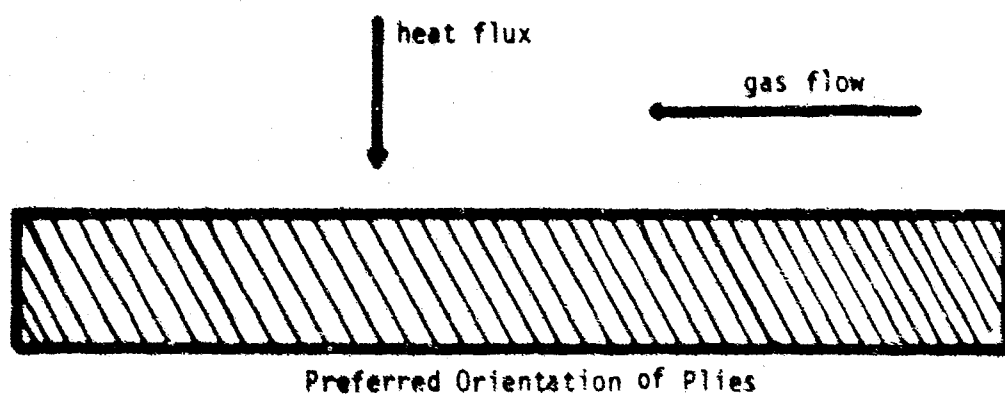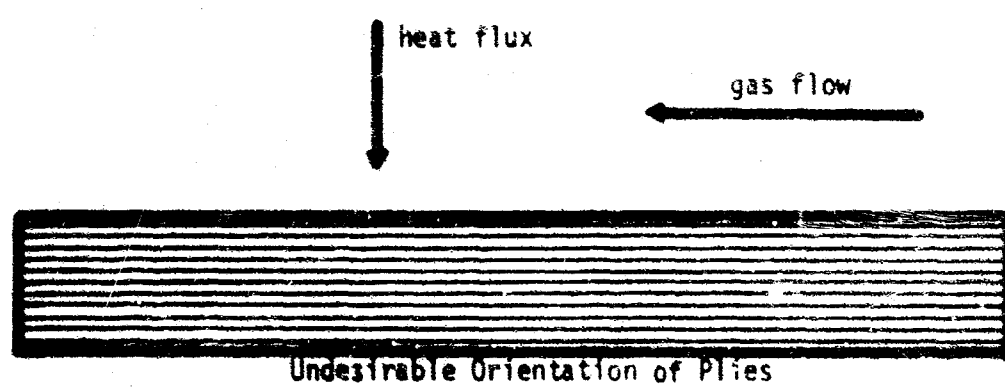
FIGURE 9. COMPARISON OF PLY ORIENTATION

c-52

Gas Flow System
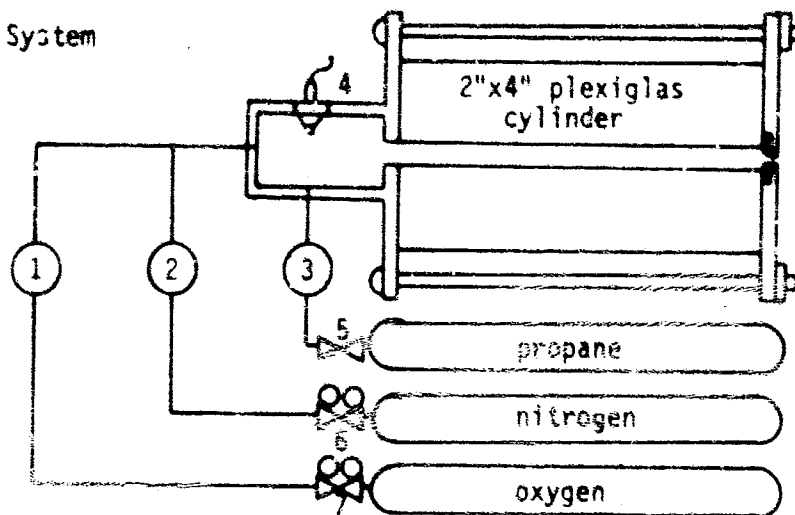
1,2,3   Solenoid Valves
  4   Spark plug
  5   Needle Valve
6,7   Regulators
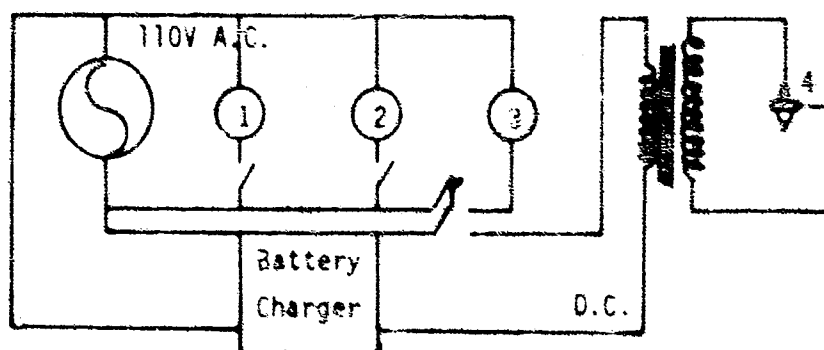
Electrical System

FIGURE 10.   HYBRID ROCKET MOTOR SCHEMATIC.

can be determined. Temperatures on the order of 4500°R and velocities ranging from very low to sonic, depending on the location in the apparatus, can be expected. Pressures obtainable will depend on the thickness of plexiglas used.

2.3.4 Hot Gas Flow Facility

Purchase of a hot-gas flow facility has been initiated. This facility will consist of a device for the controlled combustion of liquid fuel (e.g. methyl alcohol) with air, oxygen, or mixtures thereof to produce a hot gas. The system includes subsystems as described below. Air supply to the facility will be accomplished separately from the proposed facility, and consists of a 3000-psi compressor, provision for oil and water removal and approximately 400 ft^3 of air storage capacity. A schematic of the overall system appears as Fig. 11. The proposed facility subsystems are as follows:

1. Methyl alcohol (fuel) system: The fuel storage tank is stainless steel with a volume of 1.5 ft.^{3} rated at 100 psi. The fuel is pressurized with nitrogen by means of a hand loader. All required fill and drain capability is provided. Fuel flow rate is monitored by orifice flowmeter and differential pressure gage. Fuel flow is controlled by a remote throttling valve.

2. Air pressure and flow regulation system: The air pressure is regulated by a dome loaded pressure regulator. Flow control is exercised by means of remote throttling valves. Air flow rate is monitored by an orifice flowmeter and differential pressure gage. Physical properties of air are monitored at metering element. Air system is safety relieved.

3. Oxygen pressure and flow regulation system: The combustor is designed to burn either air or oxygen in the primary. The oxygen used in this manner is stored and supplied external to the present system. The pressure regulation and flow control of oxygen is accomplished in a manner similar to the air flow. The oxygen system piping is entire-

Oxygen Storage

Air Storage

Methane

Igniter System

Hot Flow Wind Tunnel

Fuel Tank

Fuel System

Nitrogen Storage

Fuel Storage

Simplified Flow Schematic,
Hot Gas Flow Facility
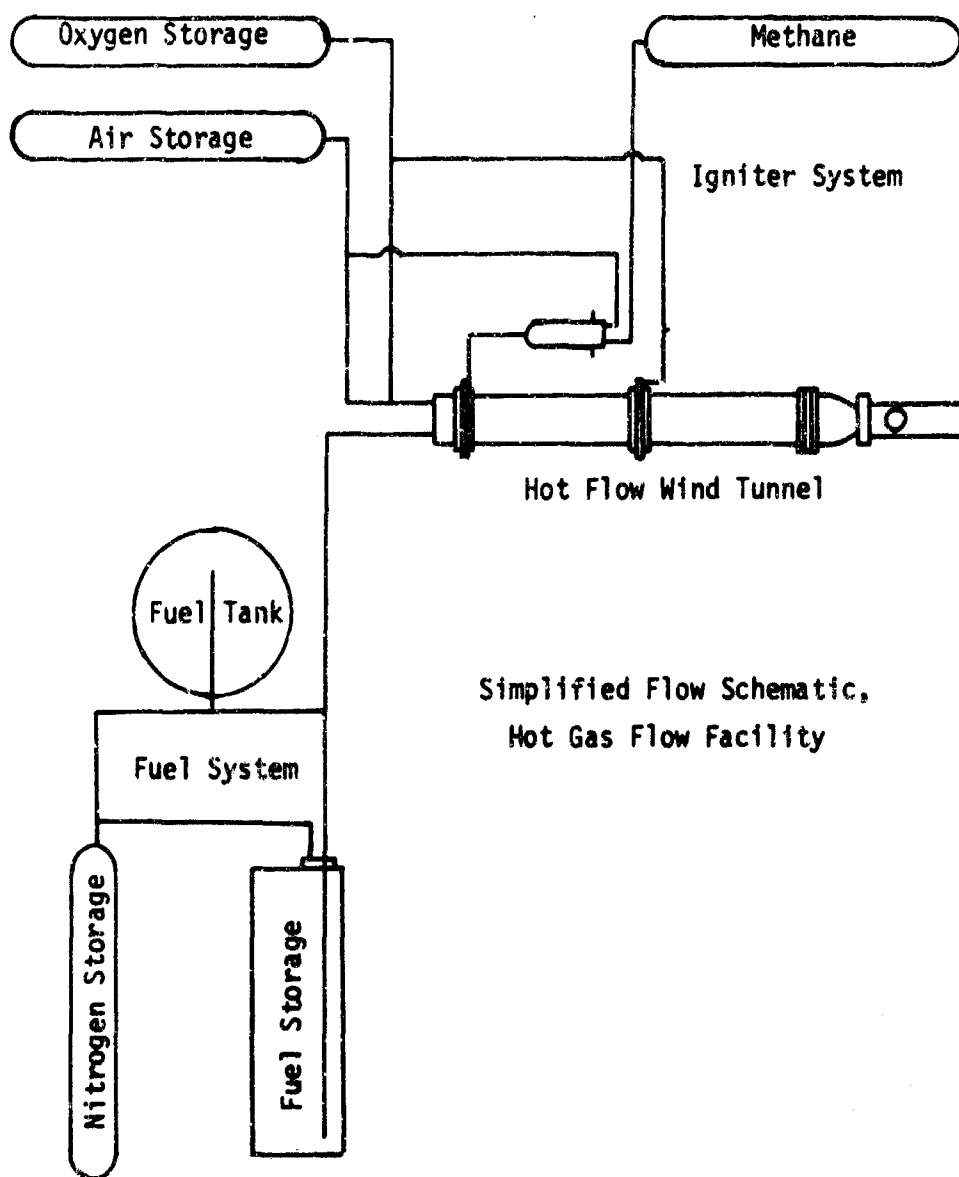
FIGURE 11. HOT GAS FLOW FACILITY SCHEMATIC

C-55

ly stainless steel.

4. General purpose air-oxygen and methyl alcohol combustor:
The combustor is fabricated entirely of stainless steel and
consists of the following components: a) a six-point tri-
plet water cooled primary injector; b) a water cooled tur-
bulence ring; c) a water cooled combustor with a 4 inch I.
D. and 36 inch length; d) a removeable secondary air injector
located 24 inches downstream of the primary injector (is
removed for operation at temperatures in excess of $1500^{\circ}F$);
e) a water cooled screen grid located at the exit of the
combustor; and f) a circular 4 inch I.D. to square transition
section.

5. Control and facility instrumentation system: The nec-
essary static instrumentation of storage pressures are pro-
vided on all tankage. Flow instrumentation required to
duplicate a run point is provided by the flow meters and
pressure and temperature sensors. Combustor total tem-
perature instrumentation are provided at the exit of the
transition section.

The facility as proposed would exhibit the following nominal operational
specifications. Total Temperature: ambient - $4500^{\circ}F$; Pressure: ambient
to 575 psia cold, 50-400 psia @$1500^{\circ}F$, 50-200 psia @$4500^{\circ}F$; Flow Rate: 0.3-
3.0 lb/sec @$T < 1500^{\circ}F$, 0.3 -2.0 lb/sec @$T < 4500^{\circ}F$. Installation of the
facility will be in tunnel 0610, located below ground level just north of
the Merrill Engineering Building. The air supply tanks are presently in
place on the surface just west of the tunnel, and the compressor is being
located in the west end of the tunnel.

2.4 *Direction of Continuing Research*

Work in progress or planned for the near future includes redesign and
fabrication of improved parts for the hybrid rocket motor previously men-
tioned. This will be done soon, as the redesigned parts will be easy to
fabricate. The rocket will then be used to investigate the response of
catalyzed and uncatalyzed materials to subsonic combustion high-shear envi-
ronments.

An optical glass dome has been procured for use in a controlled
atmosphere chamber for exposure of ablative samples in the arc-imaging
furnace. This chamber will enable us to determine the relative effects of
inert or reactive atmospheres such as CO at pressures from vacuum to
slightly above atmospheric pressure.

The thermogravimetric analysis equipment described under Phase I above
will lend itself readily to study of the $C-SiO_2$ reactions with slight
modifications for higher temperature capability. Several topics of in-
vestigation are suggested: effect of catalyst substances on the reaction,
mechanism of the catalysis, effect of particle size on the rate of reaction,
and effects of CO pressures up to 1 atm on the reaction rate. The
modifications necessary are under investigation with the cooperation of
the Materials Science and Engineering Group in the College of Engineering.

Preparation for the installation of the hot-gas flow facility is
underway. Necessary provision for high pressure air supply, cooling
water, exhaust disposal, power supply, etc., must be made. The proposed
system is to be delivered subassembled to facilitate installation.

The facility will be used to observe the thermal response of ablative
materials to clean, high-temperature products of combustion. Wide ranges
of temperature, pressure, and flow velocity are feasible. The partial
pressure of CO is also capable of large variation by adjusting the fuel/
oxidizer ratio of the facility. Thus the effect of CO pressure on the
carbon-silica reactions can be investigated in a flow environment.

3.0 PHASE III GAS-LIQUID SURFACE EFFECTS--C. Hsieh[*]

3.1 *Introduction*

The silica fibers in the plastic matrix of an ablative composite
not only provide mechanical reinforcement, but also serve an impor-
tant function in the ablation process. When subjected to sufficient
aerodynamic, thermal, and shear forces, the reinforcement materials
may eventually melt and form a glassy liquid layer on the charred
surface. Sutton[40] has shown that under certain conditions only
70% of the energy originally transferred to the surface of the
liquid layer is conducted into the non-flowing solid interior. The
molten-layer absorbs heat in several ways. Energy is absorbed
through the materials' heat of fusion and heat capacity when the
temperature of the liquid increases. At the molten-layer surface,
the materials undergo endothermic chemical reactions or vaporization[41]
and absorb significant amounts of heat. Heat transfer to the molten
layer surface can also be reduced by injecting into the gas boundary
layer foreign gases which are the products of chemical reaction or
vaporization of molten materials. Another function of the molten-
layer is to form a uniform surface on the charred materials. Whenever
a surface indentation occurs by spalling of the char, liquid silica
will flow into the hole and smooth the surface again.

The effectiveness of an ablative material is determined by the
energy absorbed per unit mass ablated. The molten-layer flows under
the shear or pressure force of the gas boundary layer, and a consider-
able portion of the ablation material may be blown off before it has
absorbed the maximum potential amount of energy and has undergone
chemical reactions or vaporization. Thus, a competition exists be-

_____

[*]Mr. Chia-lung Hsieh received a B.S. degree in Chemical
Engineering in 1966 from Tunghai University in Taiwan. Since
September 1967 he has attended the University of Utah, where
he is a candidate for a Ph.D. in Chemical Engineering, and has
worked on Phase III of this program.

tween the reactions and the blow-off of the melt layer. In order
to increase the efficiency of the ablative material, the following
properties of the system are desired: (1) high viscosity of
molten-layer; (2) small shear force acting on the surface of the
molten-layer; (3) rapid rate of chemical reactions or vaporization
of molten materials compared to flow-off; (4) strong cohesion of
glassy liquid on the charred surface. Bro[42] has pointed out that
the rate of chemical reactions are controlled by the rate of mass
transfer into its surface. If we increase the rate of evolution of
pyrolysis gases, we may, therefore, be able to increase the rate
of chemical reactions. Mass transfer can also change the velocity
profile and properties of the gas boundary layer, and so reduce the
shear force acting on the liquid surface. But increasing the
pyrolysis gas rate will also decrease the viscosity of glassy
liquid. The gas rate can be controlled by changing percentage of
plastic in the composite-material, or by adding a catalyst for the
pyrolysis of the plastic.

Since the molten-layer is formed of several different chemicals,
different surface energies exist. Some special molecules may have
a greater tendency of moving toward the liquid surface where inter-
phase chemical reactions take place. It is, therefore, desirable
to find some surface active agents which can promote this tendency
and increase the chemical reactions or vaporization rates. However,
one must be careful that the addition of surface active agents do
not reduce the viscosity of the glassy liquid or alter other
favorable properties.

Glass has a very high surface energy, and has the tendency to
form droplets. These droplets can be blown off easily by rolling
on the charred surface. This reduces the efficiency of the
ablative material and causes the roughness and unevenness on the
surface. In order to prevent the formation of droplets, it is an
important task to increase the wettability of glassy liquid on the
solid surface. The solution of this problem is to add into the
molten-layer surface active agents which can deposit a monolayer

c-59

between the molten-layer and the solid surface. If the outermost
portion of the monolayer absorbed on the solid surface has a larger
critical surface tension of wetting than the surface tension of
liquid, the molten-material can form a coherent and uniform film
covering the solid surface.[43]

3.2 *Literature Survey*

Sutton[40] was the first to investigate theoretically the
steady-state melting of an ablating semi-infinite glassy material.
He solved the problem by numerical integration of the governing
microscopic balance equations. His solution was the basis for
the more complete and rigorous treatment of steady-state melting and
vaporization by Scala and Sutton.[44] However, numerical procedures
are often too cumbersome and time-consuming, and approximate methods
of integrating simplified governing equations often illustrate the
essential features of a process. Accordingly, Dorrance[45] simplified
the problem by making the approximation of constant shear stress
across the molten-layer which permitted a couette-flow type solution.
Lees[46] obtained the approximate solution by assuming a velocity
profile for the molten-layer. Bethe and Adams[47] integrated the
simplified equations by neglecting inertial forces and assuming a
temperature profile. Rosensweig and Beecher[48] extended the method
of Bethe and Adams to a composite system involving chemical reactions.
They assumed there was an isothermal chemical reaction zone existing
between the molten-layer and gas boundary layer. Hidalgo[49] also
extended Adams' approximation for the turbulent boundary layer and
to a system involving radiation heat transfer. McFarland and
Harman[50] approached the problem by an approximate coupling between
the momentum and energy equations in the form of a velocity ex-
ponent.

Sutton[51] has shown that all approximate theories yield values
of heating and melting rates which are too large. Adams[52] has
shown that, in comparison with transient solutions, Sutton's work
(quasi-steady) yields unreliable results and fails to regard the

necessary thickness of ablative material.

The transient state of the melting of glassy material was first studied by Denison[53]. His assumptions for a flat plate molten-layer were constant shear stress and linear temperature profile through the liquid layer. Ostrach, et al[54, 55] have investigated the initial period of melting for a system without mass transfer at the gas-liquid interface. He integrated the unsteady energy equations and steady-state momentum equation without inertia force. Adams[56] also integrated the same equations by a numerical method. Chen[57] has transformed the general governing equations by Levy and Mangler transformations to obtain a numerical result for the transient state of a melting and vaporizing ablation.

Although the relationship between viscosity and liquid ablation has been thoroughly explored, the use of surface active agents for increasing chemical reactions or wettability of glassy liquid has attracted little attention. Steveiding[58, 59] has a brief discussion of the surface phenomena of ablating liquid and states that the addition of certain oxides such as FeO, B_2O, should improve the performance of the molten-layer.

3.3 *Direction for Continuing Research*

Even though a number of theoretical investigations concerning the molten-layer have appeared during the last decade, no accurate experimental data are available for comparison with these theories. The difficulty of measuring the temperature profile within the liquid layer is one reason for the lack of accurate data. In addition, the melt flow is generally not smooth but quite irregular. In order to have a complete study of the molten-layer, the development of an experimental technique is an essential for the coming year. We hope to obtain accurate measurements of temperature profile, velocity profile, and flow-off rate of the molten-layer.

As has been mentioned in the last section, the theoretical studies alone cannot provide reliable results for practical applications. In these theories, constant properties (except viscosity) of the molten-layer are assumed. But heat capacity, and heat conductivity

of glassy liquid are all functions of temperature. Citron[60] has
shown the difference between constant--and variable--properties
solutions for the molten-layer is appreciable. All the previous
investigators assumed the glassy liquid to be a Newtonian fluid.
They also assumed the viscosity of the glassy liquid as an exponential
function of temperature, and neglected the effect of pyrolyzed gases
which penetrated through the molten-layer. But at high temperatures,
glassy liquid behaves as a non-Newtonian fluid.[61] The viscosity
of the glassy liquid is reduced when the bubbles of pyrolysis gases
pass through the molten-layer. Therefore, we intend to conduct both
theoretical and experimental studies of molten-layer by treating it
as a non-Newtonian fluid. We are also interested in determining
the effect of the penetrating gases on the behavior of molten-material.

We are interested in finding some surface active agents which
can either promote the chemical reactions or change the surface energy
of molten-material and charred surface. Since gases exist within
the molten-layer, it will also be necessary to find out whether the
pyrolysis gases do have any effect on the surface phenomena of the
molten-layer. Do the gases form a monolayer between the molten-
material and charred surface? If any gases play an important role
in the surface phenomena of the molten-layer, then methods to con-
trol the rate and composition of the gas should be employed.

REFERENCES

1. Melnick, A. M.; Nolan, E. J., "The Design and Development of a
    High Heating Rate Thermogravimetric Analyzer Suitable for Use
    with Ablative Plastics," Presented at ACS Meeting, April 1968,
    San Francisco.

2. Parker, J. H.; Winkler, E. L., "The Effects of Molecular Structure
    on the Thermochemical Properties of Phenolics," NASA TR R-276.

3. Friedman, H. L., "Kinetics of Thermal Degradation of Char-Forming
    Plastics from Thermogravimetry. Application to a Phenolic Plastic,"
    Journal of Polymeric Sci., Part C, No. 6, p. 183-195.

4. Goldstein, H. E., "Pyrolysis Kinetics of Nylon 6-6, Phenolic Resin
    and Their Composites," Presented at ACS Meeting April 1968, San
    Francisco.

5. Kratch, K. M.; Hearne, L. F.; and McChesney, H. R., "Thermal
    Performance of Heat Shield Composites During Planetary Entry,"
    Presented at AIAA-NASA National Meeting, Palo Alto, California,
    September 30 - October 1. 1963.

6. Madorsky, S. L., "Thermal Degradation of Organic Polymers," Inter-
    science Publishers, New York, 1964.

7. Fleming, G. J., "Prediction of Heat Shield Performance in Terms
    of Epoxy Resin Structure," Presented at ACS Meeting, San Francisco,
    April 1968.

8. Vincent, D. N., "Thermal Degradation and Curing of Polyphenylene,"
    Presented at ACS Meeting, San Francisco, April 1968.

9. Marks, B. S., "Ablative Resins for Hyperthermal Environments,"
    Presented at ACS Meeting, San Francisco, April 1968.

10. Dickey, R. R.; Lundell, J. H.; and Parker, J. A., "The Develop-
    ment of Polybenzimidazole Composites as Ablative Heat Shields,"
    Presented at ACS Meeting, San Francisco, April 1968.

11. Wrasidlo, W. J., "Pyrolysis of Aromatic Heterocyclic Polymers,"
    paper presented at Polymer Conference Series, Wayne State
    University, May 20-24, 1968.

12. Hergenrother, P. M. and Levine, H. H., "Poly (quinoxalines):
    Synthesis and Preliminary Mechanical Properties as Laminating and
    Adhesive Resins," paper presented at the "Polymers in Space
    Research" symposium, Southern California Section of American

Chemical Society and Jet Propulsion Laboratory, Pasadena, California, July 15-17, 1968.

13. Lurie, R. M.; D'Urso, S. F.; and Mullen, C. K., "Structural Ablative Plastics," Presented at ACS Meeting, San Francisco, April 1968.

14. Cahn, L. and Schultz, H., "Aerodynamic Forces in Thermogravimetry," Analytical Chemistry, Vol. 35, p. 1729-31, October 1963.

15. Bruck, S. D., "THermogravimetric Studies on an Aromatic Polyimide in Air and in the Vacuum Region of 10^{-2} to 10^{-3} Torr Using the Cahn RG Electrobalance," Vacuum Microbalance Techniques, Vol. 4, Plenum Press 1965.

16. Cahn, L. and Peterson, N. C., "Conditions for Optimum Thermogravimetric Analysis at Atmospheric Pressure," Analytical Chemistry Vol. 39, p. 403-404, March 1967.

17. Freeman, E. S., and Carroll, B., "The Application of Thermoanalytical Techniques to Reaction Kinetics. The Thermogravimetric Evaluation of the Kinetics of the Decomposition of Calcium Oxalate Monohydrate," J. Phys. Chem., 62, 394 (1958).

18. Anderson, C. B., "Computer Program for the Conversion of Thermogravimetric Analysis Data," Aerospace Corporation, San Bernardino, California, February 1966.

19. Sykes, G. F., and Nelson, J. B.,"Thermoanalysis of Ablation Materials," Presented at 61st AICHE. National Meeting, Houston, Texas, February 19-23, 1967.

20. Anderson, G. C.; Cock, M. A.; and Wadsworth, M. E., "Isothermal Decomposition Kinetics of Potassium Dinitro Benzofuroxan," Technical Report P.O. 13-7664, Department of Metallurgy, University of Utah, Salt Lake City, Utah, May 1, 1965.

21. Bellman, R., Math. Biosciences, 1, 71-76 (1967).

22. Schmidt, D. L., "Research Trends in Ablative Plastics and Composites," a volume of technical papers presented at AIAA 6th Structures and Materials Conference, Palm Springs, California, April 5-7, 1965, pp.99-116.

23. Ladacki, M., Hamilton, J. V., and Cohz, S. N., "Heat of Pyrolysis of Resin in Silica-Phenolic Ablator," AIAA Journal, Vol. 4, 1966, pp.1798-1802.

24 Gutman, V. R., "Comment on 'Silicon Carbide in Ablative Chars,'" AIAA Journal, Vol, 5, 1967, p. 1053.

25 Ladacki, M., "Reply by Author to V. R. Gutman," AIAA Journal, Vol. 5, 1967, pp. 1053-1054.

26. Hribar, V. R., "A Critique on Internal Insulation Materials for Solid Propellant Rocket Motors," Journal of Spacecraft and Rockets, Vol. 3, 1966, pp. 1434-1436.

27. Baird, J. D., Taylor, J., "Reaction Between Silica and Carbon and the Activity of Silica in Slay Solution," Trans Faraday Soc., 54 (4) 526-39 1958.

28. Humphrey, Todd, Coughlin and King, U.S. Bur. Mines, Report Inv. 4888, 1952.

29. Beecher, N., and Rosensweig, R. E., "Ablation Mechanisms in Plastics with Inorganic Reinforcements," ARS Journal, Vol. 31, 1961, pp. 532-539.

30. Rosensweig, R. E., and Beecher, N., "Theory for the Ablation of Fiberglas-Reinforced Phenolic Resin," AIAA Journal, Vol. 1, 1963, pp. 1802-1809.

31. Ladacki, M., "Silicon Carbide in Ablative Char," AIAA Journal, Vol. 4, 1966, pp. 1445-1447.

32. Carey, M. D., and Coulbert, C. D., "Experimental Chemical Kinetic Effects in Ablative Composites," Bulletin of the 6th Liquid Propulsion Symposium, Vol. 1, Chemical Propulsion Information Agency, Los Angeles, California, September, 1964, pp. 137-152.

33. Ladacki, M., Personal communication, 29 April, 1968.

34. Sosman, Robert H., The Phases of Silica, Rutgers University Press, New Brunswick, N.J.

35. Klinger, N., Strauss, E. L., and Komarch, K. L., "Reactions Between Silica and Graphite," Journal of Am. Ceramic Soc., 49 (7), 369-375, 1966.

36. Blumenthal, J. L., Santy, M. J., and Burns, E. A., "Kinetic Studies of High-Temperature Carbon-Silica Reactions in Charred Silica-Reinforced Phenolic Resins," AIAA Journal, Vol. 4, 1966, pp. 1053-1057.

37. Romie, F. C., "Carbon-Silica Reactions in Silica-Phenolic Composites," AIAA Journal, Vol. 5, 1967, pp. 1511-1513.

38. Cutler, I. B., unpublished report of work conducted at the University of Utah, April 30, 1956.

39. Rakszawski, J. F., Rusinko, F. Jr., and Walker, P. L., Jr., "Catalysis of the Carbon-Carbon Dioxide Reaction by Iron", Proceedings of the Conferences on Carbon, Vol. 2, 1961, pp. 243-250.

40. Sutton, G. W., "The Hydrodynamics and Heat Conduction of a Melting Surface," J. of Aero. Sci., 25, 1958, p. 29-32.

41. Beecher, N., Rosenweig, R. E., "Ablation Mechanisms in Plastics with Inorganic Reinforcement," ARS, J. 31, 1961, pp. 532-539.

42. Bro, P., Steinerg, S., "Study of Chemical Surface Reactions in a High Temperature Flow System with Arc Heated Gases," ARS, J. 32, 1962, pp. 526-532.

43. Zisman, W. A., "Improving the Performance of Reinforcement Plastics," I & EC, 57, 1965, pp. 26-34.

44. Scala, S. M., Sutton, G. W., "The Two Phase Laminar Boundary Layer-- a Study of Surface Melting," Proceeding of the 1958 Heat Transfer and Fluid Mechanism Institute, pp. 231-240, Stanford University Press, Stanford, Calif. 1958.

45. Dorrance, W. H., "Viscous Hypersonic Flow," McGraw-Hill Book Company, Inc., New York, 1962, pp. 49-56.

46. Lees, L., "Similarity Parameters for Surface Melting of a Blunt Nosed Body in a High Velocity Gas Stream," ARS. J. 29, 1959, pp. 345-354.

47. Bethe, H. A., Adams, M. C.,"A Theory for the Ablation of Glassy Materials," J. of Aero, Sci., 26, 1959, pp. 321-328.

48. Rosensweig, R. E., Beecher, R., "Theory for the Ablation for Fiber- glass-Reinforced Phenolic Resin," AIAA J. 1, 1963, pp. 1802-1809.

49. Hidalgo, H., "Ablation of Glassy Material Around Blunt Bodies of Revolution," ARS. J., 30, 1960, pp. 806-814.

50. McFarland, B. L., Harmon, D. B., "Heat Transfer Through a Melting Layer with External Gas Flow," Proceeding of 1961 Heat Transfer and Fluid Mechanism Institute, Stanford University Press, Stanford, Calif., 1961, pp. 208-221.

51. Sutton, G. W., "A Comparison of Several Approximate Theories of Melting Ablation," J. of Aero Sci., 26, 1959, pp. 397-398.

52. Adams, E. W., "A Comparison of Transient and Quasi-Steady Performance of Melting-Type Re-Entry Shields," J. of Aero Sci., 27, 1960, pp. 791-792.

53. Denison, M. R., "Estimating Transient Temperature Distributions During Ablation," ARS, J. 30, 1960, pp. 562-563.

54. Ostrach, S., Goldstein, A. W., Hamman, J., "The Effect of a Decelerating Force on a Melting Boundary Layer," J. of Aero, Sci., 27, 1960, pp. 626-627.

55. Ostrach, S., McConnell, D. G., "Melting Ablation about Decelerating Spherical Bodies," AIAA Journal 3, 1965, pp. 1883-1889.

56. Adams, E. W., "A New Concept for Calculating Thermal Boundary Layer," J. of Aero. Sci., 27, 1960, pp. 543-550.

57. Chen, S. Y., Allen, S. J., "Similarity Analysis for Transient Melting and Vaporizing Ablation," ARS, J. 32, 1962, pp. 1536-1543.

58. Steverding, B., Niebealein, V. A., "Ablation for Heat Shielding," Chem. Eng. 72, July 1965, pp. 163-168.

59. Steverding, B., "Surface Activity and Perferential Ablation," AIAA J. 2, 1964, pp. 549.

60. Citron, S. J., "Steady State Melting of a Semi-Infinite Medium with Temperature-Dependent Properties," J. of Aero Sci. 27, 1960, pp. 470-472.

61. Steverding, B., "Comment on Non-Newtonian Flow," AIAA J. 2, 1964, pp. 2231.

APPENDIX A

"Catalysis of Internal Endothermic Ablation Reactions
Between Char and Reinforcement"

J. D. Seader, J. V. Larsen, R. W. Thompson, and J. D. Chidley

No. 68-505
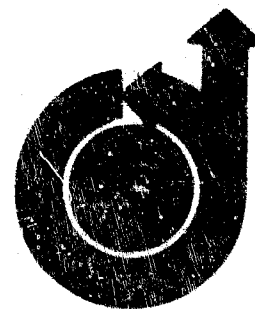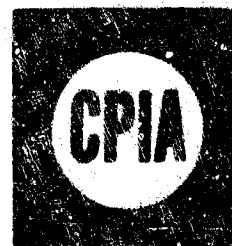
CATALYSIS OF INTERNAL ENDOTHERMIC ABLATION REACTIONS BETWEEN CHAR AND REINFORCEMENT

by

J. D. SEADER, J. V. LARSEN, R. W. THOMPSON,
and
J. D. CHIDLEY
University of Utah
Salt Lake City, Utah

AIAA Paper
No. 68-505

ICRPG/AIAA 3rd Solid Propulsion Conference

ATLANTIC CITY, NEW JERSEY/JUNE 4-6, 1968

CATALYSIS OF INTERNAL ENDOTHERMIC ABLATION REACTIONS
BETWEEN CHAR AND REINFORCEMENT

J. D. Seader*, J. V. Larsen**, R. W. Thompson‡, and J. D. Chidley†
University of Utah
Salt Lake City, Utah

Abstract

Increasing use has been made of ablative materials, such as phenolic-silica, to protect structures from high heat fluxes and high temperatures. Potentially, the heat can be absorbed to a considerable extent by endothermic chemical reactions which convert a portion of the solid material to gas. Typically, the following classes of reactions are thermodynamically feasible:

1. decomposition of the resin to form porous char and gases,

2. thermal cracking of or reactions among the pyrolysis gases as they flow through the porous char to the exposed surface of the ablative composite,

3. char oxidation by the pyrolysis gases,

4. reactions between the char and silica reinforcement.

In particular, reactions of Class 4 are highly endothermic but have been found to be relatively slow except at very high temperatures.

Preliminary experiments have been performed in an attempt to catalyze the char-reinforcement reactions, particularly the following reaction, which leads to solid silicon carbide:

$$SiO_{2(s)} + 3C_{(s)} \rightarrow SiC_{(s)} + 2CO_{(g)}.$$
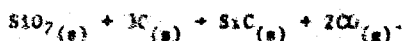
By introduction of transition-metal compounds into the composite ablative structure, significant reductions in char depth have been measured by the use of a Hg-Xe lamp image furnace. Conditions were such that surface erosion was negligible. The experimental trends are compared with theoretical predictions based on an ablation-model computer program, which includes a provision for the above reaction of Class 4.
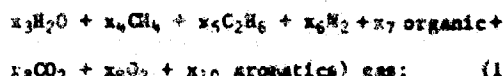
1. Introduction

For relatively short periods of time (on the order of one minute), structures may be protected by ablative materials from continuous exposure to high heat fluxes and high temperatures. Much longer times can be tolerated if the exposure is periodic or intermittent. The most commonly used ablative materials for thrust-chamber insulation and lining applications have been composites of an elastomer and/or plastic held together by a reinforcement. One such composite is phenolic-silica--a high-purity silica cloth impregnated with phenol-formaldehyde resin and subsequently cured to a tough laminated structure. A great deal of research has been and is being conducted to develop improved ablative materials which are tailored for particular applications.[1]

In use, the incident radiative and/or convective thermal energy is absorbed by the ablative composite to some extent by surface and internal endothermic chemical reactions. For composites containing plastic resin and inorganic reinforcements, the following classes of internal chemical reactions are thermodynamically feasible:

1. decomposition (pyrolysis) of the resin to form char and gases; e.g.,[2]
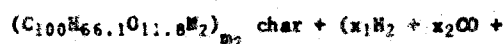
$$(C_{100}H_{89.4}O_{17.8}N_8)_{m_1} \text{ resin} \xrightarrow{1110°F}$$

$$(C_{100}H_{66.1}O_{11.8}N_2)_{m_2} \text{ char} + (x_1H_2 + x_2CO +$$

$$x_3H_2O + x_4CH_4 + x_5C_2H_6 + x_6N_2 + x_7 \text{ organic} +$$

$$x_8CO_2 + x_9O_2 + x_{10} \text{ aromatics}) \text{ gas}; \quad (1)$$

2. thermal cracking of or reactions among pyrolysis gases as they percolate through the insulative porous char to the exposed surface of the ablative composite; e.g.,

$$CH_{4(g)} \rightleftharpoons C_{(s)} + 2H_{2(g)}, \quad (2)$$

$$\text{Benzene}_{(g)} + 9H_{2(g)} \rightleftharpoons 6CH_{4(g)}; \quad (3)$$

3. char oxidation of the pyrolysis gases; e.g.,

$$C_{(s)} + CO_{2(g)} \rightleftharpoons 2CO_{(g)}, \quad (4)$$

$$C_{(s)} + H_2O_{(g)} \rightleftharpoons CO_{(g)} + H_{2(g)}; \quad (5)$$

4. reactions between the char and reinforcement; e.g.,

$$SiO_{2(s)} + C_{(s)} \rightleftharpoons SiO_{(g)} + CO_{(g)}, \quad (6)$$

$$SiO_{2(s)} + 2C_{(s)} \rightleftharpoons Si_{(l)} + 2CO_{(g)}, \quad (7)$$

$$SiO_{2(s)} + 3C_{(s)} \rightleftharpoons SiC_{(s)} + 2CO_{(g)}, \quad (8)$$

and subsequent reactions:

---
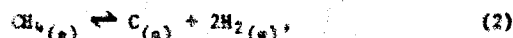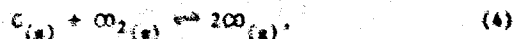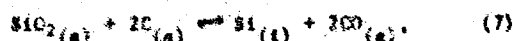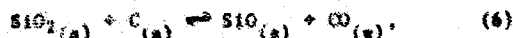
*Professor of Chemical Engineering; Member AIAA.
**Presently research engineer, U. S. Naval Ordnance Laboratory, Silver Spring, Maryland.
‡Presently graduate student, University of California, Berkeley, California.
†Graduate student.

$$SiC_{(s)} + 2SiO_{2(s)} \rightleftharpoons 3SiO_{(g)} + CO_{(g)}, \quad (9)$$

$$SiO_{2(s)} + Si_{(l)} \rightleftharpoons 2SiO_{(g)}. \quad (10)$$

$$P_{CO} = 10^{(8.71 - 15,100/T)}, \quad (11)$$

where p_{CO} is in atm and T is in °K.
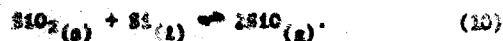
In the development of an understanding of the internal ablation processes, the reactions of Class 1 have received the most attention. These pyrolysis reactions are very important because they produce a porous char which can quite effectively insulate the virgin composite thermally from the high-energy external environment and thereby curtail the overall internal ablation rate.

Of the three classes of postpyrolytic chemical reactions, those of Class 4 are considerably more endothermic than the reactions of the other two classes. For this reason, Class 4 reactions have received some attention.[3-16] Thermodynamic, kinetic, and practical aspects of these char-reinforcement reactions are reviewed briefly in the following sections. The potential advantages of catalyzing the formation of silicon carbide according to Equation (8) are discussed. The results of preliminary catalysis experiments involving the use of transition-metal elements and compounds are presented.

II. Thermodynamic Considerations

Estimated standard heats of reaction at 25°C for several internal ablation reactions are summarized in Table 1. If it is assumed that one gram of resin undergoes pyrolysis to a char containing 0.45 grams of carbon, which is subsequently consumed according to the reaction of Equation (8), the ratio of the heat absorbed by the C-SiO₂ reaction to the heat absorbed by the resin pyrolysis is approximately 5.8.

TABLE 1. STANDARD HEATS OF REACTION FOR INTERNAL ABLATION REACTIONS.

Reaction	$\Delta H^\circ_{25°C}$, cal/gm-mole
1	+265*
2	+17,889
3	-137,134
4	+41,220
5	+31,382
6	+150,214
7	(+154,000)
8	+122,518
9	+328,124
10	+146,910

*cal/gm resin for pyrolysis at 1000°F.[2]

Beecher and Rosenzweig[3] considered the separate thermodynamic equilibria of the SiO₂-C reactions given by Equations (6-8). They stressed the importance of the equilibrium carbon-monoxide pressure and concluded that, if the kinetics of the reactions were rapid, the formation of silicon carbide would be dominant over a temperature range of approximately 1400°C to 2000°C. Table 2 includes computed carbon-monoxide pressures based on the following equation given by Rosenzweig and Beecher[4]:

TABLE 2. PREDICTED REACTION TIMES AND EQUILIBRIUM CARBON-MONOXIDE PRESSURE FOR C-SiO₂ REACTIONS.

Temperature		Reaction Time, sec		p_{CO}**
°F	°C	50%*	90%*	psia
2,500	1,371	491	1,631	5.0
2,600	1,427	246	818	9.9
2,700	1,482	129	429	18.9
2,800	1,538	70.3	234	34.3
2,900	1,593	39.8	132	61.4
3,000	1,649	23.2	77.1	105
3,100	1,703	14.0	46.4	175

*Depletion of carbon in the presence of excess SiO₂ and negligible reverse reaction.

**For Equation (8).

Other investigators[6,7,12,13] have approached the thermodynamic equilibrium problem by an alternate technique of calculating the equilibrium composition for a specified initial composition of C and SiO₂, allowing for the production of all possible chemical species. Wide temperature and pressure ranges have been covered. Unfortunately, some discrepancies among these calculations exist. Reported results of Ladacki[13] at a pressure of 5 psia show that the formation of SiC is favored over a temperature range of 2550°F to 3100°F. At 150 psia, this temperature range is shifted to about 3050°F to 3350°F.

It appears that, on the basis of all the reported thermodynamic calculations, depending on the total pressure, a temperature exists where the silicon-carbide-formation reaction given by Equation (8) is favored. Unfortunately, precise prediction of this temperature is currently in doubt.

III. Kinetic Considerations

Probably because of analytical difficulties, a thorough investigation of the kinetics of the C-SiO₂ reactions has not been reported. The studies of Beecher and Rosenzweig[3] and of Blumenthal et al.[12] have been confined to vacuum conditions for a temperature range of 1300°C to 1700°C (2372°F to 3091°F). The quantitative extent of the reactions has been largely monitored by carbon-monoxide pressure.

The initial study[3] indicated that the formation of SiC was very rapid in the temperature range where it was thermodynamically dominant. However, the subsequent study[12] led to a re-examination[11] of the initial results. As a result, the kinetics of the C-SiO₂ reaction were found to be relatively slow except at very high temperatures, where SiO₂ is in a molten but very viscous state.

A convenient first-order kinetic expression for the depletion of carbon by the C-SiO₂ reaction has been suggested by Romic[16], based on the

2

results of Blementhal et al.[12]:

$$-\frac{dC}{dt} = 15.5 \exp\left[20 - \frac{62,500}{T}\right] C,\qquad(12)$$

where C is the carbon spatial density in grams/cm^3, t is the time in hours, and T is the temperature in $°K$. It is not certain to which of the possible $C-SiO_2$ reactions Equation (12) applies. The results of calculations based on Equation (12) of the times required for 50% and 90% depletion of carbon are given in Table 2, covering a temperature range of 2500°F to 3100°F (the approximate range of the experimental kinetic tests). Also included in Table 2 is the corresponding equilibrium carbon-monoxide pressure, as predicted for the SiC-formation reaction of Equation (8) by Equation (11). For relatively low pressures, Table 2 indicates that, for the usual short-time-exposure applications of ablative composites, the chemical reaction governing the formation of SiC may be too slow at the predicted thermodynamic on-off temperature, as is discussed by Beecher and Rosensweig.[3-4]

IV. Practical Considerations

Despite the high endothermicity of the $C-SiO_2$ reactions, their desirability in ablative composites is not necessarily justified. As is pointed out by Gutman[14], if the $C-SiO_2$ reactions lead to a breakdown of the reinforced-char structure, with subsequent surface erosion (ablation), then the overall ablation rate may increase rapidly and become intolerable. However, as is discussed by Ladacki[15], in cases where dimensional integrity is not essential, the additional endothermic heat sink provided by the $C-SiO_2$ reactions may more than compensate for any resulting surface erosion.

To date, a thorough study of the desirability or undesirability of the $C-SiO_2$ reactions for the entire range of re-entry and thrust-chamber applications has not been reported. It would appear that one potential area of desirability might be in those regions of thrust chambers where surface erosion is generally not experienced and where the internal-insulation weight should be optimized. Such situations are common in small liquid-propellant space engines and in the thrust chamber and blast tube of certain solid rocket motors, where the heat fluxes are not too severe. The importance of weight reduction in solid-rocket-motor insulation was discussed recently by Bribar.[17]

By catalyzing the silicon-carbide-formation reaction, as given by Equation (8), so that it is rapid at the lower temperatures experienced, it may be possible to obtain the endothermic benefit and corresponding reduction in char depth (and, therefore, a reduction in necessary wall thickness). By carefully selecting the silica-to-resin ratio in the composite, it may even be possible to eliminate the possibility of subsequent SiC reactions, which can result in rapid surface erosion. Composites with silica-to-resin ratios as low as 0.54 were formulated by McAllister et al.[5] and showed good ablative characteristics.

V. Experimental Work

Because of the potential benefit which might be gained by the rapid formation of SiC at an on-off temperature, a study of possible catalytic

means was initiated. Experiments conducted by Cutler[18] in 1956 with silica and carbon showed that transition metals were effective in catalyzing the synthesis of silicon carbide. Therefore, it was believed that transition metals would be effective also with silica and char in pyrolyzed ablative composites. Accordingly, preliminary experiments were conducted in the present work to test this hypothesis.

Preparation of Composites

Two types of composites were fabricated; namely, prepreg and hand laid. The prepreg samples were made by cutting U. S. Polymeric PM-5204 prepreg (a high-silica fabric-reinforced prepreg employing a MIL-R-9299 phenolic resin) into two-inch squares. Transition-metal catalysts were applied to both sides of the squares. The compounds tested were SnO_2, Cr_2O_3, Fe_2O_3 (all fine powders), and Fe (#100 and #200 mesh). These powders were rubbed onto the prepreg with a dry cotton cloth. This method gave the most uniform covering of several methods tried. Samples containing 7, 10, and 15 layers of prepreg squares so prepared were paired with control samples containing no potential catalyst additive and were numbered for identification purposes. The samples were cured by the method described below.

The hand-laid samples were prepared by cutting high-purity silica cloth into two-inch squares and applying the powdered metal compounds and liquid phenolic resin in one of the following three manners:

1. The powder was applied directly to the cloth by the same procedure as was used to apply it to the prepreg. The resin was painted on the cloth with a nylon brush.

2. The powder was suspended in acetone. The suspension was applied to the cloth by soaking and then allowed to dry. The resin was then brushed on the cloth as before.

3. The powder was suspended in the resin, and the resin was brushed on the cloth.

The resin used was U. S. Polymeric P-502 (a MIL-R-9299 phenolic resin). As in the case of the prepreg, composites of 7, 10, and 15 layers were prepared and paired with similar samples containing no metal compounds.

Curing

Each of the composites containing potential catalysts was cured simultaneously with its companion control sample. A Whitehead and Company Model D-195 laminating press was used in the curing process. After the platens were preheated to 110°F, the pair of samples was sandwiched between two layers of non-heat-sealing, high-temperature cellophane in order to protect the platens from the excess resin. A pressure of 30 psig was applied to the pair of samples and a temperature of about 300°F was maintained for one hour.

Preparation for Testing

Before the samples were tested at high-energy flux, several preparation steps were required.

3

Several disc-shaped samples, each one cm in diameter, were cut from the two-inch square composite with a carbon-steel core drill. The discs were fitted to a sample holder, described below, by grinding them to a proper diameter. Each disc was numbered and weighed on a Mettler M-5 balance before heating. Before the discs were cut out, the density of the composite slab was measured. This was accomplished by weighing the slab and taking accurate measurements of its dimensions. The silica-fiber content of the composite slab was also determined by combustion in a muffle furnace at 1800°F for two hours.

Testing

The samples were heated in an arc-image-type furnace, in which the energy flux was produced by a Hg-Xe lamp. Uniform fluxes up to 70 cal/cm^2-sec could be produced. The disc samples were held in place in the burning chamber of the furnace during heating by a sample holder. This holder consisted of a steel plate with a hole one cm in diameter drilled to a depth of five mm.

Heating test times ranged from 5 to 45 seconds. A disc sample was placed in the sample holder and secured with a set-screw. The holder was then placed in the heating chamber of the image furnace. The chamber was purged with nitrogen gas to insure an inert atmosphere for heating. The gases of pyrolysis were removed from the furnace through a long tube. The heat flux was applied in the central region of the sample face.

All tests were conducted with a heat flux of 43 cal/cm^2-sec, as determined by a copper calorimeter calibration.

Analysis of Pyrolyzed Samples

The pyrolyzed disc samples were weighed as before and sawed in two so as to expose a central cross section of the char layer. The sawed surface was sanded smooth. The depth of the char was measured with a Bernell scope calibrated in 0.1-mm units.

A number of samples were mounted in Lucite and Bakelite. These samples were polished for microscopic analysis. Photo-micrographs were made of the mounted samples by use of high-speed Polaroid film. Measurements of the char depths on these photo-micrographs were used to substantiate the relative depth measurements made with the Bernell scope.

Results

Without exception, the measured char depths of the samples containing transition-metal powders were less than their corresponding control samples. In all cases, surface regression was negligible. The percentage of reduction in char depth is tabulated in Table 3 and ranged from 5% to 25%. Metallic iron powder of #100 mesh resulted in the greatest char-depth reduction, with an average for four tests of 15% reduction. The metallic oxides (MnO$_2$, Cr$_2$O$_3$, Fe$_2$O$_3$) averaged about 10% char-depth reduction.

For samples containing #200-mesh powdered iron, a plot of char depth vs. exposure time appears in Figure 1. Over most of the region studied, char depth varied with exposure time to the 0.6 power. In this case, Figure 1 shows that, with increased exposure time, the difference in char depth between the catalyzed and the control samples increased. The percentage of char-depth reduction remained about the same. With the #100-mesh iron, the char-depth reduction, as seen in Table 3, appeared to increase with exposure time.

TABLE 3. EXPERIMENTAL CHAR-DEPTH REDUCTION.[*]

Catalyst Material	Exposure Time, sec	Char-depth Reduction percent
Fe$_2$O$_3$	10	11.2
	15	11.0
	15	8.5
Fe$_2$O$_3$ (Hand-laid)	10	5.0
	15	7.7
Cr$_2$O$_3$	10	7.7
	12	10.0
	15	21.0
	35	14.8
MnO$_2$	25	11.5
	35	10.7
Fe (#100 Mesh)	10	5.5
	15	12.5
	15	17.3
	45	25.6
Fe (#200 Mesh)	5	7.7
	10	18.2
	20	10.0
	30	15.8
	40	12.5

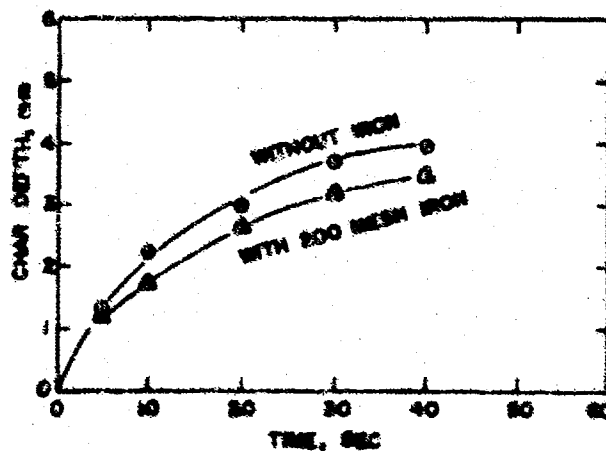[*] Data are for preprog samples except where noted for hand-laid.

FIGURE I - EXPERIMENTAL CHAR DEPTHS

VI. Computer Calculations

An existing computer program[10] based on a detailed mathematical model of the internal chemical ablation processes was utilized to predict the effect of the char-silica reactions (particularly

the silicon-carbide-formation reaction) on the char-depth, time relationship. A radiative heat flux of 44.5 cal/cm²-sec (1.14 Btu/in²-sec), which was comparable to the experimental tests, was specified with a typical 70/30 silica-phenolic composite. The results of the calculations are plotted in Figure 2. At a 60-second exposure, the predicted char-depth reduction is about 16 percent.
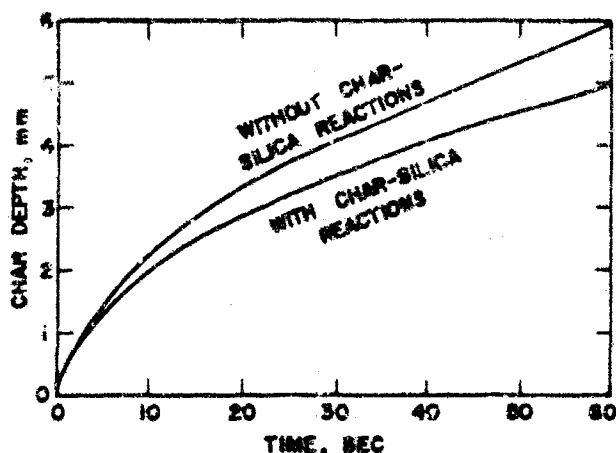

FIGURE 2 - PREDICTED CHAR DEPTHS

VII. Conclusions

The results of preliminary experiments indicate that it may be possible, in certain applications, to reduce char depth in silica-phenolic ablative composites by adding transition-metal compounds to catalyze certain char-reinforcement reactions. The concept may also be applicable to other resin and elastomer materials which are reinforced with inorganic materials.

The experiments utilized only crude methods of introducing the catalytic compounds, and chemical analyses of neither the residue nor the emitted gases were performed. Only the char-depth reduction was used as an indicator of a catalytic effect. The use of iron appeared to give the greatest reduction in char depth.

Further work in this area is continuing. Current emphasis is on the use of transition metals in such forms as carbonyls, chelates, ferrocenes, and oxalates in order to facilitate a more easily controlled catalyst introduction. In addition, chemical-composition analyses are necessary to determine actual overall chemical changes. The results of the preliminary studies are presented at this time to encourage consideration of possible applications and further discussion of the char-reinforcement reactions.

References

[1]Schmidt, D. L., "Research Trends in Ablative Plastics and Composites," a volume of technical papers presented at AIAA 6th Structures and Materials Conference, Palm Springs, California, April 5-7, 1965, pp. 99-126.

[2]Ladacki, M., Hamilton, J. V., and Cohz, S. N., "Heat of Pyrolysis of Resin in Silica-Phenolic Ablator," AIAA Journal, Vol. 4, 1966, pp. 1798-1802.

[3]Beecher, N., and Rosensweig, R. E., "Ablation Mechanisms in Plastics with Inorganic Reinforcements," ARS Journal, Vol. 31, 1961, pp. 532-539.

[4]Rosensweig, R. E., and Beecher, N., "Theory for the Ablation of Fiberglas-Reinforced Phenolic Resin," AIAA Journal, Vol. 1, 1963, pp. 1802-1809.

[5]McAllister, L. E., et al., "Behavior of Pure and Reinforced Charring Polymers During Ablation under Hypervelocity Re-entry Conditions," Chemical Engineering Progress Symposium Series, Vol. 59, No. 40, 1963, pp. 17-32.

[6]Carey, M. D., and Coulbert, C. D., "Experimental Chemical Kinetic Effects in Ablative Composites," Bulletin of the 6th Liquid Propulsion Symposium, Vol. 1, Chemical Propulsion Information Agency, Los Angeles, California, September, 1964, pp. 137-152.

[7]Kendall, R. M., and Rindall, R. A., "Analytical Evaluation of Rocket Nozzle Ablation," AIAA Paper 64-101, 1964.

[8]DeSesa, M. A., and Perkins, J. S., "Determination of Temperature Profile in Charred Phenolic Composites by Reconstruction of the Ablation Process," AIAA Paper 65-638, 1965.

[9]Wilhelm, J. R., "Ablation of Refrasil-Phenolic Nozzle Inserts in Solid Propellant Exhausts," Journal of Spacecraft and Rockets, Vol. 2, 1965, pp. 337-344.

[10]Rivers, W. J., Van Wyk, R., Seader, J. D., Friedman, H. A., and Chu, H. N., "Effects of Rocket Engine Combustion on Chamber Materials, Part I: One-dimensional Computer Program," Rocketdyne Report AFRPL-TR-65-13, January, 1965.

[11]Beecher, N., and Rosensweig, R. E., "Erratum: 'Ablation Mechanisms in Plastics with Inorganic Reinforcement,'" AIAA Journal, Vol. 1, 1965, p. 1567.

[12]Blumenthal, J. L., Santy, M. J., and Burns, E. A., "Kinetic Studies of High-Temperature Carbon-Silica Reactions in Charred Silica-Reinforced Phenolic Resins," AIAA Journal, Vol. 4, 1966, pp. 1053-1057.

[13]Ladacki, M., "Silicon Carbide in Ablative Char," AIAA Journal, Vol. 4, 1966, pp. 1445-1447.

[14]Gutman, V. R., "Comment on 'Silicon Carbide in Ablative Char,'" AIAA Journal, Vol. 5, 1967, p. 1053.

[15]Ladacki, M., "Reply by Author to V. R. Gutman," AIAA Journal, Vol. 5, 1967, pp. 1053-1054.

[16]Koaie, F. E., "Carbon-Silica Reactions in Silica-Phenolic Composites," AIAA Journal, Vol. 5, 1967, pp. 1511-1513.

[17]Brazar, V. F., "A Critique on Internal Insulation Materials for Solid Propellant Rocket Motors," Journal of Spacecraft and Rockets, Vol. 3, 1966, pp. 1434-1436.

[18]Cutler, I. B., unpublished report of work conducted at the University of Utah, April 10 1967.

BLANK PAGE

APPENDIX B

1.0 ABLATION COMPUTER PROGRAM

In order to guide the direction of Task 3, an existing one-dimensional charring ablation computer program is being utilized. This program was developed under Air Force Contract No AF04(611)-9714 in 1964 under the supervision of the Principal Investigator of Task 3 while he was employed by the Rocketdyne Division of North American Aviation.

The computer program was based on a comprehensive and detailed mathematical model of the primary physical and chemical processes occurring within and at the surface of an ablative wall of a rocket motor or thrust chamber. Only essential features of the program are described here. Complete details are presented in Reference (i).

The internal mode of the model accounts for the heat transfer, chemical reaction, and flow processes which occur within the ablative wall material. The surface mode serves as a physical and/or thermochemical boundary condition on the internal mode at the heated surface by accounting for the interaction between the wall surface and the hot combustion gases. A schematic of the model indicating the mechanisms considered is shown in Figure 1.

The internal mode is based on the following one-dimensional, rectangular coordinate, temperature-dependent properties form of the thermal energy equation:

$$(\rho C) \frac{\partial T}{\partial \tau} = \frac{\partial}{\partial y} \left(K \frac{\partial T}{\partial y} \right) - C_g G_g \frac{\partial T}{\partial y} - \sum_j r_j \, (\Delta H)_j \qquad (1)$$

In this equation, the first two terms account for the transient heat conduction within the wall; the third term accounts for the convective cooling of the porous, charred portion of the wall by the pyrolysis gases percolating through it; and the last terms account for the production or absorption of heat by the various chemical reactions that occur within the wall.

Three types of internal chemical reaction are included in the model: (1) pyrolysis of the ablative resin, (2) cracking of the high molecular

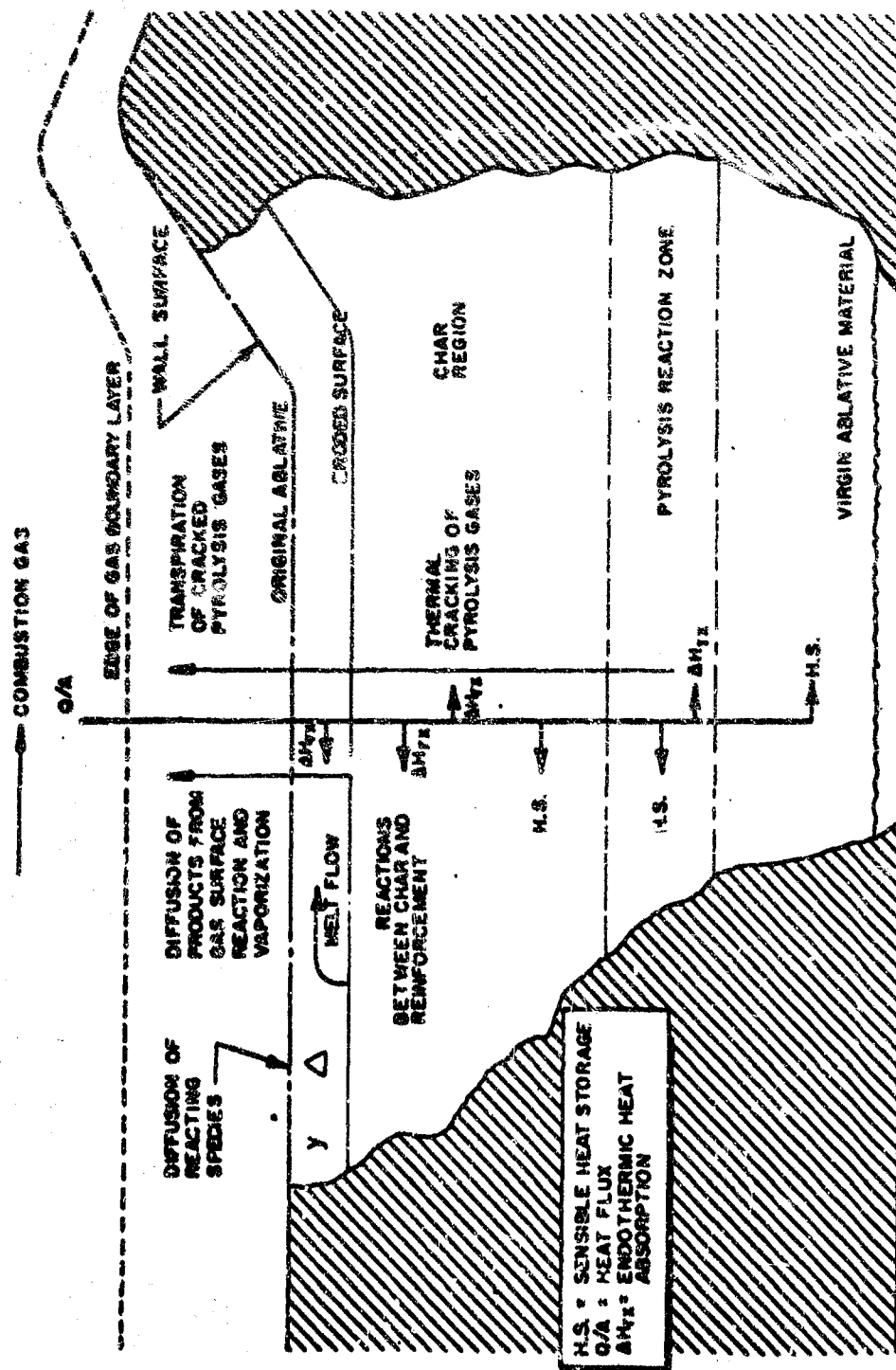* See Nomenclature for definition of symbols

cB-1

FIGURE 1. SCHEMATIC OF ONE-DIMENSIONAL ANALYTICAL ABLATIVE MODEL

SHOWING REGIONS AND PROCESSES INCLUDED IN MODEL.

weight constituents in the pyrolysis gas during percolation through the char, and (3) reactions between the reinforcement material and the carbonaceous portion of the char. Although each of these groups of reactions actually involves many different simultaneous or consecutive reactions, they are each represented in the model in terms of an overall chemical reaction for simplicity. The rates (r_j) of these representative reactions are formulated in the model with the following arrhenius-type, kinetic reaction rate expressions. For the pyrolysis reaction,

$$ r_{py} = A_{py} \, (\rho_p)_0 \; (\Gamma_g)_{py}^{\,n-1} \left[\frac{\rho_p}{(\rho_p)_0} \right]^n \; \exp \left[- \frac{(\Delta E)_{py}}{R\,T} \right] \qquad (2) $$

for the pyrolysis gas cracking reaction,

$$ r_{cr} = A_{cr} \, \rho_{g\,1} \; \exp \left[- \frac{(\Delta E)_{cr}}{R\,T} \right] \qquad (3) $$

and for the char-reinforcement reaction,

$$ r_{sc} = A_{sc} \, \rho_c^* \left[\frac{\rho_c}{\rho_c^*} \right]^{2/3} \; \exp \left[- \frac{(\Delta E)_{sc}}{R\,T} \right] \qquad (4) $$

In these expressions, the symbols ρ_i^* and ρ_i represent the true pure-state density and the actual spacial density in the composite wall of material i, respectively.

A'so, included in the computer program is the option of deleting from Eq. 1 the kinetic-rate term for the gas-cracking reactions and accounting for the heat effect of these reactions by assigning an appropriate magnitude (which may vary with temperature) to the pyrolysis gas specific heat. This is equivalent to assuming that the rates of the gas-cracking reactions are equilibrium controlled rather than kinetically controlled.

To account for the variation with time of the composition, and, therefore, the properties of the composite wall material resulting from the

chemical reactions, and to account for the production and motion of the pyrolysis gas, material-accounting or "continuity" equations of the following forms are also included in the ablation model. For the solid component materials,

$$\frac{\partial \rho_i}{\partial \tau} = \sum_j (r_i)_j \, r_j \tag{5}$$

and for the pyrolysis gas components,

$$\frac{\partial \rho_{gi}}{\partial \tau} + \frac{\partial G_{gi}}{\partial y} = \sum_j (r_{gi})_j \, r_j \tag{6}$$

where

$$j = py, \text{ cr, and sc}$$
$$i = p, r, c, \text{ and s}$$
$$gi = g1 \text{ and } g2 \text{ (uncracked and cracked gas species, respectively).}$$

Also included in the ablation model are the momentum equations

$$G_{gi} = -\left[\frac{L_m \, \rho_{gi}}{\mu_g \, p} \right] \frac{\partial p}{\partial y} \tag{7}$$

which are based on a simplified theory of slow flow through porous media, the state equation:

$$p = \left[\frac{\rho_{g1}}{M_{g1}} + \frac{\rho_{g2}}{M_{g2}} \right] R \, T \tag{8}$$

which is based on the ideal gas law, and the porosity relationship:

$$p = \left[1 - \left(\frac{\rho_p}{\rho_p^*} + \frac{\rho_r}{\rho_r^*} + \frac{\rho_c}{\rho_c^*} + \frac{\rho_s}{\rho_s^*} \right) \right] \tag{9}$$

which is based on obvious geometrical considerations.

The over-all thermophysical properties of the composite wall material appearing in Eq. 1 are obtained from the relationships

$$(\rho\ C) = [\ \rho_g\ C_g + \rho_p\ C_p + \rho_r\ C_r + \rho_c\ C_c + \rho_s\ C_s\ ] \qquad (10)$$

$$K = [P\ K_g + \frac{\rho_p}{\rho_p^*}\ K_p + \frac{\rho_r}{\rho_r^*}\ K_r + \frac{\rho_c}{\rho_c^*}\ K_c + \frac{\rho_s}{\rho_s^*}\ K_s] \qquad (11)$$

which derive from the assumption that the values of these properties are equal to the volume-weighted average of their values for the component materials. The thermophysical properties of the individual component materials are calculated from empirical expressions, fitted to experimental data, that are supplied to the computer program. .

The surface mode is primarily concerned with evaluating the rate of heat transfer from the hot combustion gas to the exposed surface of the chamber wall and the rate of surface erosion resulting from vaporization, chemical reaction with the combustion gas, and/or mechanical action such as melting and shear flow. The heat transfer to the surface is calculated, in the general case, from the relationship:

$$- (K)_\Delta\ (\frac{\partial T}{\partial y})_\Delta = \rho_e\ U_e\ (St)_{tr}\ [H_e - H_w] + (-G_g)_\Delta\ [H_g - H_w] +$$

$$(G_m)_{chem}\ [H_m - H_w] + \sigma\ \epsilon_e\ F_{gs}\ [T_e^4 - (T)_\Delta^4] -$$

$$\sigma\ \epsilon_m\ F_{se}\ (T)_\Delta^4 \qquad (12)$$

The total chemical enthalpy terms (H_j) and the mass rate of surface erosion as a result of chemical reaction, $[(G_m)_{chem}]$, which appear in this equation, are evaluated from a system of relationships derived from the well-known theories of chemical-thermodynamic equilibrium, chemical reaction kinetics, and boundary-layer-type heat and mass transfer. The effect of transpiration blocking of the convective heat transfer to the wall surface is accounted for through the use of the following empirical equation for the Stanton number:

$$(St)_{tr} = (St)_0 - \frac{0.3}{\rho_e U_e} \left[\frac{C_w}{C_e} \right]^{0.2} \left| (-G_g)_\Delta + (G_m)_{chem} \right| \qquad (13)$$

For cases where the reinforcement material melts at the higher temperature (e.g., the silica-based material), there is also included a method whereby the effective rate of surface erosion from melting and shear flow $[(G_m)_{mech}]$ can be evaluated. The total rate of surface recession resulting from these two types of surface erosion, chemical reaction, and melting, is then obtained from the relationship:

$$\rho_m \frac{d\Delta}{d\tau} = [(G_m)_{chem} + (G_m)_{mech}] \qquad (14)$$

in which the factor Δ is the linear measure of the position of the wall surface.

A unique numerical approach is used to solve the above set of coupled nonlinear partial differential equations for the internal and surface modes of the ablation process. The new technique involves the simultaneous application of the Biot variational procedure for the virgin and backup regions and numerical finite difference methods employing the Crank-Nicolson implicit procedure and including predictor-corrector techniques for the char region and pyrolysis reaction zone.

The above analysis was programmed in Fortran IV for automatic computation. The printed output from this ablation computer program consists of the location of the wall surface and the complete internal spacial distributions of the temperature, porosity, pyrolysis gas pressure, flowrate, mass concentration of cracked and uncracked pyrolysis gas species, and the bulk densities of the various solid component materials. This information can be printed out as often as the program user desires with respect to simulated ablation time.

For the specific application of the computer program to Task 3, it was found necessary to modify the surface boundary condition equation used during the initial heat-up period (prior to pyrolysis) so as to permit only a radiative input (such as would be the case for arc-image ablation tests). After making this modification, a series
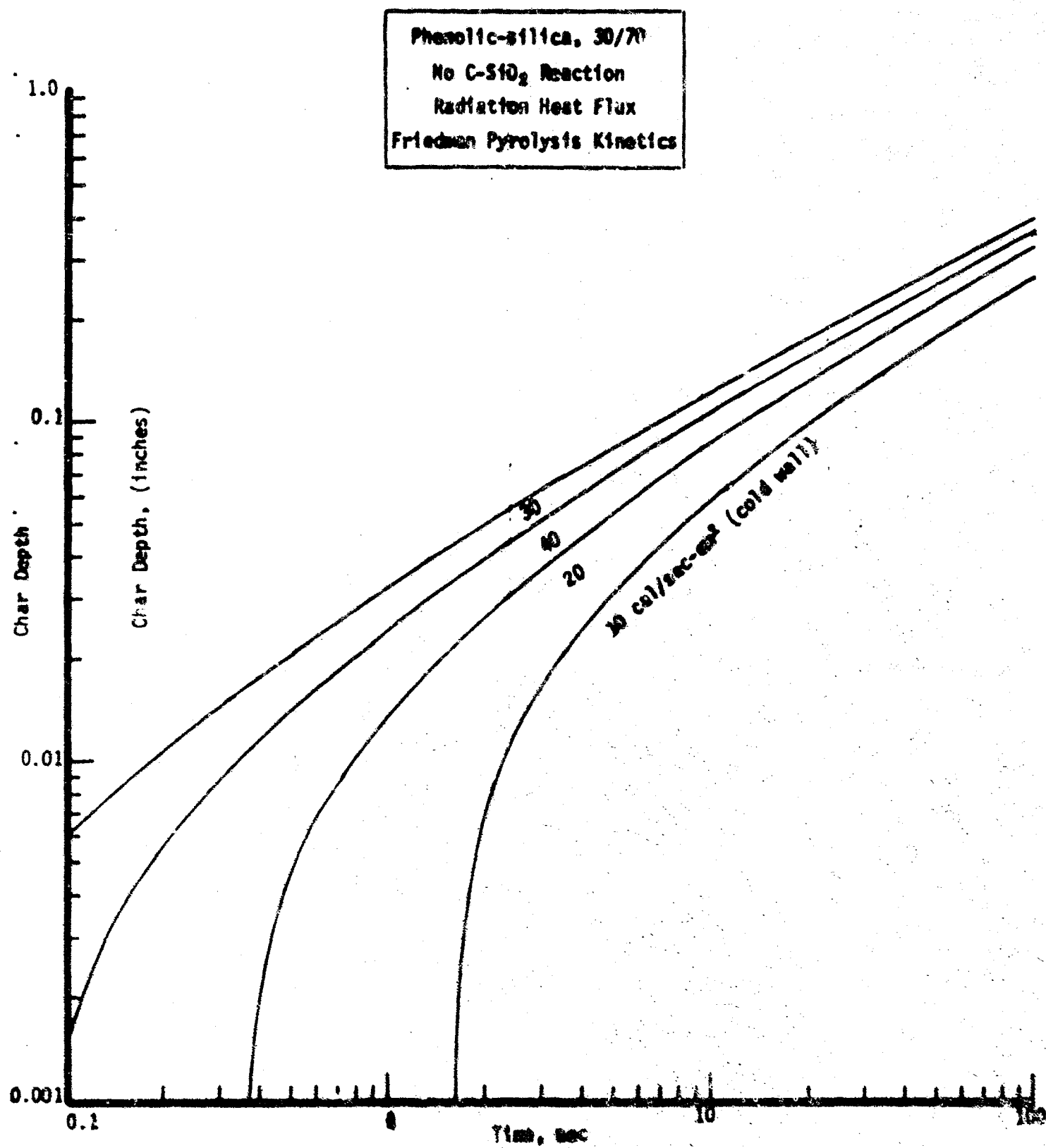
FIGURE 8. BASE-CASE CHAR-DEPTH CURVES.

B-7

Phenolic-silica, 30/70
No C-SiO₂ Reaction
Radiation Heat Flux
Friedman Pyrolysis Kinetics

80
40
20
10 cal/sec-cm² (cold wall)

Surface Temperature, °R

10,000
1,000
100

Time, sec.

0.1
1
10
100
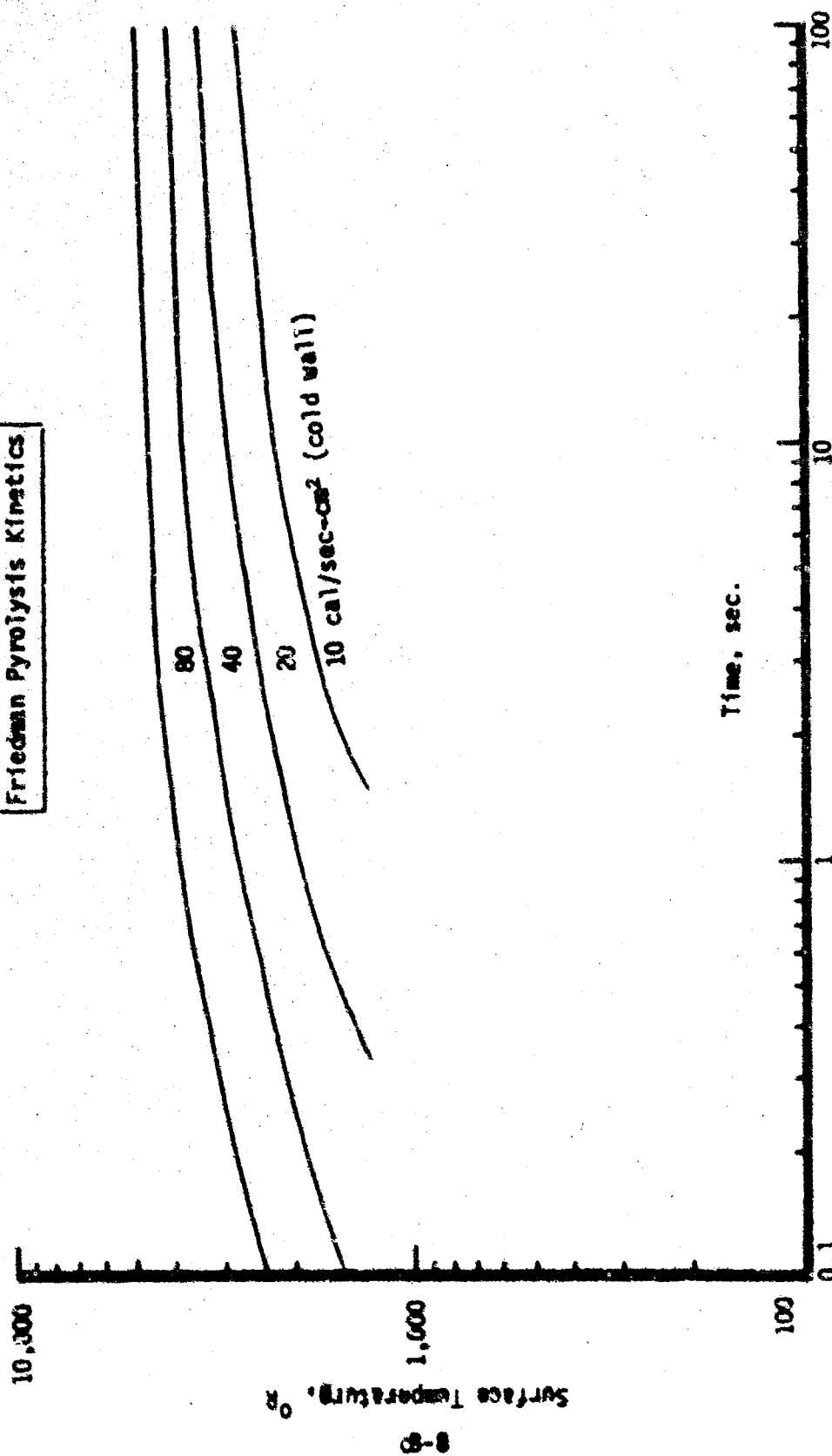
FIGURE 3. BASE-CASE SURFACE-TEMPERATURE-RISE CURVES.

8-8

of 4 base case runs were made for 30/70 phenolic-silica under
conditions of no char-reinforcement reactions and no surface
regression for radiative heat inputs of 10, 20, 40 and 80 cal/sec-cm^2.
The input data and properties utilized are listed in Table 1. Calculated
char depths and surface temperatures are plotted in Figures 2 and 3
as a function of time over the range of 0.1 to 100 seconds.

Additional calculations are currently underway which include
rapid char-reinforcement reactions. These results will be compared
to those shown in Figures 2 and 3. In addition, based on the discussion
under Phase I above, it now appears necessary to make further modification
to the program to permit the use of a series of reaction rate expressions
for resin pyrolysis.

TABLE I

DATA AND PROPERTIES FOR BASE CASE RUNS

Phenolic resin density	0.043 lbm/in^3
Silica density	0.079 lbm/in^3
Pyrolyzed phenolic density	0.076 lbm/in^3
Phenolic resin specific heat	0.30 Btu/lbm-^{0}R
Silica specific heat	0.25 Btu/lbm-^{0}R
Pyrolyzed phenolic specific heat	0.60 Btu/lbm-^{0}R
Pyrolysis gas specific heat	1.0 Btu/lbm-^{0}R
Phenolic resin thermal conductivity	2.0×10^{-6} Btu/sec-in-^{0}R
Silica thermal conductivity	1.2×10^{-5} Btu/sec-in-^{0}R
Pyrolyzed phenolic thermal conductivity	3.5×10^{-5} Btu/sec-in-^{0}R
Mass fraction of phenolic resin converted to gas	0.47
Kinetic order of pyrolysis reaction	5
Activation energy of pyrolysis reaction	9.9×10^4 Btu/lb mole
Pre-exponential factor of pyrolysis reaction	2.8×10^{14} sec^{-1}
Heat of pyrolysis	450 Btu/lbm resin
Initial Wall temperature	530^0R

NOMENCLATURE

A	=	area
A	=	reaction rate frequency factor
C	=	specific heat
(ΔE)	=	reaction activation energy
F	=	thermal radiation shape factor
G	=	mass flux of pyrolysis gas
(G_m)	=	mass rate of char surface erosion
H	=	total specific enthalpy
(ΔH)	=	heat of reaction
$(\Delta H)_m$	=	effective heat of reaction of all of the char surface erosion processes
K	=	thermal conductivity
L_m	=	permeability coefficient of char
M	=	molecular weight
n	=	kinetic order of pyrolysis reaction
P	=	porosity of char
p	=	pressure
R	=	universal gas constant
r	=	volumetric mass-rate of a chemical reaction
$(St)_o$	=	Stanton number without transpiration
$(St)_{tr}$	=	Stanton number with transpiration
T	=	temperature
U	=	velocity
y	=	perpendicular distance from surface into chamber wall

Greek Symbols:

Γ	=	mass of a product substance produced per unit mass of a reactant substance consumed in a chemical reaction
Δ	=	linear measure of the char surface recession
δ	=	char depth

ε =   thermal emissivity

σ =   Stephan-Boltzmann constant

μ =   viscosity

ρ =   actual spacial density

ρ^* =   true, pure-state density

τ =   time

Subscripts:

c =   pure carbonaceous char

cr =   pyrolysis gas-cracking reactions

$chem$ =   due to chemical reactions

e =   free-stream combustion gas

g =   total pyrolysis gas

gs =   between combustion gas and char surface

gi =   ith component of the pyrolysis gas

$g1$ =   unstable component of pyrolysis gas

$g2$ =   stable component of pyrolysis gas

i =   ith component material

j =   jth chemical reaction

m =   composite char material at chamber wall inside surface

$mech$ =   due to melting and shear flow

o =   initial value

p =   resin or plastic

py =   pyrolysis reaction

r =   reinforcement material

s =   solid products of char-reinforcement reactions

sc =   char reinforcement reactions

se =   between char surface and nozzle exit

w =   combustion gas immediately adjacent to char surface

δ =   at the reaction-virgin regions interface

Δ =   at the char surface

REFERENCES

1. Rivers, W. J., Van Wyk, R., Seader, J. D., Friedman, H. A., and Chu, H. N., "Effects of Rocket Engine Combustion on Chamber Materials, Part I: One-dimensional Computer Program," Rocketdyne Report AFRPL-TR-65-13, January 1965.

THE CHEMISTRY AND MECHANICS OF COMBUSTION

WITH

APPLICATIONS TO ROCKET ENGINE SYSTEMS

TASK 4   Radar Attenuation and Plasma Physics

R. W. Grow

October 1968

College of Engineering
UNIVERSITY OF UTAH
Salt Lake City, Utah

TABLE OF CONTENTS

TASK 4   Radar Attenuation and Plasma Physics

BLANK PAGE

1.0 INTRODUCTION

The objective of this project is to develop a method for probing
a combustion chamber by microwave techniques. Such techniques have
been used for many years to measure the ionization density and collision
frequency of the exhaust plasma beyond the exit plane, and elaborate
probing techniques have been developed at many locations to measure
attenuation through the flame for a minimum path length as well as for
an oblique path length and as a function of distance from the exit plane.
Ordinarily such measurements assume the plasma to consist of one thermo-
dynamic region. This simple model has been improved in our laboratory
by including the effect of thermodynamic shock waves in the plume to
obtain a more exact value for the ionization density and collision fre-
quency at the exit plane.[1-4] Reasonable agreement between theoretical
predictions and experimental measurements has been obtained.

In addition, analytical techniques have also been developed to
include the effect of temperature on the total ionization produced by
the constituents of the flame. In general these results are difficult
to apply because of the difficulty of knowing all the reactions that
are taking place. Particular success was achieved, however, where there
was only one source of electrons from the flame constituents. In this
case, Saha's equation relates the degree of ionization to the tempera-
ture.[1] This fact suggests that motors seeded with alkali metals can
be used to produce a single source of electrons. Experimental verifi-
cation of this technique has been achieved.[4]

The basis for relating attenuation measurements to the ionization
density and hence the temperature is given in Section 2. The applica-
tion of these techniques to the measurement of the chamber conditions
is the present objective of the project. Ultimately, techniques will be
developed to account in the analysis for the presence of pressure waves,
non-uniform combustion, and source and sink reactions. A directive
antenna for making the measurements has been developed and the design
is also included in Section 2. This project is continuing, and measure-
ments on a 1 pound charge will be made in the near future.

As a result of a special interest in the possible use of micro-waves for nondestructive detection of voids in solid propellants, a feasibility study was undertaken to investigate this possibility. The results of the study are included in Section 3.

2.0 MICROWAVE DIAGNOSTIC STUDY

Plasma characteristics are easily determined using microwave techniques. Changes in amplitude and phase of microwave radiation are caused by the presence of the plasma, and these changes can be related to various plasma parameters such as electron density, collision frequency, and temperature. Microwave diagnostic techniques are widely used and have the important feature that no physical contact with the plasma is required.[1-4]

2.1 *Theoretical Basis for Microwave Diagnostic Measurements (R.W.Grow)*

The basic mechanism involved in the interaction of electromagnetic radiation with a plasma at microwave frequencies is the induced motion of the plasma electrons. The resulting electron current is out of phase with the field and hence appears in the wave equation as an additional displacement current term and the apparent dielectric constant of the medium is changed to

$$\epsilon_{plasma} = \epsilon_0 \left(1 - \frac{\omega_p^2}{\omega^2} \right) \tag{1}$$

where

ω = radian frequency of the microwave radiation

ω_p = electron plasma radian frequency

This is an exact expression for a homogeneous plasma with no electron collisions. The change in phase angle along a path of length L within the plasma is given exactly by the equation

$$\Delta\theta = kL \left(1 - \sqrt{1 - \frac{\omega_p^2}{\omega^2}} \right) \tag{2}$$

where $k = \omega\sqrt{\mu_0\epsilon_0}$, μ_0 is the permeability, and ϵ_0 is the dielectric constant.

For plasmas of appreciable density and temperature, it is necessary to account for the electron collisions with gas molecules. Considering

d-3

a Maxwellian gas which is characterized by a constant collision fre-
quency ν, independent of electron velocity, the wave equation is
describing the propagation of electromagnetic waves in a region contain-
ing a uniform charge distribution is

$$(\Gamma^2 + k^2)E = i\omega\mu_o\rho v \tag{3}$$

where E is the electron field, ρ is the charge density, k is the phase
constant corresponding to the velocity of light, and Γ is the propaga-
tion constant. The electron velocity v is determined from Langevin's
equation

$$m\dot{v} + mg(v)v = eE \tag{4}$$

where m and e are respectively the mass and charge of an electron.
If $g(v) = \nu$, a constant, then

$$v = \frac{\frac{e}{m}E}{i\omega + \nu} \tag{5}$$

and the wave equation then yields a solution for the propagation constant
Γ. There are two unknown plasma parameters ω_p and ν. Two measurements
must be taken to find the two parameters and one may use attenuation
or phase measurements or combinations thereof since the solution for Γ
is of the form $\Gamma = \alpha + j\beta$. One possibility is to measure the attenuation co-
efficients α_1 and α_2 at two frequencies ω_1 and ω_2, respectively. When
the electron conduction current is much smaller than the displacement
current the equation for α is simplified greatly, and when α is measured
at two different frequencies ω_p and ν are given by

$$\nu = \frac{\alpha_2\omega_2^2 - \alpha_1\omega_1^2}{\alpha_1 - \alpha_1} \tag{6}$$

$$\omega_p^2 \quad \nu\,\alpha_1 c\,\frac{\omega_1^2 + \nu^2}{\nu} \tag{7}$$

The method described applies for the ideal case of a Maxwellian
gas with the collision frequency being independent of the electron
velocity. There is demand for microwave diagnostics of nonhomogeneous

d-4

plasmas containing many constituents which are non-Maxwellian. The theory must be generalized considerably if any meaningful microwave tests are to be made of plasmas of this type.

The wave equation as given by Equation (1) is still valid for this case and for v we must, in general, use the Maxwell-Boltzmann average velocity.

$$<v> = \frac{e}{m} E \frac{8\pi}{3} \int_0^\infty \beta(\frac{\beta}{\pi})^{3/2} \frac{v^4 e^{-\beta v^2}}{i\omega + \nu} dv \tag{8}$$

For convenience, one can define

$$<v> = \frac{e}{m} E (B - iD) \tag{9}$$

Then for ν constant

$$B - iD = \frac{1}{i\omega + \nu} \tag{10}$$

and the results shown previously are obtained. Actually ν is not a constant, but is given by

$$\nu = \sum_i \rho_i Q_i v \tag{11}$$

where ρ_i and Q_i are the density and collision cross-sections of the ith plasma constituent. The ρ_i's are determined from the gas composition and the functional behavior of Q_i for some common gases is given in the following table where the coefficients C_i are functions of temperature.

Gas	Q
CO, H_2	$C_1 + C_2 v$
N_2	$C_3 v$
CO_2	$C_4 v^{-1}$
H_2O, HCl	$C_5 v^{-2}$

A weighted average collision frequency may be found in terms of the temperature and gas composition. By carrying out the integration to obtain $<v>$, B and D may be found in terms of the gas temperature. From the wave equation, the attenuation α and phase β along a path of length L are given by

d-5

$$\begin{Bmatrix} \alpha \\ \beta \end{Bmatrix} = \frac{k}{\sqrt{2}} \sqrt{ \begin{Bmatrix} + \\ - \end{Bmatrix} \left[\left(\frac{\omega_p}{\omega} \right)^2 \omega D - 1 \right] + \sqrt{ \left[\left(\frac{\omega_p}{\omega} \right)^2 \omega D - 1 \right]^2 + \left(\frac{\omega_p}{\omega} \right)^4 (\omega B)^2 } } \qquad \begin{matrix} (12) \\ (13) \end{matrix}$$

For a given frequency α depends on ω_p, ρ, and T and measurements at three frequencies are required to obtain values for these parameters only from attenuation measurements. When the perfect gas laws describe the plasma adequately, ρ may be expressed in terms of T and only two measurements are required. The attenuation is increased when either the electron density or the collision frequency is increased.

In the case of a rocket exhaust plasma the effect of a shock layer can be analyzed by noting that there is now attenuation in both the central region and the outer region and the total attenuation is

$$\alpha_{total} = \alpha_I + \alpha_{II} \qquad (14)$$

where I denotes the central region and II the outer region. Since the gas conditions are discontinuous across a shock layer, there are now six unknowns, ω_{p_I}, $\omega_{p_{II}}$, ρ_I, ρ_{II}, T_I, and T_{II}. Using the assumption that the outer region is at atmospheric pressure, using the Prandtl-Meyer relations and using the perfect gas laws gives three unknowns which may be ω_{p_I}, $\omega_{p_{II}}$, and T_I so that three-frequency measurements may be used to solve for these unknowns at any particular position.

These results have only been applied to the diagnosis of the exhaust plume. It is the intent of the present project to apply them to the combustion chamber itself. The fact that the microwave measurement is essentially made external to the plasma without perturbing it has considerable significance. The difficulty of making reliable temperature measurements inside the combustion chamber has led to the present study of the feasibility of making these measurements.

Preliminary investigations have been carried out on the problems of fitting a small-scale motor with ceramic windows to provide a path for microwave energy through the combustion chamber. Initial measurements will be made on motors with fuel charges of the order of one pound. Geometrical problems associated with a chamber size for this amount of fuel and the possible beam widths for microwave energy have been investigated and the problem of making meaningful measurements in the time required for the charge to burn is also being investigated. For microwave radiation with the wavelength considerably less than the dimensions of the propellant charge, good resolution can be achieved position-wise through the plasma. Time resolution is primarily a function of the amplifiers used in the system. Demonstration of feasibility will involve showing that microwave attenuation measurements can be successfully made at 23 GHz and 70 GHz through the combustion chamber during the testing of the motors.

The experimental equipment for making measurements at these two frequencies has been selected and the arrangement of the equipment and the motor for making the experiment is presently being designed. Since the size of the motors is restricted to the order of one pound of propellant with a volume of about 5 in^3, the antennas to confine the radiation must have considerable directivity. For this reason one of the initial phases of the project has been to design a suitable antenna. A reasonably directive pattern can be achieved with a horn antenna. The pattern for a fairly large horn is shown in Figures 3 and 4 of Section 3. In order to focus the radiation through the small volume of propellant more directivity is desirable. For this reason, a dielectric horn antenna with focussing properties has been designed.

2.2 *Antenna Design (H. S. Huang and R. W. Grow)*

From Rhodes's experimental patterns, optimum dimensions were selected for both H and E plane flare as a function of flare angles ϕ_o and θ_o, respectively, and horn length L as illustrated in Figures 1
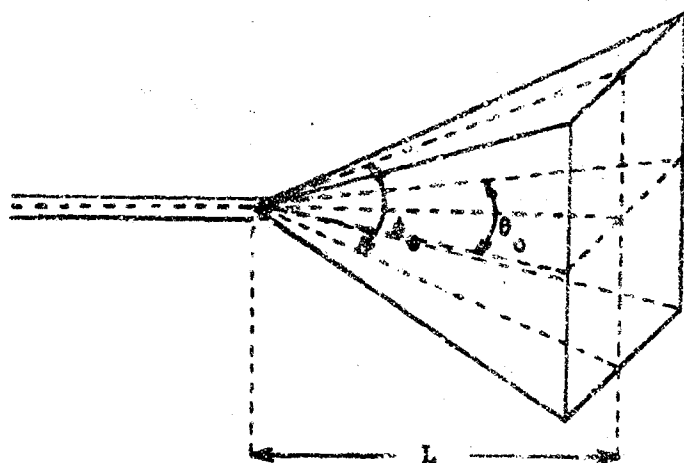
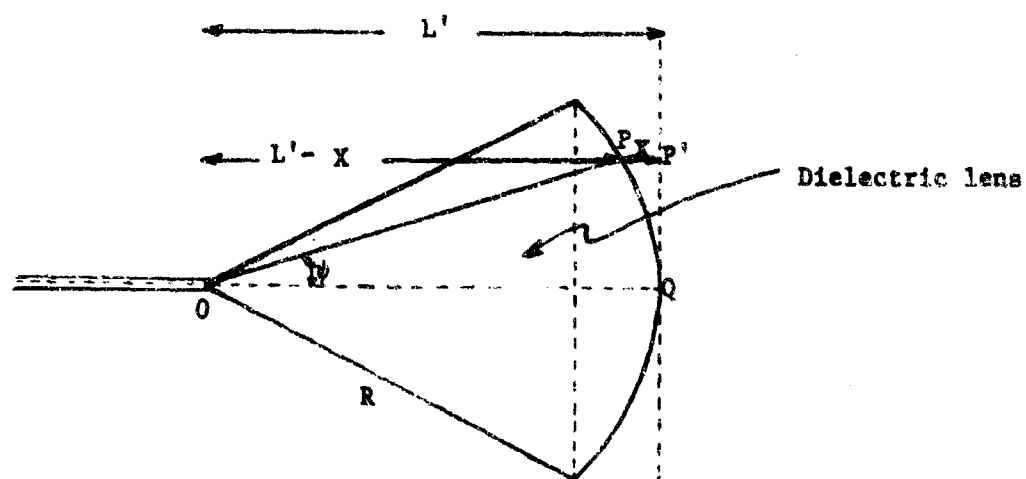Figure 1. Drawing illustrating the parameters for a horn antenna

Figure 2. Drawing of a dielectric horn insert to be inserted
in the antenna illustrated in Figure 1.

d-8

and 2. An optimum horn with a 14 degrees half-power beam width in both the H plane and E plane should have flare angles of $\phi_0 = 36°$ and $\theta_c = 29°$, respectively, and a length of 7.8 wavelengths. The directivity of the horn antenna may be increased by inserting a dielectric lens into the horn as illustrated in Figure 2. To obtain a parallel beam of radiation the electrical length of the paths must be equal. Then,

$$\frac{L'}{\lambda_d} = \frac{(L' - x)\sec \psi}{\lambda_d} + \frac{x}{\lambda_o} \tag{15}$$

where

λ_o = wave length in free space

λ_d = wave length in dielectric material

$n = \dfrac{\lambda_o}{\lambda_d}$ = index of refraction

Solving Equation 1 for L' = L + x yields

$$L' = \frac{L(n \sec \psi_1 - 1)}{n - 1} \tag{16}$$

Equation 16 expresses the length L' as a function of ψ_1. A drawing of the optimum K-band horn for a frequency of 23.6 GHz is shown in Figure 3. The data for the polar plot of the dielectric insert is given in Table 1 and a drawing of the dielectric insert to obtain a parallel beam is shown in Figure 4. This horn is presently being fabricated to investigate the actual focussing characteristics.

In addition the theory has also been developed to obtain a focused beam of radiation as shown in Figure 5.

By means of the techniques of geometrical optics, one finds L' = L + x

$$L' = \frac{n L \sec \psi_1 + (D - L) \sec \psi_1 - D}{n - \sec \psi_1} \tag{17}$$

This equation is presently being solved to obtain the design of the focused horn antennas.

d-9
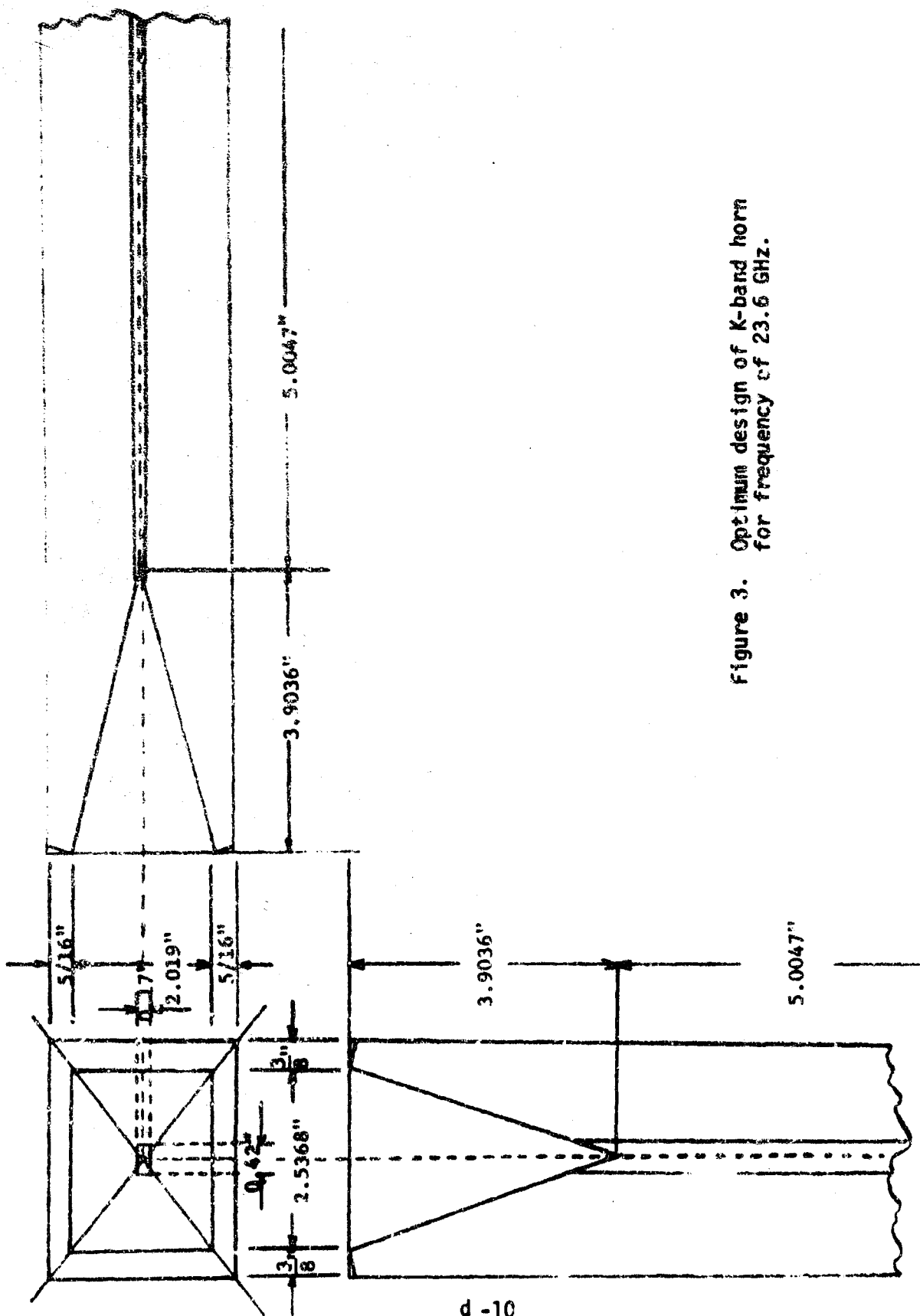
Figure 3. Optimum design of K-band horn for frequency of 23.6 GHz.
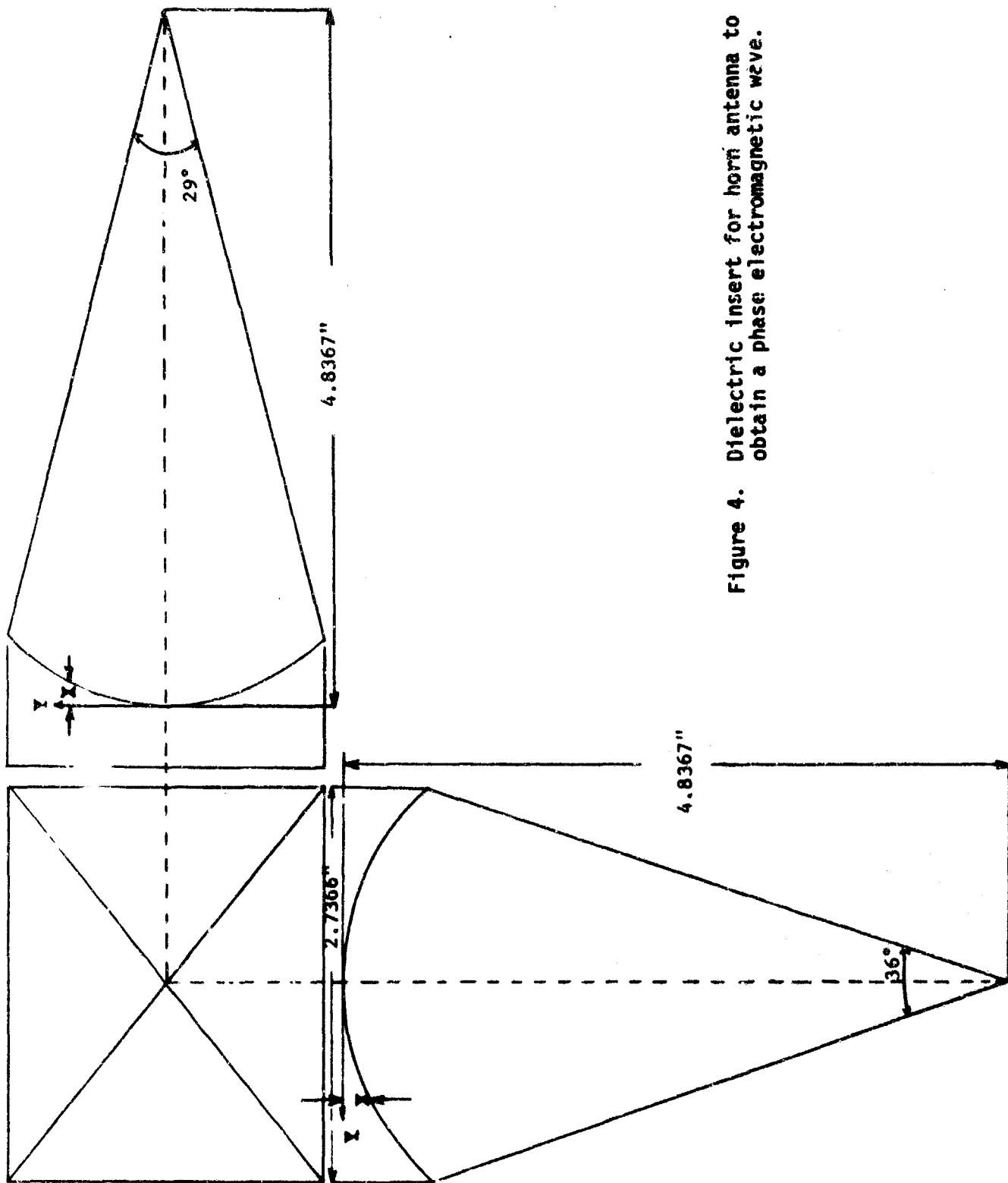
d -10

5/16"
2.019"
5/16"
3.9036"
5.0047"
3.9036"
5.0047"
2.5368"
0.42"
3"/8
3"/8

Figure 4. Dielectric insert for horn antenna to obtain a phase electromagnetic wave.

29°

4.8367"

Y

4.8367"

2.7366"

36°

Y

d-11

TABLE I

Angle (Degrees)	Radius (Meters)	Angle (Degrees)	Radius (Meters)
ψ	R	ψ	R
		13	0.11719
0	0.12285	14	0.11633
1	0.12282	15	0.11543
2	0.12271	16	0.11448
3	0.12254	17	0.11350
4	0.12229	18	0.11247
5	0.12198	19	0.11140
6	0.12160	20	0.11030
7	0.12115	21	0.10917
8	0.12064	22	0.10801
9	0.12006	23	0.10683
10	0.11943	24	0.10562
11	0.11874	25	0.10440
12	0.11799		

Subsequent to the demonstration of feasibility, within a few months the effort will be made to include the presence of shock waves and non-uniform combustion in the analysis, and attenuation measurements will be made at two or more frequencies in accordance with the complexity of the model used to describe the burning process. It is expected that this research will be performed in conjunction with Tasks 1 and 2.

The theory of wave propagation in the exhaust plasma is based upon a knowledge of the electron collision cross-section properties of all the gas constituents. The model being used includes the effect of the cross-section data to obtain the electron temperature. The previous work with exhaust plasmas accounted for the electron source and sink reactions in the flame. It is intended, as the project progresses over the next year, that in this case also the chemical reaction processes in the flame will be integrated into the electromagnetic wave theory.

3.0 FLAW DETECTION BY MICROWAVE ANALYSIS

As a result of a current interest by industrial organizations
and research laboratories in non-destructive test and inspection tech-
niques in solid fuels, for both latent defects as well as internal
dewetting, we have investigated the possibility of detecting cracks
or voids using microwave diagnostic techniques. The major problem
with such techniques is that of achieving sufficient sensitivity to
detect small defects. Several methods for making such measurements
are possible. The method we investigated was based on conventional
standing wave measurements. If an electromagnetic wave enters a sec-
ond region that has a different dielectric constant than the first
region, a reflection is produced. The combination of the incident wave
and the reflected wave produces standing waves that can be detected
by suitable instruments. If the transmitted portion of the wave
leaves the second region and enters a region like the first a sec-
ond reflection is generated. These two reflections will cancel
each other if the thickness of the second region is zero, otherwise a
net reflection is produced by the combination of the two reflected
waves. This reflection can be used to detect the presence of a defect.
The interaction of the reflection from the incident surface of the pro-
pellant and the combined reflection from the crack can be used to
determine the depth of the crack below the surface.

3.1 *Theoretical Analysis of Crack Detection (C. H. Durney)*

The principles involved in measuring the dimensions and location
of a crack in a dielectric can be illustrated by consideration of
plane-wave reflections from infinite dielectric boundaries. The
configuration shown in Figure 5.

In this development Z will be used to denote the characteristic
or plane wave impedance of the various materials, and ϵ will be used
to denote the dielectric constant. The magnitude of the reflection
coefficient in Region I can be found from Z_I, which is defined as the
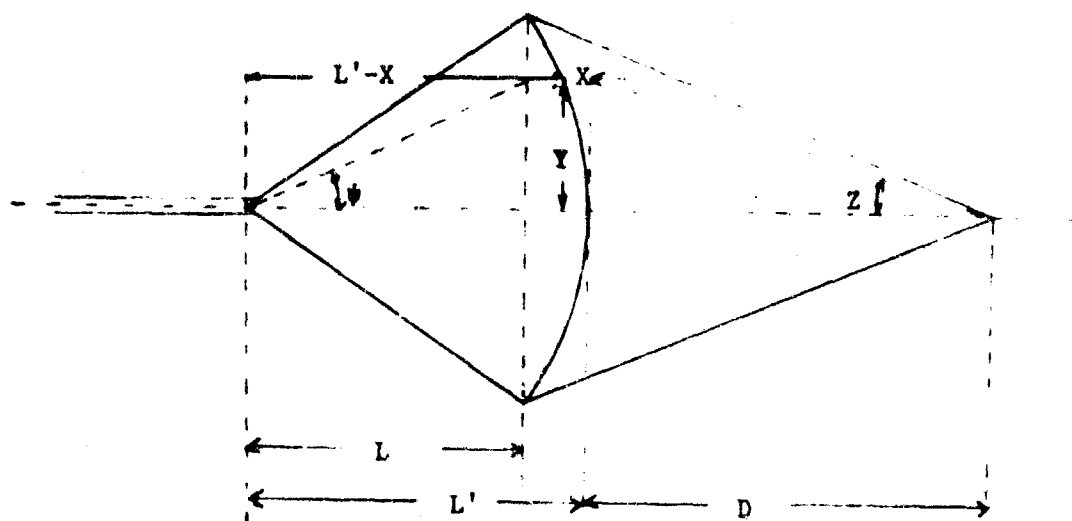plane-wave impedance at $z = 0$. Z_I can be found by transforming

d-13

Figure 5. Sketch of focused beam of radiation.

impedances. At $z = D + W$, the impedance is just Z_{01}, where $Z_{01} = \sqrt{\mu_0/\epsilon}$ is the characteristic impedance of the dielectric. At $z = D$, Z_{01} is transformed to Z_D, where Z_D is given by

$$Z_D = \frac{Z_{00}\left[Z_{01} + jZ_{00}\tan kW\right]}{\left[Z_{00} + jZ_{01}\tan kW\right]} \tag{17}$$

where $Z_{00} = \sqrt{\mu_0/\epsilon_0}$ is the characteristic impedance of free space, and $k = \omega\sqrt{\mu_0\epsilon_0}$. At $z = 0$, Z_D is transformed to Z_I, where

$$Z_I = \frac{Z_{01}\left[Z_D + jZ_{01}\tan \beta D\right]}{\left[Z_{01} + jZ_D\tan \beta D\right]} \tag{18}$$

and $\beta = \omega\sqrt{\mu_0\epsilon}$. The magnitude of the reflection coefficient in Region I is given by

$$|\rho| = \frac{\left|Z_I/Z_{00} - 1\right|}{\left|Z_I/Z_{00} + 1\right|} \tag{19}$$

and the standing-wave ratio by

$$S = \frac{1 + |\rho|}{1 - |\rho|} \tag{20}$$

For narrow cracks, $kW \ll 1$ and Equation 1 can be simplified to

$$Z_D \approx \frac{Z_{00}\left[Z_{01} + jZ_{00}\,kW\right]}{\left[Z_{00} + jZ_{01}\,kW\right]}$$

$$Z_D \approx Z_{01} + j\left(Z_{00} - \frac{Z_{01}^2}{Z_{00}}\right)kW \tag{21}$$

Equations 17, 18, 19, and 20 were programmed on a computer to determine the behavior of S as a function of frequency. Some results are shown in Figure 6. It is clear from the values for D and W accompanying the curves that the period of S is related to D and the amplitude of the ripple in S is related to W.

Some insight into these relations can be obtained by considering two limits -- a crack of zero width and a crack of infinite width. When $W = 0$, $Z_I = Z_{01}$ and

d-15

$$|\rho| = \frac{\left|\sqrt{\epsilon_o/\epsilon} - 1\right|}{\left|\sqrt{\epsilon_o/\epsilon} + 1\right|}$$

$$S = \frac{1 + |\rho|}{1 - |\rho|} = \sqrt{\frac{\epsilon}{\epsilon_o}}$$

Thus for a crack of zero width, S is constant with frequency. For $\epsilon/\epsilon_o = 12$, $S = 3.46$. This is the average value of S in Figure 6.

For an infinite crack, $Z_D = Z_{00}$ and

$$Z_I = Z_{01} \left[\frac{Z_{00} + jZ_{01} \tan \beta D}{Z_{01} + jZ_{00} \tan \beta D}\right]$$

$$\rho = \frac{j\left[\left(\frac{Z_{01}}{Z_{00}}\right)^2 - 1\right] \tan \beta D}{2\frac{Z_{01}}{Z_{00}} + j\left[\left(\frac{Z_{01}}{Z_{00}}\right)^2 + 1\right] \tan \beta D} = \frac{j\left(\frac{\epsilon_o}{\epsilon} - 1\right) \tan \beta D}{2\sqrt{\frac{\epsilon_o}{\epsilon}} + j\left(\frac{\epsilon_o}{\epsilon} + 1\right) \tan \beta D} \qquad (22)$$

$$|\rho| = \frac{\left|\frac{\epsilon_o}{\epsilon} - 1\right| \left|\tan \beta D\right|}{\sqrt{4\frac{\epsilon_o}{\epsilon} + \left(\frac{\epsilon_o}{\epsilon} + 1\right)^2 \tan^2 \beta D}} \qquad (23)$$

It is clear from Equation 23 that $|\rho|$ and hence S is a strong function of frequency because of the $\tan \beta D$ term. When $\tan \beta D = 0$ $|\rho| = 0$ and $S = 1$. When $\tan \beta D \to \infty$,

$$|\rho| = \frac{\left|\frac{\epsilon_o}{\epsilon} - 1\right|}{\frac{\epsilon_o}{\epsilon} + 1}$$

$$S = \frac{\epsilon}{\epsilon_o}$$

Thus for an infinite crack, S is a periodic function of frequency with

d-16

Incident plane-
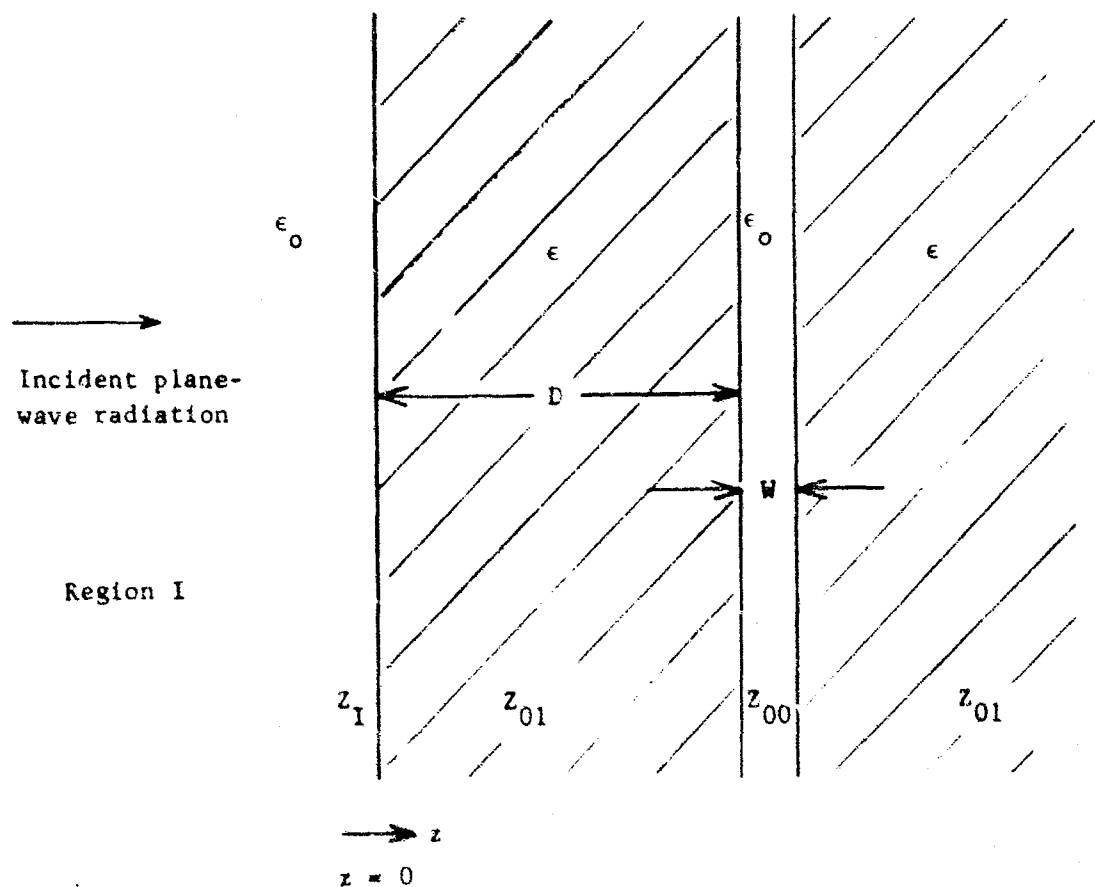wave radiation

Region I

ϵ_o ϵ ϵ_o ϵ

D

W

Z_I Z_{01} Z_{00} Z_{01}

z

$z = 0$

Figure 6.   Geometry used in calculating plane-wave reflection
            from a crack in a dielectric.

d-17

a maximum value of ϵ/ϵ_0 and a minimum value of 1. The period of S is found from

$$\Delta \beta D = \pi$$

$$2\pi\Delta f \sqrt{\mu_0 \epsilon'} \, D = \pi$$

$$\Delta f = \frac{1}{2D\sqrt{\mu_0 \epsilon'}} = \frac{c}{2D\sqrt{\frac{\epsilon}{\epsilon_0}}}$$

where c is the velocity of light in free space. Therefore D can be found from

$$D = \frac{c}{2\Delta f \sqrt{\frac{\epsilon}{\epsilon_0}}} \qquad (24)$$

where Δf is the difference in frequency from one peak to the next in S.

When a narrow crack is present, $|\rho|$ is much more complicated than the expression in Equation 23 and Equation 24 is not strictly true. However, as shown by the curves in Figure 6, Equation 24 gives a good measure of D for the cases shown. To a good approximation, the period of S is related to D by Equation 24, and the amplitude of the ripple in S is related to the width of the crack W. The larger W is, the larger the magnitude of the ripple is. When $W \to \infty$, the magnitude of the ripple in $S \to \epsilon/\epsilon_0 - 1$.

Some examples will illustrate how D can be found from the curves in Figure 7. From curve ①, peaks occur at 71.02 and 70.44 GHz. Hence $2\Delta f = 0.58$, and using Equation 24

$$D = \frac{3(10^{10})}{(.58)(3.46)10^9} = 14.95 \text{ cm}$$

Thus D is obtained from the curve and Equation 24 is 14.95 cm compared to the actual value of 15 cm. From curve ②, $2\Delta f = 71.08 - 70.35 = 0.73$ GHz. Then Equation 24 gives D as 11.89 cm compared to the actual value of 12 cm. Similarly, from curve ③, $2\Delta f = 71.02 - 70.44 = 0.58$ GHz, and D = 14.95 cm as compared to the actual value of 15 cm. From curve
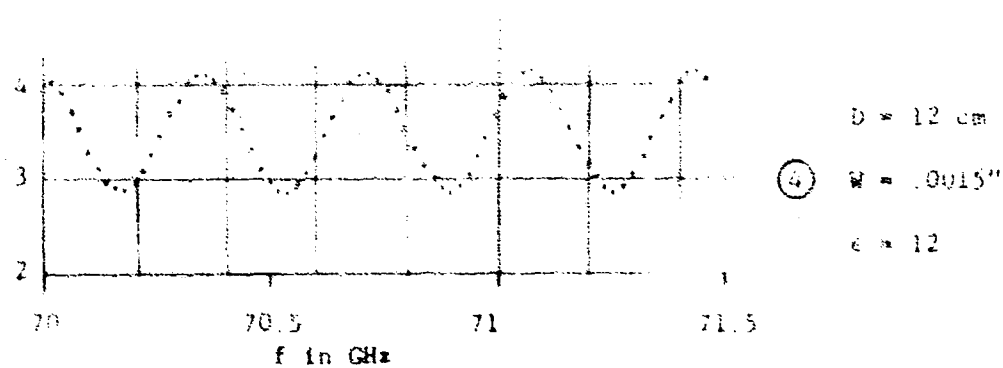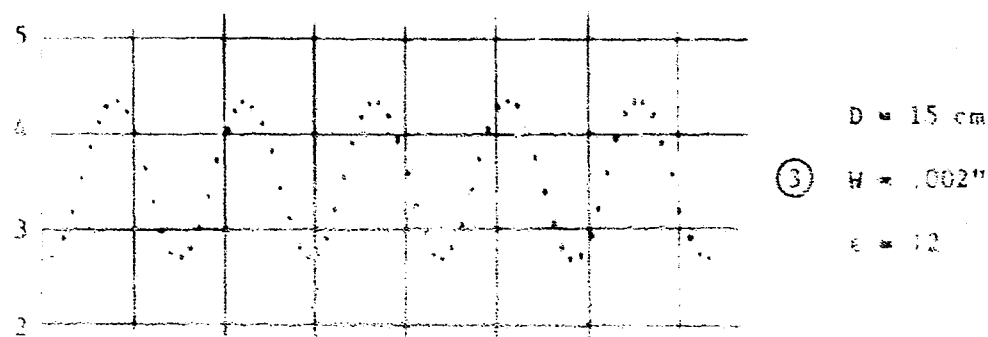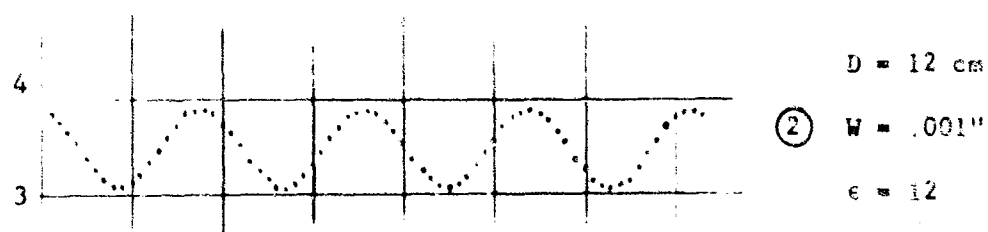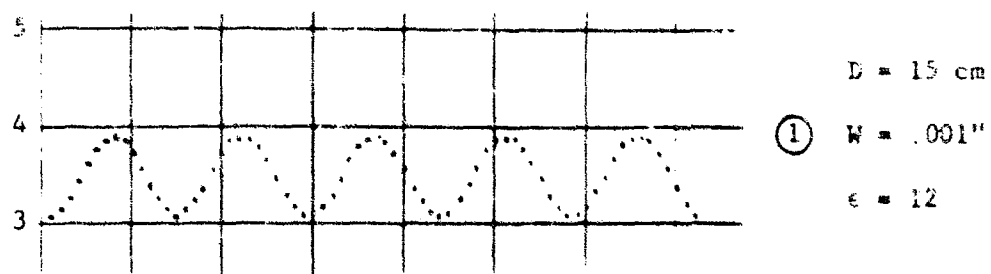
Figure 7. Plot of the computer data showing standing-wave ratio versus frequency.

(4), $2\Delta f = 71.08 - 70.36 = 0.72$ GHz. This gives $D = 12.05$ as compared to the actual value of 12 cm. This illustrates how the curves of S versus f can be used to determine D.

3.2 *Verification of Antenna Capabilities (C. H. Durney and R. W. Grow)*

The main effort has been to demonstrate that sufficient directivity can be achieved to make meaningful measurements in a particular direction either with a one-antenna transmitter-receiver combination or a two-antenna combination with the transmitter and receiver connected to separate antennas. In addition it was desired to demonstrate that reflections from a crack could be observed with a directive antenna.

The initial experiments were attempted at 70 GHz where a well-designed horn antenna shown in Figure 8 and with antenna patterns shown in Figure 9 was available. A klystron and most other necessary components with the exception of a slotted line were also available. The effort was made to modify a slide screw tuner for use as a slotted line, but this proved unsuccessful. The effort was then made to make confirming experiments with 26-40 GHz equipment. A slotted line and a klystron were available along with other necessary wave guide components. The major problem in this frequency band was the unavailability of an antenna. An antenna similar to that available at 70 GHz scaled to the 26-40 wave guide band was fabricated from sheet aluminum. Experimental results indicated that this antenna was not really as good as the prototype and had considerable loss and some inherent reflections.

The effort was then made to make experimental measurements of the reflections from the blocks of propellants. Figure 10 shows the measured VSWR from two 3" x 6" x 6" blocks placed such that the energy passed through the 3" block, encountered a crack, and then passed through the second 3" block. Comparison of these results with the theory of Section 3.1 was very encouraging, particularly since the frequency spacing corresponding to the period checks the theoretical value for a 3" spacing between the two reflections quite closely.

$$D = \frac{c}{2\Delta f \sqrt{\frac{\epsilon}{\epsilon_o}}} = \frac{3 \times 10^{10}}{2 \times 0.85 \times 10^9 \times 3.5} \approx 5 \text{ cm} = 2"$$

d-20
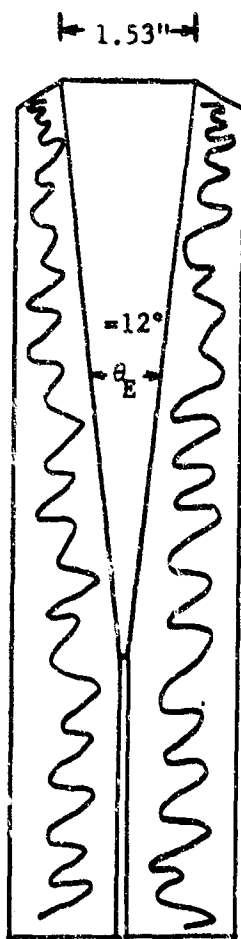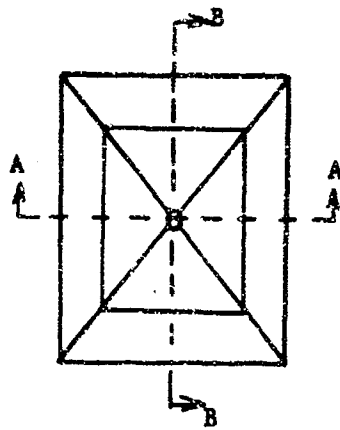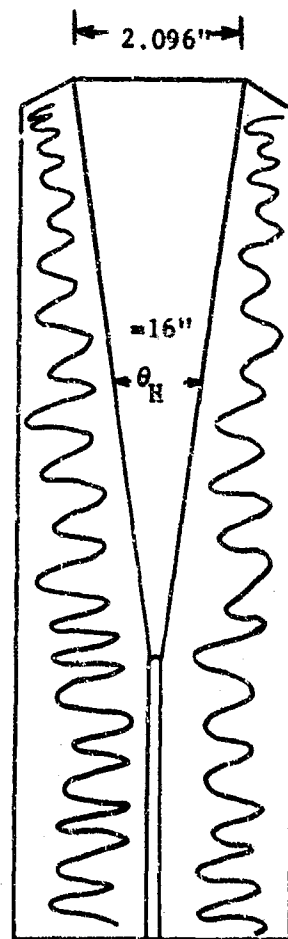
Figure 8. Basic design of 71.4 Gc horns.

d-21
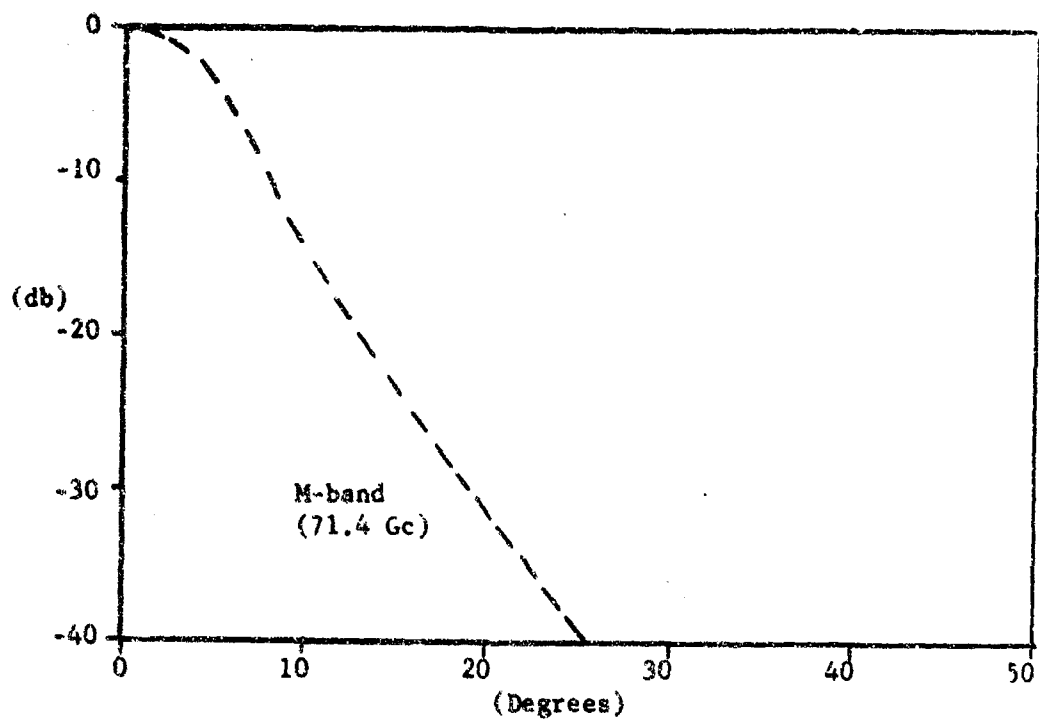
Figure 9.   E-plane patterns for M-band horn antennas.
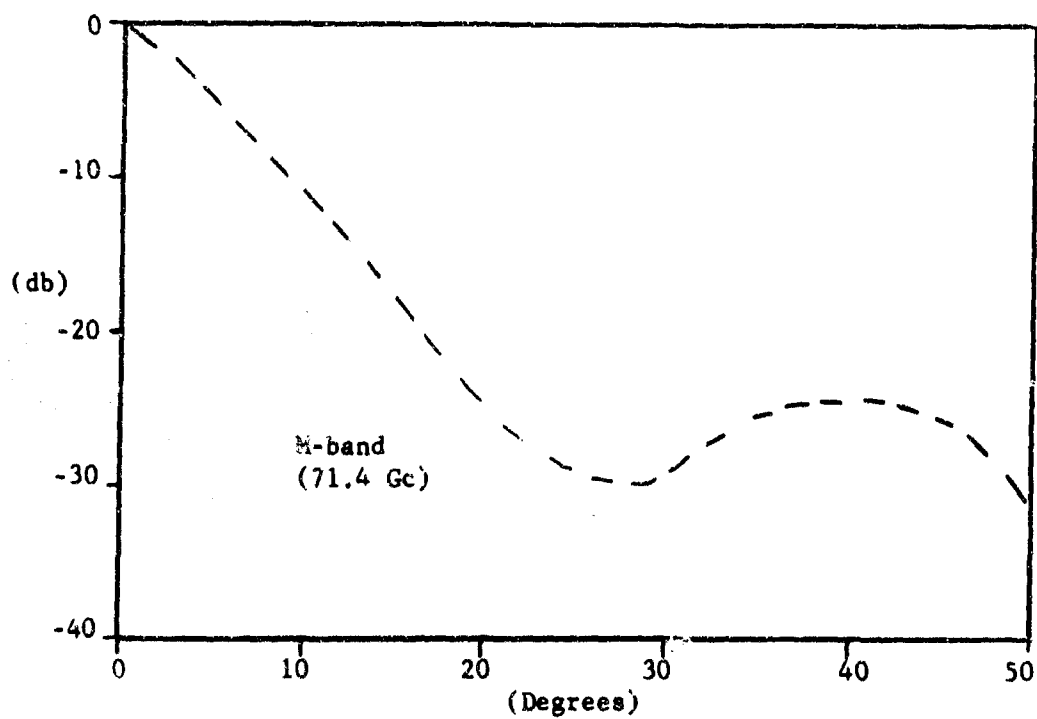
Figure 9.   H-plane patterns for M-band horn antennas.

d-22
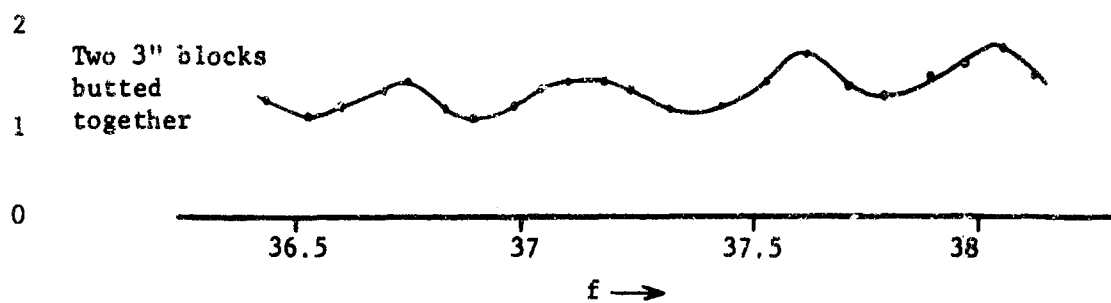
Figure 10. Measured VSWR from two blocks of propellant.

Other measurements soon demonstrated, however, that this rippled behavior was independent of the block since the same periodicity was characteristic of one 3" block, one 6" block or anything else except no reflection, in which case the match was close to perfect VSWR = 1.

These facts suggested that the material was considerably more lossy than previously measured and reported by other workers. The next effort was devoted to measuring the loss of the propellant around 36-40 GHz. A block of propellant the size of the wave guide cross section was fabricated 0.46" in length so that it could be inserted in the wave guide, and a short was also fabricated. The short proved to be very effective with a VSWR of about 80 to 1. The propellant block was then inserted in the wave guide and the data of Figure 11 were recorded. These results indicated that the reflection of the propellant was about equal to the reflection of the short attenuated with a double pass through the propellant. Since the expected VSWR of the propellant is about 3.5, then the effective reflection coefficient of the short is

$$\rho = \frac{3.5 - 1}{3.5 + 1} = 0.55$$

Since $\rho = 1$ from the short, then the two-way loss through 0.46" of propellant is 5.2 db. Hence the loss is

$$\frac{L_{db}}{in} = \frac{5.2}{0.92} = 5.75 \frac{db}{in}$$

An alternate approach may be taken. The period for 0.46" is

$$\Delta f \sqrt{\frac{\epsilon}{\epsilon_o}} = \frac{c}{2D} = \frac{3 \times 10^{10}}{2 \times 0.46 \times 2.54}$$

$$= 1.28 \times 10^{10}$$

$$= 12.8 \times 10^{9} \text{ GHz}$$
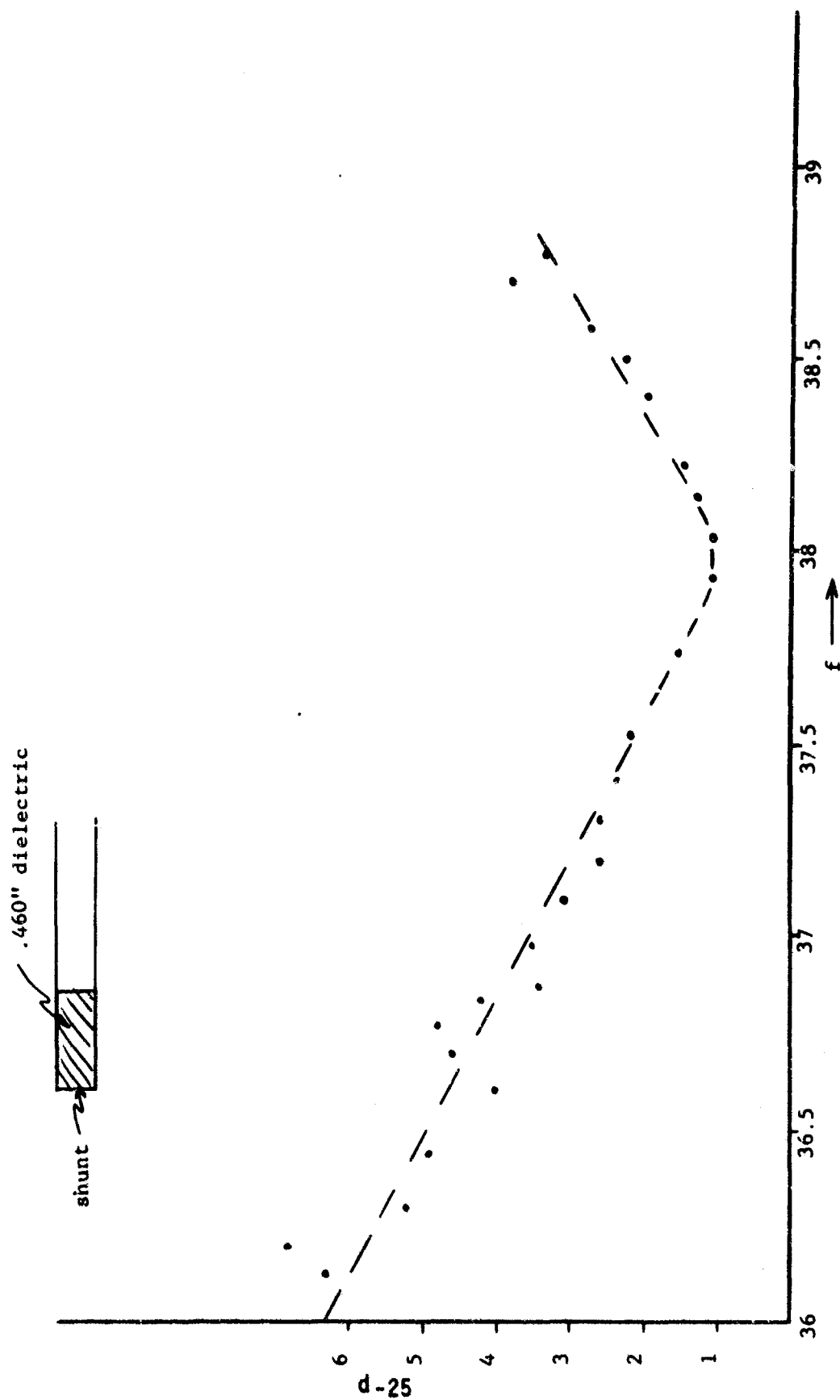
Figure 11. VSWR produced by propellant in a shorted wave guide.

If $\sqrt{\epsilon/\epsilon_0}$ = 3.5, then

$$\Delta f = \frac{12.8}{3.5} = 3.66 \text{ GHz}$$

Although the klystron did not tune over a wide enough bandwidth to
obtain a complete period, it is apparent that the half period is greater
than 2 GHz. Estimating that the peak VSWR must be close to 7.5 gives a
value of $\sqrt{\epsilon/\epsilon_0}$ = 2.74 rather than 3.5 and a period of 4.66 GHz, which
looks more reasonable than the 3.66 GHz above. Following through on
this logic would give a reflection coefficient of

$$\rho = \frac{2.74 - 1}{2.74 + 1} = 0.465$$

and a loss figure of

$$\frac{L_{db}}{in} = \frac{6.65}{0.92} = 7.2 \frac{db}{in}$$

Thus it appears that the dielectric constant around 38 GHz is close to
$\sqrt{7.5}$ and the loss is close to 7.2 db/in.

These facts explain why the crack was not observed in the initial
measurements reported in this section.

3.3 *Feasibility of Microwave Techniques (R. W. Grow)*

The information presented in Sections 3.1 and 3.2 is encouraging
in some respects since the theoretical basis of the method is proved,
but the physical loss of the propellant is much larger than expected
and increases the complexity of any experimental system for applying
the technique. At least two possibilities exist for overcoming the
loss. These are as follows:

     1. Filling the horn antenna with dielectric material.

     2. Amplifying the observed frequency-dependent
        variations.

The effort will be made to show how these facts can help solve the
problem.

The first possibility is important because the major problem with
a large amount of loss is the large reflection with a VSWR near 2.74
that occurs at the front face of the propellant. If the magnitude of

d-26

this reflection is reduced, the net result is an effective amplification of the ripple that will be observed. Since alumina has a dielectric constant of about 9, then the effective impedance transformation would be from 3 to 2.74, which will minimize the amount of reflection from the first boundary. One other technique that can be applied is to reduce the size of the incident wave in the detector to account for the loss of the wave guides and horn antenna.

In addition the horn antenna filled with dielectric will be one-third as large as the unfilled horn, once again improving the realizability of the microwave detection. It is still proposed that the technique be applied at 70 GHz so that the size of the horn shown in Figure 1 would be reduced by one-third.

The second possibility cited earlier can be utilized either with the first possibility or without it so as to amplify the variations thus received. The experimental setup is illustrated schematically in Figure 12. It is believed that the device proposed can be made into a reliable instrument.
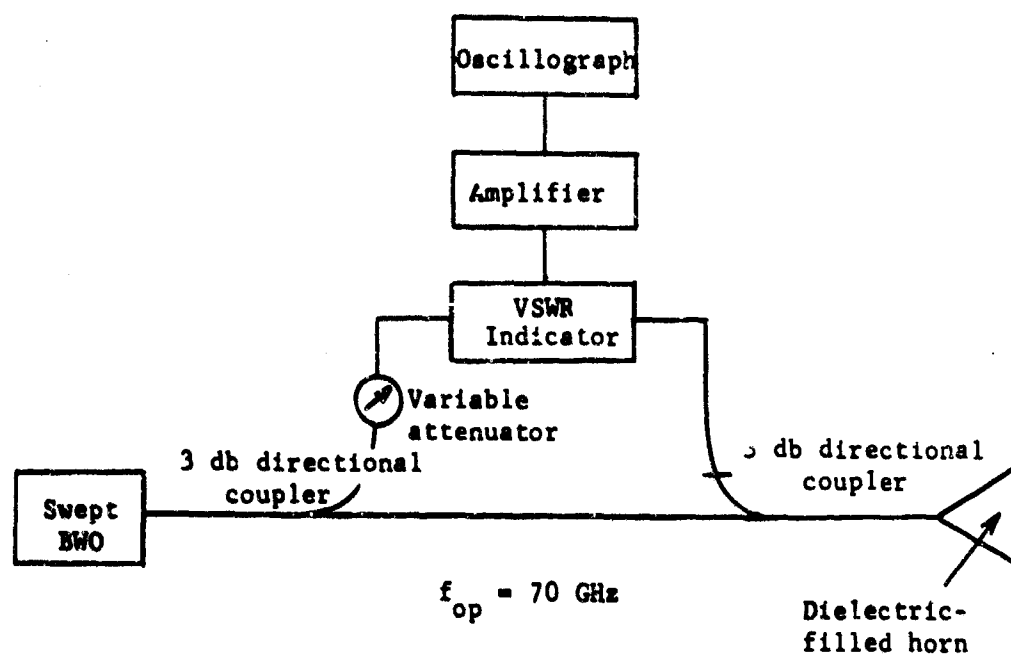
Figure 12. Schematic of the proposed experimental setup.

REFERENCES

1. Jones, A. S., Grow, R. W., and Johnson, C. C., "Microwave Diagnosis of Non-ideal Plasmas," Technical Report SSD-2, September 1963, classified Confidential.

2. Grow, R. W., Johnson, C. C., and Jones, A. S., "Multi-Frequency Attenuation Measurements Made on the Exhausts of Solid Propellant Rockets," Conference on Ions in Flames and Rocket Exhausts, Palm Springs, California, October 10-12, 1962, classified Confidential.

3. Grow, R. W., Johnson, C. C., and Jones, A. S., "Microwave Diagnostics of Plasmas," International Symposium on Plasma Phenomena and Measurement, San Diego, California, October-November 1963. Transactions PTGNS, January 1964.

4. Technical Documentary Report No. FFD-TDR-64-225, November 30, 1964, Vols. 1 and 2. Prepared under Contract No. AF 04(695)-439 by the Hercules Powder Company and the University of Utah Microwave Device and Physical Electronics Laboratory, classified Confidential.

THE CHEMISTRY AND MECHANICS OF COMBUSTION
WITH
APPLICATIONS TO ROCKET ENGINE SYSTEMS

TASK 5 High Solids Loading in Propellants

J. E. Fitzgerald

October 1968

College of Engineering
UNIVERSITY OF UTAH
Salt Lake City, Utah

PREFACE

A fundamental problem in the practical use of solid propellant rocket motors is that of stress analysis. While ballistic properties are equally critical, the motor must be a sound mechanical system, capable of undergoing the purely mechanical loads which may be imposed. This immediately necessitates the ability to analyze these systems. Moreover, since the minimization of weight is desirable, it is important that analysis be very good, thereby allowing optimization with a large degree of confidence.

Initial analysis techniques applied were those of linear elasticity. The results of such analyses naturally did not reflect the problem accurately, due to the viscous nature of propellant materials. Subsequent use of linear viscoelasticity proved generally profitable, although erroneous results still occur for highly solid loaded propellants. It seems clear that the theory of nonlinear viscoelasticity is potentially more useful, and that further study is desirable.

For the above reasons, the study discussed herein was undertaken. It is intended that the mechanical and thermal characterization of propellants be carried out, in a closely allied theoretical and experimental program. The theoretical results will guide experimental efforts and permit the development of a truly descriptive theory of propellant behavior. At the completion of these preliminary steps, the studies of continua from the mechanics point of view will be extended to embrace the chemical and molecular morphological aspects in conjunction with investigators of Task 1.

TABLE OF CONTENTS
TASK 5   High Solids Loading in Propellants

1.0 INTRODUCTION

As a logical prelude to engineering use of the equations of state connecting stress, strain, time, and temperature, a determination will be made of the proper mathematical formulation for the governing constitutive equations in conjunction with appropriate laboratory tests. These results will be integrated with the objectives of Task 6 which is concerned with high rate and high stress inputs to rate and temperature dependent materials.

2.0 DEFORMATION AND BALANCE FOR NON-POLAR MATERIALS

Consider a material body, B, with bounding surface, S, consisting of particles or material points possessing continuous mass density, ρ, in all configurations. In the reference state at time zero, t = o, each particle will be labeled with a position vector $\underset{\sim}{X}$ having coordinates X_K, K = 1, 2, 3 referred to the origin in Euclidean 3 - space.

Where the spatial vector of a geometric point location in the 3 - space is x with coordinates x_k, k = 1, 2, 3, the motion of a material particle of the body may be designated as

$$\underset{\sim}{x} = x \, (\underset{\sim}{X}, t) \tag{1}$$

which describes the location, $\underset{\sim}{x}$, of the particle $\underset{\sim}{X}$ at subsequent time, t. These are called Eulerian or spatial coordinates.

An alternate form for the motion is

$$\underset{\sim}{X} = X \, (\underset{\sim}{x}, t) \tag{2}$$

which describes which particle, $\underset{\sim}{X}$, occupies location $\underset{\sim}{x}$, at time t; Lagrangian or material coordinates.

A motion of the body B is thus a continuous sequence of configurations

in time denoted by $\underset{\sim}{x} = x\,(\underset{\sim}{X},t)$ or in component notation by $x_k = x_k(X_K,t)$.

The deformation gradient (Eulerian) is the spatial partial derivative of the motion, $\underset{\sim}{x}$, of particle X with respect to the neighboring particles,

$$x_{k,K} \equiv \frac{\partial x_k(X_K,t)}{\partial X_K} \qquad (3)$$

The Lagrangian deformation gradient is the spatial partial derivative of the material at point $\underset{\sim}{x}$ with respect to neighboring geometric points;

$$X_{K,k} \equiv \frac{\partial X_K(x_k,t)}{\partial x_k} \qquad (4)$$

The chain rule of differentiation yields the relation

$$x_{k,K}X_{K,\ell} = \delta_{k\ell} \; ; \; X_{K,k}\, x_{k,L} = \delta_{KL} \qquad (5)$$

where δ is the Kronecker delta.

The square of the distance between two material points is dS^2 with

$$dS^2 = c_{k\ell}\, dx_k dx_\ell \qquad (6)$$

where
$$c_{k\ell}(\underset{\sim}{x},t) \equiv \underset{\sim}{c}_k \cdot \underset{\sim}{c}_\ell = X_{K,k}\, X_{K,\ell}, \text{ the} \qquad (6\text{-}a)$$

Cauchy deformation tensor and the distance between two points in the deformed configuration is

$$ds^2 = C_{KL}\, dX_K dX_L \qquad (7)$$

with
$$C_{KL}(\underset{\sim}{X},t) \equiv C_K \cdot C_L = x_{k,K}\, x_{k,L}, \text{ Greens} \qquad (7\text{-}a)$$

deformation tensor (both are symmetric and positive definite).

The Lagrangian strain tensor is then defined as

$$2E_{KL} \equiv C_{KL}\,(\underset{\sim}{X},t) - \delta_{KL} \qquad (8)$$

e-2

and the Eulerian as

$$2e_{k\ell} \equiv \delta_{k\ell} - c_{k\ell} \; (\underline{x}, t) \qquad\qquad (8\text{-}a)$$

Continuity of matter is expressed by the positive semi-definite requirement on the Jacobian

$$0 < J \leqslant M \; ; \; M < \infty \qquad\qquad (9)$$

with $\qquad J = \dfrac{\rho_0}{\rho} = \det \; \dfrac{\partial x_k}{\partial X_K} \qquad$ where ρ_0 is the reference

mass density.

The other balance equations necessary are (Reference 1)

Balance of mass:

$$\dot{\rho} + \rho V_{k,k} = 0 \quad \text{in} \quad \tilde{B} \qquad\qquad (10)$$

Balance of momentum:

$$t_{k\ell,k} + \rho \; (f_\ell - \dot{V}_\ell) = 0 \quad \text{in} \quad \tilde{B} \qquad\qquad (11)$$

Balance of moment of momentum:

$$t_{k\ell} = t_{\ell k} \; \text{(non-polar)} \quad \text{in} \quad \tilde{B} \qquad\qquad (12)$$

Balance of energy:

$$\rho \dot{\varepsilon} = t_{k\ell} \; V_{\ell,k} + q_{k,k} + \rho h \quad \text{in} \quad \tilde{B} \qquad\qquad (13)$$

Clausius-Duhem inequality (Rate of Entropy production) in $\tilde{B}$

$$\rho\gamma \equiv \rho\dot{\eta} - \rho \; \frac{h}{\theta} - \text{div} \; \frac{\underline{q}}{\theta} \geqslant 0 \quad \text{in} \quad \tilde{B} \qquad\qquad (14)$$

where $\tilde{B} \subset B - \sigma(t)$ with

$\sigma(t)$ a moving discontinuity surface in B and

V_k = velocity = $\dfrac{\partial x_k}{\partial_t}$ $\underline{X}$

$t_{k\ell}$ = stress tensor

f_ℓ = body force per unit mass

ϵ = internal energy density/unit mass

$\underset{\sim}{q}$ = inward directed heat vector to surface S

h = energy source/unit mass

θ = temperature

η = entropy/unit mass

γ = local entropy production defined by Eq. (14)

The related jump conditions are, related to the above

Mass continuity jump on $\sigma(t)$

$$[\rho \underset{\sim}{v}] \cdot \underset{\sim}{n} - [\rho] \underset{\sim}{v} \cdot \underset{\sim}{n} = 0 \qquad \text{(10-a)}$$

Momentum jump on $\sigma(t)$

$$[t_{k\ell}] n_k - [\rho v_\ell \underset{\sim}{v}] \cdot n + [\rho v_\ell] \underset{\sim}{v} \cdot n = 0 \qquad \text{(11-a)}$$

Moment of momentum on $\sigma(t)$

$$t_{k\ell} = t_{k\ell} \qquad \text{(12-a)}$$

Energy jump on $\sigma(t)$

$$[(\rho \epsilon + \tfrac{1}{2} \rho v_\ell v_\ell)(v_k - v_k) - t_{k\ell} v_\ell - q_k] n_k = 0 \qquad \text{(13-a)}$$

Entropy jump on $\sigma(t)$

$$[\rho \eta (\underset{\sim}{v} - \underset{\sim}{v})] \cdot \underset{\sim}{n} - [\underline{S}] \cdot \underset{\sim}{n} \geq 0 \qquad \text{(14-a)}$$

e -4

where

$$\underline{v} \cdot \underline{n} = \text{normal component to } \sigma(t) \text{ of material velocity}$$

$$\underline{u} \cdot \underline{n} = \text{normal component of jump surface velocity}$$

$$\underline{S} = \text{entropy influx across } \sigma(t)$$

2.1 *Constitutive Equations*

2.1.1 Introduction

Whereas the deformation and balance equations are restrictions on the motion of any material, the so-called constitutive equations are necessary to specify the characteristics of a given class of materials. It is in this area that three different approaches may be used, namely

(a) Axiomatic - which ensures internal logic and consistency, but which may not describe any material of interest or may be in error based upon unfounded axiomatic choices.

(b) Empirical - which will generally correctly describe the material behavior over precisely those inputs used to determine the constitutive laws in the first place, but will probably be incorrect beyond that domain. Also the "laws" are unable to violate basic physical premises.

(c) Boot-strapping, - involves coupling of the axiomatic approach with carefully selected tests to both verify chosen axioms and to elucidate alternate mechanisms.

The third approach is the primary method to be used in this present research program.

2.1.2 Basic Axioms

2.1.2.1 Axiom of equipresence[2]

"A quantity present as an independent variable in one constitutive equation is so present in all, to the extent that its appearance is not forbidden by the general laws of physics or rules of invariance".

2.1.2.2 Axiom of objectivity[1]

The motion of a body shall not reflect the difference in observers (or in another form, the frame of reference).

e-5

Where $\underset{\sim}{x}$ and $\underset{\sim}{x}$ are two different frames of reference, they shall be forced to coincide by a rigid body motion, Q_k, and a time shift, b, where

$$\bar{x}_k(\underline{X},\bar{t}) = Q_{k\ell}(t)x_\ell(\underline{X},t) + b_k(t) \qquad (15)$$

where $\underline{Q}(t)$ is a proper orthogonal transformation, $\underline{b}(t)$ is a translation, and $\bar{t}$ is a time shift with $\bar{t} = t - a$. The axiom states that all constitutive equations must be form invariant for all $\underline{Q}$, $\underline{b}$, and a. Many of the older rheological equations and "ad hoc" 3-dimensionalized viscoelastic equations violate this axiom and hence have doubtful meaning in a physical sense. The transformation, Q, obeys the rules $(Q^T = Q$ transpose)

$$\underline{Q}\,\underline{Q}^T = \underline{Q}^T\,Q = I \qquad \det\underline{Q} = +1 \qquad (16)$$

(for $|\det\underline{Q}| = 1$ we have spatial isotropy).

Invariance with $\underline{b}$ implies spatial homogeneity (not material homogeneity) and the $\bar{t}$ shift implies time constancy of the material. This last time shift would not be removed for materials with aging characteristics, however,* because the shift would refer to a reference state, tr, and would only shift a newly made material to a new reference state tr.

2.1.2.3 Axiom of Memory

Classical elastic materials possess no memory and respond only to the forces imposed at the present time. Viscoelastic materials, however, can be shown to possess memory or hereditary characteristics[3]. Some materials have been characterized as having a fading or short term memory[4] with a rather thorough thermodynamic treatment. Lastly, a viscoelastic material may be considered rate dependent and respond to all time derivatives of the force at the present time or form a constitutive equation in differential equation forms [1].

It is in this axiom that the problem of material characterization arises when coupled with (14) and (14-a) the Clausius-Duhem inequality.

---

* Note: This is an example for which observation would restrict the axioms used.

2.1.3 Theoretical Problem

Consider a material where, to generalize, we assume the present value of stress is determined by the entire past motion history of the entire body, then

$$\underset{\sim}{t}(X,t) = \underset{B}{\underset{\sim}{f}}(X,t,\underset{\sim}{x}(\bar{X},t-s)) \quad , \quad 0 \leqslant s < \infty \tag{17}$$

where $\underset{\sim}{f}$ is a functional whose present value depends on the motion history, $\underset{\sim}{x}$, the time t, and the particle X. Thus memory, aging effects, and inhomogeneity are included.

We next assume that the motions causing stress are short range in effect so that we need consider the history of motion $\bar{X}_{N(X)}$, only in the neighborhood of X. Application of the objectivity axiom[5] then restricts the general constitutive equation(17) to one where the history of the deformation gradients rather than the history of motion as such governs the response[6].

Thus, (17) becomes

$$\underset{\sim}{t}(X,t) = \underset{\sim}{f}(F(X,t-s)) \quad ; \quad 0 \leqslant s < \infty \tag{18}$$

where herein F is the deformation gradient history at the material point X. So that finally we have

$$t_{k\ell} = F_{KL}(\underset{\sim}{C},\underset{\sim}{X}) X_{K,k} X_{L,\ell} \tag{19}$$

where $\underset{\sim}{C} = \underset{\sim}{C}(t-s)$ expresses the history of the Green deformation tensor.

The principal of equipresence can now be invoked to write the constitutive equations for stress, heat flow, internal energy, and entropy in two different forms: (1) Hereditary materials, or (2) Rate dependent materials.

2.1.3.1 Hereditary Materials

In this case, one has

$$t_{k\ell} = F_{KL}(\underset{\sim}{C}(t-s); \theta(t-s), \underset{\sim}{X}) X_{K,k} X_{L,\ell} \tag{20-a}$$

$$q_k = Q_K(\underline{C}(t-s); \theta(t-s), \underline{X}) \, X_{K,k} \qquad (20\text{-}b)$$

$$\epsilon = E(\underline{C}(t-s); \theta(t-s), \underline{X}) \qquad (20\text{-}c)$$

$$\eta = N(\underline{C}(t-s); \theta(t-s), \underline{X}) \qquad (20\text{-}d)$$

wherein the entire history of the strain, $\underline{C}$, and temperature, θ, for each material point, $\underline{X}$, are included. It is implicit in the above relations that the temperature history includes the gradient of the temperature, $\theta_{,k}$.

2.1.3.2 Rate Dependent Material

If the time histories are sufficiently smooth to allow a Taylor expansion of the type

$$x(\underline{X};t') = x(\underline{X};t) + (t'-t)\dot{x}(\underline{X};t) + \ldots + \left(\frac{t'-t}{p!}\right)^p x^{(p)}(\underline{X};t) \qquad (21)$$

for all the independent variables (axiom of smooth memory), and if the neighborhoods are assumed smooth enough to allow a similar expansion about the point X, we obtain the constitutive relations for rate dependent non-simple materials, namely

$$
\begin{aligned}
t_{k\ell} = F_{KL}[& C_{MN}, \dot{C}_{MN}, \ddot{C}_{MN}, \ldots C_{MN}^{(p)} \\
& C_{MN,k}, C_{MN,k_1 k_2}, \ldots C_{MN,k_1} \cdots k_Q \\
& \dot{C}_{MN,k}, \ddot{C}_{MN,k} \cdots C_{MN,k}^{(p)} \\
& \theta, \dot{\theta}, \ddot{\theta}, \ldots \theta^{(p)} \\
& \theta_{,k_1}, \theta_{,k_1 k_2} \ldots \theta_{,k_1} \cdots k_Q \\
& \dot{\theta}_{,k}, \ddot{\theta}_{,k} \cdots \theta_{,k}^{(p)}, X \,] \, X_{K,k} \, X_{L,\ell} \qquad (22\text{-}a)
\end{aligned}
$$

$$q_k = Q_k[C_{MN}, \dot{C}_{MN}, \ddot{C}_{MN}, \text{------}\theta_k^{(P)}, X] \, X_{K,k} \qquad (22\text{-}b)$$

$$\varepsilon = E[C_{MN}, \dot{C}_{MN}, \ddot{C}_{MN}, \text{------}\theta_k^{(P)}, X] \qquad (22\text{-}c)$$

$$\eta = N[C_{MN}, \dot{C}_{MN}, \ddot{C}_{MN}, \text{------}\theta_k^{(P)}, X] \qquad (22\text{-}d)$$

wherein the F_{KL}, Q_k, E, N are now not functionals but rather tensor valued functions of the P rates and Q gradients of the independent variables with

$$x^{(P)} = \left. \frac{\partial^P x}{\partial t^P} \right|_{\underline{X}'}$$

The memory here comes about in a limited way through the higher rate and gradient derivatives.

We thus see that the memory functional under proper smoothness conditions on time yields from

$$c(t\text{-}s) = c(t) - s\dot{c}(t) + \frac{s^2}{2} \ddot{c}(t) + \cdots \qquad (23)$$

the relation

$$T[(t\text{-}s)] = F(C, \dot{C}, \ddot{C}, \cdots) \qquad (24)$$

where F is a function. Similar results hold for the gradient expansion. Materials whose dependence on X vanishes (homogeneity) and whose gradient dependence is no greater than the first derivative are called simple materials and will be used for the rest of the exposition since the main experimental points do not depend on the higher spatial gradients. Thus the rate dependent simple material constitutive equations become

$$t_{k\ell} = \varepsilon_{KL}(C_{MN}, \dot{C}_{MN}, \ddot{C}_{MN}, \cdots C_{MN}^{(p)},$$
$$\theta, \dot{\theta}, \ddot{\theta}, \cdots \theta^{(p)}$$
$$\theta_{,k}, \dot{\theta}_{,k}, \ddot{\theta}_{,k}, \cdots \theta_{,k}^{(p)}) \, X_{K,k}, X_{L,\ell} \qquad (25)$$

and the simple memory type materials yield

$$t_{k\ell} = F_{KL}(\underset{\sim}{C}(t-s); \theta(t-s), \theta,_k(t-s)) \, X_{K,k}, X_{L,\ell} \tag{26}$$

with analogous expressions for ϵ, η and q.

It should be remarked at this point that in actual practice there is some overlay between the two forms of expression discussed above. For example, assume a simple hereditary linear material whose constitutive equation can be expressed by the Lebesgue-Stieltjes integral in the form

$$\underset{\sim}{t} = \int_{-\infty}^{t} G(t-s)\partial\epsilon(s) \tag{27}$$

Riesz[7] has shown in a 1909 paper that the expression (27) is the most general linear functional possible with certain boundedness conditions on $\partial\epsilon(s)$. When the strain history has discontinuities in the strain or any of its derivatives (as occurs in a constant strain rate test using two successive values of the rate) certain discontinuity terms or saltus functions arise so that the Riemann form of the integral then becomes

$$\underset{\sim}{t} = \int_{-\infty}^{t} G(t-s) \frac{\partial\epsilon}{\partial s} \, ds + \sum_{i=1}^{r} a_i \epsilon(s_i) + \sum_{j=1}^{m} b_j \dot{\epsilon}(s_j) + \ldots + \sum_{k=1}^{q} g_k \epsilon^{(k)}(s_k) \tag{28}$$

where there may be discontinuities in any of the strain rate histories of magnitude $\epsilon^{(k)}(S_k)$ at time S_k back from time t. This behavior is commonly seen in the case where $a_i = G(t)$ and the $b_i = \eta(t)$, the relaxation modulus and viscosity, respectively. Thus for certain non-smooth strain histories, the hereditary functional form of a simple linear material can lead to rate effects explicitly appearing in the constitutive expression.

2.1.4 Thermodynamic Restrictions

Returning to (14), the Clausius-Duhem form of the second law of thermodynamics, we see that this equation must be satisfied by all of the constitutive equations if we are to have a thermodynamically admissible form of

e-10

expression. Upon introducing the expressions

$$\dot{C}_{KL} = D \frac{C_{KL}}{Dt} = 2d_{k\ell} \, x_{k,K} \, x_{\ell,L} \qquad (29)$$

where the deformation rate tensor is

$$d_{k\ell} = \frac{1}{2} \left(V_{k,\ell} + V_{\ell,k} \right) \qquad (30)$$

and the free energy, ψ, is defined

$$\psi \equiv \epsilon - \theta\eta$$

we can rewrite (14) as

$$- \frac{\rho}{\theta} \left(\dot{\psi} + \eta\dot{\theta} \right) + \frac{1}{\theta} \, t_{k\ell} \, V_{\ell,k} - \frac{1}{\theta^2} \, q_k \theta_{,k} \geq 0 \qquad (31)$$

for all independent processes. If furthermore, it is assumed that the stress functional for t can be separated by assuming a stored energy part and a dissipative part, then one can write (c=Green tensor following),

$$\underline{t} = {}_E\underline{F}(c, \, \theta, \, \theta_{,k}) + {}_D\underline{F}(c, \, \dot{c}, \, \ddot{c}, \, \theta, \, \dot{\theta}, \, \cdots \,) \qquad (32)$$

2.1.4.1 Rate Type Material Restrictions

Substituting (25), with the temperature rates eliminated, as well as the temperature gradient for convenience, and for rate type materials

$$t_{k\ell} = F_{KL}(c, \, \dot{c}, \, \ddot{c}, \ldots c^{(p)}, \, \theta) \, X_{K,k}, \, X_{L,\ell} \qquad (33\text{-}a)$$

$$q_k = Q_k(c, \, \dot{c}, \, \ddot{c}, \ldots c^{(p)}, \, \theta) \, X_{k,k} \qquad (33\text{-}b)$$

$$\epsilon = E(c, \, \dot{c}, \, \ddot{c}, \ldots c^{(p)}, \, \theta) \qquad (33\text{-}c)$$

$$\eta = N(c, \, \dot{c}, \, \ddot{c}, \ldots c^{(p)}, \, \theta) \qquad (33\text{-}d)$$

into (31) we obtain expressions where the coefficients of the independent

variables are set equal to zero since these variables can be changed arbitrarily. The coefficients then lead to the following restrictions on the constitutive equations;

$$t_{k\ell} = 2\rho \frac{\partial \psi}{\partial c_{kL}} x_{k,k} x_{L,\ell} + \frac{\rho}{\rho 0} {}_D F_{kL} x_{k,K} x_{\ell,L} \tag{34}$$

$$q_k = 0 \quad \text{(no heat conduction)} \tag{35}$$

$$\varepsilon = \psi - \theta \frac{\partial \psi}{\partial \theta} \tag{36}$$

$$\eta = - \frac{\partial \psi}{\partial \theta} \tag{37}$$

with the free energy,

$$\frac{\partial \psi}{\partial c_{kL}^{(p)}} = 0 \tag{38}$$

and the dissipation,

$$_D F_{kL} \dot{c}_{kL} - 2\rho_0 \sum_{\alpha=1}^{p-1} \frac{\partial \psi}{\partial c_{kL}^{(\alpha)}} c_{kL}^{(\alpha+1)} \geq 0 \tag{39}$$

We note that if $\dot{c} = \ddot{c} = \ldots = c^{(p)} = 0$

then

$$_D F_{kL} = 0 \quad \text{and} \quad \frac{\partial \psi}{\partial c_{kL}^{(n)}} = 0 \qquad n = 1,2 --, p - 1$$

showing that the dissipation is at least linear in the strain rate but is independent of strain. The free energy has no linear strain rate dependence. For the condition $c, \dot{c} \neq 0 \quad \ddot{c} = \dddot{c} = \ldots = c^{(p)} = 0$, (39) yields

$$_D F_{kL} \dot{c}_{kL} - 2\rho_0 \left\{ \frac{\partial \psi}{\partial \dot{c}_{kL}} \ddot{c}_{kL} \right\} \geq 0 \tag{40}$$

Since $\ddot{c} = 0$, $_D F_{kL} \dot{c}_{kL} \geq 0$ and dissipation occurs. If $\ddot{c} \neq 0$, we obtain

$$_D F_{kL} \dot{c}_{kL} - 2\rho_c \left\{ \frac{\partial \psi}{\partial \dot{c}_{kL}} \ddot{c}_{kL} \right\} \geq 0 \quad \text{and} \quad \frac{\partial \psi}{\partial \dot{c}_{kL}} = 0 \tag{41}$$

e-12

Thus the free energy is independent of $\overset{\cdot}{c}$ but the dissipation is now

$$D^F{}_{kL} \geqslant 2\, \rho_0\, \frac{\overset{\cdot}{c}_{kL}}{\overset{\cdot}{c}_{kL}}\, \frac{\partial \psi}{\partial \overset{\cdot}{c}_{kL}} \tag{42}$$

and the stress is (for the equality)

$$t_{k\ell} = 2\,\rho\, \frac{\partial \psi}{\partial c_{kL}}\, x_{K,k}\, x_{L,\ell} + 2\,\rho\, \frac{\overset{\cdot}{c}_{kL}}{\overset{\cdot}{c}_{kL}}\, \frac{\partial \psi}{\partial \overset{\cdot}{c}_{kL}}\, x_{K,k}\, x_{L,\ell} \tag{43}$$

and we have that the second derivative affects the stress dissipation.

Those familiar with classical physics will perhaps be annoyed with the notion that certain state variables such as the free energy are herein functions of the strain rates and, implicit in the smooth time history expansion, are therefore path dependent.

However, tentative acceptance of this result is logically better than either denying the existence of strain rate dependent materials (Maxwell models) or abandoning the concept of equipresence until experimental verification causes such a course of action. The usual linear theory uses only a c and $\overset{\cdot}{c}$ in the function and thus avoids this problem.

2.1.4.2 Hereditary Material Restrictions

Applying the same procedure to (26) with $\theta,_k$ and X suppressed leads to

$$t_{k\ell} = 2\, \frac{\rho}{\rho_0}\, x_{k,k} x_{L,\ell}\, \frac{\partial \Sigma}{\partial c_{kL}} + \frac{4\rho}{\rho_0}\, x_{K,k} x_{L,\ell} \int_0^t \phi_{kLMN}(s) \overset{\cdot}{c}_{MN}(s)\, ds \tag{44}$$

Where we have neglected higher order integrals, Σ is herein a stress potential $= \rho_0 \psi$.

Including the discontinuity terms of (28) again introduces second order rate effects.

2.1.5 Experimental Aspects

The second and higher order rate terms can be properly eliminated only after experimental verification. The linearization of the thermodynamics equations or other methods do not properly face the problem. The importance of the results is obvious in that too many thermomechanically coupled problems produce several fold disparities in the predicted and observed results.

e-13

2.1.6. Current Experimental and Theoretical Program

The theoretical development of both rate dependent and hereditary materials, with discontinuous strain histories is continuing. The purpose here is to solve various coupled thermomechanical strain inputs so that observable differences in the response as compared to linear theory can be predicted. It will of course be desirable here to separate strain energy and entropy effects on the observed stresses. Experimental effort is now under way to explicitly evaluate the effect of both $\dot{\varepsilon}$ and $\ddot{\varepsilon}$ (strain rate and second derivative effects). In order to accomplish this task two operational amplifiers have been adapted as a function generator for the Instron testing machine. By this means a continuous parabolic input strain function with continuous first derivative is produced. The second derivative is discontinuous and of constant value between the discontinuities (but of reversing sign). This test should definitively show whether any of the materials being tested are of the $\ddot{\varepsilon}$ rate type in the context herein. Further tests relative to the coupled heat conduction are in the preliminary stages, including those pertaining to bulk compression effects. Since volumetric changes are important in the analysis, a precision gas dilatometer has been constructed and tests are currently under way on highly filled polymers.

The resolution of the above problems on a closely coupled theoretical-experimental approach is considered necessary before one can with confidence handle the thermal stress problems and high loading rate problems of highly filled solid propellant materials.

REFERENCES

1. Eringen, A. C., <u>Mechanics of Continua</u>, John Wiley and Sons, New York, 1967.

2. Truesdell, C., <u>Six Lectures on Modern Natural Philosophy</u>, Springer-Verlay, New York, 1966, p.42.

3. Volterra, V., Theory of Functionals
   Blacke and Son Limited, 1930.

4. Coleman, B. and Noll, W., "Revue of Modern Physics," Vol. 33, p. 239.

5. Leigh, D. C., <u>Nonlinear Continuum Mechanics</u>, McGraw-Hill Book Co. Inc., New York, 1968, p.148.

6. Eringen, A. C. and Grot, R. A., "Continuum Theory of Nonlinear Visco-elasticity," Purdue University, Report No. 32, October 1965.

7. Riesz, Nagy, <u>Functional Analysis</u>, Ongar, 1960.

THE CHEMISTRY AND MECHANICS OF COMBUSTION
WITH
APPLICATIONS TO ROCKET ENGINE SYSTEMS

TASK 6 Transition to Detonation Mechanisms

G. A. Secor

October 1968

College of Engineering
UNIVERSITY OF UTAH
Salt Lake City, Utah

PREFACE

The question of detonation mechanisms is of direct importance to solid propellant rocket fuels. Conditions leading to detonation occur as a result of high frequency mechanical disturbances, such as strong shock waves; which can be induced by direct environmental or tactical loadings.

The process of detonation is one whereby energy is released more rapidly than it can be carried away from a zone behind the wave front. The energy released then generates the shock ahead of it. The mechanism by which this energy is made available is open to question. In fact, there is perhaps no single mechanism that is responsible for the process. Various methods of production of the required energy have been postulated, all aimed at producing "hot-spots," small areas in which the energy is concentrated, so that an amount of energy not sufficient for detonation of the total mass can cause local chemical reaction. Such mechanisms include (a) compression of interstitial gases, (b) intergranular friction, and (c) high-velocity flow.

The mechanisms above seek a micro-explanation to the problem. A possible macro-explanation to the same problem lies in the area of continuum mechanics--specifically in the area of viscoelasticity. It is well known that many materials are most adequately described neither as elastic nor as a fluid, rather as a viscoelastic medium. Such materials exhibit effects characteristic of both regimes, yet are solids. In particular, these materials allow energy to be irreversibly dissipated in mechanical processes. Hence, the study of the viscoelastic response of propellant-like materials to high rate, high intensity loadings may throw new light upon possible detonation mechanisms.

The purpose of this study is to explore a mechanism in which viscous dissipation is the proximate cause of detonation, taking the theory of viscoelasticity as a starting point.

TABLE OF CONTENTS
TASK 6   Transition to Detonation Mechanisms

1.0 INTRODUCTION

This task involves an investigation of the mechanisms whereby mechanically imposed shock waves can cause propellant materials to become thermally unstable and detonate. The immediate objective is to explore a viscous dissipation mechanism by formulating the field equations governing the viscoelastic deformation in a continuum, with specific attention focussed upon the equation of state and the effects of rate dependence of the several observable parameters. Our initial presupposition therefore is that dissipative effects due to viscoelastic material response can cause sufficient internal temperature rise to induce detonation. By implication, effects of thermomechanical coupling are deemed important, as well as nonlinearity in material response.

The project began with the background study of general articles related to detonation, particularly those in the area of coupled thermo-viscoelasticity and viscoelastic wave propagation. Two conclusions were reached: (1) extensive literature exists in the theoretical area of coupled thermoviscoelasticity, but the actual amount of correlation with experimental data is rather small; (2) the analytical solution of problems in shock wave propagation is beyond the state of the art for materials of the type under consideration, leaving numerical techniques as the only reasonable approach.

It was therefore decided that study be directed toward experimental measurements on shock waves, the nature of various dissipative mechanisms, and an exploration of numerical analysis techniques.

2.0 EXPERIMENTAL WORK

This particular phase of the project is being carried on in conjunction with experimental studies into the range of linearity of viscoelastic materials. The behavior of materials is viewed as presenting a spectrum from low level stress waves to high intensity waves for which the materials behave essentially as fluids. Thus the comparison study is conceived as one in which the systematic exploration of the transition region is begun.

A facility is nearing completion by which both projects may be served. The aim is the capability to test samples of representative materials under shock conditions. This facility consists, as shown in the accompanying photos, of a gas shock tube which allows a traveling shock wave to impinge on the end of a specimen. The shock is provided by rupturing a diaphragm between a driver chamber containing high pressure gas and the shock tube itself. For this task the aim of the studies will be to determine the mechanical and state variables (velocity, temperature, etc.) necessary to evaluate the material constants appearing in any proposed constitutive law. In this area Tasks 5 and 6 share many of the same aims--i.e. a determination of the specific constants which appear in any material characterization. While Task 5 is essentially involved only in state tests, Task 6 is concerned with dynamic tests. It is not possible, in practice, to fully evaluate material behavior by only static or dynamic testing.

In order to gain the above information, the shock tube is being instrumented as fully as possible. Pressure transducers are mounted on the tube to monitor incident and reflected pressure, the output being displayed on an oscilloscope. Particle velocity measurements will be made by magnetic techniques as used by other investigators.[1, 2] An attempt will be made to measure temperature rise due to the wave passage. Tentative plans call for use of thermocouples embedded in the material for this measurement. While the rise time of the thermocouple is anticipated to be too long for instantaneous measurements, the heat conductivity of the materials involved is small enough that some idea of instantaneous results will be gained.

The facility is now in the check-out stage.

3.0 THEORETICAL STUDIES

3.1 *The General Problem*

The solution to a general problem in material behavior consists of a set of "functions" satisfying the following equations:

1. conservation of mass

$$\dot{\rho} + \rho \dot{u}_{i,i} = 0 \tag{1}$$

2. conservation of momentum

$$\sigma_{ij,j} = \rho \ddot{u}_i \tag{2}$$

3. conservation of energy

$$\sigma_{ij} \dot{u}_{i,j} - q_{i,i} = \rho \dot{e} \tag{3}$$

and initial and boundary conditions. In the above equations the superposed dot indicates the time derivative (material derivative), and the subscripts denote spacial derivatives.* These equations introduce a number of functions; density ρ, displacement vector components u_i, stress tensor components σ_{ij}, internal energy e, temperature T, and heat flux vector components q_i. Additionally, there may be applied body forces in (2) and internal heat supply in (3). Inspection of (1), (2), and (3) indicates that the number of independent equations is only 5, while there are 15 unknown functions. This discrepancy is rectified by constitutive laws--relations which identify the material behavior.

Constitutive laws fall into three types: (1) stress-strain laws; (2) heat flow laws; and (3) equations of state. The stress-strain laws are of the form

$$\sigma_{ij} = F(\text{———————}). \tag{4}$$

The heat flow laws are of the form

$$q_i = G(\text{———————}). \tag{5}$$

The equation of state has the form

$$\epsilon = H(\text{——— ———}). \tag{6}$$

---

* A rectangular cartesian reference system is used so that distinction between covariant and contravariant derivatives is unnecessary.

The notation (—————————)indicates that the arguments are the relevant quantities in each case. There are then 10 additional equations to make the system well-determined. For the moment the forms of (4)--(6) remain unspecified.

The solutions of classical elasticity are concerned only with (2) in a linearized form. The only relevant constitutive law is (4), in the usual notation

$$\sigma_{ij} = \lambda\delta_{ij} u_{k,k} + \mu (u_{i,j} + u_{j,i}). \tag{7}$$

The classical heat conduction problem uses only (3), (5) and (6). In (3) the statement is made that heat flow goes into an increase in internal energy and mechanical work is neglected; in (6) the internal energy is made only a function of temperature; and for (5) we have the well-known Fourier law

$$q_i = -k\frac{\partial T}{\partial x_i} . \tag{8}$$

Either of these problems in independent of the other. In both cases voluminous literature is available. The further complication that is not unfamiliar is the partially coupled theory. In this case the heat conduction problem is unchanged, but the stress is allowed to depend on temperature as in the linear th ry where the additional term $(-3 \alpha K(T-T_o)\delta_{ij})$ appears on the right hand side of (7), k being the bulk modulus, α the coefficient of expansion, and T_o a reference temperature at which the body is unstressed. The temperature problem can then be solved independently, and applied as an input to the stress problem.

The above restrictive cases have in common the feature that internal energy is either neglected or only a function of temperature. When the fully coupled problem is considered, one must admit that (4), (5), and (6) can, in general, all involve the independent variables u_i, t, and derivatives of these quantities. In fact, the whole history of the independent variables may be necessary to yield the instantaneous values of σ_{ij}, Q_i, and e. Now the general problem is far more complex, both qualitatively and quantitatively. Mechanical disturbances cause thermal disturbances, and vice versa. It is not only difficult to solve these problems exactly, it is also difficult to

be sure what this sort of coupling means in any but simple problems. The most critical difficulty, however, lies in the area of establishing equations (4)--(5). In particular, (4) and (6) are open to much speculation. Probably the most pertinent work is that of Coleman[3] in the area of thermoviscoelasticity. This is so because the irreversible effects of such theories could lead to temperature rises during the passage of waves.

As a result of the considerations discussed above, some time has been devoted to the study of coupled theories of thermoviscoelasticity. These studies have led to the production of two internal technical reports[4, 5]

3.2 *Constitutive Law*

In principle, the problem stated above is solvable given the constitutive laws (4)--(6). That is, it could be done numerically, in a step-by-step fashion, if in no other way. The constitutive laws embody the differences that are observed in response of various materials to loads, and are consequently the critical link in the solution process. It is this area that is presently under study by many investigators. As a guide to constructing constitutive laws, certain principles should be observed:

1. Equipresence: If in (4)--(6) a certain independent variable appears as the argument in one equation, it should be assumed present in all until otherwise demonstrated.

2. Material indifference: the material behavior is independent of observer's coordinate system and thus all constitutive laws should be written so that an arbitrary rigid rotation of the body does not change the law.

There are additional such requirements, but these are the only two which need explicit mention in our present context. Another guide in formulating constitutive laws is the Second Law of Thermodynamics--the rate of entropy production is greater than or equal to zero, never negative. This law is regarded as a restriction on any constitutive relation for any admissible process. With such requirements as these, a rational study of constitutive laws is possible.

For the present purpose the validity of the usual Fourier Law of heat

f-5

conduction is accepted. Such acceptance, however, is not necessary. For example, reference (6) discusses the classical law as a first-order approximation to a more general law. Reference (3) admits a history dependence of the heat flux on strain and temperature. It is of some interest to study the heat flow phenomenon for the following reason: if, in fact, the diffusion type equation is replaced by, e.g., a wave equation, then heat flow is no longer an instantaneous effect.

References (5, 7, 8, 9) discuss the general problem of coupled thermoviscoelasticity. The approach used in (7) is to define a non-equilibrium thermodynamics. The material law used there is one in which equilibrium is characterized by a hydrodynamic law, and no shear stresses are developed at equilibrium. For non-equilibrium processes, shear stress can be developed so that a solid-like behavior is observed. Such a constitutive law is essentially a fluid theory, and is not desired for the present study.

Coleman (3) has studies constitutive laws in materials with fading memory.* He assumes that the stress, internal energy, and heat flux are functionals of the history of the deformation gradient ("strain"), and temperature, and of the present value of grad T. To be consistent with the Second Law of Thermodynamics, it is then necessary that the dependence on grad T vanish from the stress and internal energy. Thus, the constitutive laws for stress and internal energy can be written

$$\tilde{\sigma} = \overset{\infty}{\underset{s=0}{\tilde{F}}} [\tilde{F}(t-s), T(t-s)]$$

$$\tag{9}$$

$$e = \overset{\infty}{\underset{s=0}{\tilde{E}}} [\tilde{F}(t-s), T(t-s)] .$$

In (9) $\tilde{\sigma}$ and $\tilde{F}$ are the stress and displacement gradient tensors, and the notation $\overset{\infty}{\underset{s=0}{\tilde{F}}}$, $\overset{\infty}{\underset{s=0}{e}}$ indicates the dependence of $\tilde{\sigma}$ and E on all values of the arguments for $-\infty < \tau \le t$. This result is of interest in the formulation of constitutive laws as it indicates the variables of primary concern.

---
* Such materials are characterized by the notion that disturbances in the near past produce greater responses than disturbances in the farther past.

Christensen and Naghdi[8] and Lianis[9] have pursued the above question further, making use of a further result of Coleman's. (Christensen and Naghdi actually rederive that result from first principles.) Coleman has also shown that if the free energy is written as a functional of $\tilde{F}$ and T, then the stress and entropy functionals are derivable from the free energy by a process of differentiation. On the other hand, if the entropy is written as a functional of E and $\tilde{F}$, then the stress and temperature are derivable as functionals of E and $\tilde{F}$.

Christensen and Naghdi explore the linear coupled theory in terms of a simple integral form for the free energy, which leads to the results for stress and entropy

$$\sigma_{ij} = D_{ij} + \int_{-\infty}^{t} G_{ijk\ell}(t-\tau,0) \frac{\partial \varepsilon_{k\ell}}{\partial \tau} d\tau - \int_{-\infty}^{t} \phi_{ij}(0,t-\tau) \frac{\partial T}{\partial \tau} d\tau \qquad (10)$$

$$\rho S = \lambda(0) + \int_{-\infty}^{t} \phi_{ij}(t-\tau,0) \frac{\partial \varepsilon_{ij}}{\partial \tau} d\tau + \int_{-\infty}^{t} m(t-\tau,0) \frac{\partial T}{\partial \tau} d\tau \qquad (11)$$

In (10) and (11) ε_{ij} is the usual infinitesimal strain, s the specific entropy, and the other quantities material constants and functions.

Lianis starts directly from Coleman's work and assumes a form for the free energy. This particular form attempts to incorporate the notion of "thermorheologically simple" materials[10] into a single integral expression. The explicit representation for the free energy, ψ, is

$$\psi = \int_{0}^{\infty} \hat{L} \left\{ \tilde{F}(t-s) - \tilde{F}(t), \int_{0}^{s} b[T(t-\lambda) - T_0]d\lambda ; \right.$$

$$\left. \tilde{F}(t), (T(t)-T_0) \right\} b[T(t-s) - T_0]ds . \qquad (12)$$

In (12) $\hat{L}$ is a function, possibly non-linear, of the arguments shown, and the function $b(T-T_0)$ is the so-called shift function familiar to the area of polymers. This particular representation has two virtues that immediately present themselves:

1. The integral is a single one, avoiding the
   unwieldly multiple-integral representation
   of nonlinear viscoelasticity. The nonlin-
   earity is expressed by the nature of $\hat{L}$, an
   ordinary function.

2. The inclusion of the thermorheological simple
   character of many polymers (an experimental
   fact) is appealing.

By the application of the rules whereby constitutive laws are formulated,
the general expression is put into an explicit form consistent with iso-
tropy, material indifference, etc. This form is given in (9).

3.3 *Study Under Thamie*

The approaches by Christensen and Naghdi, and by Lianis, have got-
ten more to the heart of the problem than any other in that an attempt
has been made to display the constitutive law in detail. It would con-
ceivably be possible to measure the functions required. However, it
appears that there still remains a better formulation for computational
purposes.

We proceed from the assumption that any solution to the fully
coupled problems is almost surely going to be numerical. In particular,
it will be a straightforward finite-difference, step-forward-in-time,
solution. Consideration of techniques of this type shows the following
sequence of steps:

1. Given all the stresses at a particular time t_o,
   solve equation (2) for the accelerations.

2. From accelerations determine the new positions
   of points, as well as strains, etc., at $t_o + \Delta t$.

3. Given the stresses, etc., at the time t_o, solve
   for $\dot{E}$ from (3), and thus get the value E at
   $t_o + \Delta t$.

4. From the constitutive laws (4)--(6) determine
   σ_{ij}, q_i, T at $t_o + \Delta t$.

In step 4 it is obvious that it would be far more desirable to have T as a functional of, say, $\bar{F}$ and E, than other variables. This is true because we then derive T from $\bar{F}$ and E directly rather than inverting an integral law of possibly very complex nature. It is, in fact, possible to rationally reach such a representation. This representation is the subject of (4) and (5).

Taking an expression for the entropy in terms of integrals over the history of strain, ε_{ij}, and internal energy E, it is possible to derive, as done in (4), following the ideas of (8), the following expressions for the stress and for the temperature

$$\frac{-\sigma_{ij}}{\rho T} = \int_{-\infty}^{t} G_2(t-\tau) \frac{\partial \varepsilon_{ij}}{\partial \tau} d\tau + \delta_{ij}\left[\int_{-\infty}^{t} G_1(t-\tau) \frac{\partial \varepsilon_{kk}}{\partial \tau} d\tau \right.$$
$$\left. + \int_{-\infty}^{t} \phi(0,t-\tau) \frac{\partial e}{\partial \tau} d\tau \right] , \tag{13}$$

$$\frac{1}{T} = \frac{1}{T_0} + \int_{-\infty}^{t} \phi(t-\tau\ 0) \frac{\partial \varepsilon_{kk}}{\partial \tau} d\tau + \int_{-\infty}^{t} m(t-\tau) \frac{\partial e}{\partial \tau} d\tau . \tag{14}$$

The functions G_1, G_2, ϕ, and m appearing in (13) and (14) are material properties. In a fashion similar to that of Lianis, the entropy functional can be expressed in terms of a linear integral of a nonlinear function of the quantities $\bar{F}$ and E. This yields, as shown in (5), expressions similar to (13) and (14), in which the arguments of the single integral are various derivatives of the original nonlinear function. It is not particularly relevant to display the result obtained here, since it is reasonably complex, and certainly not suggestive of any particular interpretation.

At present, investigation of the meaning of these alternates is being carried on.

4.0 NUMERICAL STUDIES

While the original thought was to adopt some two-dimensional computer program to the present purpose, such ideas have been discarded. The effects of boundaries are significant quantitatively as well as qualitatively in wave propagation problems, but at least the qualitative effects can be inferred. The quantitative effects are rather hard to achieve. In this case the use of two-dimensional computer programs goes beyond the available level of support due to the time-consuming nature of such calculations. As an alternative, the one-dimensional wave propagation program WONDY,[11] has been adapted for use at Utah. The following description of the program is taken from reference (11).

> WONDY is a versatile FORTRAN code for computing wave propagation in one dimension in rectangular, cylindrical or spherical coordinates. The code is based on conventional finite difference analogs to the Lagrangian equations of motion and is similar in many respects to other such codes.
>
> Considerable effort has been expanded to produce a very flexible code. Routines for equations of state or constitutive relations, special boundary routines, radiation energy addition, as well as the initializing routine are written as self-contained subroutines, and new routines are easily written to cover problems not handled by the original set. In this way most problems of motion in one dimension may be handled without difficulty.

Inclusion of internal energy in the program allows the study of temperature rise for assumed equations of state.

5.0 PRESENT STUDIES

At present the possible upper bound on temperature rise in shock
processes is being studied. A variety of elementary mechanisms under
consideration in order to obtain order-of-magnitude quantities. These
mechanisms include viscous effects, i.e. the temperature rise behind a
shock in a Maxwell material, and micro-mechanisms such as bubble col-
lapse and solid inclusions. These simple analyses are intended to
put the various mechanisms into three categories as far as their
ability to produce detonation: impossible, marginal, and likely.
While the idea of Task VI was that viscous effects are responsible
in a large part, it seems wise to deduce a quantitative limit, in
order that redirection of Task VI might occur if warranted.

DOCUMENT CONTROL DATA - R & D

(Security classification of title, body of abstract and indexing annotation must be entered when the overall report is classified)

1. ORIGINATING ACTIVITY *(Corporate author)*	2a. REPORT SECURITY CLASSIFICATION
University of Utah College of Engineering Salt Lake City, Utah 84412	UNCLASSIFIED
	2b. GROUP

3. REPORT TITLE

THE CHEMISTRY AND MECHANICS OF COMBUSTION WITH APPLICATIONS TO ROCKET ENGINE SYSTEMS

4. DESCRIPTIVE NOTES *(Type of report and inclusive dates)*

Scientific   Interim

5. AUTHOR(S) *(First name, middle initial, last name)*

M L Williams

6. REPORT DATE	7a. TOTAL NO. OF PAGES	7b. NO. OF REFS
October 1968	195	122

8a. CONTRACT OR GRANT NO. F44620-68-C-0022	9a. ORIGINATOR'S REPORT NUMBER(S)
b. PROJECT NO. 7921-02	UTEC DO 68-065
c. 6144501F	9b. OTHER REPORT NO(S) *(Any other numbers that may be assigned this report)* AFOSR 69-0178TR
d. 681314	

10. DISTRIBUTION STATEMENT

2. This document is subject to special export controls and each transmittal to foreign governments or foreign nationals may be made only with prior approval of AFOSR (SREO-1)

11. SUPPLEMENTARY NOTES	12. SPONSORING MILITARY ACTIVITY
TECH, OTHER	AF Office of Scientific Research (SREP) 1400 Wilson Boulevard Arlington, Virginia 22209

13. ABSTRACT

The purpose of this program, which is integrated with our academic objectives, is to study the interdependence of combustion processes and the physics-mechanical behavior of solid fuel materials within the context of a rocket engine system. It is intended to capitalize upon a quantitative understanding of molecular structure which affects both the combustion and mechanics behavior, and treat the propellant fuel and associated inert components as a materials system--from processing, to a determination of the constitutive equation as needed to assess structural integrity, and failure under various environmental and loading conditions. Concurrently, the tasks are concerned with propellant as an energy source--from ignition, through burning, gas dynamics, interaction with nozzle and insulation components, and consideration of electron noise and radar attenuation in the plume. Six task areas are presently envisioned, each of which is under the direction of a Principal Investigator. The six areas include: (1) Combustion and Transport Mechanisms (2) Flow and Heat Transfer; (3) Ablation Mechanisms; (4) Radiation Attenuation and Plasma Physics; (5) Mechanics of Solids (6) Transition to Detonation Mechanisms.

KEY WORDS	LINK A		LINK B		LINK C	
	ROLE	WT	ROLE	WT	ROLE	WT
Solid Rockets						
Solid Rocket Combustion						
Ablation Mechanisms						
Microwave Diagnostics						
Crack Detection						
Solid Propellant Mechanics						
Transition to Detonation						